



**MONASH** University

**The effects of rotation and free  
surface proximity on flow-induced  
vibration of a sphere**

by

**Anchal Sareen**

---

A thesis submitted to Monash University

for the degree of

Doctor of Philosophy

---

May 2018

Department of Mechanical and Aerospace Engineering

Monash University



# Copyright notices

1. © Anchal Sareen (2018).

Under the Copyright Act 1968, this thesis must be used only under the normal conditions of scholarly fair dealing. In particular no results or conclusions should be extracted from it, nor should it be copied or closely paraphrased in whole or in part without the written consent of the author. Proper written acknowledgement should be made for any assistance obtained from this thesis.

2. I certify that I have made all reasonable efforts to secure copyright permissions for third-party content included in this thesis and have not knowingly added copyright content to my work without the owner's permission.



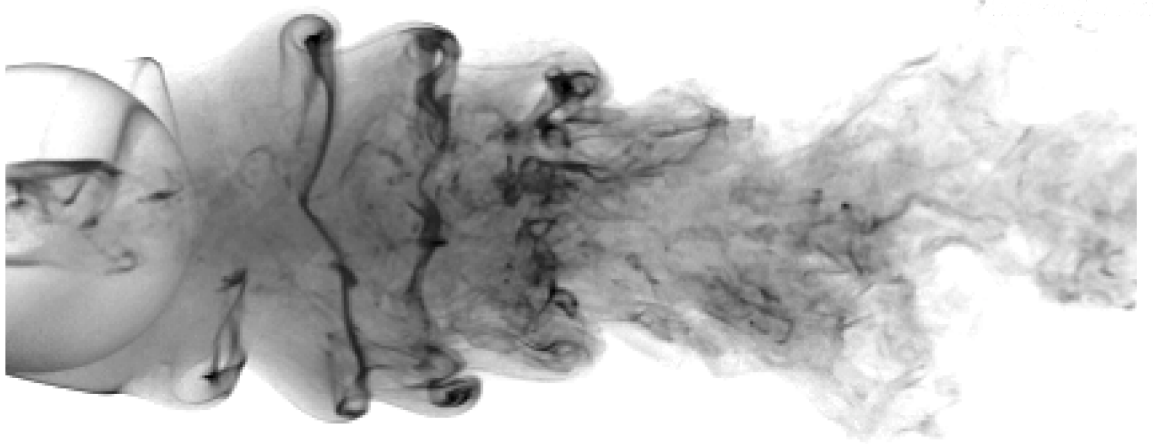


*This thesis is dedicated to my parents  
Kailash Rai,  
and  
Herjas Rani.*



---

*However turbulent or chaotic  
life may seem  
there is always some order  
you can focus on.*



---

re

# Abstract

Flow-induced vibration (FIV) of an elastically mounted sphere represents one of the most generic fundamental fluid-structure interaction problems. Since FIV can lead to structural failures, numerous studies have focused on understanding the underlying principles of FIV and its suppression. This thesis investigates the effects of rotation and surface proximity on the flow-induced vibration of an elastically mounted sphere, employing simultaneous displacement, force and vorticity measurements. It is found that when a constant transverse rotation is imposed onto a sphere, the mean transverse force acting on the sphere increases due to the Magnus Effect. In consequence, the mean position of the sphere oscillation also shifts towards the direction of the Magnus force. Due to asymmetry induced in the wake, the total fluctuating transverse force acting on the sphere decreases. This leads to a progressive decrease in the vibration amplitude response as the rotation ratio is increased.

Similar dynamics are observed when a non-rotating sphere approaches a free surface, whereby an asymmetry in the vortex shedding is observed decreasing the total fluctuating transverse force acting on the sphere. However, in this case, asymmetry is induced due to diffusion of the upper vortex loop (closer to the free surface) into the free surface. On the other hand, the dynamics of a piercing sphere are very different. The vibration response and the associated wake structures of a piercing sphere are found to be very different to that of a fully submerged sphere. The FIV response of a piercing sphere exhibits two different regimes with characteristically different behaviours. Surprisingly, for some immersion ratios, the vibration response is even higher than that for the fully-submerged case.

Apart from the above mechanisms, where the vibrations are reduced in consequence of a reduced fluctuating force acting on the sphere, vibrations can also be reduced by deviating the vortex shedding frequency from the natural frequency of the system, inhibiting the ‘lock-in’ phenomenon. When sinusoidal rotary oscillation is imposed onto a sphere such that its forcing frequency is in close proximity to the natural frequency of the system, vibrations lock to the forcing frequency instead of the natural frequency. Vibrations are greatly suppressed in this ‘lock-on’ region. During lock-on, the wake structures remain similar to those for an oscillating sphere without any imposed rotation; however, there is a change in the timing of the vortex formation. Surprisingly, rotary oscillations can also instigate the intriguing FIV response ‘Rotary-induced vibration’ that is intrinsically different to other previously known FIV responses: combining vortex-induced vibration and galloping.



# Publications and awards from this work

The following is the list of Journal and Conference publications that were derived from the current work:

## Journal Publications

- SAREEN, A., ZHAO, J., LO JACONO, D., SHERIDAN, J., HOURIGAN, K., & THOMPSON, M. C. 2018 Vortex-induced vibration of a rotating sphere. *Journal of Fluid Mechanics* **837**, 258–292.
- SAREEN, A., ZHAO, J., SHERIDAN, J., HOURIGAN, K., & THOMPSON, M. C. 2018 Vortex-induced vibrations of a sphere close to a free surface. *Journal of Fluid Mechanics* **846**, 1023–1058.
- SAREEN, A., ZHAO, J., SHERIDAN, J., HOURIGAN, K., & THOMPSON, M. C. 2018 The effect of rotary oscillation on the flow-induced vibration of a sphere. *Journal of Fluid Mechanics* **855**, 703–735.

## Conference Proceedings

- SAREEN, A., ZHAO, J., LO JACONO, D., SHERIDAN, J., HOURIGAN, K. & THOMPSON, M. C. 2016 Flow past a transversely rotating sphere. *In Proceedings of the 11th International Conference on Flow Induced Vibration and Noise*. The Hague, The Netherlands. 4-6 July 2016. The Hague, The Netherlands.
- SAREEN, A., ZHAO, J., LO JACONO, D., SHERIDAN, J., HOURIGAN, K. & THOMPSON, M. C. 2016 Vortex-induced vibration of a transversely rotating sphere. *In Proceedings of the 20th Australasian Fluid Mechanics Conference*. 5-8 December 2016. Perth, Australia.
- SAREEN, A., ZHAO, J., SHERIDAN, J., HOURIGAN, K. & THOMPSON, M. C. 2018 Effect of free surface on the VIV response of a sphere. *7th Conference on Bluff Body Wakes and Vortex-Induced Vibrations (BBVIV-7)*, 3-6 July 2018. Carry-le-Rouet (Marseille), France

---

## Awards and other achievements

- Recipient of the ‘*David Wilkinson’s award for the outstanding research paper presentation by a student*’ at the 20th Australasian Fluid Mechanics Conference, 5-8 December 2016. Perth, Australia.
- Recipient of Monash University’s Postgraduate Publication Award (PPA). PPA is an award offered to a selected high achieving students for publishing their research work after they have submitted their thesis.
- The publication by the author titled ‘Vortex-induced vibration of a sphere close to a free surface’ has been chosen to be featured on the cover of *Journal of Fluid Mechanics* volume 846.



## Thesis including published works declaration

I hereby declare that this thesis contains no material which has been accepted for the award of any other degree or diploma at any university or equivalent institution and that, to the best of my knowledge and belief, this thesis contains no material previously published or written by another person, except where due reference is made in the text of the thesis.

This thesis includes *two* original papers published in peer reviewed journals. The ideas, development and writing up of all the papers in the thesis were the principal responsibility of myself, the student, working within the Department of Mechanical and Aerospace Engineering under the supervision of Prof. Mark Thompson.

In the case of chapter 5 and chapter 6, my contribution to the work involved the following:

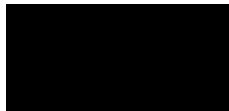
| Thesis Chapter | Publication Title                             | Status                 | Nature and % of student contribution                                     | Co-author name(s) Nature and % of Co-author's contribution*  | Co-author(s), Monash student Y/N* |
|----------------|---|------------------------|--|--|-----------------------------------|
| Chapter 5      | Vortex-induced vibration of a rotating sphere | Published and in press | 85%.<br>Performing experiments, data analysis, paper writing and editing | 1) <b>Jisheng Zhao</b> : Project supervision and paper review.<br>Contribution: NA<br>2) <b>David Lo Jacono</b> : Help in data analysis and paper review<br>Contribution: NA<br>3) <b>John Sheridan</b> : Project conception and supervision.<br>Contribution: NA<br>4) <b>Kerry Hourigan</b> : Project conception, supervision and paper review.<br>Contribution: NA<br>5) <b>Mark Thompson</b> : Project conception, supervision and paper revision.<br>Contribution: NA | No                                |

|           |  |                        |   |   |    |
|-----------|--|------------------------|---|---|----|
| Chapter 6 | Vortex-induced vibration of a sphere close to a free surface                       | Published and in press | 85%.<br>Performing experiments , data analysis, paper writing and editing | <p>1) <b>Jisheng Zhao:</b> Project supervision and paper review.<br/>Contribution: NA</p> <p>2) <b>John Sheridan:</b> Project conception and supervision.<br/>Contribution: NA</p> <p>3) <b>Kerry Hourigan:</b> Project conception, supervision and paper revision.<br/>Contribution: NA</p> <p>4) <b>Mark Thompson:</b> Project conception, supervision and paper revision.<br/>Contribution: NA</p> | No |
| Chapter 7 | The effect of imposed rotary oscillation on the flow-induced vibration of a sphere | Published and in press | 85%.<br>Performing experiments , data analysis, paper writing and editing | <p>1) <b>Jisheng Zhao:</b> Project supervision and paper review.<br/>Contribution: NA</p> <p>2) <b>John Sheridan:</b> Project conception and supervision.<br/>Contribution: NA</p> <p>3) <b>Kerry Hourigan:</b> Project conception, supervision and paper revision.<br/>Contribution: NA</p> <p>4) <b>Mark Thompson:</b> Project conception, supervision and paper revision.<br/>Contribution: NA</p> | No |

---

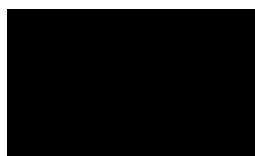
I have not renumbered sections of submitted or published papers to generate a consistent presentation within the thesis.

**Student signature:**



**Date: 1/11/2018**

The undersigned hereby certify that the above declaration correctly reflects the nature and extent of the student's and co-authors' contributions to this work.



**Main Supervisor signature:**

**Date: 1/11/2018**

---

# Acknowledgements

*Time has a wonderful way of showing  
us what really matters*

---

Three and a half years from now, somehow it didn't feel so daunting embarking on this journey alone so far away from my loved ones. Coming from a conservative family, chasing my dreams was not always easy. I am glad that I did it and that my family is by my side. This journey turned out to be a fruitful experience to me not only professionally but also personally as it helped me explore myself in creative ways. I would like to thank everyone who was part of this journey helping and assisting in some way or the other.

Special thanks to my primary supervisors Prof. Mark Thompson, Kerry Hourigan, John Sheridan. Of course, this wouldn't have been possible without their never ending support and guidance. I cannot simply describe in words here how many ways they have helped me achieve this goal. I might need to write another thesis chapter elaborating on this. I also owe sincere thanks my co-supervisor Dr. Jisheng Zhao for his assistance and guidance throughout this journey. I appreciate the time and energy that he invested on this research project. I also thank Asst. Prof. David Lo Jacono who assisted and guided me in the initial stages of the research when I was struggling with the laboratory equipment issues. He helped me go in depth of the problems and troubleshoot them.

I would also like to acknowledge the financial support from Australian Research Council (ARC) Discovery Project grants DP150102879 and DP170100275 for supporting my research. I acknowledge the support of a Monash Graduate Scholarship (MGS) and Monash International Postgraduate Research Scholarship (MIPRS). Furthermore, I would like to acknowledge the Postgraduate Travel Grant Award that included financial contribution from the Department of Mechanical and Aerospace Engineering, Engineering Faculty and Monash University.

I extend my gratitude to the workshop staff especially Hugh Venables, Nat DeRose, Santosh, Mark Symonds, Andrew Smith and Narendra who helped me build the experimental setup. They were always very helpful and gave valuable suggestions whenever I needed them. I will take this opportunity to also thank the administrative staff of the Department of Mechanical and Aerospace Engineering specially Stelios Konstantinidis, Fiona Pyrczak, Bev Pearce, Bill Belbin and Jacelyn Tan for assisting me with the administrative stuff.

I wish to thank all my friends and colleagues who supported me in so many different ways and assisted me maintain my calm over 3.5 years here. Special thanks to my friends: Shantanu, Methma, Komal and my extended family Jag, Mishu, Anika and Indermohan. I also acknowledge the Aikido club members at Monash University. As ironically as it sounds, the Aikido dojo was the place where I felt rejuvenated and

---

centered after a tiring and stressful day. I simply would not have been capable of completing this thesis without the unwavering support and encouragement of my best friend and partner Jagmohan. He also proof read some chapters of this thesis. Finally, I would like to acknowledge the pillars of my strength, my parents: Kailash Rai and Harjas Rani. I shower my heartfelt gratitude to my loving father and mother who supported my decisions and stayed by my side. Without your support, my entire life wouldn't have been possible.

# Nomenclature

## English Symbols

| Symbol           | Description  |
|------------------|--|
| 2D               | Two-dimensional  |
| 3D               | Three-dimensional  |
| $A$              | Oscillation amplitude  |
| $A^*$            | Normalised oscillation amplitude                                   |
| $A_{10}^*$       | Mean of the top 10 percent of the normalised oscillation amplitude |
| $A_{max}^*$      | Maximum normalised oscillation amplitude                           |
| $A_{rms}^*$      | Root mean square normalised oscillation amplitude                  |
| $c$              | Damping coefficient  |
| $k$              | Spring constant  |
| $C_A$            | Added mass coefficient   |
| $C_D$            | Drag force coefficient   |
| $C_L$            | Lift force coefficient   |
| $C_{vor}$        | Vortex force coefficient   |
| $C_y$            | Transverse lift force coefficient                                  |
| $C'_{y_{rms}}$   | Fluctuating transverse force coefficient                           |
| $\overline{C_y}$ | Mean transverse force coefficient                                  |
| $C_{EA}$         | Effective added mass coefficient                                   |
| $D$              | Sphere diameter  |
| $D_r$            | Support rod diameter   |
| $D^*$            | Diameter ratio ( $D/D_r$ )   |
| DOF              | Degree of freedom  |
| $f$              | Oscillation frequency (Hz)   |

*Continued on next page...*

---

*Continued from previous page...*

| Symbol    | Description  |
|-----------|--|
| $f_{na}$  | Natural frequency of the system in air (Hz)  |
| $f_{nw}$  | Natural frequency of the system in water (Hz)  |
| $f_r$     | Forcing frequency (Hz)   |
| $f_R$     | Forcing frequency ratio ( $f_r/f_{nw}$ )   |
| $f_{St}$  | Vortex shedding frequency of a stationary sphere (Hz)  |
| $f^*$     | Normalised oscillation frequency, $f^* = f/f_{nw}$   |
| $F_y$     | Total transverse fluid force   |
| $F_D$     | Drag force   |
| $F_L$     | Total lift force   |
| $F_{vor}$ | Vortex force   |
| FIV       | Flow-induced vibration   |
| FLAIR     | Fluids Laboratory for Aeronautical and Industrial Research                                     |
| $h$       | Immersion depth of the sphere  |
| $h^*$     | Immersion ratio, $h^* = h/D$   |
| $m$       | Total oscillating mass of the system   |
| $m_A$     | Added mass   |
| $m_d$     | Displaced fluid mass, $\pi\rho D^3/6$  |
| $m^*$     | Mass ratio ( $m/m_d$ )   |
| PIV       | Particle image velocimetry   |
| px        | Pixels   |
| $Re$      | Reynolds number based on free-stream velocity and the diameter of the sphere ( $Re = UD/\nu$ ) |
| $St$      | Strouhal number  |
| $t$       | Time   |
| $T$       | Oscillation period   |
| TTL       | Transistor-transistor logic  |
| $u, v, w$ | Velocity components in the x, y and z directions respectively                                  |
| $U$       | Free-stream velocity   |
| $U^*$     | Reduced velocity ( $U/f_{nw}D$ )   |
| $U_S^*$   | Scaled reduced velocity ( $U^*St/f^*$ )  |
| $V$       | Voltage  |

*Continued on next page...*



---

*Continued from previous page...*

| Symbol     | Description                           |
|------------|---------------------------------------|
| VIV        | Vortex-induced vibration              |
| $y$        | Transverse displacement of the sphere |
| $\dot{y}$  | Transverse velocity of the sphere     |
| $\ddot{y}$ | Transverse acceleration of the sphere |

## Greek Symbols

| Symbol               | Description   |
|----------------------|---|
| $\S$                 | Thesis section  |
| $\alpha$             | Rotation ratio ( $\alpha = \omega D/2U$ )                                   |
| $\alpha_R$           | Forcing velocity ratio ( $\alpha = D\dot{\theta}_{max}/2U$ )                |
| $\delta$             | Standard deviation  |
| $\Delta t$           | PIV time interval separating each image pair (ms)                           |
| $\eta$               | Free decay rate   |
| $\mu$                | Dynamic viscosity ( $\text{kg}\cdot\text{m}^{-1}\text{s}^{-1}$ )            |
| $\nu$                | Kinematic viscosity, $\mu/\rho$ ( $\text{m}^2\text{s}^{-1}$ )               |
| $\omega$             | Rotational speed of the sphere  |
| $\rho$               | Density ( $\text{kg}\cdot\text{m}^{-3}$ )                                   |
| $\theta$             | Angular displacement  |
| $\dot{\theta}_{max}$ | Maximum angular velocity of the sphere                                      |
| $\phi_{total}$       | Phase angle between the transverse lift force and the cylinder displacement |
| $\phi_{vortex}$      | Phase angle between the vortex force and the cylinder displacement          |
| $\zeta$              | Structural damping ratio  |
| $\zeta_a$            | Structural damping ratio in air   |
| $\zeta_w$            | Structural damping ratio in water   |

## Subscripts

| Symbol | Description            |
|--------|------------------------|
| $max$  | Maximum addition value |
| $rms$  | Root mean square value |

---

# Contents

|          |  |           |
|----------|--|-----------|
| <b>1</b> | <b>Introduction</b>  | <b>1</b>  |
| 1.1      | Structure of the thesis . . . . .                                | 3         |
| <b>2</b> | <b>A Review of the Literature</b>                                | <b>5</b>  |
| 2.1      | Stationary sphere . . . . .                                      | 5         |
| 2.2      | Vortex-induced vibration of a sphere . . . . .                   | 12        |
| 2.2.1    | Modes of Vibration . . . . .                                     | 12        |
| 2.2.2    | Effect of the mass-damping parameter and mass ratio . . . . .    | 15        |
| 2.2.3    | Wake structures . . . . .  | 15        |
| 2.3      | Effect of transverse rotation . . . . .                          | 20        |
| 2.4      | Effect of sinusoidal rotary oscillation . . . . .                | 22        |
| 2.5      | Effect of free surface on the VIV response of a sphere . . . . . | 24        |
| 2.6      | Chapter summary and research questions . . . . .                 | 26        |
| <b>3</b> | <b>Experimental Methodology</b>                                  | <b>29</b> |
| 3.1      | Overview . . . . .   | 29        |
| 3.2      | Experimental arrangement . . . . .                               | 29        |
| 3.3      | Displacement measurements . . . . .                              | 31        |
| 3.4      | Air-bearing rig . . . . .  | 31        |
| 3.5      | Force measurements . . . . .                                     | 33        |
| 3.6      | Details of the rotation rig and the support setup . . . . .      | 37        |
| 3.6.1    | Rotation rig . . . . .   | 37        |
| 3.6.2    | Sphere models and the support setup . . . . .                    | 37        |
| 3.7      | Flow visualisations . . . . .                                    | 39        |
| 3.7.1    | Hydrogen-bubble and dye visualisations . . . . .                 | 39        |
| 3.7.2    | Particle image velocimetry (PIV) . . . . .                       | 40        |
| 3.7.2.1  | Cross-plane PIV . . . . .  | 41        |
| 3.7.2.2  | Equatorial PIV . . . . .   | 43        |
| 3.8      | Experimental procedures and Validation of the setup . . . . .    | 44        |
| 3.8.1    | Free decay tests . . . . .                                       | 44        |
| 3.8.2    | VIV of a non-rotating sphere: Validation . . . . .               | 45        |
| 3.9      | Chapter summary . . . . .  | 48        |
| <b>4</b> | <b>Flow past a transversely rotating sphere</b>                  | <b>49</b> |
| 4.1      | Abstract . . . . .   | 49        |
| 4.2      | Introduction . . . . .   | 49        |
| 4.3      | Experimental arrangement . . . . .                               | 51        |
| 4.4      | Stationary sphere validation . . . . .                           | 52        |
| 4.5      | Forces on a rotating sphere . . . . .                            | 52        |

## Contents

---

|          |  |            |
|----------|--|------------|
| 4.6      | Physics of the varying Magnus effect . . . . .                           | 54         |
| 4.7      | Concluding remarks . . . . .   | 57         |
| <b>5</b> | <b>Vortex-induced vibration of a rotating sphere</b>                     | <b>59</b>  |
| 5.1      | Overview of the chapter . . . . .  | 59         |
| <b>6</b> | <b>Effect of free surface on the flow-induced vibrations of a sphere</b> | <b>97</b>  |
| <b>7</b> | <b>Flow-induced Vibration of a Rotary Oscillating Sphere</b>             | <b>135</b> |
| 7.1      | Overview of the chapter . . . . .  | 135        |
| <b>8</b> | <b>Conclusions and Recommendations for Future Work</b>                   | <b>171</b> |
| 8.1      | Conclusions . . . . .  | 171        |
| 8.1.1    | VIV of a transversely rotating sphere . . . . .                          | 171        |
| 8.1.2    | Effect of free surface on the VIV response of a sphere . . . . .         | 172        |
| 8.1.3    | Effect of rotary oscillation on the VIV response of a sphere . . . . .   | 172        |
| 8.2      | Recommendations for future work . . . . .                                | 173        |
| 8.2.1    | Effect of rotary oscillation . . . . .                                   | 173        |
| 8.2.2    | Effect of a free surface . . . . .                                       | 173        |
| 8.2.3    | Passive control . . . . .  | 174        |
|          | <b>Bibliography</b>  | <b>175</b> |

# List of Tables

|     |  |    |
|-----|--|----|
| 2.1 | Different transitions in the wake of a sphere . . . . .                              | 8  |
| 2.2 | Non-dimensional parameters for characterising the VIV response of a sphere . . . . . | 13 |



# List of Figures

|      |  |    |
|------|--|----|
| 2.1  | Wake past a sphere in the hairpin shedding regime . . . . .  | 6  |
| 2.2  | Evolution of the wake transition . . . . .   | 6  |
| 2.3  | Schematic representation of the vortex structures at high Reynolds numbers . . . . .   | 8  |
| 2.4  | Strouhal number vs. Reynolds number for spheres . . . . .  | 9  |
| 2.5  | Definition sketch for the transverse vortex-induced vibration of a sphere  | 10 |
| 2.6  | Amplitude and frequency response versus normalized flow velocity for a sphere and a cylinder . . . . .   | 14 |
| 2.7  | Vibration response of an elastically mounted sphere with 2-DOF compared to 1-DOF . . . . .   | 16 |
| 2.8  | Effect of mass-damping . . . . .   | 17 |
| 2.9  | Streamwise vorticity plots measured at $1.5D$ downstream of the sphere .   | 18 |
| 2.10 | Three-dimensional structures for both Mode I and Mode II . . . . .   | 19 |
| 2.11 | The vibration response of a cylinder for different rotational rates . . . .  | 21 |
| 2.12 | . . . . .  | 24 |
| 2.13 | Flow regime of an elastically mounted cylinder at $\alpha_R = 2$ for $Re = 350$ .<br>The data reported by Du & Sun (2015) . . . . .  | 24 |
| 3.1  | Schematic of the present experimental arrangement. . . . .   | 30 |
| 3.2  | An illustration of the current spring mass system (shown on the left) that can be reduced to an equivalent spring mass system shown on the right. . . . .  | 32 |
| 3.3  | Figures showing the output readings of the ATI sensor . . . . .  | 33 |
| 3.4  | Figures showing the temperature rise of the load cell . . . . .  | 34 |
| 3.5  | Schematic showing the mass bottom $m_b$ and mass top $m_t$ . . . . .   | 35 |
| 3.6  | Comparison of the direct force measurement with the derived one from the equation of motion . . . . .  | 36 |
| 3.7  | Figure showing the comparison between the derived force coefficients and the direct measurement from the force sensor. . . . .   | 36 |
| 3.8  | Time trace of the output signal from the encoder (shown on left) along with the power spectra of the signal shown on the right. The input parameters were $f_R = 0.5$ & $\alpha_R = 0.5$ for (a), $f_R = 5$ & $\alpha_R = 0.5$ for (b), $f_R = 0.5$ & $\alpha_R = 2$ for (c), and $f_R = 5$ & $\alpha_R = 2$ for (d). The corresponding output values are shown on top of each figure. . . . . | 38 |
| 3.9  | Schematic showing the cylindrical shroud support arrangement . . . . .   | 39 |
| 3.10 | The vibration response of a sphere for three different support rod arrangements . . . . .  | 40 |
| 3.11 | Schematic of the present experimental arrangement for the PIV measurement. . . . .   | 42 |

## List of Figures

---

|      |   |    |
|------|---|----|
| 3.12 | PIV phase-band averaging method . . . . .   | 43 |
| 3.13 | An example of the free decay test in the air . . . . .  | 45 |
| 3.14 | Amplitude response of a fully submerged sphere obtained in the current study . . . . .  | 46 |
| 3.15 | Variation of the total phase $\phi_{total}$ and vortex phase $\phi_{vortex}$ with $U^*$ . . . . .   | 47 |
| 4.1  | Schematic showing the experimental arrangement (not to scale) for this study. . . . .   | 51 |
| 4.2  | Variation of the drag coefficient $C_D$ of a stationary sphere with Reynolds number. Zoomed in view of the current results is shown on the right. . . . .   | 52 |
| 4.3  | Variation of the lift coefficient $C_L$ (top) and the drag coefficient $C_D$ (bottom) with the rotation ratio $\alpha$ for the current experiment compared to other studies at higher Reynolds numbers. . . . .   | 53 |
| 4.4  | Variation of the lift coefficient $C_L$ with the rotation ratio $\alpha$ for previous studies showing inconsistencies in the reported data for similar Reynolds numbers. Left: High Reynolds numbers experimental studies. Right: Low Reynolds numbers studies. . . . .   | 54 |
| 4.5  | Dye visualisation for a rotating sphere at $Re = 3510$ at marked spin ratios $\alpha$ . The figure shows the top view when the sphere is rotating in the clockwise direction and the flow is from left to right. . . . .  | 55 |
| 4.6  | Instantaneous velocity contours near the flow separation at the advancing side of the sphere at (a) $\alpha = 0.1$ , (b) $\alpha = 0.4$ , (c) $\alpha = 0.9$ and (d) $\alpha = 1.5$ . For this set of images, the flow is from right to left and the sphere rotates in the clockwise direction. The Reynolds number is $2.75 \times 10^4$ . . . . . | 56 |
| 4.7  | Variation of the separation angle at the advancing side, $\theta_{adv}$ , with the rotation ratio $\alpha$ . The correlated transverse lift coefficient is also shown in the bottom. The dashed lines highlight the region where sudden increase in $\theta_{adv}$ is observed associated with a sudden drop in the lift coefficient. . . . .       | 57 |





# Chapter 1

## Introduction

---

*Great mindset brings in great results.*

---

Flow-induced vibration (FIV) is encountered in a multitude of engineering applications. Since FIV is a common cause of structural fatigue and damage, it is a cause of concern for many cylindrical structures like riser tubes in offshore engineering, heat exchanger tubes, pipelines, cylinder arrays in cooling systems, and civil engineering structures like chimneys and bridges. The Tacoma Narrows Bridge collapse in 1940s is an example of a serious structural failure caused by FIV. Among several different forms of FIV, the two common fundamental types are vortex-induced vibration (VIV) and galloping. VIV is caused by an alternate vortex shedding in the wake of an elastically mounted bluff body. On the other hand, galloping is characterised by low-frequency body oscillations in which the vibration amplitude increases monotonically with the flow velocity. Bluff bodies with a circular cross section like a circular cylinder and a sphere are immune to galloping in a steady flow unless an asymmetry is introduced into the system. The current thesis principally focuses on the VIV phenomenon. The important characteristic of such a phenomenon is ‘lock-in’ or ‘synchronisation’. The classic definition of lock-in is described as the synchronisation of the vortex shedding frequency and the body oscillation frequency with the natural frequency of the system. However, several studies have reported a marked departure of the oscillation frequency from the natural frequency during ‘lock-in’ in low mass-ratio systems of  $m^* = \mathcal{O}(10)$  ( $m^*$  is defined as the ratio of the total oscillating mass to the displaced fluid mass). VIV occurs for a wide range of flow velocities, over which large body oscillation amplitudes are observed reaching up to an order of magnitude of one characteristic length (i.e. diameter of a circular cylinder or a sphere).

Considering the potential destructive effect of such vibrations on structures, a large number of fundamental studies have focused on VIV that are summarised in the comprehensive reviews of Bearman (1984), Blevins (1990), Sarpkaya (2004), Williamson & Govardhan (2004), Païdoussis *et al.* (2010) and Naudascher & Rockwell (2012). Apart from cylindrical structures, VIV is also a cause of concern for three-dimensional bodies, the simplest case of which is the sphere. Several fundamental studies have investigated the VIV response of an elastically mounted sphere in the past. Many practical situations where VIV of a spherical body is encountered are marine buoys, underwater vessels, submarines, tethered or towed spherical structures and underwater mines, among other ocean engineering applications. Despite its ubiquitous practical significance in ocean engineering, the VIV response of a sphere in such scenarios is not well understood. For

instance, it is not known how the proximity to a free surface affects the VIV response of a sphere and its wake structures. Furthermore, there appears to be no study so far investigating the VIV response of a semi-submerged sphere that pierces the free surface in spite of the fact that the offshore petroleum drilling and production operations often consist of semi-submerged spherical structures. In light of this research gap, one of the aims of this thesis is to experimentally investigate the effect of proximity to a free surface on the VIV response of submerged and semi-submerged spheres.

Over the last four decades, a plethora of research studies have also focused on investigating means of suppressing vortex-induced vibrations. For this reason, several active and passive control methods have been studied for cylinders in order to suppress VIV. Choi *et al.* (2008) provide a comprehensive review on various control methods employed for flow over cylinders. Passive control methods do not consume external energy and are fairly insensitive to changes in the flow direction. However, it is difficult to dramatically reduce VIV, and the drag often increases. On the other hand, active control methods such as moving-surface boundary-layer control (MSBC) and windward suction/leeward blowing reduce VIV to a much lower level; however, the efficacy of both of these active methods depends on the flow direction. Recently, the control of VIV by rotary motion is receiving increased attention due to its insensitivity to flow direction, efficacy over a broader range of flow parameters, and a greater extent of VIV reduction.

Previous studies on rigidly mounted spheres at low Reynolds numbers have demonstrated that when a constant transverse rotation is imposed on a sphere, the vortex shedding is suppressed for a certain range of rotation ratios (Loth 2008; Kim 2009; Poon *et al.* 2010, 2014). Please note here, if the free-stream direction is considered as  $x$ -axis and the vortex-induced vibrations are observed in  $y$ -axis (also shown in figure 2.5), then the constant rotation should be imposed onto the sphere such that the axis of rotation is perpendicular to both the  $x$ -axis and the  $y$ -axis, i.e., in the  $z$ -axis.

The question arises as to whether imposed rotation can suppress the vortex shedding once the sphere is elastically mounted? This question has not been addressed yet for a sphere. However, recently, researchers have tried addressing this question for a circular cylinder. Surprisingly, it was found for an elastically mounted cylinder that the peak vibration amplitude increased up to  $\sim 76\%$  over the non-rotating case (Wong *et al.* 2017). Similar results were obtained numerically for relatively lower Reynolds numbers as well (Bourguet & Lo Jacono 2014). One can ask if similar behaviour would be observed for a 3D bluff body, a sphere? The second aim of the current thesis is to answer the above posed questions.

For an elastically mounted circular cylinder, a recent numerical study by Du & Sun (2015) illustrated that the VIV of a cylinder can be effectively suppressed for appropriate control parameters by imposing sinusoidal rotary oscillations (axis of rotation in the  $z$ -axis). However, the possibilities of using such a control method in controlling the VIV response of a basic three-dimensional bluff body, a sphere, still remains unexplored. There do not appear to be any studies so far reporting the effect of rotary oscillations on the VIV response of a sphere. Therefore, in view of this research gap, the third aim of this thesis is to experimentally investigate the effect of rotary oscillations on the VIV response of a sphere.

To summarise, this thesis attempts to answer the following fundamental questions and provide specific insight into the underlying flow physics:

1. *What is the effect of free-surface proximity on the VIV response of a sphere?*
2. *What is the effect of sinusoidal rotary oscillation on the VIV response of a sphere?*

### 3. What is the effect of transverse rotation on the VIV response of a sphere?

In order to address the questions highlighted above, a comprehensive series of systematic experiments were undertaken. The sphere response is studied for a wide range of forcing and flow parameters using simultaneous displacement, force and vorticity measurements. Particle image velocimetry (PIV) measurements in the cross-plane and the equatorial plane (containing the principal transverse vibrations) are used to understand the underlying dynamics. Flow visualisation using hydrogen bubbles and Fluorescein dye is also undertaken in selected cases to provide further insight.

## 1.1 Structure of the thesis

The structure of the thesis is as follows:

**Chapter 2:** A brief review of the relevant literature is presented. The open questions are identified and the research gaps in the literature are established.

**Chapter 3:** An overview of the experimental methodologies, facilities, equipment and procedures employed in the current study is provided.

**Chapter 4:** The effect of transverse rotation on the force coefficients of a rigidly-mounted sphere is investigated. This short chapter on a rigidly mounted sphere provides reference results for studying the rotation effects on an elastically mounted sphere.

**Chapter 5:** The effect of transverse rotation on the VIV response of an elastically mounted sphere is presented. This chapter includes the publication by the author entitled ‘Vortex-induced vibration of a rotating sphere’ published in the *Journal of Fluid Mechanics* (2018), vol. **837**, pp. 258-292.

**Chapter 6:** The effect of a free surface on the flow-induced vibration of a sphere is presented. This chapter includes the publication by the author entitled ‘Vortex-induced vibrations of a sphere close to a free surface’ published in the *Journal of Fluid Mechanics* (2018), vol **846**, pp. 1023-1058.

**Chapter 7:** The effect of imposed rotary oscillation is investigated on the flow-induced vibration of a sphere. The findings of this study are reported in a publication that is currently under review for the *Journal of Fluid Mechanics*.

**Chapter 8:** Finally, this chapter briefly draws conclusions and provides a summary of the main findings. It also includes recommendations for potential future work.



## Chapter 2

# A Review of the Literature

*Imagination is more important than knowledge.*

---

Albert Einstein

In this chapter, a review of previous relevant studies is presented. The literature review is divided into six sections. § 2.1 briefly discusses the flow past a stationary sphere, followed by § 2.2 on the VIV of a sphere without any imposed rotation. Section § 2.3 focuses on the effect of imposed transverse rotation on the VIV response of a sphere, followed by § 2.4 on the effect of rotary oscillation. § 2.5 discusses in detail the effect of proximity to a free surface on the flow-induced vibration of a sphere, and finally § 2.6 draws conclusions and identifies the research gaps to be addressed in the thesis.

### 2.1 Stationary sphere

Flow past a stationary sphere may be considered as a simplified case of the general family of 3D bluff bodies around us. As for the flow around its two-dimensional counterpart, the cylinder, instabilities are known to generate fully three-dimensional unsteady flow in spite of the symmetry of the body. The Reynolds number, which quantifies the ratio of the inertial force to the viscous force, is a powerful non-dimensional parameter that helps to characterise various flow regimes within similar fluids in fluid-structure interaction problems. The Reynolds number for flow around a sphere is usually defined by

$$Re = \frac{UD}{\nu}, \quad (2.1)$$

where  $U$  is the free-stream velocity,  $D$  is the diameter of the sphere and  $\nu$  is the kinematic viscosity of the fluid. The behaviour of the flow past a stationary sphere for varying Reynolds numbers has been studied by various researchers. Taneda (1956) visualised the flow past a sphere for a Reynolds number range of  $5 < Re < 300$ . He found that the critical  $Re$  for the flow separation from the surface of the sphere was 24. This resulted in the generation of a stationary axisymmetric vortex ring. He also reported oscillations in the wake behind a sphere for  $Re \sim 130$ . Later, Magarvey & Bishop (1961) performed some dye visualisations for the passage of a liquid drop of an immiscible liquid in a liquid phase for  $0 < Re < 2500$  and observed vortex ring structures similar to those observed by Taneda (1956). Magarvey & Bishop (1961) reported that the rings remain stable and axisymmetric up to  $Re = 210$ . For  $210 < Re < 270$  in their study, the flow remained steady but lost its axisymmetry, and dye was released in two

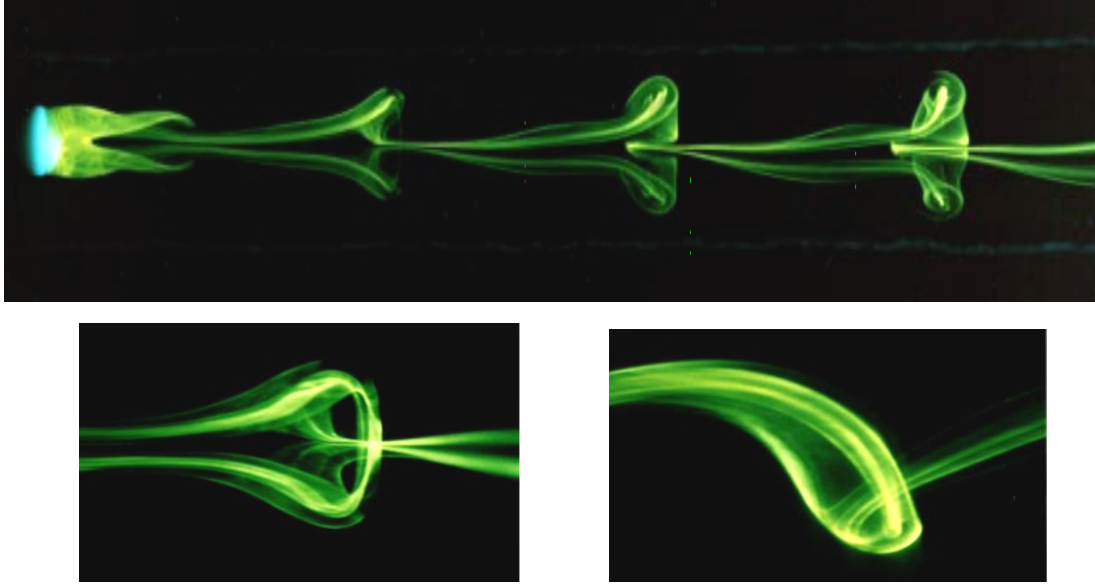


FIGURE 2.1: Wake past a sphere in the hairpin shedding regime for  $Re = 320$  (shown on the top). Images at the bottom show the close-up view of the oscillating wake at about seven diameters behind the sphere, seen simultaneously from the top (shown on the left) and the side (shown on the right). Images taken from [Leweke \*et al.\* \(1999\)](#)

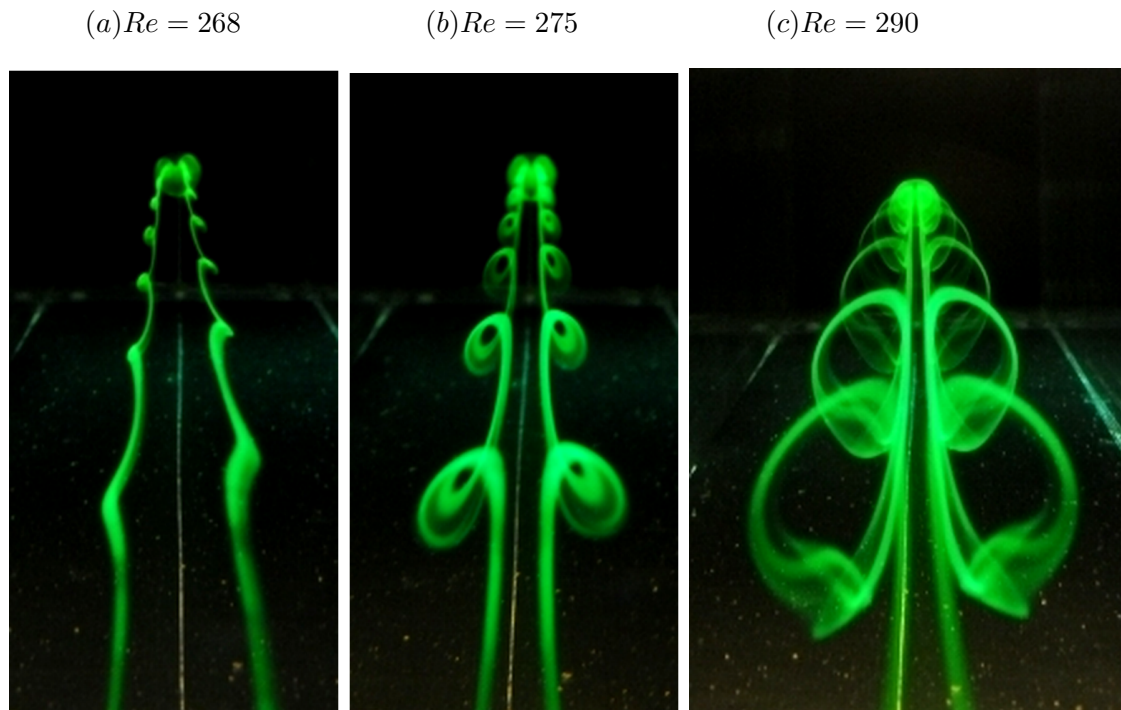


FIGURE 2.2: Images showing the evolution of the oscillation in the between the second and the third sphere wake transition. Image courtesy: [The Polish-French cooperation in fluid dynamics](#).

parallel threads. At  $Re = 270$ , the double-threaded wake itself became unstable, and vortex loops or hairpin vortices began shedding from the sphere. Although the liquid drops tested by Magarvey & Bishop (1961) were deformable, they could still be considered to be of semi-rigid spherical shape due to the presence of surface impurities at the liquid-liquid interface that effectively lead to a no-slip boundary condition. Leweke *et al.* (1999) reported in their paper some striking dye-visualisation images showing the wake for a sphere in the hairpin shedding regime, as also shown in figure 2.1. The close-up top view and the side view of the wake clearly shows how the horseshoe-type vortex loop is connected to the trailing legs of the loop shed in the previous cycle. Later, Gumowski *et al.* (2008) proposed another transition including three-dimensional peristaltic oscillations of the two trailing vortices prior to the hairpin shedding mode. Figure 2.2 shows some spectacular dye-visualisation images taken by Gumowski *et al.* (2008) showing the evolution of transition from the double-threaded wake regime to the hairpin shedding regime. Nakamura (1976) also observed axisymmetric wakes behind spherical shells up to  $Re = 190$ , but unlike Taneda (1956), they found a recirculating eddy behind the sphere for  $Re = 7.3$ . It should be noted that Nakamura used spherical shells with adjustable mass in order to cover a large range of  $Re$ , and the free movement of the inside mass could have potentially affected the sphere's motion and the wake development.

Several numerical studies have also been conducted (see Thompson *et al.* (2001), Johnson & Patel (1999), Ghidersa & Dušek (2000) and Tomboulides & Orszag (2000)) to study the wake structures behind a sphere. Tomboulides & Orszag (2000) conducted direct numerical simulations (DNS) for  $25 < Re < 1000$  and observed steady axisymmetric flow for  $Re < 212$  with initial separation at  $Re = 20$ . They identified two early bifurcations of the sphere wake, one at  $Re = 212$  leading to a three-dimensional time independent state, and the second one for  $250 < Re < 285$  resulting in a time periodic flow. They also reported a double-threaded wake structure consisting of two opposite-signed streamwise vortices, which generally appear as two dye threads emanating from the recirculating region of the sphere in dye visualisation experiments. However, at higher Reynolds number ( $Re > 800$ ), the hairpin-shaped vortices begin to change from laminar to turbulent vortices with alternate fluctuations, and the pattern continues at least up to  $Re = 3.7 \times 10^5$  (Sakamoto & Haniu 1990).

Taneda (1978) revealed in his flow-visualisations that at very high Reynolds numbers of  $3.8 \times 10^5 \leq Re \leq 10^6$ , the sphere wake consists of streamwise line vortices that rotate slowly and randomly about the streamwise axis. Figure 2.3 shows a schematic representation of the vortex structures past a sphere at high Reynolds numbers. As evident from the schematic, the vortex sheet shed from the sphere rolls up to form a pair of streamwise vortices. In a cross-plane downstream of the sphere, one can see a counter-rotating vortex pair (see the back view in figure 2.3). In the current study, vorticity measurements will be carried out in a cross-plane that is placed 1.5 diameters downstream from the sphere to investigate the dynamics of the counter-rotating vortex pair. Table 2.1 summarises the wake transitions that occur as a function of the Reynolds number for a stationary sphere.

Over a range of Reynolds number, the vortex shedding past a stationary sphere occurs at a well-defined frequency. The non-dimensionalised frequency of the vortex shedding is called Strouhal number that is expressed as

$$St = \frac{f_{St} D}{U}, \quad (2.2)$$



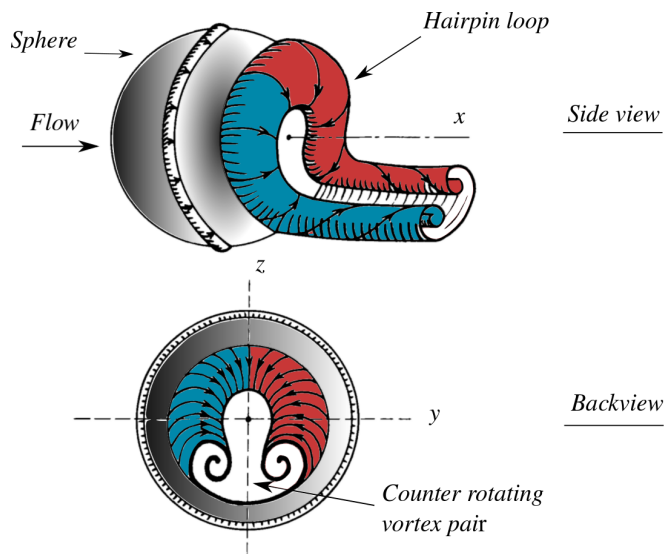
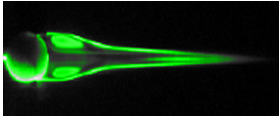
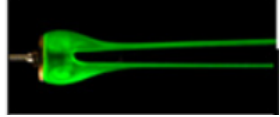
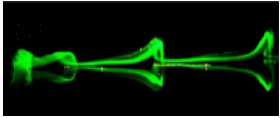
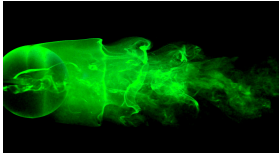


FIGURE 2.3: Schematic representation of the vortex structures at high Reynolds numbers in the range  $3.8 \times 10^5 \leq Re \leq 10^6$ . The lines with arrows indicates the streamlines on the vortex sheet. The schematic has been adapted from Taneda (1978).

---

|                  |  |   |
|------------------|--|---|
| $Re < 210$       | Axisymmetric wake state                |  |
| $210 < Re < 280$ | Planar symmetric, double-threaded wake |  |
| $280 < Re < 800$ | Steady to unsteady transition          |  |
| $Re > 800$       | Turbulent                              |  |

---

TABLE 2.1: Different transitions that occur in the wake of a stationary sphere for different Reynolds numbers.

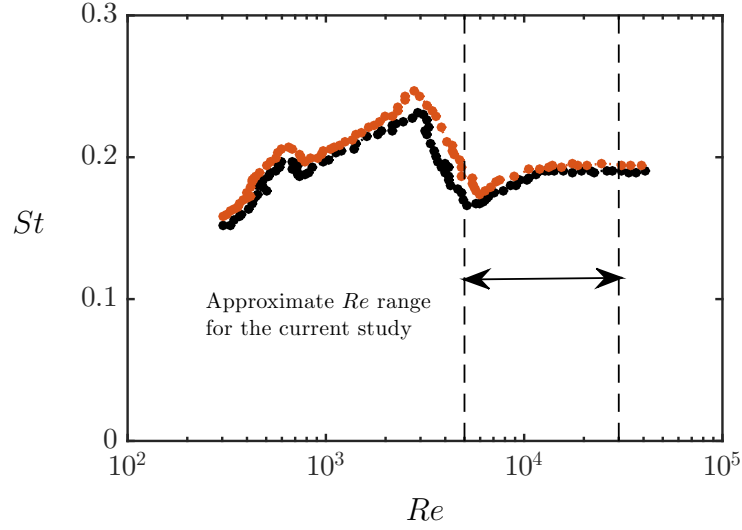


FIGURE 2.4: Strouhal number vs. Reynolds number for spheres. The two curves show the upper and lower bounds of the data taken by Sakamoto & Haniu (1990) for spheres of different sizes.

where  $f_{St}$  is the dominant vortex shedding frequency of a stationary sphere. Figure 2.4 shows the variation of the Strouhal number with the Reynolds number (based on the sphere diameter) for a stationary sphere (Sakamoto & Haniu (1990)). The approximate range of Reynolds numbers in the current study is also highlighted in the figure. This regular periodic shedding past the sphere leads to large fluctuating pressure forces in the direction transverse to the flow that might lead to vibrations in the transverse direction, as will be discussed in the following section.

## Vortex-induced vibrations (VIV)

In the above section, it was briefly discussed that the vortex shedding leads to large fluctuating pressure forces in the direction transverse to the flow. When a sphere is elastically mounted and the frequency of the fluctuations is close to the natural frequency of the system, it can cause large-amplitude vibrations of the sphere. This type of vibration caused by the fluctuating forces due to vortex shedding is known as vortex-induced vibration (VIV). The important feature of such a system is ‘lock-in’ or ‘synchronisation’. The classic definition of the lock-in phenomenon is described as the synchronisation of the vortex shedding frequency  $f_{st}$  and the body oscillation frequency  $f$  with the natural frequency of the system  $f_{nw}$ , i.e.,  $f \sim f_{st} \sim f_{nw}$  or  $f^* = f/f_{nw} \sim 1$  (see Blevins (1990) and Sumer (2006)). This definition may not be appropriate for systems of mass ratio of the order of 10 ( $m^* = \mathcal{O}(10)$ ) that are mostly encountered for structures vibrating in water. In such systems, several studies have reported a marked departure of  $f^*$  from unity during lock-in (Moe & Wu 1990; Khalak & Williamson 1997; Gharib *et al.* 1998; Govardhan & Williamson 2000). Khalak & Williamson (1999) hence suggested a more suitable definition of synchronisation as the locking of the body oscillation frequency with the frequency of the periodic wake vortex mode.

Although vibrations can also be observed in the streamwise direction, the vibrational amplitudes are significantly larger in the transverse direction. For example, in the case of a sphere, the peak transverse vibrations are  $\sim 300\%$  larger than the peak inline

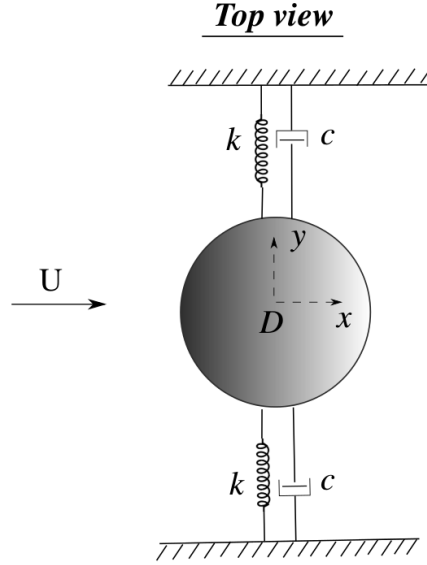


FIGURE 2.5: Definition sketch for the transverse vortex-induced vibration of a sphere. The hydro-elastic system is simplified as a 1-DOF system constrained to move only in the cross-flow direction. Here,  $U$  is the free-stream velocity,  $k$  the spring constant,  $D$  the sphere diameter, and  $c$  is the structural damping of the system.

vibrations. Therefore, VIV problems are often simplified as one degree of freedom (1-DOF) system constrained to move only in the cross-flow direction. Figure 2.5 shows a schematic of the current fluid-structure problem, where the sphere is constrained to move freely in the direction transverse to the flow. The governing equation of motion for a sphere undergoing transverse VIV in this case can be described by

$$m\ddot{y} + c\dot{y} + ky = F_y, \quad (2.3)$$

where  $m$  is the total oscillating mass of the system,  $c$  is the structural damping,  $F_y$  is the transverse fluid force, and  $k$  is the spring constant. As an approximation, it is often assumed that the transverse force  $F_y(t)$  and the response displacement  $y(t)$  are both sinusoidal and represented by

$$y(t) = A \sin(2\pi ft), \quad (2.4)$$

$$F_y(t) = F_o \sin(2\pi ft + \phi), \quad (2.5)$$

where  $F_o$  is the amplitude of  $F_y$ , and  $\phi$  is the phase difference between the fluid force and the body displacement.

VIV response of a bluff body is represented, in general, by the vibration amplitude ratio  $A^*$ , and the frequency ratio  $f^*$ , as a function of  $U^*$ . The vibration amplitude ratio  $A^*$  is the non-dimensionalised oscillation amplitude. Several definitions of  $A^*$  are available in the literature, the most common one is  $A_{max}^*$  that is the ratio of maximum amplitude of the oscillation to the sphere diameter. As  $A_{max}^*$  takes the value of a single sample out of a fairly large sample, it might not be a true representative of the amplitude response in some cases. Therefore, some researchers use  $A_{10}^*$  that takes the value of the mean of the top 10% of the peak amplitudes. Another definition is  $A_{rms}^*$  that takes the rms of the displacement signal. Although, all the above definitions are equally useful measure to showcase the behaviour of the amplitude response, the most

common definition in use for the sphere studies (as used previously by the benchmark studies) is  $A_{rms}^*$  defined as

$$A^* = \sqrt{2}A_{rms}/D. \quad (2.6)$$

Here,  $A_{rms}$  is the rms of the sphere vibration amplitude. The frequency ratio  $f^*$ , is defined as

$$f^* = f/f_{nw}, \quad (2.7)$$

where  $f$  is the frequency of the sphere oscillations and  $f_{nw}$  is the natural frequency of the system in water. The reduced velocity  $U^*$  is defined as

$$U^* = \frac{U}{f_{nw}D}. \quad (2.8)$$

The other important non-dimensional parameter characterising such systems is the mass ratio  $m^*$  defined as

$$m^* = m/m_d, \quad (2.9)$$

where  $m$  is the total oscillating mass of the system and  $m_d$  is the displaced fluid mass. All the set of relevant parameters for studying the VIV of spheres are listed in the table 2.2.

Based on the suggestions of [Lighthill \(1986\)](#) and as performed for the VIV of a tethered sphere by [Govardhan & Williamson \(2000\)](#), the total transverse fluid force ( $F_y$ ) acting on a sphere can be split into a potential force ( $F_p$ ), comprising the potential added mass force, and a vortex force component ( $F_v$ ) that is due to the vorticity dynamics. From potential theory, the instantaneous  $F_p$  acting on the sphere can be expressed as

$$F_p(t) = -C_A m_d \ddot{y}(t), \quad (2.10)$$

where  $C_A$  is the potential added mass coefficient ( $C_A = 0.5$  for a sphere). Thus, the vortex force  $F_v$  can be computed from the equation

$$F_v(t) = F_y(t) - F_p(t). \quad (2.11)$$

If all the forces are normalised by  $(\frac{1}{2}\rho U^2 \pi D^2/4)$ , this reduces to

$$C_{vortex}(t) = C_y(t) - C_{pot}(t). \quad (2.12)$$

Here,  $C_{pot}$  (the potential-flow lift coefficient) can be calculated based on the instantaneous body acceleration  $\ddot{y}(t)$ . Reverting back to the dimensional forces for the moment, two equivalent forms can be written for the equation of motion

$$m\ddot{y} + c\dot{y} + ky = F_o \sin(\omega t + \phi_{total}), \quad (2.13)$$

and for vortex force

$$(m + m_A)\ddot{y} + c\dot{y} + ky = F_v \sin(\omega t + \phi_{vortex}). \quad (2.14)$$

The vortex phase  $\phi_{vortex}$ , first introduced by [Govardhan & Williamson \(2000\)](#), is the phase difference between  $C_{vortex}(t)$  and the body displacement  $y(t)$ . The more conventionally used total phase  $\phi_{total}$  is the phase difference between the total force  $C_y$  and the body displacement  $y(t)$ . In general, phase jumps are associated with a switch from one VIV mode to another, and have even been used to distinguish between different modes ([Govardhan & Williamson 2005](#)).

## 2.2 Vortex-induced vibration of a sphere

Large vibrations due to VIV can occur in a variety of engineering situations, such as with flows past bridges, transmission lines, aircraft control surfaces, offshore structures, engines, heat exchangers, marine cables, towed cables, drilling and production risers in petroleum production, moored structures, tethered structures, pipelines, and other hydrodynamic and hydroacoustic applications. VIV is a significant cause of fatigue damage that can lead to structural failures. Numerous studies have focused on understanding the underlying principles of vortex-induced vibrations and its suppression, especially for cylinders. The immense practical significance of VIV has led to various comprehensive studies in the past.

Some of the pioneer work in this field has been carried out by Michael Triantafyllou's research group at MIT and Charles Williamson's research group at Cornell University. The low mass ratio water channel experiments on cylinders reported by [Khalak & Williamson \(1996, 1997, 1999\)](#) expanded our understanding and characterisation of VIV vibration responses. On the other hand, [Hover \*et al.\* \(1997, 1998\)](#) developed a novel and versatile force-feedback system that measures the forces acting on the test cylinder to drive in real time a numerical simulation of an equivalent mass-dashpot-spring system. The computed motion is then imposed onto the test cylinder. Using this ingenious experiment, they suggested a 3D vortex formation process for the upper-lower branch transition for a cylinder ([Hover \*et al.\* 2004](#)). As bodies become more directly practical, they become more complex in shape; however, many of the phenomena discovered for simpler geometries like a circular cylinder carry across to more involved structures. For example, in the case of a tapered cylinder, [Techet \*et al.\* \(1998\)](#) discovered 2S and 2P modes occurring along different spanwise lengths of their tapered cylinder (2S-2P hybrid mode).

However, unlike the situation for cylinders and slender bodies, there are relatively fewer studies on VIV of elastically-mounted or tethered spheres despite its ubiquitous practical significance, such as marine buoys, underwater mines, other offshore structures, and tethered or towed spherical objects. [Govardhan & Williamson \(1997\)](#), [Williamson & Govardhan \(1997\)](#), [Jauvtis \*et al.\* \(2001\)](#) and [Govardhan & Williamson \(2005\)](#) were the first systematic and elaborate experimental studies carried out by Prof. Williamson's research group at Cornell university, investigating the VIV response of a sphere. Followed by these benchmark studies, several experimental and numerical studies focused on the VIV response of a sphere ([Pregalato 2003](#); [van Hout \*et al.\* 2010](#); [van Hout \*et al.\* 2013](#); [Behara \*et al.\* 2011](#); [Lee \*et al.\* 2013](#); [Krakovich \*et al.\* 2013](#); [Behara & Sotiropoulos 2016](#)). Based on the previous benchmark studies on the VIV response of a sphere, the overall findings will be discussed in detail in the following subsections.

### 2.2.1 Modes of Vibration

[Williamson & Govardhan \(1997\)](#) and [Govardhan & Williamson \(1997\)](#) were the first to investigate the VIV response of a sphere. They found that within a range of flow velocities, where the oscillation frequency  $f$  is of the order of the vortex shedding frequency of a stationary sphere  $f_{st}$ , two modes of highly periodic large vibrations occur, namely mode I and mode II.

As one increases the flow speed, the response transitions from mode I to mode II at a point where the vortex phase  $\phi_{vortex}$  (phase difference between the vortex force and displacement) crosses through  $90^\circ$ . Within the mode II regime, the total phase

## 2.2. Vortex-induced vibration of a sphere

|                            |             |                         |
|----------------------------|-------------|-------------------------|
| Amplitude ratio            | $A_{rms}^*$ | $A_{rms}/D$             |
| Damping ratio              | $\zeta$     | $c/\sqrt{k(m + m_A)}$   |
| Frequency ratio            | $f^*$       | $f/f_{nw}$              |
| Mass ratio                 | $m^*$       | $m/m_d$                 |
| Mass-damping parameter     | $\xi$       | $(m^* + C_A)\zeta$      |
| Reduced velocity           | $U^*$       | $U/(f_{nw}D)$           |
| Reynolds number            | $Re$        | $UD/\nu$                |
| Scaled normalised velocity | $U_S^*$     | $(U^*/f^*)S = f_{vo}/f$ |
| Strouhal number            | $S$         | $f_{vo}D/U$             |

TABLE 2.2: Non-dimensional parameters that are often used to characterise VIV response of a sphere. In this table:  $A_{rms}$  is the rms of the vibration amplitude in  $y$  direction;  $D$  is the sphere diameter;  $f$  is the body oscillation frequency; and  $f_{nw}$  is the natural frequency of the system in quiescent water. In addition,  $m$  is the total oscillating mass;  $c$  is the structural damping factor with  $k$  the spring constant;  $U$  is the free-stream velocity;  $\nu$  is the kinematic viscosity;  $m_A$  denotes the added mass, defined by  $m_A = C_A m_d$ , where  $m_d$  is the mass of the displaced fluid and  $C_A$  is the added mass coefficient (0.5 for a sphere);  $f_{vo}$  is the vortex shedding frequency of a fixed body.

$\phi_{total}$  (phase difference between the total transverse force and displacement) crosses through  $90^\circ$ . This is somewhat similar to the case of its two-dimensional counterpart, the cylinder, where there are three distinct modes, namely ‘Initial’, ‘Upper’ and ‘Lower’, as shown by [Khalak & Williamson \(1999\)](#). These modes are separated by two phase jumps; initial $\leftrightarrow$  upper transition is associated with a jump in  $\phi_{total}$ , and upper $\leftrightarrow$  lower transition is associated with a jump in  $\phi_{vortex}$ . However, these phase jumps are abrupt for a cylinder. In contrast, for a sphere, both  $\phi_{total}$  and  $\phi_{vortex}$  increase continuously and gradually as the response transitions from mode I to mode II. Figure 2.2.1 shows the amplitude response of a sphere in comparison with that of a cylinder. In both the cases, similar multiple response modes are observed with similar characteristics whereby the body’s oscillation frequency rises well above its natural frequency ( $f^* > 1$ ). Both principal modes of sphere vibrations are associated with the ‘lock-in’ of the vortex formation frequency to the natural frequency of the system. For an elastically mounted sphere with 2-DOF (tethered sphere), mode II and mode III are separated by a desynchronised region in between them (see figure 2.7). However, for a sphere with 1-DOF, the response proceeds gradually and continuously from mode II and mode III as the flow velocity is increased. The differences in the response for 1-DOF and 2-DOF problems are highlighted in figure 2.7. [Govardhan & Williamson \(2005\)](#) suggested that this behaviour is peculiarly associated with constraining the motion of the sphere in the transverse direction.

The synchronisation regime discussed so far where mode I and mode II are observed corresponds to flow speeds where  $f_{st} \sim \mathcal{O}(f)$ . This region can be termed fundamental synchronisation regime of the sphere VIV response that extends from

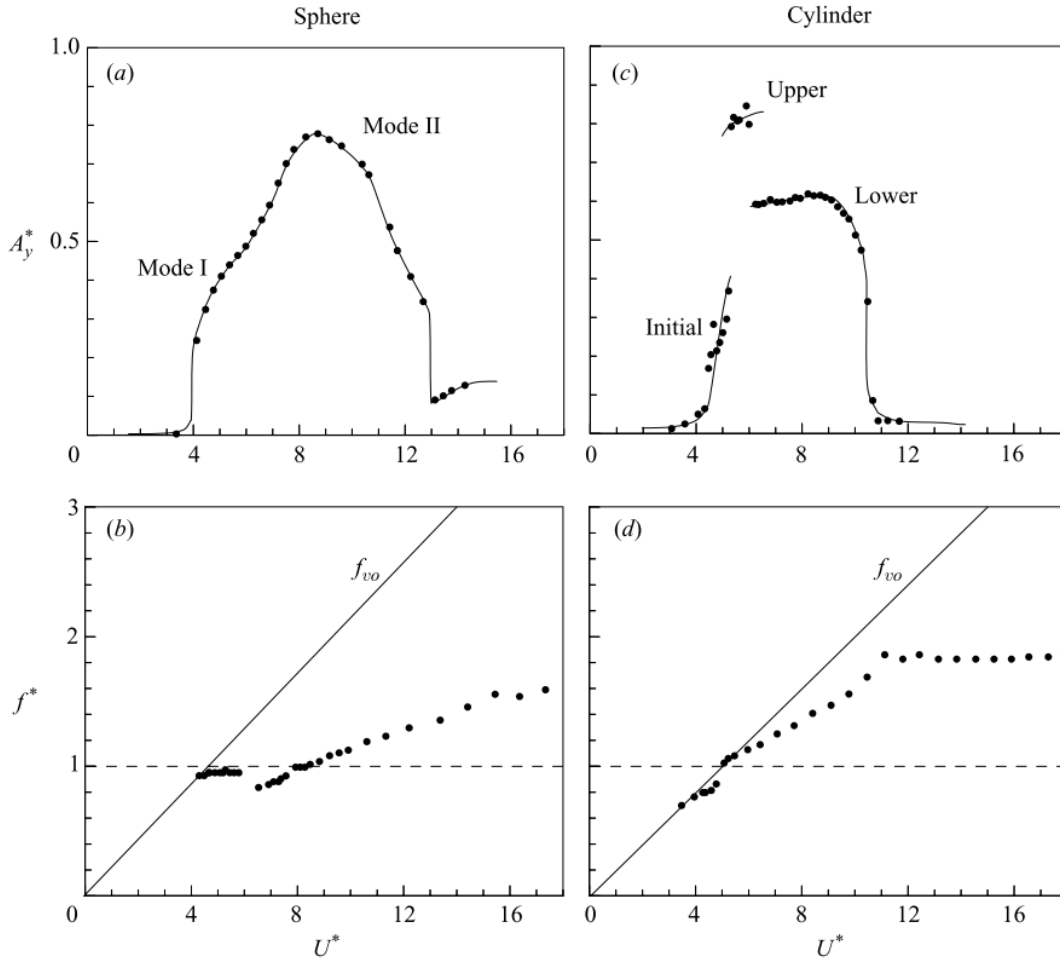


FIGURE 2.6: Amplitude and frequency response versus normalized flow velocity for a sphere and a cylinder. In (a) and (b), amplitude ( $A^*$ ) and frequency ( $f^*$ ) response for somewhat different experimental conditions are given: (a)  $m^* = 2.83$ ; (b)  $m^* = 0.76$ , where  $\zeta = 0.008$  in both cases. In (c) and (d), VIV response for a cylinder is given ((c)  $m^* = 0.76$ , where  $\zeta = 0.008$ ; (d)  $m^* = 1.19$ ,  $\zeta = 0.005$ ). Image reproduced from Govardhan & Williamson (2005).

a non-dimensionalised velocity range of  $U^* \sim 5 - 10$ . For the case of a cylinder, no significant response is observed outside the fundamental synchronisation regime. In contrast, however, Jauvtis *et al.* (2001) discovered in their wind tunnel experiments that a sphere exhibits large periodic vibrations even outside this regime. Such vibrations have been termed mode III, which occurs for a higher reduced velocity range of  $U^* \sim 20 - 40$ , where  $f_{st} \gg f$ . It was found that the principal vortex shedding frequency was 3 – 8 times higher than the sphere oscillation frequency, hence such a vibration phenomenon could not be explained using the classical ‘lock-in’ theory. Later, Govardhan & Williamson (2005) suggested that in the absence of any body vibration in mode III, there would be no fluid forcing at the low natural frequency of the system. However, if the body was perturbed, it could generate a self-sustaining vortex force that could amplify and saturate the body vibrations to large amplitudes. They categorised mode III as ‘movement-induced excitation’ (Naudascher & Rockwell 2012). van Hout *et al.* (2010) and Lee *et al.* (2013) also observed several regimes of vibrations



for a heavy tethered sphere and a neutrally buoyant tethered sphere, respectively. The former reported a response region III, which was linked to the mode III state reported by Jauvtis *et al.* (2001), and the latter reported a chaotic regime VI, which was linked to mode IV reported by Jauvtis *et al.* (2001). Both these studies reported these modes to exhibit non-stationary chaotic dynamics, where large variation in amplitude is observed. At extremely high velocities ( $U^* > 100$ ), a fourth mode of unsteady vibrations, namely mode IV, with low periodicity was found by Jauvtis *et al.* (2001). In this mode, the unsteady vibrations were characterised by intermittent bursts with large amplitude vibrations. The origin of these large transient bursts of vibrations still remains unknown.

To summarise, the sphere vibration response consists of two highly periodic fundamental modes of vibrations, namely mode I and mode II. These modes are observed in the reduced velocity range of  $U^* \sim 5 - 10$ . In terms of the wake structures, both the modes are characterised by two-sided chain of streamwise vortex loops (as it will also be discussed in detail in section 2.2.3). However, there is a distinct change in the timing of vortex pair formation for modes I and II (Govardhan & Williamson (2005)). Mode III, on the other hand, is a type of ‘movement-induced vibration’, and is observed for reduced velocity range of  $U^* \sim 20 - 40$ . In terms of wake structures, Govardhan & Williamson (2005) found that mode III typically consists of thread-like streamwise structures underlying multiple small-scale structures in the wake.

### 2.2.2 Effect of the mass-damping parameter and mass ratio

Govardhan & Williamson (2005) performed a comprehensive series of experiments and produced a ‘Griffin plot’ for a sphere, to see the variation of the peak amplitude response  $A_{max}^*$  with a combined mass-damping parameter  $(m^* + C_A)\zeta$ , as shown in figure 2.8. Similar to the case of a cylinder, when the mass-damping is increased, the peak vibration amplitude drops, and there is a decrease in the range of  $(U^*/f^*)S$  over which the large periodic vibrations are observed, as clear from figure 2.8(a). The saturation amplitude of  $A^* \simeq 0.9$  is reached for very low mass-damping systems ( $(m^* + C_A)\zeta \leq 10^{-2}$ ). However, for a very high mass-damping of  $(m^* + C_A)\zeta > 0.5$ , there are almost no vibrations. In figure 2.8 (b), the data is presented from a large range of mass ratios ( $m^* = 0.5 - 200$ ) studied by the Cornell group, suggesting that the combined mass-damping parameter is very useful in terms of collapsing the peak-amplitude data for different mass ratios. Govardhan & Williamson (1997) studied the response of a tethered sphere for a very low mass ratio of  $m^* \sim 0.76$ . They found that at such low mass ratios, the two fundamental modes can be separated by non-periodic vibrations. This is unlike higher mass ratio systems, where the response is highly periodic and progresses gradually from mode I to mode II as the reduced velocity is increased. This corroborates the effect of mass ratio on the vibration response of a sphere. For very low mass ratios, one can observe non-periodic vibrations between the two fundamental modes. Furthermore, the synchronisation regime widens considerably, and the peak amplitude response also increases substantially with a saturation amplitude of  $A^* \simeq 0.9$ .

### 2.2.3 Wake structures

The principal vorticity dynamics associated with VIV for a sphere is the motion of streamwise vortex pairs rather than the dynamics of vorticity normal to the flow as in the case of a cylinder VIV. Govardhan & Williamson (2005) suggested that the wake structures behind the sphere at high Reynolds numbers can be compared to trailing



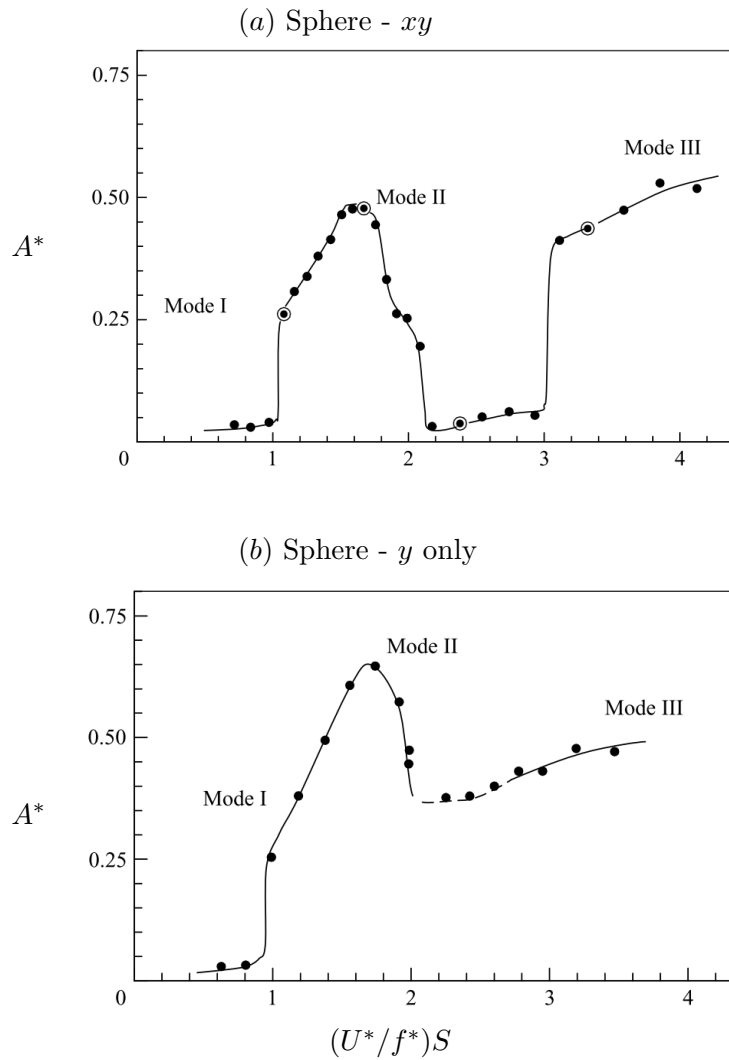


FIGURE 2.7: Vibration response of an elastically mounted sphere with 2-DOF (shown in (a)) compared to 1-DOF (shown in (b)). 2-DOF system exhibits a desynchronised region between mode II and mode III. The mass-damping is (a)  $(m^* + C_A)\zeta = 0.0305$  and (b)  $(m^* + C_A)\zeta = 0.9214$ . The images taken from Govardhan & Williamson (2005).

vortices behind aircraft wings. They computed the transverse lift acting on a sphere from the knowledge of the spacing and strength of the trailing tip vortices and directly compared this lift with the force measurements from a force sensor. A reasonable agreement between the two led them to conclude that most of the transverse force acting on the sphere is given by the dynamics of the streamwise vorticity. They also carried out extensive vorticity measurements to visualise the three-dimensional vortex structures in the wake of a sphere undergoing VIV at a high Reynolds number of  $Re \approx 3000$ . They found that the dominant wake structures for both the modes were chains of streamwise vortex loops on alternating sides of the wake, very similar to the wake of a stationary sphere in the hairpin shedding regime as discussed in § 2. A central distinction between the wake behind a stationary sphere and that behind an oscillating sphere is the fact that in the static case, the vortex loops are formed in an irregular fashion, and the azimuthal location at which the loops are formed changes every cycle, whereas when a sphere oscillates, loops maintain symmetry with the horizontal plane containing the

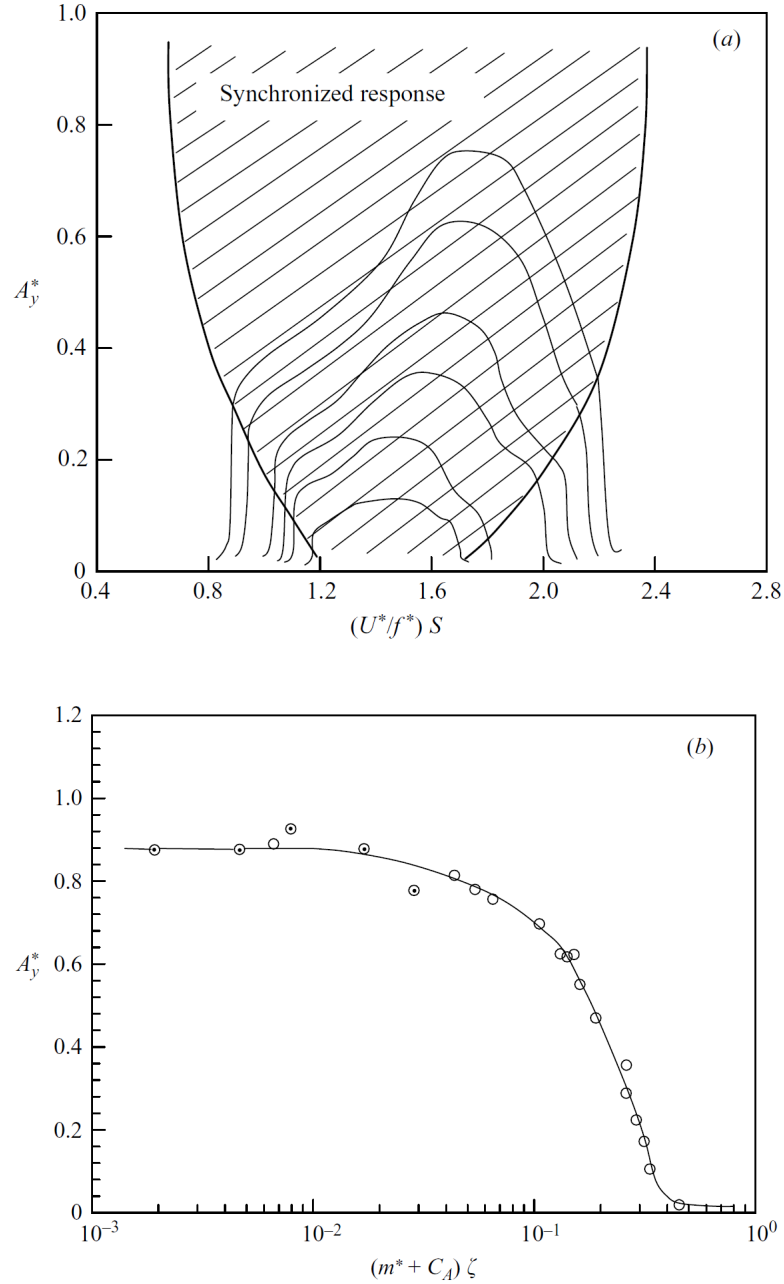


FIGURE 2.8: (a) Synchronised response of a sphere for varying mass-damping parameter and (b) Griffin plot showing the variation of the peak vibration amplitude of a sphere with the mass-damping parameter. In (b), the open symbols represent 1-DOF motion, bull's eyes present 2-DOF motion of the sphere. Following parameters apply to (a) for increasing amplitude plots:  $(m^* + C_A)\zeta = 0.333, 0.290, 0.261, 0.190, 0.151, 0.029$ ;  $m^* = 198.4, 156.6, 60.6, 53.6, 27.5, 2.8$ . Reynolds number at  $A_{max}^* = 3800, 4500, 6300, 5300, 5500, 9100$ . The images are reproduced from [Govardhan & Williamson \(2005\)](#).

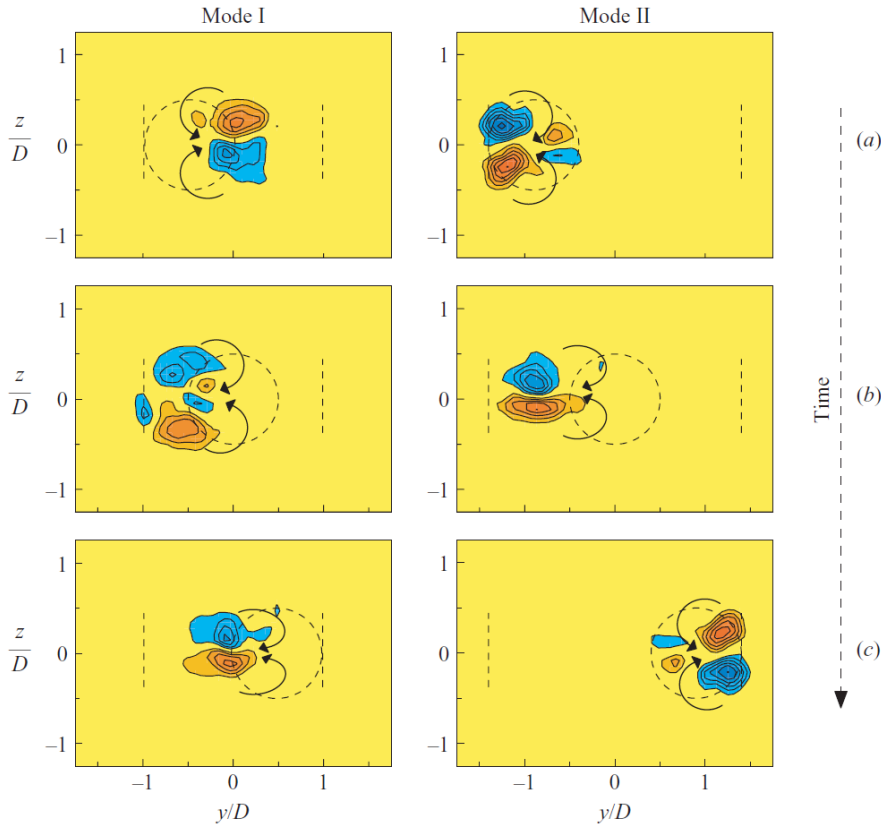


FIGURE 2.9: Streamwise vorticity plots measured at  $1.5D$  downstream of the sphere showing counter-rotating vortex pair for both mode I and mode II. Each of the plots are separated by a quarter-period.  $Re \approx 3000$  in both the cases. Image taken from Govardhan & Williamson (2005).

principal transverse vibrations. The heads of those vortex loops pinch off to form vortex rings several times the body diameter in the downstream. By observing the vertical velocity in the equatorial plane, one can see a horizontal cut through the developing vortex ring, showing a pair of opposite signs of vorticity somewhat similar to the 2P mode of an oscillating cylinder (although its formation is further downstream than for the cylinder).

However, by observing streamwise vorticity in a cross-plane closer to the sphere, one can see a dominant counter-rotating streamwise vortex pairs for both the modes. Figure 2.9 shows the streamwise vorticity measurements at  $1.5D$  downstream of the sphere showing counter-rotating vortex pair for both mode I and mode II. As the sphere oscillates from one side to the other, the observed vorticity changes sign. This is consistent with the fact that as the sphere oscillates from one side to the other, hairpin loops from opposite sides are shed downstream into the wake. Figure 2.10 shows a spatio-temporal reconstruction of the sphere wake in both mode I and mode II using the measured time sequence of streamwise vorticity by Govardhan & Williamson (2005). One can clearly see interlinked two-sided chain of vortex loops in the resulting three-dimensional structure in both the modes. In the current study, an analogous approach will be utilised to study the wake dynamics. Similar to the measurements by the above benchmark study, streamwise vorticity measurements will be carried out at a distance  $\approx 1.5D$  downstream of the sphere to highlight the dominant counter-rotating

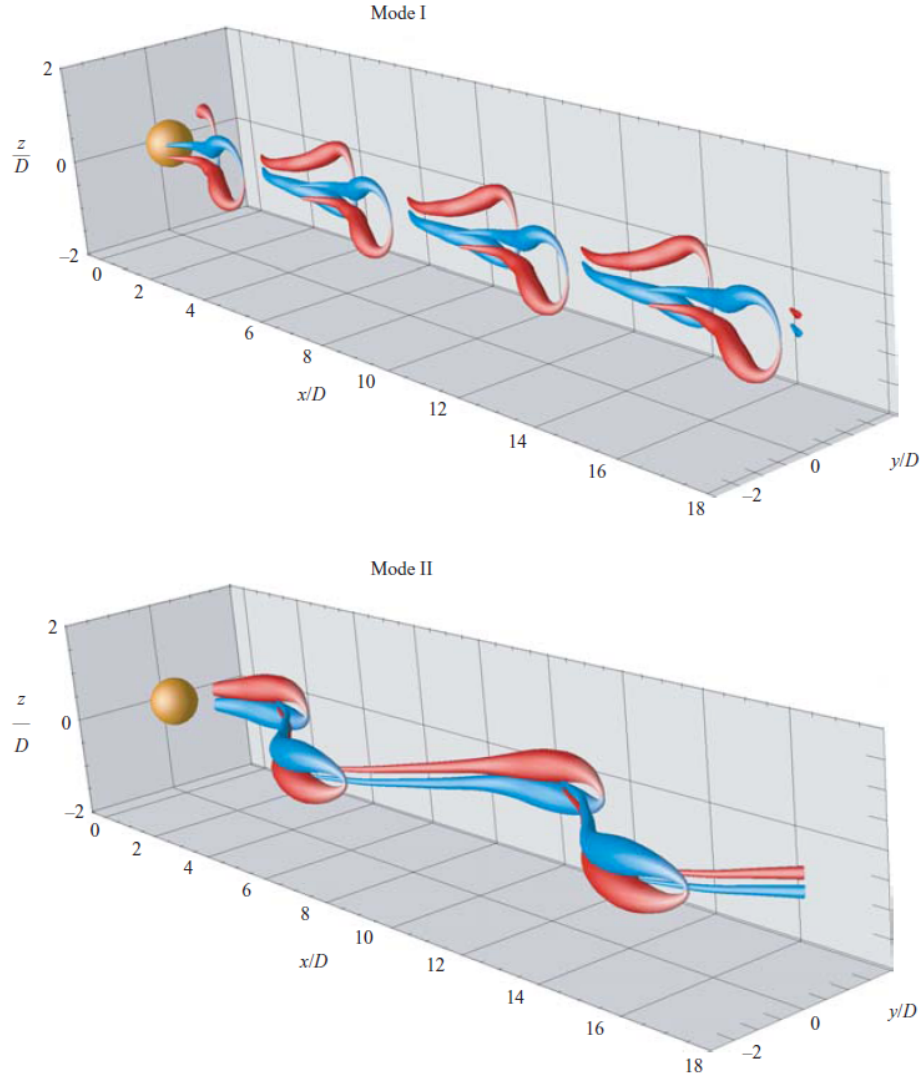


FIGURE 2.10: Three-dimensional structures for both Mode I and Mode II showing a two-sided chain of streamwise vortex loops. Blue and red indicates clockwise and anti-clockwise vorticity, respectively.  $Re \approx 3000$ . Image taken from Govardhan & Williamson (2005).

vortex pair in the wake.

## Effect of imposed rotary motion on the VIV response of a sphere

As discussed earlier, large-amplitude vibrations caused by VIV over a wide range of Reynolds number is a common cause of serious structural fatigue and damage, which has led to a plethora of research studies focusing on suppressing VIV over the last four decades. For this reason, several active and passive control methods have been studied previously for 2D bluff bodies. Choi *et al.* (2008) provide a review on various control methods employed for flow over bluff bodies. Although passive control methods do not consume external energy and are fairly insensitive to changes in the flow direction, their use tends to encounter difficulty in dramatically reducing VIV, and the drag often increases. In contrast, active control methods such as moving-surface boundary-layer

control (MSBC) (Mittal 2001) and windward suction leeward blowing (WSLB) (Dong *et al.* 2008) reduce VIV to a much lower level; however, the efficacy of both these active methods depends on the flow direction.

The control of VIV by rotary motion has received increased attention recently due to its insensitivity to flow direction, efficacy over a broader range of flow parameters, and the greater extent of VIV reduction. Studies by Du & Sun (2015) and Wong *et al.* (2017) illustrated that the VIV of an elastically mounted cylinder can be effectively suppressed using appropriate control parameters. However, the possibilities of utilising such control methods in controlling the VIV response of a sphere still remain unexplored. In the current study, the potential of this control method in controlling the VIV response of a sphere is investigated through a series of systematic and extensive experiments. Two different approaches are employed to prohibiting the lock-in phenomenon, and thereby reducing the large vibrations for a three-dimensional bluff body. In the first approach, suppression of VIV is achieved by means of an imposed transverse rotation. In this approach, the aim is to reduce the strength of the vortex street, which can be associated with a reduction of the transverse force acting on the sphere leading to a reduced vibration response. This approach is discussed in detail in § 2.3. In the second approach, an external forcing is imposed onto the sphere in the form of sinusoidal rotary oscillations with a forcing frequency that is close to the natural frequency of the system. This leads to locking of the vortex shedding frequency of the sphere to the forcing frequency instead of the natural frequency (otherwise known as ‘lock-on’), thus prohibiting the resonance. This approach will be discussed in detail in § 2.4. In the following two sections, the relevant previous literature related to the above two proposed approaches is discussed.

### 2.3 Effect of transverse rotation

A lot of literature is available reporting the effect of imposed constant rotation on a rigidly mounted sphere. Previous numerical studies on the effect of rotation on rigidly mounted rotating spheres have revealed suppression of the vortex shedding for a certain range of rotation rates (Loth 2008; Kim 2009; Poon *et al.* 2010, 2014). These studies were performed computationally at relatively low Reynolds numbers ( $Re \leq 1000$ ). On the other hand, there have been some experimental studies conducted at considerably higher Reynolds numbers ( $Re \geq 6 \times 10^4$ ) that focused mainly on the effect of transverse rotation on the fluid forces, e.g., the *inverse Magnus effect* (Macoll 1928; Barlow & Domanski 2008; Kray *et al.* 2012; Kim *et al.* 2014), where the rotation induced lift suddenly changes direction as the Reynolds number is increased. It is still unknown if the rotation suppresses vortex shedding at such high Reynolds numbers. Nevertheless, all these studies have observed a sudden dip in the lift and drag coefficients for a certain rotation ratio (which varies with  $Re$ ).

All these studies were performed on a rigidly mounted sphere. The question arises as to whether imposed rotation can suppress the vortex shedding once the sphere is elastically mounted? It is known that an elastically mounted sphere undergoes large vibration due to VIV. In this case, can the imposed constant rotation potentially suppress the vibrations? This question has not been addressed yet for a sphere; however, there were many studies reporting the effect of constant rotation on the VIV response of an elastically mounted cylinder. Bourguet & Lo Jacono (2014) appear to have been

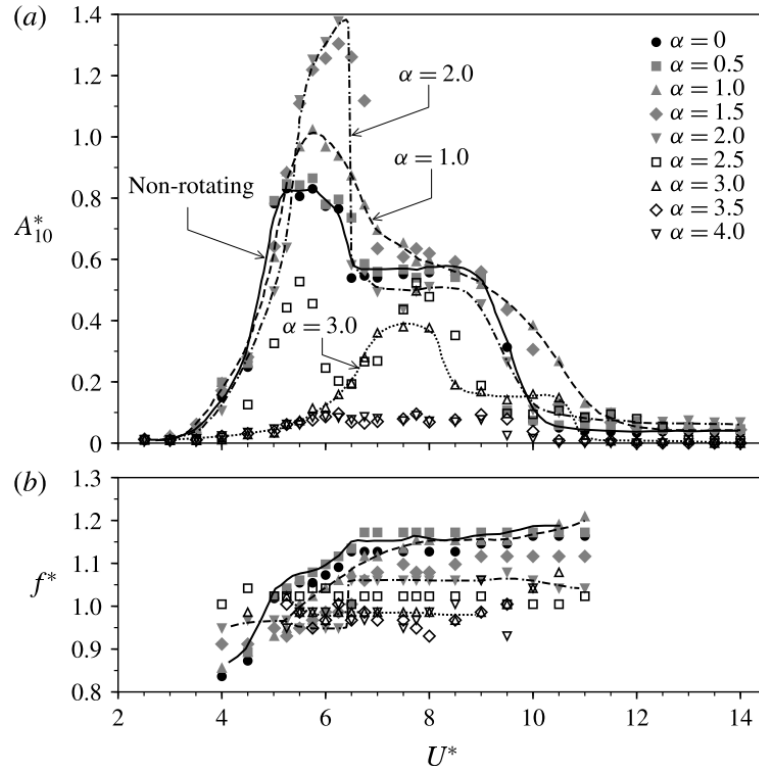


FIGURE 2.11: The vibration amplitude and frequency response for an elastically mounted circular cylinder for different rotation rates as a function of reduced velocity. The figure is reproduced from [Wong \*et al.\* \(2017\)](#).

the first to study computationally the effect of imposed transverse rotation on the VIV response of a circular cylinder at  $Re = 100$ . Notably, they found that the peak amplitude increases to  $\sim 1.9$  cylinder diameters, which is three times that of the non-rotating case, as the rotation ratio was increased from 0 to 3.75. This study was followed by another numerical study by [Zhao \*et al.\* \(2014b\)](#) at low Reynolds numbers. Later, [Seyed-Aghazadeh & Modarres-Sadeghi \(2015\)](#) studied the same problem experimentally, over the Reynolds number range  $Re = 350\text{--}1000$ . In contrast to the study by [Bourguet & Lo Jacono \(2014\)](#), [Seyed-Aghazadeh & Modarres-Sadeghi \(2015\)](#) found that the imposed rotation did not significantly influence the amplitude of oscillations. However, with the increase in rotation rate, the synchronisation regime became narrower, and for  $\alpha \geq 2.4$ , the cylinder oscillations were completely suppressed. Very recently, [Wong \*et al.\* \(2017\)](#) carried out an experimental investigation on the effect of imposed rotation on the VIV response of a circular cylinder for  $1100 \leq Re \leq 6300$ . They demonstrated an increase of up to  $\sim 76\%$  in the peak oscillation amplitude over the non-rotating case for rotation rates close to 2 in the upper amplitude response branch. They reported that increasing the rotation rate from  $0 \leq \alpha \leq 2$  both broadens the synchronisation regime and increases the peak amplitude response. Figure 2.11 shows the VIV response of a circular cylinder for various rotation rates as a function of reduced velocity. As clear from the figure, significant cylinder vibrations were observed for rotation rates up to  $\alpha \approx 3.5$ . It is interesting to note here that although the experimental study by [Seyed-Aghazadeh & Modarres-Sadeghi \(2015\)](#) was performed for relatively different Reynolds numbers, the results are drastically different to the results of the studies by [Wong \*et al.\* \(2017\)](#) and [Bourguet & Lo Jacono \(2014\)](#). Thus, even for VIV of a rotating cylinder, there

appear to be conflicting results on the effect of rotation on the VIV response. One question to be addressed is whether similar features are exhibited in the case of a rotating sphere. Specifically, the current study examines the effect of the body rotation on the VIV response of an elastically mounted sphere. This study aims to address the following fundamental questions: How does constant imposed transverse rotation affect the VIV response of the sphere, does it suppress or enhance the response, and how does this depend on rotation rate? How does the rotation affect the flow near the sphere surface and in the wake? The current study will endeavour to address these questions in chapter 5.

## 2.4 Effect of sinusoidal rotary oscillation

As mentioned earlier, VIV can also be suppressed by forced sinusoidal rotary oscillations of the bluff body, to prohibit the phenomenon of resonance or ‘lock-in’ by deviating the vortex shedding frequency from the natural frequency of the system towards the forcing frequency (also known as ‘lock-on’). The two important parameters characterising the rotary oscillation motion of the sphere are the forcing frequency ratio  $f_R$  and the forcing velocity ratio  $\alpha_R$ . The forcing frequency ratio is expressed as the ratio of forcing frequency,  $f_r$ , and the natural frequency of the system,  $f_{nw}$ , as

$$f_R = f_r / f_{nw}. \quad (2.15)$$

Alternatively, sometimes the non-dimensional forcing Strouhal number is used to characterise the forcing

$$S_f = \frac{f_r D}{U}.$$

The other key parameter, the forcing velocity ratio  $\alpha_R$ , is expressed as the ratio of the maximum tangential velocity of the sphere surface and the free-stream velocity  $U$  as

$$\alpha_R = \frac{D \dot{\theta}_{max}}{2U}, \quad (2.16)$$

where  $\dot{\theta}_{max}$  is the maximum angular velocity of the sphere.

The sinusoidal rotation imposed on the sphere can be expressed as

$$\theta(t) = \theta_o \sin(2\pi f_r t), \quad (2.17)$$

where  $\theta$  is time-dependent imposed angular displacement,  $\theta_o$  is maximum angular displacement and  $f_r$  is the forcing frequency. In terms of the angular velocity, the imposed rotation can be represented as

$$\dot{\theta} = 2\pi f_r \theta_o \cos(2\pi f_r t). \quad (2.18)$$

The velocity ratio  $\alpha_R$ , which is the ratio of the maximum tangential velocity of the sphere to the free-stream velocity, hence, can also be written as

$$\alpha_R = \frac{\pi f_r \theta_o D}{U}. \quad (2.19)$$

It is known from the previous studies that  $f_R$  and  $\alpha_R$  are two crucial parameters in determining the response of a bluff body.



This approach of controlling the wake by utilising sinusoidal rotary motion has been extensively investigated on a fixed cylinder over the last four decades. Taneda (1978) was the first to examine this experimentally for a rotary oscillating cylinder, and reported the disappearance of vortex shedding for very high forcing frequencies. Later, Tokumaru & Dimotakis (1991) reported a drag reduction of up to 80% for a certain range of forcing frequencies and amplitudes of sinusoidal rotary oscillations. This pioneering study inspired a number of systematic numerical studies aimed at understanding this wake control and the underlying dynamics, such as (Lu & Sato 1996; Chou 1997; Baek & Sung 2000; Mahfouz & Badr 2000; Cheng *et al.* 2001; Shiels & Leonard 2001; Tokumaru & Dimotakis 1991; Lee & Lee 2006; Choi *et al.* 2002; Kumar *et al.* 2013). It is known for the case of a fixed cylinder that for a certain range of forcing frequency ratios encompassing the natural frequency of the system, the vortex shedding locks to the forcing frequency, leading to the ‘lock-on’ phenomenon (Chou 1997; Baek & Sung 2000). The state is accompanied by a significant drag reduction (Tokumaru & Dimotakis 1991; Lu & Sato 1996; Chou 1997). The lock-on region widens with increasing rotational speed (Mahfouz & Badr 2000). The boundaries of lock-on and non-lock-on regions are associated with the modulation of the drag, lift and velocity (Choi *et al.* 2002), and the non-lock-on regions exhibit quasi-periodicity (Baek & Sung 2000). Several studies have focused on understanding the underlying dynamics. It was found that the lock-on region is associated with enhanced separation and vortex coalescence in the wake (Cheng *et al.* 2001; Shiels & Leonard 2001; Lee & Lee 2006). The experimental investigation by Thiria *et al.* (2006) also revealed that the phase lag between the vortex shedding and the rotary motion of the cylinder effectively gives either a constructive or destructive contribution to the wake, leading to a global decrease or increase in fluctuations in the wake. All the above mentioned studies were performed for a rigidly mounted cylinder under imposed sinusoidal rotation. However, once the cylinder is given a degree of freedom in the transverse direction, the dynamics could be very different.

Recently, Du & Sun (2015) investigated numerically the potential of rotary oscillations to suppress VIV of an elastically mounted cylinder at  $Re = 350$ . They found ‘lock-on’ for a certain range of frequency ratio, which led to switching of vortex shedding from the natural frequency to the forcing frequency, inhibiting resonance or VIV. The extent of the lock-on region for a cylinder, as  $f_R$  is varied, is shown in figure 2.12(a). A reduction in the amplitude of the cylinder vibration of up to 99% of the cylinder diameter was achieved with  $f_R = 1.8$  at a velocity ratio of  $\alpha_R = 2$ . Furthermore, they also demonstrated that high enough velocity ratios need to be attained for effective suppression. As evident from figure 2.12(b), the response is not effectively controlled for  $\alpha_R < 1$ . Figure 2.12 (c) shows the flow regime where lock-on is observed for a freely vibrating cylinder at  $Re = 350$  and  $\alpha_R = 2$ . It is clear from the figure that the lock-on regime became narrower with an increase in reduced velocity in their study. Their vorticity measurements revealed that the strength of the vortex shedding was not suppressed although transverse vibrations were suppressed. This led them to conclude that in the lock-on region, the vibrations are suppressed due to switching of the vortex shedding frequency from the natural frequency of the system to the forcing frequency.

The above mentioned studies demonstrated the potential of rotary oscillations in controlling the VIV of a cylinder. There do not appear to be any studies so far investigating the potential of rotary oscillations in wake control for 3D bluff bodies, such as



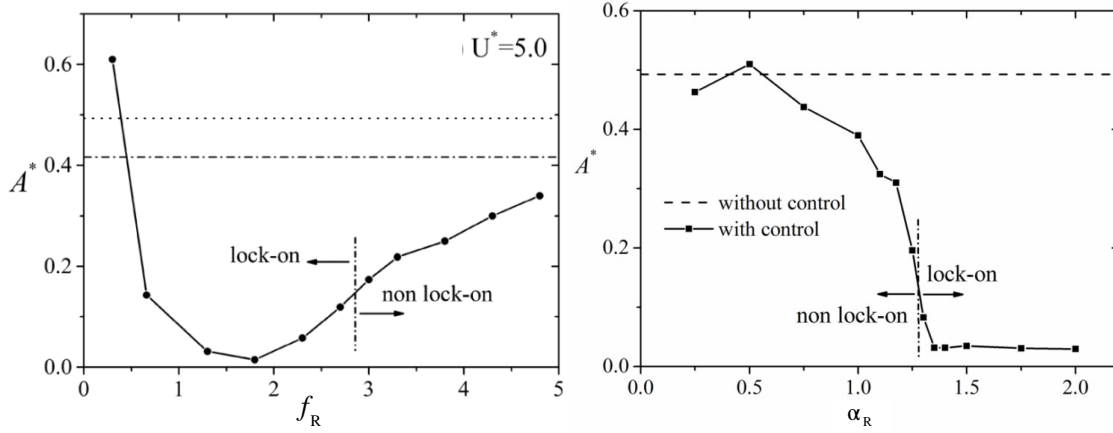


FIGURE 2.12: Vibration amplitude  $A^*$  as a function of forcing frequency ratio  $f_R$  (shown on the left) and as a function of the forcing velocity ratio  $\alpha_R$  (shown on the right). The figures are reproduced from Du & Sun (2015).

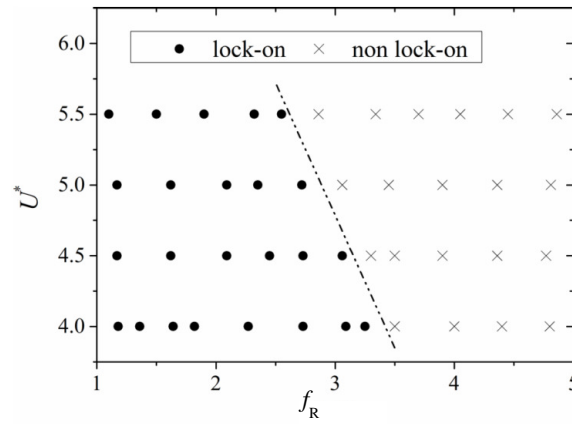


FIGURE 2.13: Flow regime of an elastically mounted cylinder at  $\alpha_R = 2$  for  $Re = 350$ . The data reported by Du & Sun (2015)

spheres. However, a sphere is the most basic 3D body shape; it is certainly the one with the most symmetry, and clearly spheres can undergo significant amplitude VIV. The current study aims to produce an understanding of the effect of imposed rotary oscillations on the VIV response of a sphere for a wide range of forcing and flow parameters. One question to be addressed is whether similar features (as discussed above for a fixed cylinder) are exhibited in the case of an elastically mounted sphere. Specifically, this study aims to address the following fundamental questions: Is ‘lock-on’ also observed for a sphere exhibiting a 3D wake? If so, how does the lock-on range depend on various forcing and flow parameters? How does this phenomenon affect the 3D wake structures of the flow past a sphere? The current study will endeavour to address these questions in chapter 7.

## 2.5 Effect of free surface on the VIV response of a sphere

One of the most practical situations where one encounters flow past elastically mounted spheres is in the area of ocean engineering applications, eg., offshore structures, buoys,

underwater vessels, submarines and floating power generation equipments, etc. Most of these applications consist of structures very close to the free surface or piercing it. Moreover, floating ocean structures for offshore petroleum drilling and production operations also consist of submerged and semi-submerged structures. The VIV response of 3D structures in such situations may be characteristically very different to those in a fully submerged condition. Now the question emerges as to how the proximity to a free surface can affect the VIV response of a sphere? Without addressing this question, our attempt to understand completely the flow-induced vibration past a sphere remains incomplete.

Despite ubiquitous practical applications, the flow past a sphere close to a free surface, and also piercing it, is not well understood. Many studies have reported on the two-dimensional counterpart, the cylinder, elaborating on the effect of a free surface on the flow past that geometry. Reichl *et al.* (2005) studied the two-dimensional flow past a cylinder close to a free surface at  $Re = 180$ . Their major finding was that for low Froude number ( $Fr \leq 0.3$ ), where the surface deformation is minimal, the flow is largely governed by geometric constraints and behaves similar to the flow past a cylinder close to a no-slip wall. However, for higher Froude numbers, where surface deformation becomes substantial, there is a significant surface vorticity generation that can diffuse or convect into the main flow, altering the development of vortex shedding. The flow in such cases is characterised by two metastable states, which can coexist for the same system parameters. Such metastable states were previously observed in the experimental investigations by Sheridan *et al.* (1995) and Sheridan *et al.* (1997). The latter authors investigated experimentally the flow past a cylinder close to a free surface over the Froude number range of  $0.47 \leq Fr \leq 0.72$  and Reynolds number range  $5990 \leq Re \leq 9120$ . They reported that the flow past a cylinder close to a free surface at high Froude number gives rise to fundamental classes of near wake structures that are distinctly different from the wake of a completely submerged cylinder located far beneath the free surface. Considering the limiting case of a piercing cylinder, Yu *et al.* (2008) studied the flow past a cylinder piercing the free surface numerically for  $Re = 1 \times 10^5$  at Froude numbers up to  $Fr = 3$ . Their results showed that the free surface inhibits the vortex generation in the near wake, leading to reduced vorticity and vortex shedding. For  $Fr = 0.8$ , the vortex structures exhibited strong 3D features; however, the flow in the deep wake remained 2D. Furthermore, at  $Fr = 2$ , the free-surface effect propagated throughout the wake, inhibiting regular vortex shedding past the cylinder. Similar results were observed numerically by Inoue *et al.* (1993) and Kawamura *et al.* (2002) for a piercing cylinder. The latter study reported a diverging Kelvin wave system at the free surface and observed surface fluctuations related to the shear-layer instabilities under the free surface. From all these studies, it can be inferred for a cylinder that the free surface acts like a rigid-free-slip boundary for low Froude numbers of  $Fr \leq 0.5$ . For  $0.8 \leq Fr < 2$ , the free surface influences the shedding near the free surface, leading to 3D features very close to the free surface; however, for very high Froude numbers of  $Fr \geq 2$ , the free surface was significantly deformed; there were then strong wave-wake interactions, and the periodic vortex shedding was suppressed for cylinder depths less than one diameter from the free surface.

Although the above mentioned studies focused on fixed cylinders, significant attenuation and alteration of the vortex shedding can be expected for an elastically mounted cylinder. A very recent study by de Oliveira Barbosa *et al.* (2017) reported the effect of

proximity to a solid wall boundary on the VIV response of a freely vibrating cylinder. They observed a reduction in the amplitude response for gaps between 0.75 and 2 diameters and an increase in the amplitude and frequency of oscillations for gaps smaller than 0.75 diameters, when the cylinder actually impacted the boundary. In contrast to the vast literature available on cylinders regarding the effect of wall boundary and free surface, the literature on the VIV of a basic three dimensional body like a sphere is extremely sparse.

There is a brief preliminary study by [Miraudo \*et al.\* \(2014\)](#) on the dynamic response of a light ( $m^* = 1.34$ ) tethered sphere in a shallow water flow. Although their study lacked any forces or vorticity measurements to support their claims, they indicated a reduction in the vibration response amplitude with the presence of a free surface. They also stated that for  $0 < h^* \leq 0.5$ , there was no mode II, and mode I occurred for relatively lower reduced velocities compared to the fully submerged case. This claim, however, was not backed up by simultaneous force measurements. It is known from the previous benchmark studies that the total phase difference  $\phi_{total}$  and vortex phase difference  $\phi_{vortex}$  are the key determinative factors in identifying the two modes of vibrations. The other prime limitation of the study was that there were large variations in the blockage ratio with the immersion depth in their experimental setup. Also, there were appreciable wall effects, as the sphere was placed close to the channel floor (3 mm from the channel wall), which were neglected. Although, not of direct relevance to the present problem, it should be mentioned here that there have been some previous investigations on the water entry of spheres ([Truscott & Techet 2009b,a](#); [Aristoff & Bush 2009](#); [Aristoff \*et al.\* 2010](#))

One can decipher here that it is not yet well understood how the proximity to the free surface affects the VIV response. How the flow structures past a sphere are affected when it is close to a free surface? What happens to the different modes of vibrations? Furthermore, there appears to be no study so far investigating the VIV response of a semi-submerged sphere that pierces the free surface. It is still unknown if the case of a semi-submerged sphere, which is quite ubiquitous in ocean engineering, oscillates more vigorously than a fully submerged sphere or if the vibrations are greatly reduced due to the free surface? All these questions remain unanswered. That being the case, the current study will endeavour to address these questions in chapter 6.

## 2.6 Chapter summary and research questions

In this chapter, a review of the relevant literature was presented. In the process, several unanswered questions were identified and the gaps in the literature were established. In this section, those gaps are summarised and presented again. Here, the principal research questions to be addressed in the current study are proposed.

1. As it was discussed in § 2.3, previous studies performed on rigidly mounted spheres reported suppression of vortex shedding for a certain range of rotational rates when the transverse rotation was imposed onto the sphere. One can conjecture here that an imposed rotation may suppress vibrations once the sphere is elastically mounted. However, for the case of an elastically mounted circular cylinder, studies have shown conflicting results in terms of the effect of transverse rotation on the vibration amplitude response of a cylinder. One may ask here, how the imposed transverse rotation will affect the vibration response of a sphere once it

is elastically mounted? Therefore, for this study, the first research question to be addressed is:

***What is the effect of imposed transverse rotation on the vortex-induced vibrations of an elastically mounted sphere?***

2. It was revealed in § 2.4 that some recent studies on elastically mounted cylinders have demonstrated an effective control of vortex induced vibrations employing sinusoidal rotary oscillations of the cylinder for a certain range of control parameters. However, the potential of this control method has not been investigated yet on a 3D bluff body prototype, a sphere. Hence, in this study, the second research question to be addressed is:

***What is the effect of imposed sinusoidal rotary oscillation on the flow-induced vibration of a sphere?***

3. In § 2.5, it was discussed that the proximity to a free surface can have a strong influence on the wake past a fixed cylinder. Furthermore, a recent preliminary study on tethered spheres also indicated a considerable reduction in the vibration response due to proximity to a free surface. On the other hand, there is no study so far, to the best of the author's knowledge, reporting the dynamics of a semi-submerged sphere. As a consequence, the third research question to be addressed in the current study is:

***What is the effect of proximity to a free surface on the flow-induced vibration of a fully submerged sphere? How does the response change when the sphere pierces the free surface?***

The above proposed research questions are addressed by carrying out an extensive series of systematic experiments employing simultaneous displacement, force and vorticity measurements. The sphere response will be measured for a wide range of forcing and flow parameters. Particle image velocimetry (PIV) in the cross-plane and the equatorial plane is employed to understand the underlying dynamics. The flow-visualisation using hydrogen-bubbles and dye are also performed in some cases. In the following chapter 3, the experimental methodologies, procedures and equipments employed in this study are presented in detail.



## Chapter 3

# Experimental Methodology

*However difficult life may seem there is always something you can do and succeed at.*

---

Stephen Hawking

### 3.1 Overview

This chapter provides an overview of the experimental methodologies, facilities, equipments and procedures employed in the current study. In § 3.2, an outline of the complete experimental arrangement is given. In the following sections, each method and the equipment used is then described in detail. § 3.3 discusses the displacement measurement procedure followed by § 3.4 which elaborates on the air bearing rig, and § 3.5 provides details of the force measurement methods. In § 3.6, the rotation rig and the support setup is explained followed by § 3.7 which provides comprehensive details of the flow visualisation techniques employed in the current study.

### 3.2 Experimental arrangement

The experiments were conducted in the recirculating free-surface water channel of the Fluids Laboratory for Aeronautical and Industrial Research (FLAIR), Monash University, Australia. The test section of the water channel has dimensions of 600 mm in width, 800 mm in depth and 4000 mm in length. A mixed-flow pump that is powered by an AC electric motor drives the water channel. The free-stream velocity in the channel could be varied continuously over the range  $0.05 \leq U \leq 0.45 \text{ ms}^{-1}$ , corresponding to the pump frequency range 5 – 50 Hz. The operational frequency of the pump was controlled digitally using the LabVIEW® software. The flow quality in the channel was maintained by regular cleaning, and the periodic measurement of free-stream velocity and turbulent intensity. The upstream flow in the channel was conditioned by a combination of mesh, honeycomb and a three dimensional 3:1 ratio contraction. This enabled the free-stream turbulence level in the test section to be less than 1%. Further characterisation details of the water channel facility can be found in Zhao (2012).

A schematic of the experimental setup is shown in figure 3.1. A low-friction air bearing system was placed above the water channel that provided low structural damping and constrained the body motion to be in the transverse direction to the oncoming

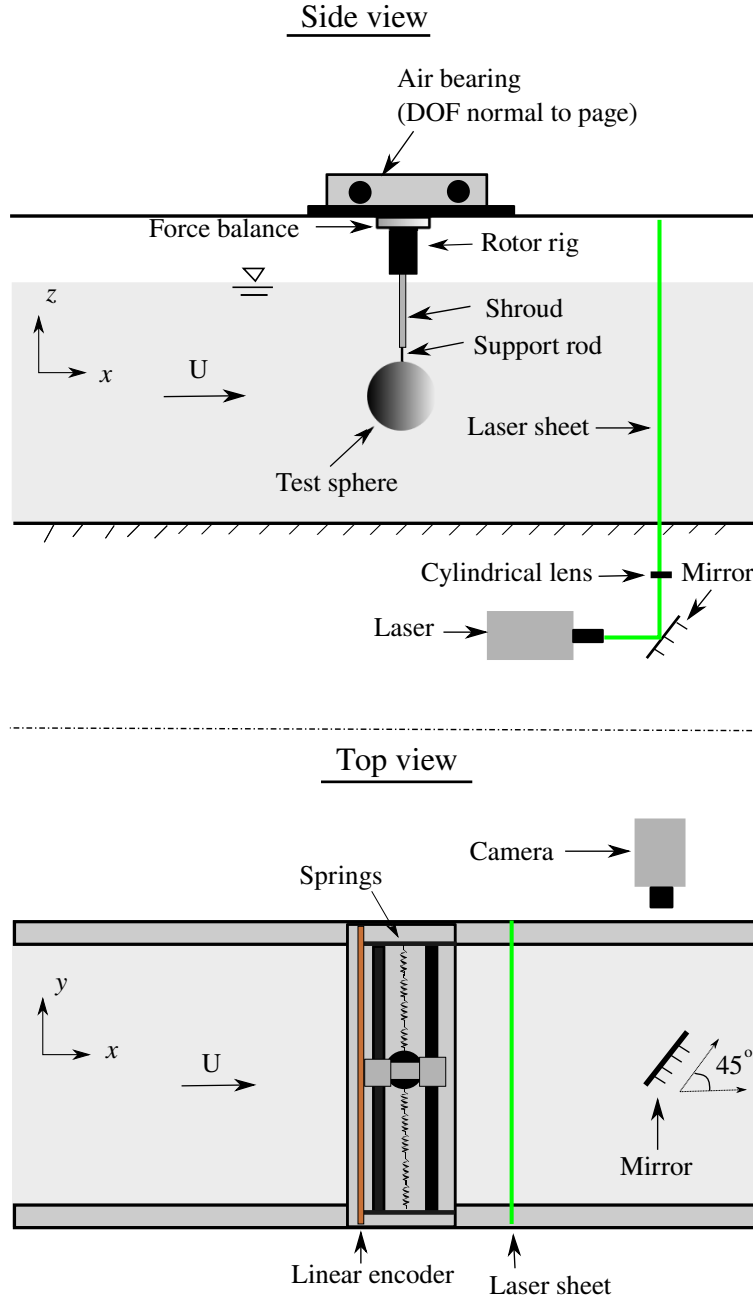


FIGURE 3.1: Schematic of the present experimental arrangement.

free-stream. The sphere model was vertically supported by a thin stiff driving rod that was adapted to a rotor mechanism. The rotor mechanism was mounted to a 6-axis force sensor coupled with the carriage. The set of experiments aimed at investigating the effect of free surface were performed without the rotor rig. Particle image velocimetry (PIV) was used along with the simultaneous displacement and force measurements to detect and identify the main fluid structures in the region of interest. Details of each experimental technique will be discussed in detail in the following sections.

### 3.3 Displacement measurements

The body displacement was measured using a non-contact magnetostrictive linear variable differential transformer (LVDT) (model SE 750-10000 manufactured by Macro Sensor<sup>™</sup>, USA). Typically, an LVDT consists of a cylindrical magnetic core unit (usually attached to the oscillating mass whose displacement is to be measured) and a coil assembly secured in a cylindrical stainless steel housing. It works on the principle of a transformer, where a primary winding is excited by an external voltage source, and it generates magnetic flux coupled to two secondary windings. Depending on the position of the magnetic core, the voltage difference between the two secondaries change linearly. A constant 24V DC was used to excite the LVDT and its output voltage ranged from 0-10V, corresponding to a linear measurement range of 0-250mm. The accuracy of the LVDT was within  $\pm 0.01\%$  of the 250 mm range available.

One should note here that the total transverse force acting on the sphere can be derived from the measured displacement signal using the equation of motion 2.16. Precise determination of the force signal relies heavily on how accurately the velocity and acceleration signals can be derived from the measured displacement signal. It was observed that the LVDT signal could be prone to the electromagnetic noise emitted by the driving motor, which decreased the accuracy of the force measurements. To rectify this, an optical linear encoder (model: RGH24, Renishaw, UK) with a resolution of  $1\text{ }\mu\text{m}$  was also employed to measure the displacement signal. An optical encoder consists of a linear scale containing alternating reference markers, and an optical sensor unit that has a light source and a photo sensor. The linear scale in the current study was a gold plated metallic strip with scaled facets with a  $20\text{ }\mu\text{m}$  pitch. It was powered by an external 5V DC supply. In the present setup, the scale was attached to the fixed base plate of the air-bearing rig and the optical sensor unit was installed onto the moving carriage. As the sensor unit moves with the oscillating body, it receives pulses of light reflected by the linear scale's markers that are registered as voltage signals. Since the linear encoder was digital, electromagnetic noise did not affect the accuracy of the displacement signal measurement. This considerably improved accuracy and enabled reliable velocity and acceleration signals to be derived, which, in turn, enabled an accurate determination of the lift force signal as discussed above. This was tested through a direct comparison against the lift force determined by the force sensor over a wide range of  $U^*$ . It was found that the lift force measured using the force sensor matched well that derived from the linear encoder and the LVDT signals, indicating accurate measurements of the displacement and the lift force from several techniques. This aspect will be elaborated in detail in § 3.5.

### 3.4 Air-bearing rig

The current hydro-elastic problem was modeled using a low-friction airbearing system that provided low-structural damping and constrained the body motion to be in the transverse direction to the incoming free-stream. Similar air bearings have been extensively used in the past to experimentally simulate the low-friction condition in such systems (Feng 1968; Khalak & Williamson 1997; Govardhan & Williamson 2005; Zhao *et al.* 2014a). The current airbearing system was designed by Zhao *et al.* (2018) and constructed in house by FLAIR and the Department of Mechanical and Aerospace Engineering.



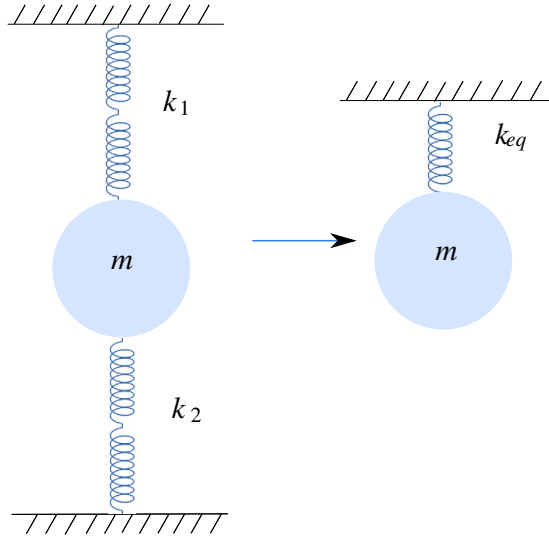


FIGURE 3.2: An illustration of the current spring mass system (shown on the left) that can be reduced to an equivalent spring mass system shown on the right.

The current setup utilised 4 porous carbon air bushings commercially manufactured by NEWWAY<sup>®</sup> Air bearings, USA. The oscillating mass was supported by two hollow carbon fiber guide shafts. It was found through several tests that the precision of the guide shafts is absolutely crucial to the performance of the air-bearing rig. Replacing the carbon fiber shafts with the aircraft grade stainless steel shafts with 0.007mm tolerance and a surface finish 16 RMS significantly improved the air bearing performance. Compressed air was supplied to all the four air bushings at a pressure of 90 PSI that provided the frictionless motion by creating a uniform thin layer of air acting as a lubricant between the guide shafts and the bushings. It was important for the performance of the bushings that the compressed air supply was filtered and regulated upstream to maintain a continuous steady supply of clean and dry air. The structural stiffness of the airbearing system was controlled by extension springs that were attached to both sides of a slider carriage. For the current experiments, 2 stainless steel springs, model B17-129, commercially manufactured by Century Spring Corp<sup>®</sup> were attached in series on both the sides of the carriage. Each spring had an outer diameter of 7.137 mm, wire diameter of 0.381 mm, free length of 63.5 mm, and spring constant of  $k \approx 5.25 \text{ Nm}^{-1}$ . Figure 3.2 shows an illustration of the current spring mass system and its equivalent spring mass system. The two springs on each side of the moving oscillating mass are in series giving rise to an effective spring constant of  $k_1 = k/2$  &  $k_2 = k/2$ .  $k_1$  and  $k_2$  are now in parallel giving rise to a total equivalent spring constant for the system to be  $k_{eq} = k$ . Hence, the overall spring constant of the system was the same as the individual spring constant, i.e.,  $5.25 \text{ Nm}^{-2}$ . It was found that the heavy motor and encoder wires can change the effective spring constant of the system. Also, they can cause errors in the total oscillating mass of the system. Therefore, the thick and heavy motor wires were replaced with very thin wires, and they were clamped at the carriage first and then again at the ceiling so as to minimise obstruction to the low-friction motion in the transverse direction. This also helped to reduce errors in the direct force measurements.

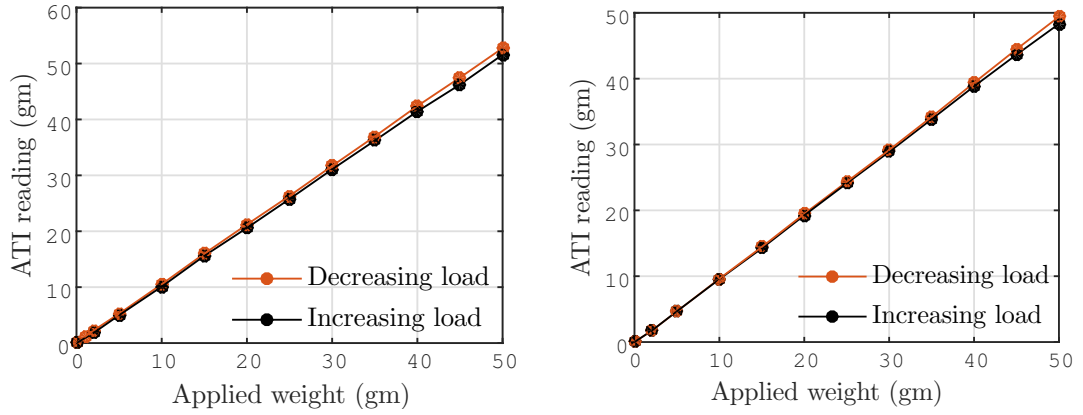


FIGURE 3.3: Figures showing the output reading of the ATI sensor for progressively increasing/decreasing applied load in  $x$  direction (left) and in  $y$  direction (right).

### 3.5 Force measurements

The forces acting on the sphere were measured using a multi-axis load cell (Mini40, ATI-IA), which measures six-component forces and moments ( $F_x$ ,  $F_y$ ,  $F_z$ ,  $M_x$ ,  $M_y$ ,  $M_z$ ) with a resolution of  $1/200$  N for  $F_x$  and  $F_y$ , and  $1/100$  N for  $F_z$ . This load cell is highly sensitive, based on silicon strain gauges, which provide a signal 75 times stronger than the conventional foil gauges. It saturates at any load greater than its maximum sensing range value, which is 20N in  $F_x$  and  $F_y$ , 60N in  $F_z$ , and 1 Nm in  $M_x$ ,  $M_y$  and  $M_z$ . For each data set, the raw analog voltages corresponding to all of the components of ( $F_x$ ,  $F_y$ ,  $F_z$ ,  $M_x$ ,  $M_y$ ,  $M_z$ ) were acquired at 100Hz for more than 100 oscillation cycles at each flow velocity, and were converted to a digital signal using a differential-ended DAQ board system. The raw voltages were then converted to forces using a  $6 \times 6$  calibration matrix (provided by ATI) that decouples all of the components to provide the required drag and lift forces presented in this study.

The data sampling and recording were controlled via customized LabVIEW®8.5 VI programs (see [Zhao 2012](#)), while the data processing and analysis were performed using MATLAB codes. The acquired signal was filtered using a Butterworth filter with an order of 4 and a cut off frequency of 2. The performance of the load cell was examined by placing the ATI in the current experimental arrangement (see figure 2.5) and then applying known loads in the  $x$  and  $y$  direction. Figure 3.3 shows the calibration curves for the force sensor showing the output reading of the sensor as the applied load is progressively increased and then decreased. Although, the commercially made ATI sensor is extremely sensitive and accurate, it is susceptible to temperature changes, and can give erroneous force readings if not properly insulated from heat sources (*e.g.* the motor). As the stepper motor heats up during its operation, the heat conducts to the sensor leading to large drifts in the force signal. A 10 mm non-conducting acetal plate was installed between the rotor rig and the sensor to reduce the heat conduction. This considerably reduced the temperature rise of the load cell and brought the drifting in the force signal to acceptable levels. The results from one of the dry tests (performed outside the water channel) is presented in figure 3.4, where the motor was run at 300 rpm for 5000 seconds and the temperature of the ATI was recorded using a resistance temperature detector. For this test, the sphere was not attached to the rig so as to make sure that no fluid forces are involved. The figure shows the force signal drifting as a function of the temperature rise of the ATI load cell for the case when the insu-

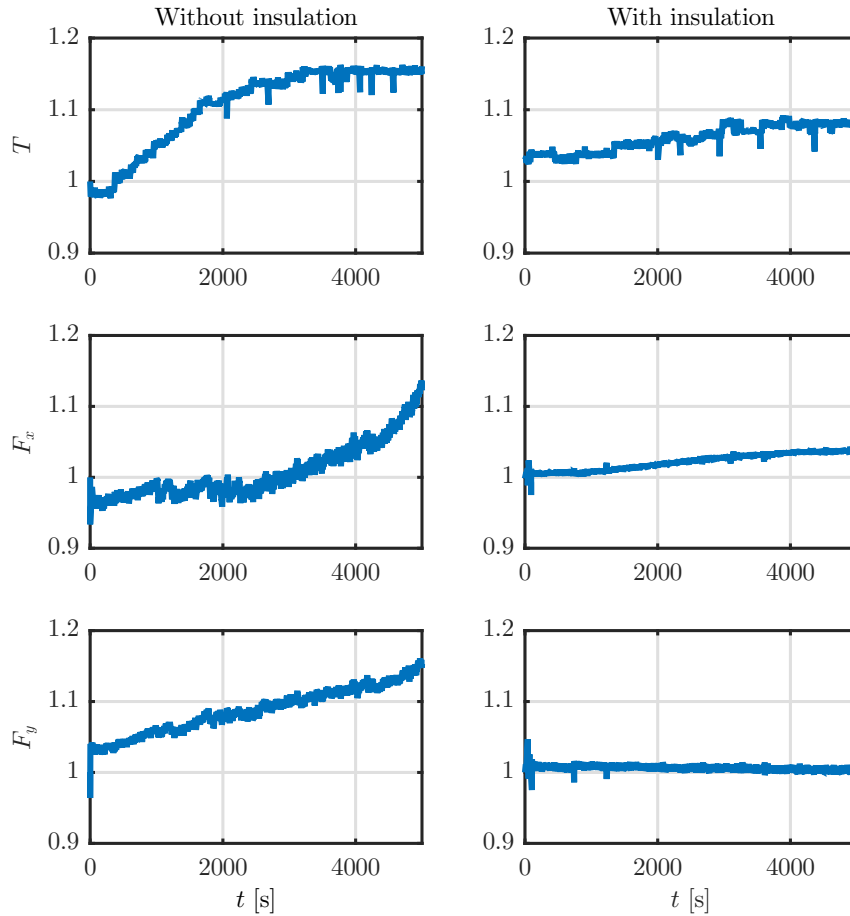
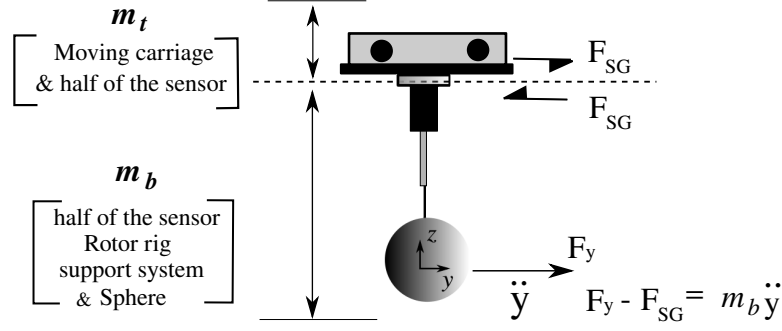


FIGURE 3.4: Figures showing the temperature rise of the load cell correlated with the drifting in  $F_x$  and  $F_y$  with insulation installed (shown on right) compared to when it is not installed (shown on left). The motor was run at 300 rpm for 5000 seconds in this test and the sphere was not attached to the rig.  $T$  is normalised temperature of the force sensor and  $F_x$  and  $F_y$  are normalised forces in the  $x$ -axis and  $y$ -axis, respectively.

lation is not installed (shown on the left) compared to the case when the insulation is installed (shown on the right). As evident from the figure, the rise in the sensor's temperature translates almost linearly into the rise in  $F_x$ . For this particular case, there was  $\sim 17\%$  increase in the sensor temperature due to operating motor that led to  $\sim 17\%$  increase in  $F_x$  and  $\sim 11.3\%$  increase in  $F_y$ . However, installing the insulation reduced the temperature rise to only  $\sim 4\%$ , which reduced the drift in  $F_x$  to 3% and the drift in  $F_y$  to less than 0.5% in 5000 seconds. Note here that during the actual experiments, the signal was recorded for  $\sim 100$  sphere oscillation cycles, i.e., only  $\sim 500$  seconds. so the drifting was reduced to insignificant levels in both  $F_y$  and  $F_x$ . It should be pointed out here that the signal drifting is very difficult to predict as it varies with the rotational rate of the motor and other environmental factors. Thus, it was always advisable to bias the sensor regularly so as to get correct readings. In the current experiments, the sensor was biased after every 4-5 data points by stopping the motor and the pump. A reference signal was recorded after the sphere reached a complete halt.


 FIGURE 3.5: Schematic showing the mass bottom  $m_b$  and mass top  $m_t$ .

In the current experimental arrangement (see figure 3.5), the force sensor is placed above the rotor rig. In this situation, the force measured by the strain gauge or force sensor in the  $y$ -direction,  $F_{SG}$ , is not the direct measurement of the total transverse force acting on the sphere ( $F_y$ ). One has to consider the inertial term accounting for the accelerating mass below the load cell as given by the following equation

$$F_y = F_{SG} + m_b \ddot{y}, \quad (3.1)$$

where,  $m_b$  is the mass below the strain gauge that includes the sphere, support structure, rotation rig, and half of the mass of the sensor (See figure 3.5). Accurate estimation of  $F_y$  relies on how accurately  $\ddot{y}$  is derived from the measured displacement signal. This method of force measurement has been termed the ‘*direct force measurement*’ in the current study, although, it is also a derived quantity in a sense. As discussed earlier,  $F_y$  can also be computed from the measured displacement signal using the equation of motion recollected below

$$F_y = m\ddot{y} + c\dot{y} + ky.$$

$F_y$  computed using this approach has been termed ‘*derived force measurement*’. This approach of computing  $F_y$  from the measured displacement signal is only appropriate where highly accurate digital displacement measurements are possible. It also requires, of course, accurate measurements of the relevant parameters of the spring-mass system (total oscillating mass, spring constant and the structural damping). One can examine the accuracy of the force sensor by directly comparing the forces computed using the two approaches. As shown in figure 3.5,  $F_{SG}$  is the direct reading output from the force sensor that can also be computed from equation 2.16 by considering the top mass  $m_t$  of the system as shown below.

$$F_{SG} = m_t \ddot{y} + c\dot{y} + ky.$$

Such a comparison is shown in figure 3.6 for three different reduced velocities in three vibration modes of the sphere VIV response. The force derived from the above equation considering the top mass of the system (shown in black) closely matches the direct force sensor reading  $F_{SG}$  (shown in red) in all the three modes of vibrations. Figure 3.7 shows the variation of the rms of the total transverse force coefficient  $C_{y\,rms}$  with the reduced velocity, computed from both the approaches. This comparison demonstrates that the force sensor was able to accurately measure the forces in the current experimental arrangement.

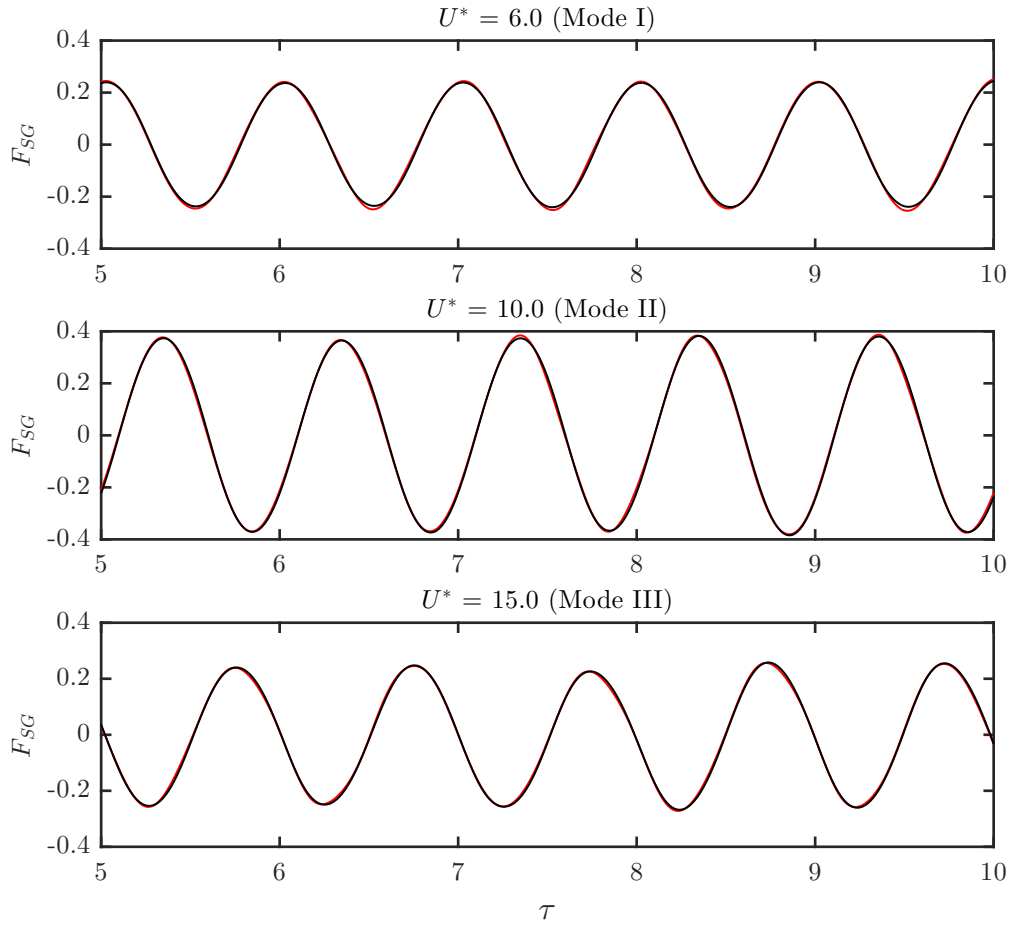


FIGURE 3.6: Comparison of the direct force measurement with the derived one from the equation of motion. Red color represents the measured signal, and black color represents the derived signal.

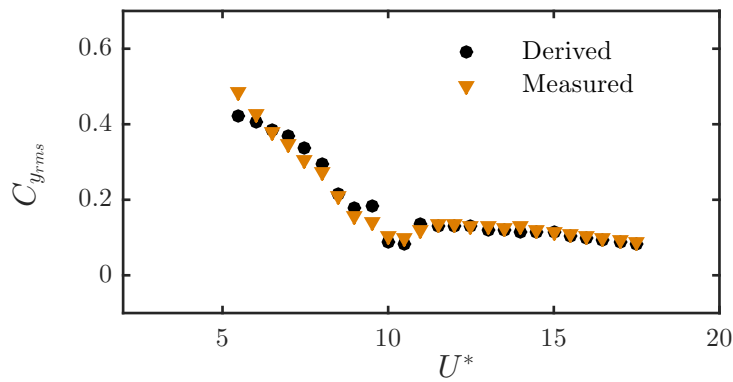


FIGURE 3.7: Figure showing the comparison between the derived force coefficients and the direct measurement from the force sensor.

Most of the force coefficients reported in the current study employed the derived force measurements. The force measurements from the load cell suffered from a greater degree of noise, presumably from the electromagnetic sources. More importantly, the load cell suffered large drifts in the force signal due to the motor operation; hence the preference for the force derived from the displacement signal. In the first study discussed in § 5, force coefficients utilising both the approaches have been reported. However, the latter two studies discussed in § 6 and § 7, report only the derived force measurements.

## 3.6 Details of the rotation rig and the support setup

### 3.6.1 Rotation rig

The rotary motion was driven using a miniature low-voltage micro-stepping motor (model: LV172, Parker Hannifin, USA) with a resolution of 25 000 steps/revolution, which was installed inside the rotor mechanism shown in figure 3.9. The rotation speed was monitored using a digital optical rotary encoder (model: E5-1000, US Digital, USA) with a resolution of 4000 counts/revolution. The motion control was realised using Parker® 6K motor controllers and drivers. The laboratory computer hosted a digital input-output interface that communicated with the 6K controller. All the motor control parameters such as motor-controller scaling, operation modes, rotational rates, frequency and amplitude of the sinusoidal rotary motion were input into the 6K controller’s user interface. This information enabled the controller to control the DC motor drivers that regulate the motion of the stepper motor. More details of the motion control system can be found in Wong *et al.* (2017); Zhao *et al.* (2018).

To ensure that the motor was following the input motion profile precisely, the output signal from the optical encoder built into the rotation rig was recorded and monitored during the experiments. For experiments involving constant rotation (§ 5), the relative error in the output rotation rate of the motor over the entire range of input rotation rates tested in the current study was less than 0.22 %. For experiments involving the rotary oscillations (§ 7), the relative error in the output frequency of the sinusoidal motion profile was found to be less than 3% for the entire range of input frequencies tested in the current study. The relative error in the output amplitude of the sinusoidal motion profile was less than 2%. Figure 3.8 shows the output motion profile of the sphere for various input frequencies and amplitudes in mode I. The zero position of the sinusoidal motion profile was found to drift with time, as is evident from the figure. The drift increased with the increase in the forcing frequency. The maximum drift was found to be less than  $\alpha_R = 0.057$  over 50 cycles for  $\alpha_R = 0.5$  and  $f_R = 5$ . It was assumed that such a small deviation or drift from the rotational zero position is unlikely to affect the overall response of the cylinder.

### 3.6.2 Sphere models and the support setup

The sphere models used in the current study were solid spherical balls precision-machined from acrylic plastic with a very smooth surface finish. The accuracy of the diameter was within  $\pm 20 \mu\text{m}$ . In the current study, several sphere sizes of  $D = 40 \text{ mm}$ ,  $70 \text{ mm}$ ,  $80 \text{ mm}$  and  $120 \text{ mm}$  were used. However, most of the experiments were performed using a  $80 \text{ mm}$  sphere. The spherical models were supported using a cylindrical support rod  $3 \text{ mm}$  in diameter, manufactured from hardened nitrided stainless steel for

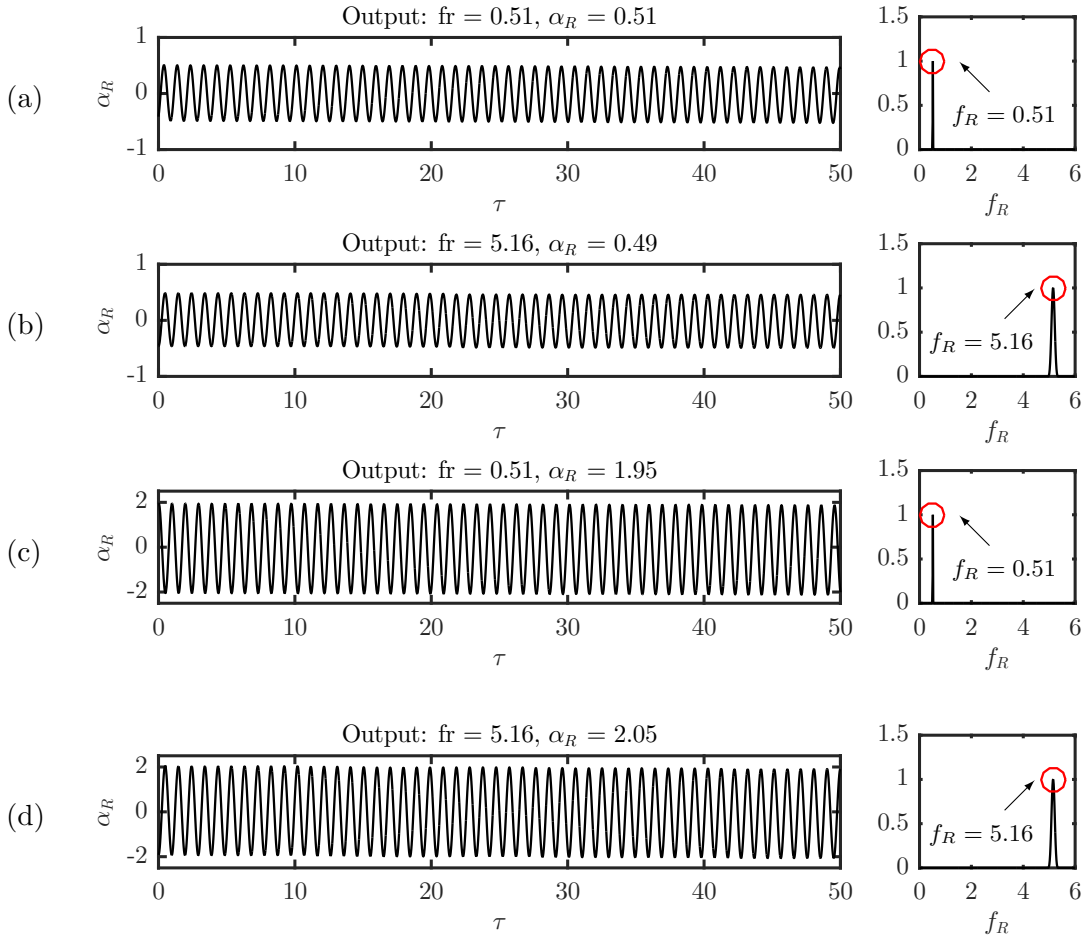


FIGURE 3.8: Time trace of the output signal from the encoder (shown on left) along with the power spectra of the signal shown on the right. The input parameters were  $f_R=0.5$  &  $\alpha_R=0.5$  for (a),  $f_R=5$  &  $\alpha_R=0.5$  for (b),  $f_R=0.5$  &  $\alpha_R=2$  for (c), and  $f_R=5$  &  $\alpha_R=2$  for (d). The corresponding output values are shown on top of each figure.

extra stiffness and to maintain straightness. This gave a diameter ratio  $D^*$  between the sphere and the support rod of 23.3. The immersion depth (measured from the top of the sphere to the free surface) of the sphere was  $1D$ . This support arrangement was used for studying the effect of free surface discussed later in chapter 6. However, for experiments involving the forced rotation of the sphere (chapter 7 and chapter 5), this support arrangement was not appropriate mainly for two reasons. The primary reason was that this support arrangement experienced significant wobbling with the applied rotation to the sphere. Secondly, the rotating support rod can experience large Magnus force and can potentially interfere with the sphere wake. For this reason, another support arrangement was employed consisting of a fixed cylindrical shroud covering the thin rotating rod. This decreased the diameter ratio to  $D^* = 12.6$ . Decreasing the diameter ratio can significantly affect the amplitude response of a sphere as shown in figure 3.10. As evident from the figure, the peak vibration amplitude decreased by almost 26 % by changing the  $D^*$  from 23.3 to 12.6. Hence, another arrangement was employed, where the shroud was set to approximately  $0.5D$  to minimise its influence while maintaining the structural support for the driving rod having an immersed length

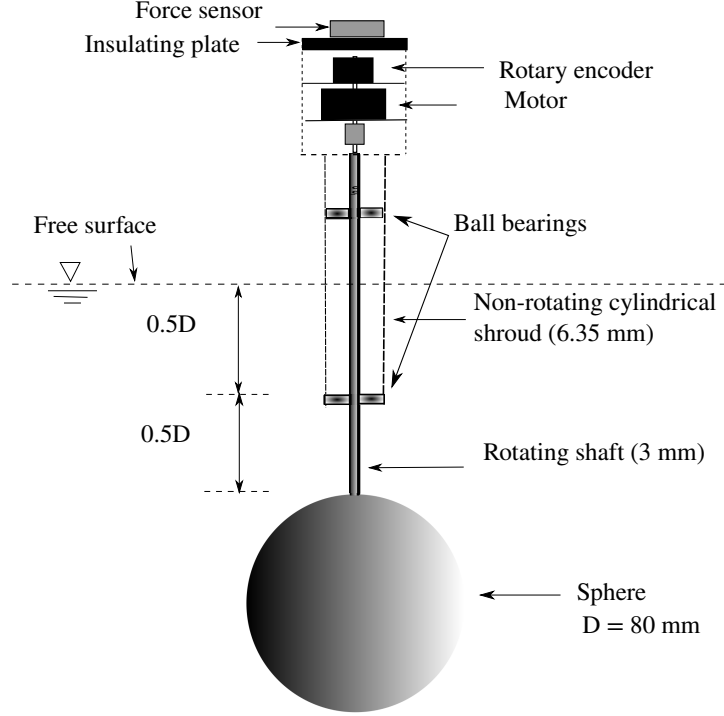


FIGURE 3.9: Schematic showing the cylindrical shroud support arrangement

of  $0.5D$  exposed beyond the shroud. The total immersed length of the support setup for the sphere was still  $\sim 1D$ . With this shroud arrangement, the vibration amplitudes recovered, reaching values similar to the  $D^* = 23.3$  case, as shown in figure 3.10. This shroud-setup provided extra rigidity to the support, and was able to limit the wobbling deflection associated with the sphere rotation to within  $\pm 0.01D$ , thereby minimising undesirable perturbations to the structural dynamics and near-body wake by stabilising the sphere's rotary motion. This setup also helped limit the undesirable wake deflection that would be caused by the large Magnus force on the unshrouded rotating cylindrical rod. Hence, this shroud arrangement was used for all the experiments involving the forced rotation of the sphere.

Systematic experiments were performed in this study investigating the effect of free surface on the VIV response of a sphere, these are included in chapter 6. It was found that depending on the immersion ratio  $h^*$ , which is the ratio of the immersion depth to the sphere diameter, and the diameter ratio  $D^*$ , the VIV response of a sphere can change significantly. Based on experimental evidence, it was established that the optimum value of  $h^*$  for studying the VIV response of a fully submerged sphere, for the support rod and the free surface effects to be minimised, varies from  $h^* \sim 0.6 - 1.75$ . Hence, the immersed length of  $1D$  was chosen ( $h^* = 1$ ) for studying the VIV response of a fully-submerged sphere.

## 3.7 Flow visualisations

### 3.7.1 Hydrogen-bubble and dye visualisations

For experiments involving constant rotation of the sphere, hydrogen-bubble and dye visualisations were performed to visualise the wake deflection. For the hydrogen-bubble visualisations, a  $50\mu$  platinum wire, 500 mm long, was used to generate a continuous



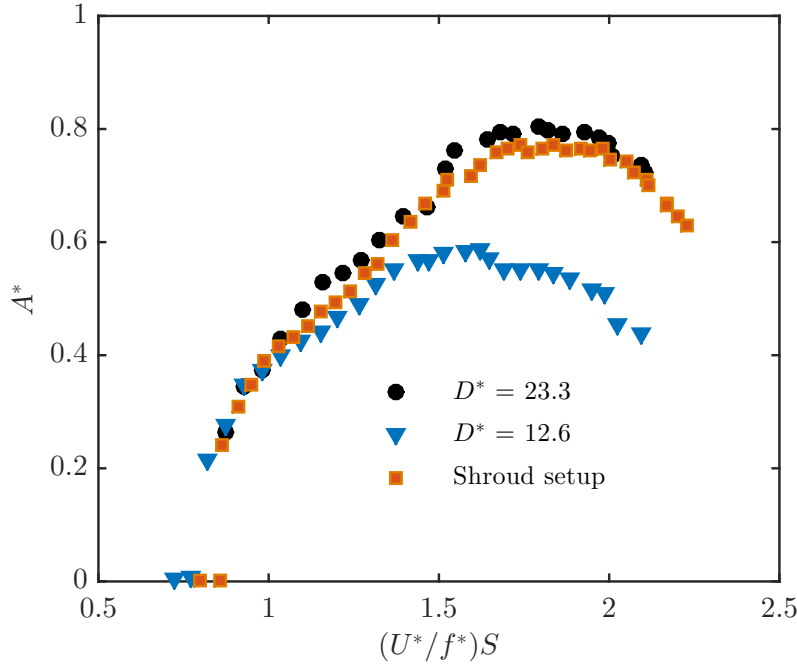


FIGURE 3.10: The vibration response of a sphere for three different support rod arrangements. The data shown in square symbols correspond to the shroud-arrangement used in the current study, where  $D_r = 3$  mm for  $0.5D$  immersed length (closer to the sphere) followed by a stationary shroud of  $D_r = 6.35$  for another  $0.5D$  immersed length. The total immersed length for all the three arrangements shown in the above figure is  $1D$ .

sheet of hydrogen bubbles in the flow. The platinum wire was soldered in an F-shaped stainless steel frame, and positioned upstream and parallel to the sphere axis. A potential of 50 VDC was found sufficient to produce a dense sheet of hydrogen bubbles. No additional electrolytes were added to the tunnel flow. A continuous Nd:Yag laser was used to illuminate the bubble sheet. A Nikon D7000 camera with 28mm lens was used to record videos. Dye visualisation was also employed to visualise the flow. For this purpose, a Fluoresceine dye was injected using a pitot tube (1 mm in diameter) placed upstream of the sphere. As the dye propagates along a line in the flow, it mixes with the surrounding fluid, and the dye lines lose their clarity, and rapidly decay. Thus, this method of visualisation is restricted mainly to low fluid velocity. An ultraviolet lamp was used to illuminate the dye. Images were recorded using a digital camera (model: D7000, Nikon, Japan) equipped with a 50 mm lens that was positioned beneath the water channel glass floor.

### 3.7.2 Particle image velocimetry (PIV)

Unlike the above-mentioned flow visualisation methods of dye and hydrogen bubble, Particle image velocimetry is a non-intrusive flow-visualisation technique. It enables instantaneous and high-spatial resolution velocity field measurements. One can derive additional information such as vorticity, circulation and pressure distributions through post-processing the data obtained from the PIV. This technique is extensively used in experimental investigations, and has been documented in detail in [Adrian \(1991\)](#) and [Raffel \*et al.\* \(2007\)](#). In the current study, vorticity field measurement using PIV were performed in the central equatorial plane ( $x$ -  $y$  plane) as well as the cross-plane ( $y$ - $z$

plane). The details of each PIV setup are given below:

### 3.7.2.1 Cross-plane PIV

The flow was seeded with  $13\text{ }\mu\text{m}$  hollow micro-spheres having a specific weight of  $1.1\text{ gm}^{-3}$ . In general, the particle density should be such that a  $32 \times 32$  pixel window has approximately 4-5 particles. Fewer number of particles usually lead to error vectors during cross-correlation. A non-coalescing solution was added in the water in order to avoid coalescence of the particles. Laser reflection from big particles ( $\mathcal{O}(1\text{ mm})$ ) can potentially burn the sensor of a highly sensitive camera like the one used in the current study.

A continuous laser (model: MLL-N-532-5W, CNI, China) was placed beneath the water channel glass floor to generate a laser sheet of thickness  $\sim 3\text{ mm}$  parallel to the  $y$ - $z$  plane. The cross-plane PIV setup is shown in figure 3.1. Imaging was performed using a high-speed camera (model: Dimax S4, PCO, AG) with a resolution of  $2016 \times 2016$  pixels<sup>2</sup> capable of capturing double images with a single exposure. This camera was equipped with a 105 mm Nikon lens for the cross-plane PIV. By placing a scale in the field of view and capturing an image by the camera, one can calculate the magnification factor ( $\mathcal{M}$ ) in pixel  $\text{mm}^{-1}$  an essential piece of information for converting a distance unit in images from pixels to a desired unit, mm in this case. The magnification factor was found to be  $10.72\text{ pixel mm}^{-1}$ . A mirror was placed at  $45^\circ$  angle to the freestream direction towards the downstream side of the sphere. The mirror was placed more than 6 diameters away from the sphere to avoid any upstream effects.

An external TTL signal generator was used to trigger the camera and the laser at a sampling frequency in a sequence of 3100 image pairs. Each recorded image in a pair was separated by a time  $\Delta t$ . The signal generator's TTL signal pulses were recorded simultaneously with the sphere displacement signal measured by the LVDT or the linear encoder. Hence, the position of the sphere was known at every instant the laser was fired. This information is necessary for phase-averaging the data fields, which will be discussed later. For studying the wake of bluff bodies, usually a constant spatial shift of  $\delta d \approx 8\text{-}10$  pixels is sought between the two images in a pair. Hence, an approximate  $\Delta t$  to be used in the equatorial PIV can be deduced for every flow velocity by using the equation  $\Delta t = \delta d / U$ . However, for the cross-plane PIV,  $\Delta t$  calculated using the above equation may be too large. Since the through-plane velocity of the tracer particles is relatively large compared to the in-plane velocity, the particles captured in the first image in a pair may already have passed through the plane when the second image is captured. Hence, for the cross-plane PIV, one has to process a few image pairs in situ and find a suitable  $\Delta t$  by trial and error.

The PIV images were processed and the velocity fields deduced using in-house PIV software developed originally by Fouras *et al.* (2008). The images in each pair are first divided into a grid of  $32 \times 32$  pixel<sup>2</sup> interrogation windows. Fast Fourier Transform (FFT) is then applied for calculating the discrete cross-correlation function between the interrogation windows sampled from the two images in a pair with a 50% window overlap. The average displacements ( $\Delta x$  and  $\Delta y$ ) of the particles in the interrogation window are calculated statistically by locating the peak value in the cross-correlation calculation. The location of the peak can be computed to a sub-pixel accuracy using a least-square fit of the Gaussian function (Fouras & Soria 1998). An inverse Fourier Transfer was then used to compute the velocity vectors. Thus, with the known values of  $\Delta t$  and  $\mathcal{M}$ , the two-dimensional local velocity vectors can be accurately determined

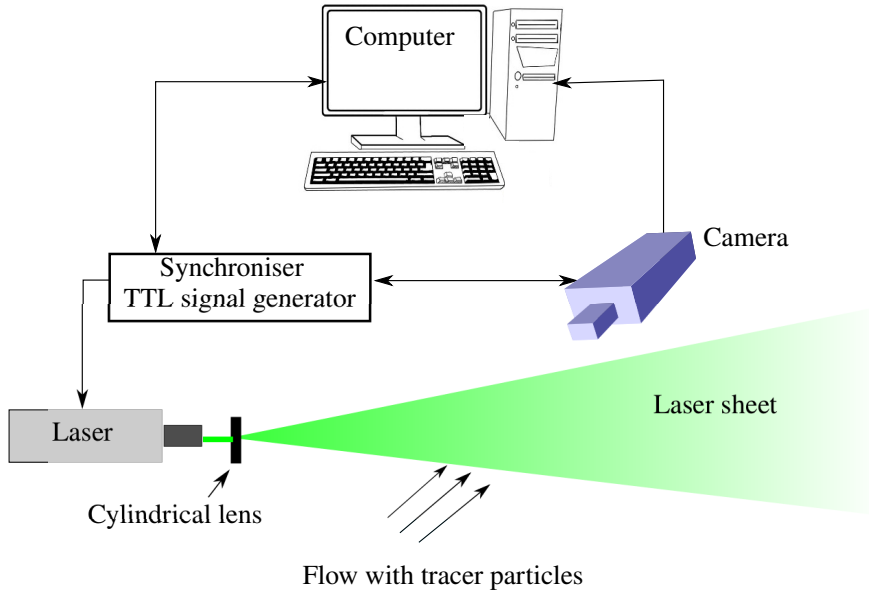


FIGURE 3.11: Schematic of the present experimental arrangement for the PIV measurement.

within the interrogation windows using the following equations

$$u = \frac{\Delta x}{\Delta t}; v = \frac{\Delta y}{\Delta t}. \quad (3.2)$$

Vorticity field ( $\omega$ ) is an important quantity to examine the flow structures and can easily be derived from the planar velocity field by using the following equation

$$\omega_z = \frac{\partial v}{\partial x} - \frac{\partial u}{\partial y}, \quad (3.3)$$

where,  $\omega_z$  is out-of-plane  $z$  component vorticity vector that is relevant for the present study. The accuracy of the vorticity measurements depend on the spatial distance between the velocity points in the interrogation windows in an image pair and also on the accuracy of the velocity field calculation. Fouras & Soria (1998) demonstrated in their study that by applying a second order polynomial fit  $\chi^2$  to the local velocity components with analytic differentiation, the accuracy of the vorticity calculation is improved compared to other methods based on finite difference calculations. Hence, the current study used the  $\chi^2_{21}$  method developed by Fouras & Soria (1998) that uses 21 surrounding velocity sampling points to calculate the vorticity fields. The vorticity field reported in the current study were non-dimensionalised using the following equation

$$\omega_z^* = \frac{\omega_z D}{U},$$

where,  $D$  is the sphere diameter. To highlight the significant large-scale structures that dominate the sphere wake, the PIV measurements were phase-averaged over more than 100 cycles. A phase-band averaging method was used for phase-averaging. For each PIV measurement case, a set of 3100 image pairs were sampled at 10 Hz. Each image set was sorted into 24 phase bins based on the sphere's displacement and velocity (see figure 3.12), resulting in more than 120 image pairs for averaging at each phase. The final phase-averaged vorticity fields were also smoothed slightly using an iterative Laplace filter to remove short length-scale structures and to better highlight the larger-scale structures that dominate the wake.

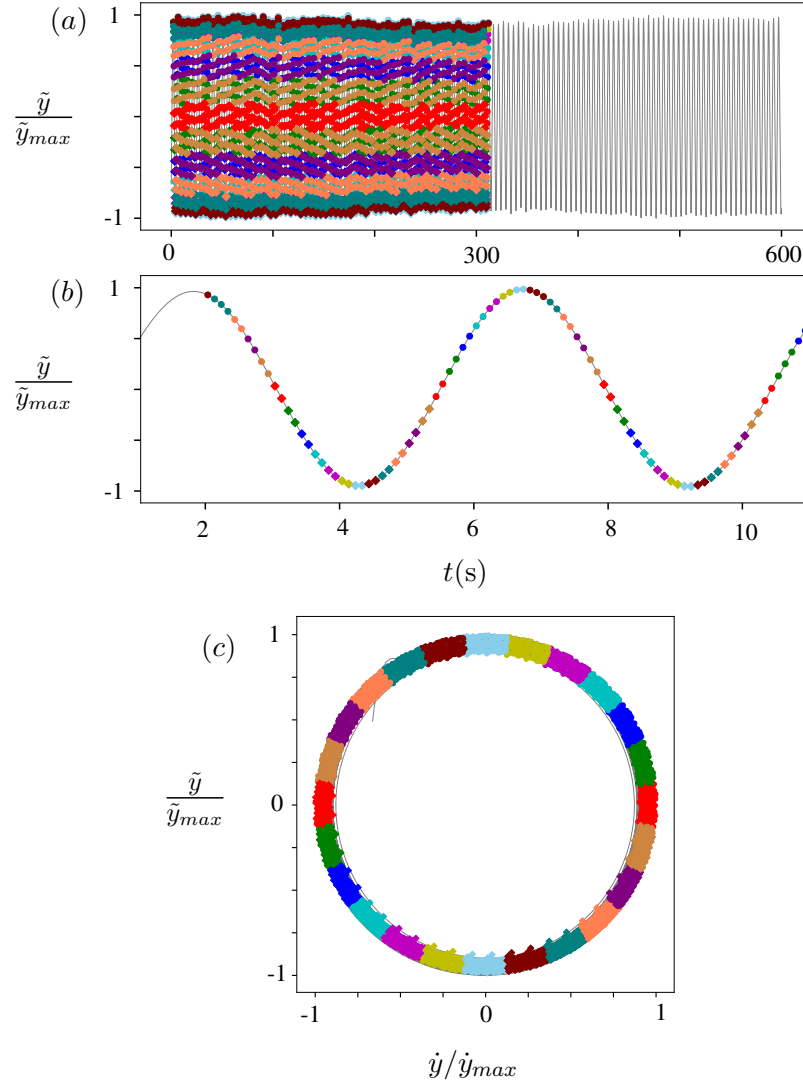


FIGURE 3.12: PIV phase-band averaging method

### 3.7.2.2 Equatorial PIV

The experimental procedure for the equatorial PIV was the same as the cross-plane PIV except for a few differences that are highlighted here.

For the equatorial PIV, the continuous laser was placed on the side of the channel to generate a laser sheet parallel to the  $x$ - $y$  plane. The camera was positioned below the water channel focusing on the laser plane through the glass floor of the channel. The camera was equipped with a 50 mm Nikon lens giving rise to a Magnification factor of  $7.36 \text{ pixel mm}^{-1}$  for the field-of-view in the equatorial-plane. This PIV arrangement was employed in the first study on the effect of constant rotation on the VIV response of a sphere (§ 5). However, the PIV was performed in the cross-plane.

### 3.8 Experimental procedures and Validation of the setup

#### 3.8.1 Free decay tests

Structural damping is an important parameter characterising the FIV response of bluff bodies. FIV systems can experience three different kinds of damping sources: (1) structural damping due to relative motion between different parts of the system and impact; (2) fluid damping due to hydrodynamic forces exerted by the surrounding fluid; (3) flexural damping due to flexing of materials. In the current problem, since the sphere and the support system are rigid, only structural and fluid damping are considered. Experimentally, this is measured employing a free decay test in air. For the free decay test in the current experiments, the system was given an initial known displacement  $A_o$  and then released to freely oscillate. The resultant damped motion was recorded for the calculation of the structural damping and natural frequency of the system. In order to minimise the air resistance, the sphere and the support system were removed and an equivalent congregated mass was attached to the air bearing rig carriage.

Under no external force, the governing equation for a 1-DOF damped free vibration system can be given by

$$\ddot{y} + 2\zeta\omega_n\dot{y} + \omega_n^2 y = 0, \quad (3.4)$$

where,  $\zeta$  is the structural damping ratio defined by  $\zeta = c/(2\sqrt{km})$ , and  $\omega_n$  is the natural angular frequency of the system defined by  $\omega_n = \sqrt{k/m}$ . The solution to the above equation for an underdamped system ( $0 < \zeta < 1$ ) can be represented by

$$y(t) = A_o e^{-\zeta\omega_n t} \sin(\sqrt{1 - \zeta^2}\omega_n t). \quad (3.5)$$

The decay rate of the system, defined as  $\eta = -\zeta\omega_n$ , can thus be estimated from the slope of a plot of  $\ln y_{max}$  vs. time,  $t$ . For a very lightly damped system ( $\zeta \ll 1$ ), the damped natural angular frequency  $\omega_d$  can be approximated as the undamped natural angular frequency  $\omega_n$  as shown below

$$\omega_d = \sqrt{1 - \zeta^2}\omega_n \rightarrow \omega_n \forall \zeta \ll 1. \quad (3.6)$$

Consequently, the damped natural frequency  $f_d$  can also be approximated as  $f_n$  and can be given by

$$f_d \approx f_n = \frac{\omega_n}{2\pi} = \frac{1}{2\pi} \sqrt{\frac{k}{m}} \quad (3.7)$$

For the current set of experiments, since the system is very lightly damped, the natural frequency and the damping ratio in vacuum are assumed to be equal to their respective values in air.

On similar lines, a free decay test in water was also performed to measure the natural frequency of the system in water. During a free decay test in water, the system is not only damped due to structural damping but also due to fluid damping. In stationary water, the natural frequency of the system in water can be expressed as

$$f_{nw} = \frac{1}{2\pi} \sqrt{\frac{k}{m + m_A}}, \quad (3.8)$$

where  $m_A$  is the added mass of the bluff body defined by  $m_A = C_A m_d$ . Here,  $C_A$  is the added mass coefficient (0.5 for the case of a sphere) and  $m_d$  is the displacement fluid

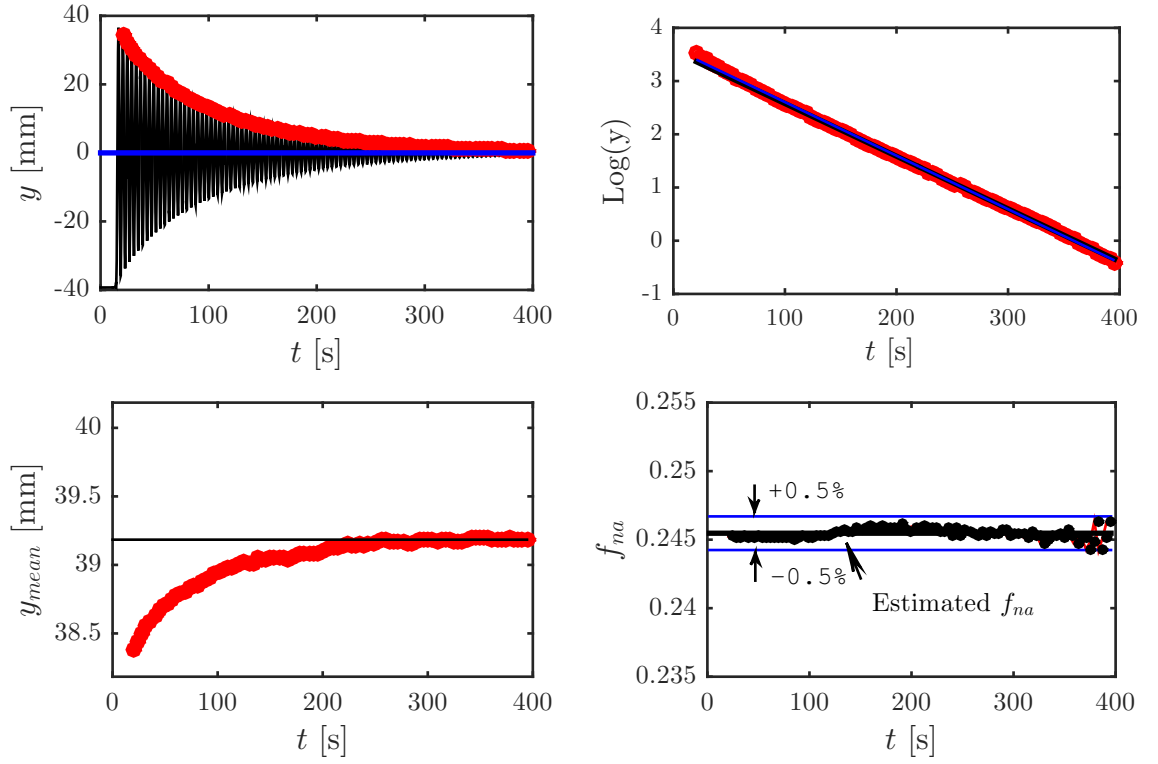


FIGURE 3.13: An example of the free decay test in the air

mass. Figure 3.13 shows an example of free decay tests performed in air for a sphere of diameter  $D = 80\text{mm}$  for a mass ratio of  $m^* = 7.8$ . As shown in Figure 3.13(b), the logarithmic maxima of free decay response closely followed the best linear fitting line. Also, the natural frequency for every cycle of the free decay test was within 0.5% of the estimated natural frequency  $f_{na}$ . The estimated natural frequencies in air and water give an added mass coefficient of  $C_A = ((f_{na}/f_{nw})^2 - 1)m^* = 0.52$  that is in good agreement with the known potential added mass for a sphere. The free decay tests in air and water demonstrated that the current experimental rig exhibited the response of a linear 1-DOF spring-mass system and that the performance of the air-bearing rig was reliable. It was also established through various repeatability tests that the damping ratio and the natural frequencies were repeatable for the current experimental rig.

#### 3.8.2 VIV of a non-rotating sphere: Validation

In this section, the experimental methodologies discussed in the previous section will be employed to reproduce the VIV response of a non-rotating and fully submerged sphere. The results will be directly compared against the benchmark studies.

For this set of experiments, the spherical model was 80 mm in diameter supported with a cylindrical support rod 3 mm in diameter. The immersed length of the support rod was one diameter (80 mm). The free decay tests were conducted individually in air and water to obtain the natural frequency in air,  $f_{na} = 0.254$ , and in water,  $f_{nw} = 0.245$ . The mass ratio was  $m^* = 7.8$  and the structural damping of the system was  $\zeta = 0.002$ . The response was studied for the  $U^*$  range of  $3 \leq U^* \leq 20$ , corresponding to a Reynolds number range of approximately  $5000 \leq Re \leq 30\,000$ . The signal was acquired at 100 Hz

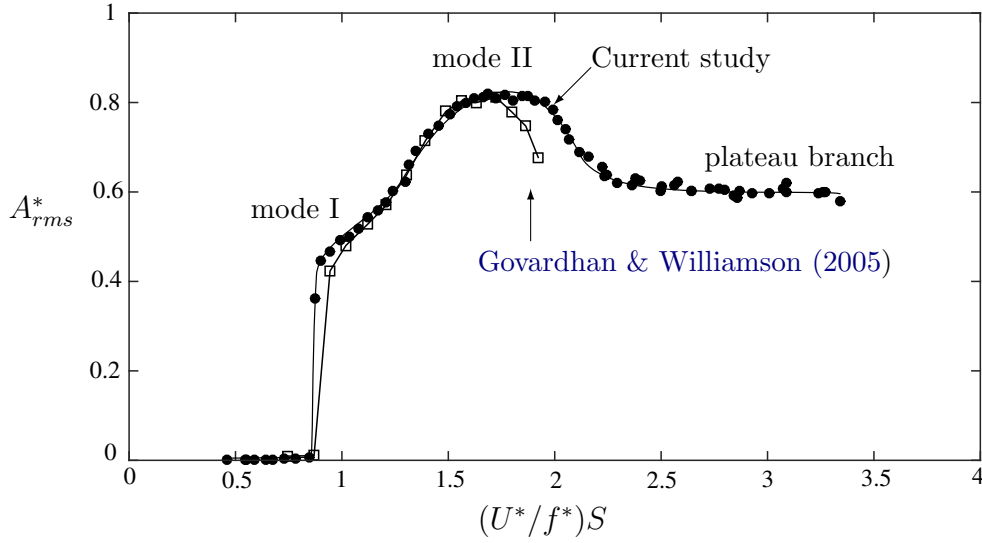


FIGURE 3.14: Amplitude response of a fully submerged sphere obtained in the current study compared to that reported by Govardhan & Williamson (2005). The mass damping in the current study is  $(m^* + C_A)\zeta = 0.0169$ , compared to approximately 0.03 in their study.

for approximately 170 cycles at each data point in this set of experiments.

In figure 3.14, the results from the current study are directly compared to the results reported by Govardhan & Williamson (2005) for a similar mass ratio of  $m^* = 7$ . The mass damping of the current study was  $(m^* + C_A)\zeta = 0.0169$ , compared to approximately 0.03 in their study. For comparison with their study here,  $A_{rms}^*$  is plotted against the scaled  $U_S^*$ , defined as  $U_S^* = (U^*/f^*)S \equiv f_{vo}/f$ , where  $S$  is the Strouhal number for the vortex shedding ( $\approx 0.18$  in this case).

As evident from the figure, the amplitude response of a sphere in the current study closely follows the trend reported by Govardhan & Williamson (2005). The vibrations lock-in at  $U_S^* \approx 0.87$ , corresponding to a  $U^*$  value of 4.5, continuously progressing from mode I to mode II and reaching a peak saturation amplitude of 0.8 in both cases. Although, in the study by Govardhan & Williamson (2005), the response at this mass ratio is reported only until  $U_S^* = 2$ , the current study reveals that after the peak response in mode II, the amplitude response smoothly drops to a lower plateau that extends towards mode III as  $U_S^* \rightarrow 3$ . The vibrations in the ‘plateau’ region exhibit slight differences to the highly periodic vibrations in mode II, albeit the frequency of oscillation stays close to the natural frequency of the system over the entire  $U_S^*$  range examined in the current study.

Unlike the case of a tethered sphere with a very low mass ratio, where the two vibration modes are distinctly separated by a desynchronised region, there is no such separation between the two modes in 1-DOF hydroelastic VIV and with higher mass ratio in this study. The transition between the modes is continuous and gradual with  $U^*$ , hence it is difficult to differentiate between the two modes by just looking at the amplitude response. The transition from one mode to the other is made clear through observations of the phase differences between the force and the sphere displacement signals for the two modes.

Figure 3.15 shows the variation of the total phase  $\phi_{total}$  and the vortex phase  $\phi_{vortex}$  with  $U^*$ , correlated with the amplitude response. The results reported by Govardhan

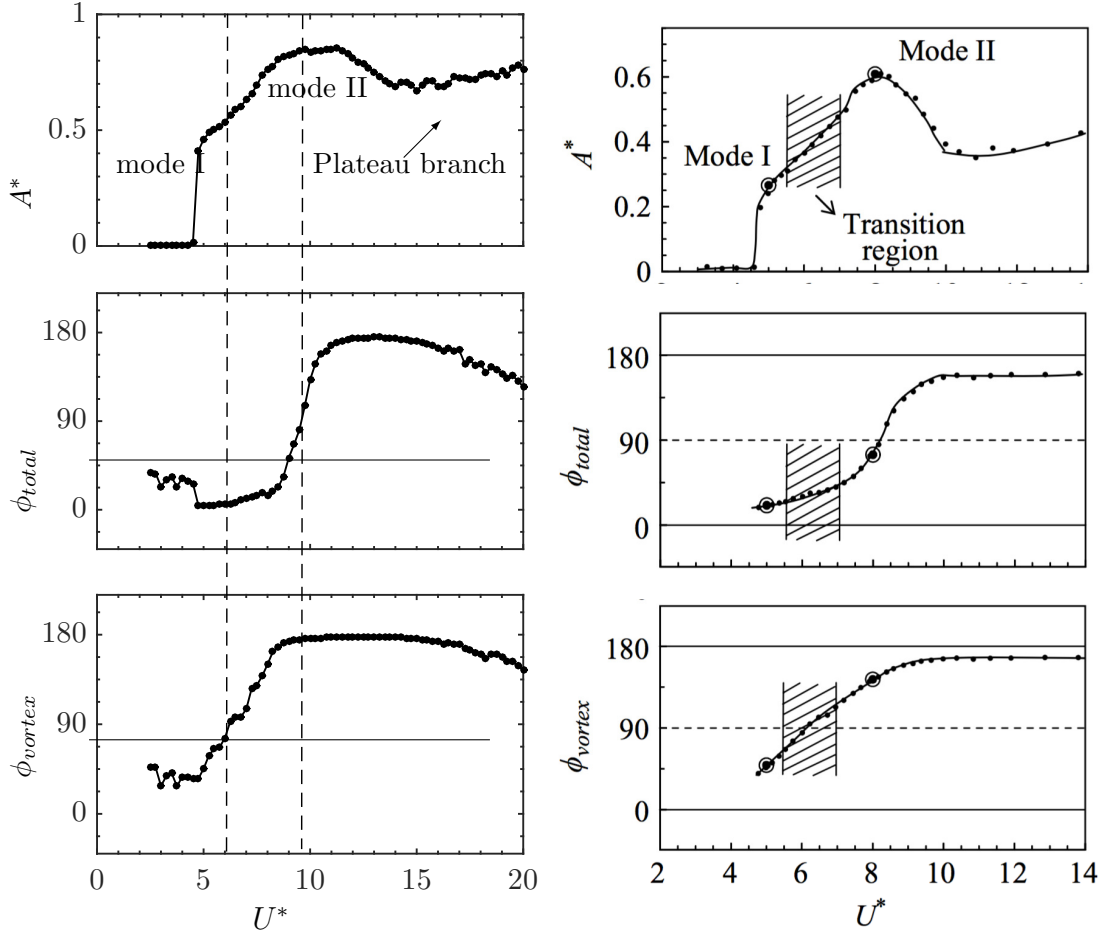


FIGURE 3.15: Left: Variation of the total phase  $\phi_{total}$  (middle) and vortex phase  $\phi_{vortex}$  (bottom) with  $U^*$ , correlated with the amplitude response (top). Right: The variation of the same response quantities reported by Govardhan & Williamson (2005) are presented for comparison.

& Williamson (2005) for relatively a higher mass ratio of  $m^* = 31.1$  are also shown for comparison. The response undergoes a transition from mode I to mode II when  $\phi_{vortex}$  crosses through  $90^\circ$ , corresponding to the ‘inflection point’ in the amplitude response. Likewise, within the mode II regime,  $\phi_{total}$  passes continuously through  $90^\circ$ , corresponding to the peak of the amplitude response. The variations in the total and the vortex phases obtained for  $m^* = 7.8$  in the current study closely match the trends of the phases reported by Govardhan & Williamson (2005) previously for a higher mass ratio of  $m^* = 31.1$ .

In the current study, with the  $U^*$  range further extended beyond  $U^* = 14$ , a slight decrease in both the total phase,  $\phi_{total}$ , and the vortex phase,  $\phi_{vortex}$ , was observed as shown in the figure 3.15. Simultaneously a slight increase in the vibration amplitude is also evident in the figure. This corresponds to the ‘plateau branch’ mentioned above in figure 3.14 when  $(U^*/f^*)S \rightarrow 3$ . Jauvtis *et al.* (2001) reported the existence of another mode of vibration, mode III, for higher  $U^*$  values varying from 20 to 40 for a tethered sphere of mass,  $m^* = 80$  in wind-tunnel experiments. Therefore, the vibrations in the ‘plateau branch’ can be considered to be approaching the mode III response of the



sphere vibrations.

Herein, it is demonstrated that the vibration amplitude response as well the trends in the total phase difference and vortex phase difference for an elastically mounted sphere with 1-DOF obtained with the current study closely follows the trends reported by previous benchmark studies.

### 3.9 Chapter summary

To summarise, the present chapter gave details of the experimental methodologies and equipment that were employed in the current study. Extensive tests were performed to confirm the repeatability and optimal performance of all the experimental methods. The rig was able to reproduce the results from the benchmark studies, further demonstrating the optimal performance of the experimental methods. Now, in the following sections, these methodologies are utilised to explore the research questions that were posed for the current study.

## Chapter 4

# Flow past a transversely rotating sphere

*If you can't explain it simply, you don't understand it well enough.*

---

Albert Einstein

### 4.1 Abstract

Rotating bluff bodies are known to experience a side force due to a well-known phenomenon called the Magnus effect. The Magnus effect is evident in many sports (cricket, soccer, baseball, and football), where spinning balls are observed to change their trajectories dramatically. In this chapter, we have experimentally investigated the effect of imposed transverse rotation on the drag and lift forces experienced by a sphere in the intermediate Reynolds number range ( $10^3 < Re < 10^4$ ). The results show the considerable effects of Reynolds number and the rotation ratio  $\alpha$  (the ratio of the equatorial velocity of a sphere to the free stream velocity) on the force coefficients. A sudden drop was observed in both the lift and drag coefficients at a ‘critical’  $\alpha$  value, before a recovery at a higher alpha value. This is unlike the behaviour for low Reynolds number flow ( $Re < 1000$ ), where the drag and lift coefficients monotonically increase. Flow visualisations reveal that the boundary layer on the advancing side undergoes transition to turbulence close to the critical  $\alpha$  that leads to an increase in the advancing side separation angle, which could be related to the sudden drop in the force coefficients.

### 4.2 Introduction

Flow-structure interaction of rotating bluff bodies has been intriguing to scientists for centuries. It finds applications not only in sports where spinning balls are known to change trajectories but also in ship propulsion (Flettner rotors), external ballistics, particle-laden flows, saltation of particles, and aeronautic applications. Rotating bluff bodies are known to experience a side force (the Magnus force) due to a well-known phenomenon called the Magnus effect, which is a consequence of the asymmetry of flow separation on the advancing and retreating sides of a rotating body. The sphere, which is the three-dimensional body with the highest symmetry, represents the ideal body to investigate the flow physics further before tackling more complex bodies that

surround us. Interestingly, the discovery of the Magnus effect for a sphere occurred almost two centuries earlier than that of its two-dimensional counterpart, the circular cylinder. However, there have been fewer experimental studies on rotating spheres due to the challenges of developing experimental setups and drive systems that do not unduly interfere with the flow over them. Most of the previous literature on transversely rotating spheres can be broadly classified into two groups: the first set of studies are mostly numerical studies that focused on low Reynolds numbers of  $Re \leq 1000$  (e.g., Poon *et al.* (2010); Loth (2008); Tanaka *et al.* (1990); Tsuji *et al.* (1985)). The second set of studies are mostly experimental studies that focused on very high Reynolds numbers of  $Re \geq 6 \times 10^5$  (e.g., Macoll (1928); Barlow & Domanski (2008); Kray *et al.* (2012); Kim *et al.* (2014)). Both these set of studies found different characteristic drag and lift profiles for varying rotation rates. Studies performed at low Reynolds numbers showed a monotonic increase in the force coefficients with the rotation rate  $\alpha$ . However, the studies performed at high Reynolds numbers focused mainly on the *inverse Magnus effect*, where one observes a sudden change in the direction of the lift force at a ‘critical’ rotation ratio. They observed the inverse Magnus effect for a narrow range of rotation ratios at very high Reynolds numbers ( $Re \geq 0.8 \times 10^5$ ). The question arises as to how the force coefficients will look like in the intermediate Reynolds number range ( $10^3 < Re < 10^4$ ). Do the coefficients increase monotonically similar to that reported for low Reynolds numbers or there is a sudden drop in the coefficients similar to that observed at high Reynolds numbers? In any case, what is the underlying dynamics? These questions remain unanswered. Moreover, the small magnitude of forces for intermediate Reynolds numbers make measurements even more challenging, at least in low viscosity working fluids such as water and air. That is the reason, many previous experimental studies on rotating spheres have been focused on higher Reynolds numbers in spite of the relevance of intermediate Reynolds numbers to many engineering applications, such as particle flows where particle-particle and particle-wall collisions can lead to combined translational and rotational motion of the spherical particles. Moreover, due to difficulty of measuring quantitatively the flow near the surface of a rotating sphere, the details behind the Magnus effect are not well understood. Recently, lifting devices using the Magnus effect have been receiving attention due to their high lift forces and stall resistance in spite of the added complexity of driving mechanisms. It is crucial to know the rotation rates for which the forces suddenly drop for more effective and safer designs. Therefore, in the current chapter, the effect of the rotation ratio on the drag and lift profiles of a sphere is studied for intermediate Reynolds numbers. Flow-visualisations using Fluorescein dye, and Particle Image Velocimetry measurements were also performed to understand the underlying dynamics.

The aerodynamic forces on a spinning sphere, the drag ( $F_D$ ) and lift ( $F_L$ ) forces, depend on various flow parameters such as density  $\rho$ , viscosity  $\mu$ , sphere diameter  $D$ , and sphere angular velocity  $\omega$ . From dimensional analysis, we obtain:

$$Re = \frac{\rho U D}{\mu}, \quad (4.1)$$

$$\alpha = \frac{D\omega}{2U}, \quad (4.2)$$

$$C_D, C_L = f(Re, \alpha), \quad (4.3)$$

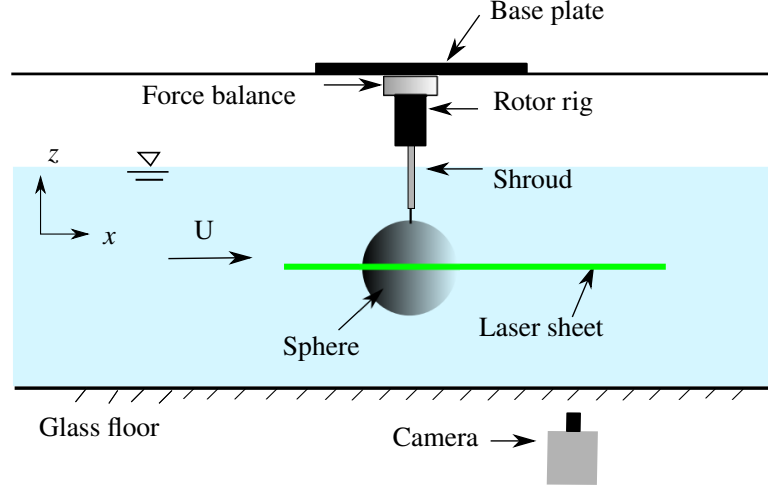


FIGURE 4.1: Schematic showing the experimental arrangement (not to scale) for this study.

where the drag and lift coefficients,  $C_D$  and  $C_L$ , are defined as follows:

$$C_D = \frac{F_D}{\frac{1}{2}\rho U^2 A}, \quad (4.4)$$

$$C_L = \frac{F_L}{\frac{1}{2}\rho U^2 A}, \quad (4.5)$$

where  $A$  is sphere projected area ( $A = \pi D^2/4$ ).

### 4.3 Experimental arrangement

The spherical model used was 80 mm in diameter, with a smooth surface finish. It was supported from the top apex using a cylindrical support rod. In order to avoid any interference, the driving shaft (3 mm in diameter) was covered with a fixed cylindrical shroud, 6.35 mm in diameter. The sphere was placed more than 2 diameters beneath the free surface in order to minimize any free-surface effects. In order to drive the sphere over a range of rotational speeds, a miniature low-voltage LV172 Parker stepper motor was used. It was controlled using a Parker 6K controller. The vibration of the sphere due to rotation was minimised by adopting a very stiff fixed support shaft supported by miniature ball bearings at the end. More details of the rotation rig can be found in [Wong \*et al.\* \(2017\)](#).

The forces acting on the sphere were measured using a multi-axis load cell (Mini40, ATI-IA), which measures six-component forces and moments ( $F_x$ ,  $F_y$ ,  $F_z$ ,  $M_x$ ,  $M_y$ ,  $M_z$ ) with a resolution of 0.005 N for  $F_x$  and  $F_y$ , and 0.01 N for  $F_z$ , respectively. For each data set, the raw analogue voltages were acquired at 100 Hz for 300 s at each flow velocity, and were converted to a digital signal using a differential-ended DAQ board system. Fluorescein dye was used for flow visualisations. The dye was injected using a pitot tube placed upstream of the sphere. PIV measurements were also carried out in the equatorial plane in order to measure the separation angle. For this purpose, the flow was seeded with 13  $\mu\text{m}$  hollow micro-spheres having a specific weight of  $1.1 \text{ gm}^{-3}$ . Imaging was performed using a high-speed camera (model: Dimax S4, PCO, AG) with a resolution of  $2016 \times 2016$  pixels<sup>2</sup>. This camera was equipped with a 200 mm Nikon lens, giving a magnification of  $34.28 \text{ pixel mm}^{-1}$  for the field-of-view. Velocity fields

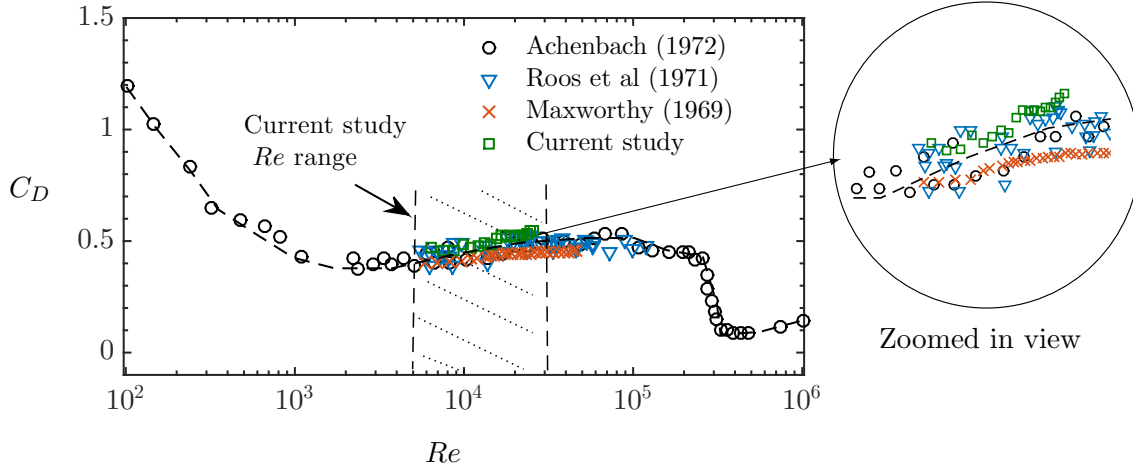


FIGURE 4.2: Variation of the drag coefficient  $C_D$  of a stationary sphere with Reynolds number. Zoomed in view of the current results is shown on the right.

were deduced using in-house PIV software developed originally by Fouras *et al.* (2008), using  $32 \times 32$  pixel<sup>2</sup> interrogation windows in a grid layout with 50% window overlap. The overall schematic of the experimental arrangement is shown in figure 4.1.

#### 4.4 Stationary sphere validation

In order to verify the performance of the force balance in the current experimental arrangement, the drag coefficient on a stationary sphere (70 mm in diameter) supported using a cylindrical support rod of diameter 6.35 mm was measured. The sphere surface was two diameters beneath the free surface. The force on the isolated support rod was measured after removing the sphere and correcting the end condition using an end plate. That force was subtracted from the measured force to correct the drag coefficient. Figure 4.2 shows that the drag coefficient estimated in the current experimental arrangement collapses well and agrees with previous literature. It also suggests to reasonable accuracy that the force on the cylinder and sphere add linearly to give the force on the rod/sphere combination. As also highlighted in the figure, the Reynolds number range for the current study lies in the ‘subcritical’ regime, where the drag coefficient stays approximately constant for a wide range of Reynolds numbers. This intermediate Reynolds number regime is not well explored in the literature in terms of the effect of rotation on the force coefficients, as discussed in the previous section. Therefore, in the following sections, the effect of rotation on the force coefficients in the intermediate Reynolds number regime will be studied in detail. Results will be presented for a few selected Reynolds numbers in this regime.

#### 4.5 Forces on a rotating sphere

Figure 4.3 shows the variation of the lift coefficient  $C_L$ , and the drag coefficient  $C_D$ , with the spin ratio  $\alpha$  in all the three Reynolds number regimes for a selected set of Reynolds numbers. Previous numerical study by Poon *et al.* (2014) performed at lower Reynolds numbers ( $Re \leq 1000$ ) demonstrated a monotonic increase of lift and drag coefficients with the rotation ratio  $\alpha$ . However, the present study reveals a sharp drop in the force coefficients beyond a certain  $\alpha$  value. When the Reynolds number

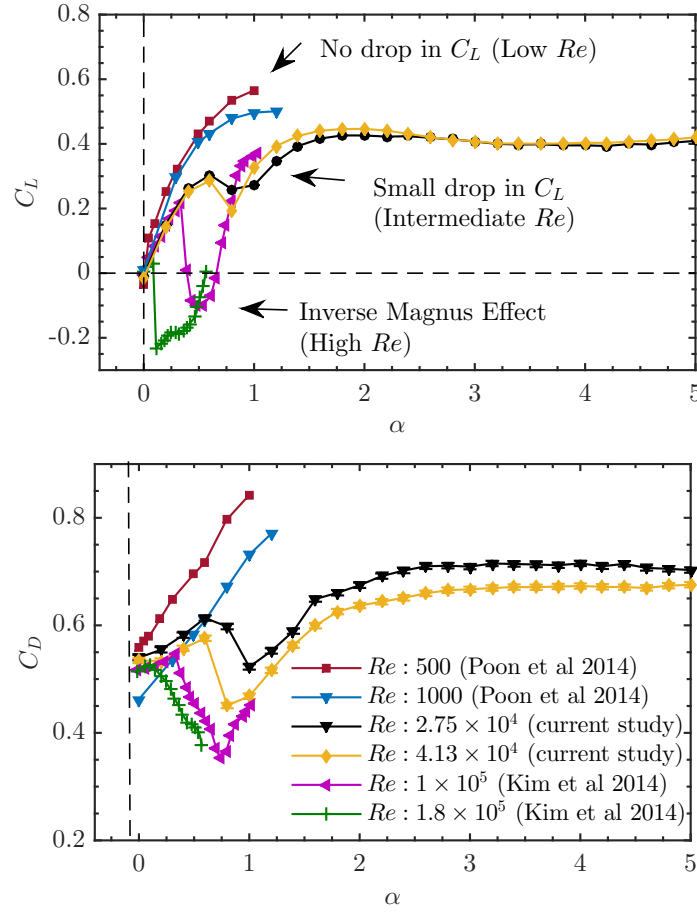


FIGURE 4.3: Variation of the lift coefficient  $C_L$  (top) and the drag coefficient  $C_D$  (bottom) with the rotation ratio  $\alpha$  for the current experiment compared to other studies at higher Reynolds numbers.

is increased from  $2.75 \times 10^4$  to  $4.13 \times 10^4$  in the current study, no significant change is observed in  $C_L$ . However,  $C_D$  decreases significantly, and the ‘critical’ alpha value where the sudden stop is observed, also decreases. The results are consistent with those from the previous experimental study at higher Reynolds numbers [Kim et al. \(2014\)](#), which also revealed a sudden drop in the force coefficients, but for relatively lower  $\alpha$  values. One should note here that for very high Reynolds numbers of  $Re \geq 10^5$ , the dip in coefficients become dramatic, reaching negative  $C_L$  values for a certain range of  $\alpha$  ([Kim et al. 2014](#)). For these rotational rates, the inverse Magnus effect is observed, where the lift force acts in the opposite direction to that predicted by the Magnus effect.

Overall, one can see here that the critical  $\alpha$  decreases with the increase in Reynolds number. Also, the sudden drop in the coefficients become progressively smaller in magnitude with the decrease in Reynolds number, and disappears ultimately for low Reynolds numbers (at least in the range reported by the previous studies). However, further studies might be required at low Reynolds number investigating the Magnus effect at high rotational rates ( $\alpha > 2$ ) to confirm this claim as one may expect to see a drop in coefficients (albeit very small in magnitude) at high rotation rates.

These results together with those from previous studies reveal that the ‘critical’ spin ratio and the drop in force coefficients are Reynolds number dependent. The current study indicates the drop can even be observed at  $Re = 2.75 \times 10^4$ , almost an order of

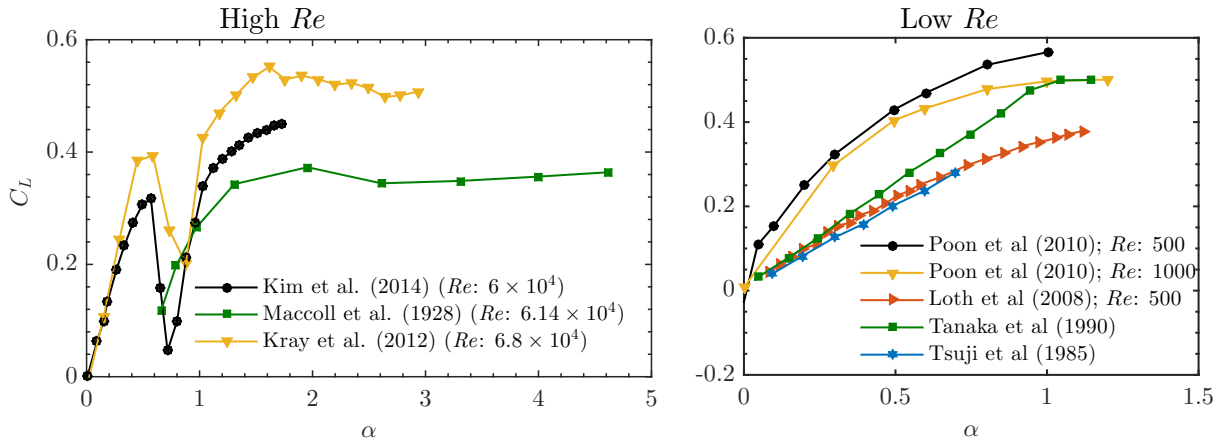


FIGURE 4.4: Variation of the lift coefficient  $C_L$  with the rotation ratio  $\alpha$  for previous studies showing inconsistencies in the reported data for similar Reynolds numbers. Left: High Reynolds numbers experimental studies. Right: Low Reynolds numbers studies.

magnitude below the critical Reynolds number of a sphere.

It is worth mentioning here that although the previous experimental studies by Kim *et al.* (2014), Maccoll (1928) and Kray *et al.* (2012) were performed for a similar Reynolds number of  $\approx 6 \times 10^4$ , there are large variations in the reported data, as evident from figure 4.4(a). Even at low Reynolds numbers, there are inconsistencies in the data reported by different studies, see for e.g., figure 4.4(b). Because of these inconsistencies in the reported data in the past, it was difficult to discern an overall trend in the variation of the force coefficients over a wide range of Reynolds numbers.

## 4.6 Physics of the varying Magnus effect

In order to understand the underlying physics behind the sudden dip in the coefficients, flow visualisations using Fluorescein dye were carried out. Figure 4.5 shows the top view of the dye visualisations for a sphere rotating in the clockwise direction for various spin ratios at a relatively smaller Reynolds number of  $Re = 3510$ . At this Reynolds number the dye visualisations are much clearer, allowing the boundary layer transition to be more easily observed as  $\alpha$  is increased. In these flow visualisations, the flow is from left to right. We observe that as  $\alpha$  changes from 0 to 0.2, the wake loses its symmetry and deflects in the direction of rotation, due to the Magnus effect. The wake deflects increasingly more with increasing  $\alpha$ , correlated with an increasing Magnus force. At  $\alpha = 1.5$ , the boundary layer on the advancing side shows signs of turbulent transition that might be leading to separation delay due to increased crossflow momentum transport. At  $\alpha = 3$ , both the boundary layers become turbulent, and a further increase in rotation rate does not lead to any further increase in the force coefficients.

In order to get a quantitative measure of the changes in the separation angles due to turbulent transition, Particle image velocimetry (PIV) was performed in the equatorial plane passing through the centre of the sphere. Previous studies have shown that the lift coefficients are directly related to the advancing and retreating side separation angles (see Kim *et al.* (2014)) for a transversely rotating sphere. The retreating side separation angles increase linearly with the increase in the spin ratio. However, the variation of the advancing side separation angle ( $\theta_{adv}$ ) plays a key role in dictating the magnitude and direction of the lift force acting on the sphere. Hence, in the current study, the



(a)  $\alpha = 0$ 

(b)  $\alpha = 0.2$ 

(c)  $\alpha = 1.5$ 

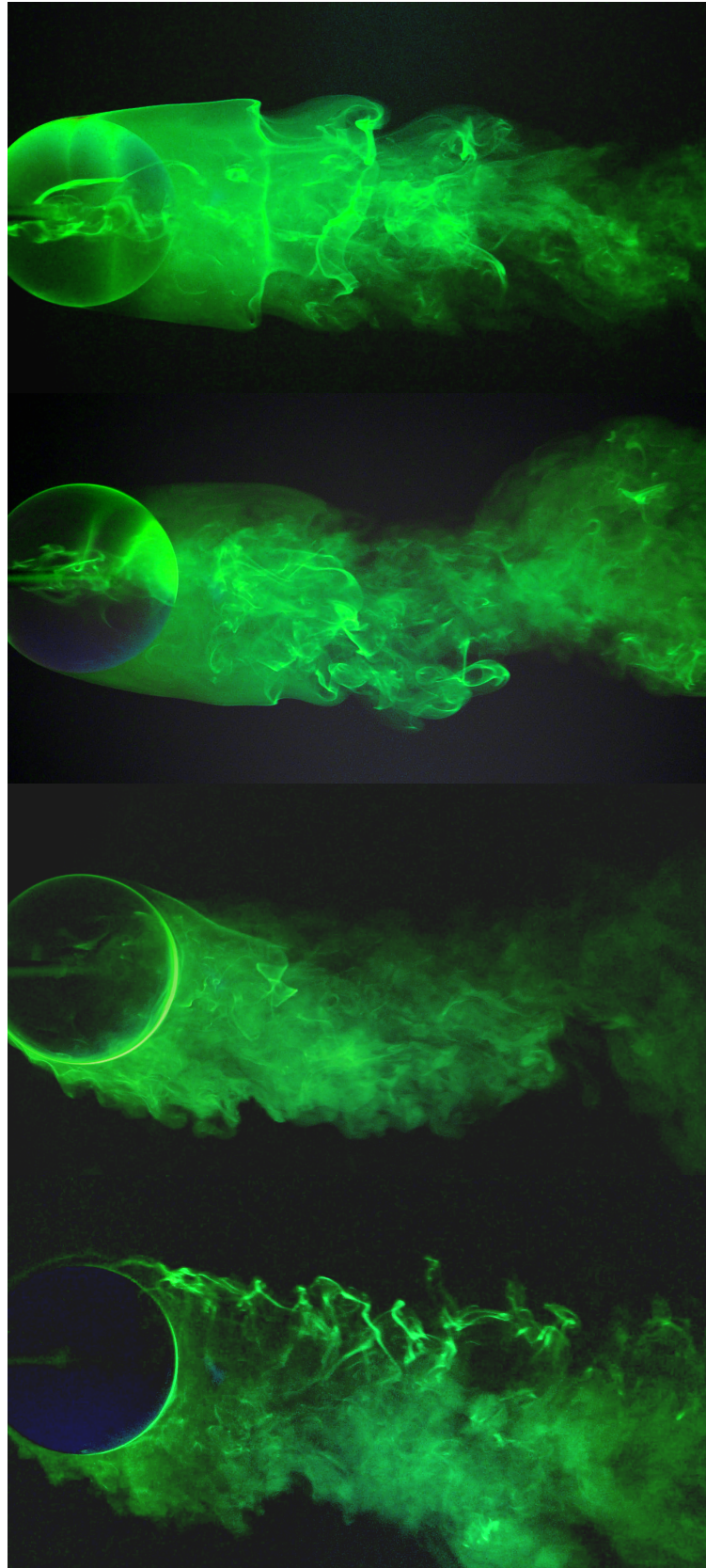
(d)  $\alpha = 3$ 


FIGURE 4.5: Dye visualisation for a rotating sphere at  $Re = 3510$  at marked spin ratios  $\alpha$ . The figure shows the top view when the sphere is rotating in the clockwise direction and the flow is from left to right.



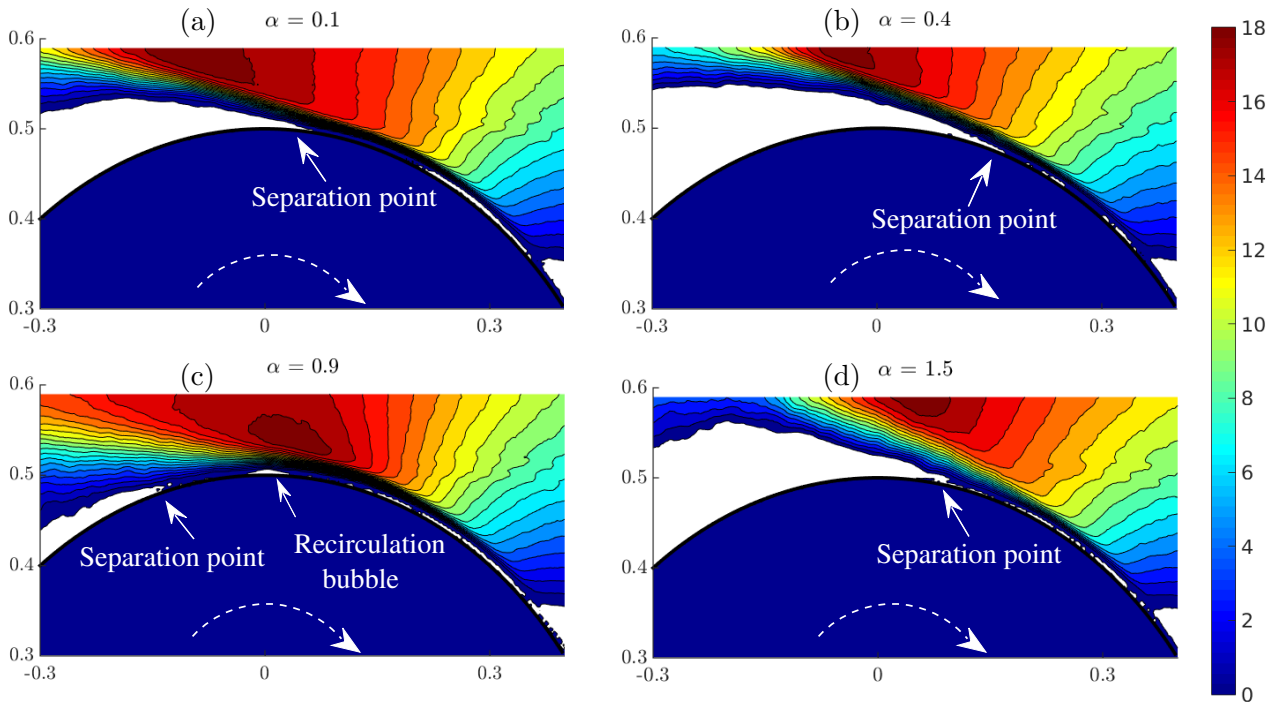


FIGURE 4.6: Instantaneous velocity contours near the flow separation at the advancing side of the sphere at (a)  $\alpha = 0.1$ , (b)  $\alpha = 0.4$ , (c)  $\alpha = 0.9$  and (d)  $\alpha = 1.5$ . For this set of images, the flow is from right to left and the sphere rotates in the clockwise direction. The Reynolds number is  $2.75 \times 10^4$ .

advancing side separation angles were estimated from the velocity fields based on the criterion:  $u_\theta = 0$  and  $\partial u_\theta / \partial r = 0$ , where  $(r, \theta)$  are polar coordinates with the origin at the centre of the sphere. Figure 4.6 shows instantaneous velocity contours near the separation point at four different spin ratios. The flow separation at the advancing side of the sphere is clearly visible in the velocity contours. When the spin ratio is increased from  $\alpha = 0.1$  to  $\alpha = 0.4$ , the separation angle clearly decreases. However, when the spin ratio is further increased to  $\alpha = 0.9$ , which lies in the critical regime, the flow reattaches to the sphere. A small recirculation bubble is also evident. This delays the flow separation at the advancing side of the sphere. With a further increase in the spin ratio to  $\alpha = 1.5$ , the flow reattachment is absent and a turbulent boundary-layer flow is formed without the formation of any separation bubble. Figure 4.7 shows the variation of  $\theta_{adv}$  with the spin ratio correlated with the variation of the lift coefficient. As evident from the figure, when the spin ratio is increased from 0 to  $\approx 0.5$ ,  $\theta_{adv}$  decreases almost linearly. This bends the wake towards the advancing side of the sphere leading to an increased Magnus force towards the retreating side. A correlated increase in the lift coefficient is also evident in the figure. Beyond  $\alpha = 0.5$ , a sudden increase in the separation angle is observed correlated with a sudden drop in the lift coefficient. In the ‘critical regime’, the flow reattaches due to an increased momentum caused by transition to turbulence. This causes a delay in the flow separation that increases  $\theta_{adv}$ . When  $\alpha$  is further increased to higher values beyond the critical regime,  $\theta_{adv}$  starts decreasing again and  $C_L$  starts increasing. At this stage the boundary layer on the retreating side becomes turbulent too. For very high rotation rates ( $\alpha > 2$ ), both the boundary layers become turbulent (also seen in the dye visualisations in figure 4.5). There is no Magnus

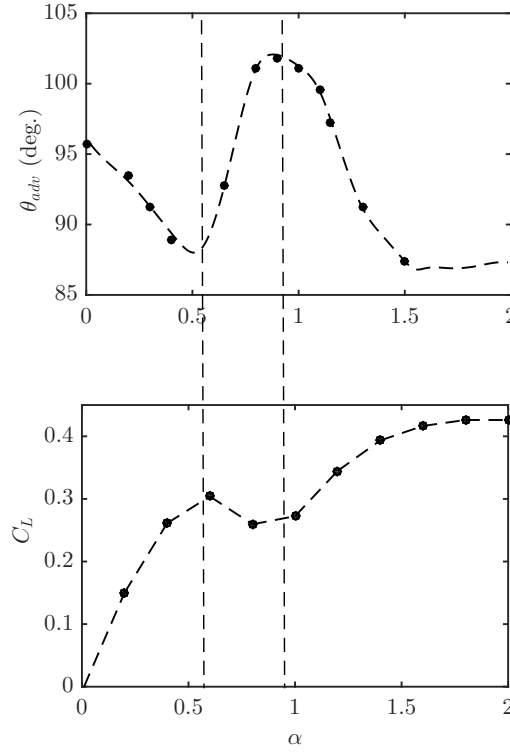


FIGURE 4.7: Variation of the separation angle at the advancing side,  $\theta_{adv}$ , with the rotation ratio  $\alpha$ . The correlated transverse lift coefficient is also shown in the bottom. The dashed lines highlight the region where sudden increase in  $\theta_{adv}$  is observed associated with a sudden drop in the lift coefficient.

effect beyond this rotation ratio and hence, there is no further increase in the force coefficients. One can also infer here that for the Magnus effect to manifest, asymmetry in the boundary layers is required. If both the advancing and the retreating boundary layers are either laminar or turbulent, the Magnus effect is not observed.

## 4.7 Concluding remarks

In this study, we have shown that in the intermediate Reynolds number regime, a sudden drop in the force coefficients is observed with the spin ratio. The critical  $\alpha$  and the drop in force coefficients depend on the Reynolds number. Flow visualisations reveal that the boundary layer at the advancing side is turbulent in the critical regime. However, for high spin ratios of  $\alpha > 2$ , both the advancing and retreating side boundary layers transition to turbulence beyond which a further increase in coefficients is not observed. It is also shown using the PIV measurements that there is a sudden increase in the advancing side separation angle in the critical regime, where the flow reattaches to the sphere and a small recirculation bubble is formed. For higher spin ratios, the advancing side boundary layer becomes turbulent and the separation angle starts decreasing again. The current study helps us understand the underlying mechanism of the varying Magnus effect for intermediate Reynolds numbers, and attempts to connect and bridge the previous studies that were either performed for lower Reynolds numbers ( $Re \leq 1000$ ) or much higher Reynolds numbers ( $Re \geq 6 \times 10^4$ ). Due to limitations in acquiring accurate force measurements in experiments at such Reynolds numbers, a wider range

of Reynolds numbers could not be studied. However, in the intermediate Reynolds number range studied, dips in the lift and drag coefficients are still observed, which presumably translate directly to the inverse Magnus effect at higher Reynolds numbers. Thus, the present study should be helpful in elucidating the underlying principles of the varying Magnus effect as the Reynolds number approaches the critical regime.

## Chapter 5

# Vortex-induced vibration of a rotating sphere

*Work hard in silence, let your success  
be your noise*

---

Frank Ocean

### 5.1 Overview of the chapter

In this chapter, the publication by the author entitled ‘Vortex-induced vibration of a rotating sphere’ published in the *Journal of Fluid Mechanics* (2018), vol. **837**, pp. 258-292, has been reproduced with permission Cambridge University Press© 2017. In this paper, the effect of transverse rotation on the VIV response of an elastically mounted sphere that is free to oscillate in the transverse direction has been investigated through an extensive series of experiments employing simultaneous displacement, force and vorticity measurements. The vibration response is studied for a wide parameter space of rotational rate varying in the range  $0 \leq \alpha \leq 7.5$ , and reduced velocity in the range  $3 \leq U^* \leq 18$ . The Reynolds numbers in the current study varied in the range  $3000 \leq Re \leq 30000$ .

Interestingly, unlike its two-dimensional counterpart, the cylinder, the VIV response of the sphere reduced gradually and steadily with increasing rotation rate, leading to almost complete suppression for  $\alpha \geq 6$ . The synchronisation regime became narrower with increasing  $\alpha$ , and the peak amplitude response decreased almost linearly for  $\alpha \lesssim 1$ . The time-averaged mean displacement increased towards the retreating side of the sphere with increasing  $\alpha$ , due to an increase in the mean Magnus force. However, the oscillation frequency remained close to the natural frequency of the system for all cases. Recurrence analysis revealed a transition from a periodic to a chaotic state in the recurrence map, complementing the occurrence of broadband frequency spectra at the onset of bifurcation. Flow visualisations using the hydrogen bubbles and the PIV techniques were performed in the equatorial plane containing the principal transverse vibration. It was found that the flow was continuously drawn from the retreating side to the advancing side of the sphere with increasing rotation rate, which led to entrainment of fluid onto the advancing side. This entrainment of fluid gave rise to large one-sided vortex shedding. For the rotation rates where VIV was found to be almost completely

suppressed, the wake was found to be deflected towards the advancing side with large-scale flow structures for all shedding cycles.

## Vortex-induced vibration of a rotating sphere

A. Sareen<sup>1</sup>, J. Zhao<sup>1,†</sup>, D. Lo Jacono<sup>2</sup>, J. Sheridan<sup>1</sup>, K. Hourigan<sup>1</sup>  
and M. C. Thompson<sup>1</sup>

<sup>1</sup>Fluids Laboratory for Aeronautical and Industrial Research (FLAIR), Department of Mechanical and Aerospace Engineering, Monash University, Melbourne, VIC 3800, Australia

<sup>2</sup>Institut de Mécanique des Fluides de Toulouse (IMFT), Université de Toulouse, CNRS, Toulouse, France

(Received 6 March 2017; revised 13 October 2017; accepted 16 November 2017;  
first published online 20 December 2017)

Vortex-induced vibration (VIV) of a sphere represents one of the most generic fundamental fluid–structure interaction problems. Since vortex-induced vibration can lead to structural failure, numerous studies have focused on understanding the underlying principles of VIV and its suppression. This paper reports on an experimental investigation of the effect of imposed axial rotation on the dynamics of vortex-induced vibration of a sphere that is free to oscillate in the cross-flow direction, by employing simultaneous displacement and force measurements. The VIV response was investigated over a wide range of reduced velocities (i.e. velocity normalised by the natural frequency of the system):  $3 \leq U^* \leq 18$ , corresponding to a Reynolds number range of  $5000 < Re < 30\,000$ , while the rotation ratio, defined as the ratio between the sphere surface and inflow speeds,  $\alpha = |\omega|D/(2U)$ , was varied in increments over the range of  $0 \leq \alpha \leq 7.5$ . It is found that the vibration amplitude exhibits a typical inverted bell-shaped variation with reduced velocity, similar to the classic VIV response for a non-rotating sphere but without the higher reduced velocity response tail. The vibration amplitude decreases monotonically and gradually as the imposed transverse rotation rate is increased up to  $\alpha = 6$ , beyond which the body vibration is significantly reduced. The synchronisation regime, defined as the reduced velocity range where large vibrations close to the natural frequency are observed, also becomes narrower as  $\alpha$  is increased, with the peak saturation amplitude observed at progressively lower reduced velocities. In addition, for small rotation rates, the peak amplitude decreases almost linearly with  $\alpha$ . The imposed rotation not only reduces vibration amplitudes, but also makes the body vibrations less periodic. The frequency spectra revealed the occurrence of a broadband spectrum with an increase in the imposed rotation rate. Recurrence analysis of the structural vibration response demonstrated a transition from periodic to chaotic in a modified recurrence map complementing the appearance of broadband spectra at the onset of bifurcation. Despite considerable changes in flow structure, the vortex phase ( $\phi_{vortex}$ ), defined as the phase between the vortex force and the body displacement, follows the same pattern as for the non-rotating case, with the  $\phi_{vortex}$  increasing gradually from low values in Mode I of the sphere vibration to almost  $180^\circ$  as the system undergoes a continuous transition to Mode II of the sphere vibration at higher reduced velocity. The total phase ( $\phi_{total}$ ), defined as the phase between the transverse lift force and the body displacement, only increases from low values after the peak amplitude

<sup>†</sup> Email address for correspondence: [jisheng.zhao@monash.edu](mailto:jisheng.zhao@monash.edu)

response in Mode II has been reached. It reaches its maximum value ( $\sim 165^\circ$ ) close to the transition from the Mode II upper plateau to the lower plateau, reminiscent of the behaviour seen for the upper to lower branch transition for cylinder VIV. Hydrogen-bubble visualisations and particle image velocimetry (PIV) performed in the equatorial plane provided further insights into the flow dynamics near the sphere surface. The mean wake is found to be deflected towards the advancing side of the sphere, associated with an increase in the Magnus force. For higher rotation ratios, the near-wake rear recirculation zone is absent and the flow is highly vectored from the retreating side to the advancing side, giving rise to large-scale shedding. For a very high rotation ratio of  $\alpha = 6$ , for which vibrations are found to be suppressed, a one-sided large-scale shedding pattern is observed, similar to the shear-layer instability one-sided shedding observed previously for a rigidly mounted rotating sphere.

**Key words:** flow–structure interactions, vortex streets, wakes

## 1. Introduction

Vortex-induced vibration (VIV) of structures can occur in a variety of engineering situations, such as with flows past bridges, transmission lines, aircraft control surfaces, offshore structures, engines, heat exchangers, marine cables, towed cables, drilling and production risers in petroleum production, moored structures, tethered structures, pipelines and other hydrodynamic and hydroacoustic applications. VIV is a significant cause of fatigue damage that can lead to structural failures. Numerous studies have focused on understanding the underlying principles of flow-induced vibrations and its suppression, especially for cylinders. The immense practical significance of VIV has led to various comprehensive reviews, including Bearman (1984), Blevins (1990), Sarpkaya (2004), Williamson & Govardhan (2004), Païdoussis, Price & De Langre (2010) and Naudascher & Rockwell (2012). However, unlike the situation for cylinders, there are relatively fewer studies on VIV of elastically mounted or tethered spheres (e.g. Govardhan & Williamson 1997; Williamson & Govardhan 1997; Jauvtis, Govardhan & Williamson 2001; Pregalato 2003; Govardhan & Williamson 2005; van Hout, Krakovich & Gottlieb 2010; Behara, Borazjani & Sotiropoulos 2011; Krakovich, Eshbal & van Hout 2013; Lee, Hourigan & Thompson 2013; van Hout, Katz & Greenblatt 2013a,b; Behara & Sotiropoulos 2016), despite its ubiquitous practical significance, such as marine buoys, underwater mines, other offshore structures and tethered or towed spherical objects. Because of the geometric shape of the body, VIV of a sphere represents one of the most fundamental fluid–structure interaction problems. It is a generic symmetrical three-dimensional prototype, and improved understanding of VIV of a sphere provides a framework to comprehend VIV of more complex three-dimensional bluff bodies around us.

Govardhan & Williamson (1997) and Williamson & Govardhan (1997) reported, for the first time, the dynamics and forcing of a tethered sphere in a fluid flow. They found that a tethered sphere could oscillate at a saturation peak-to-peak amplitude of close to two body diameters. Jauvtis *et al.* (2001) discovered the existence of multiple modes of vortex-induced vibration of a tethered sphere in a free stream, namely Modes I, II and III. The first two modes, which occur over a velocity range of  $U^* \sim 5$ –10, were associated with lock-in of the system natural frequency with the vortex formation frequency, as occurs for the 2S and 2P modes for an excited cylinder. However, Mode III, which occurs over a broad range of high velocity

ranging from  $U^* \sim 20\text{--}40$ , does not have any apparent counterpart in the circular cylinder VIV case. This was later categorised and explained as a ‘movement-induced vibration’ by Govardhan & Williamson (2005). They further found an unsteady mode of vibration, Mode IV, at very high reduced velocities, characterised by intermittent bursts of large-amplitude vibration. The physical origin of such a mode of vibration still remains unknown.

Previous numerical studies on the effect of rotation on rigidly mounted rotating spheres at low Reynolds numbers ( $Re \leq 300$ ) (Kim 2009; Poon *et al.* 2014) have revealed suppression of the vortex shedding for a certain range of rotation rates. These studies were performed computationally at relatively low Reynolds numbers. On the other hand, there have been some experimental studies conducted at considerably higher Reynolds numbers ( $Re \geq 6 \times 10^4$ ) that focus mainly on the effect of transverse rotation on the fluid forces, e.g. the inverse Magnus effect (Macoll 1928; Barlow & Domanski 2008; Kray, Franke & Frank 2012; Kim *et al.* 2014), where the rotation-induced lift suddenly changes direction as the Reynolds number is increased. It is still unknown if the rotation suppresses vortex shedding at such high Reynolds numbers. Nevertheless, all these studies have observed a sudden dip in the lift and drag coefficients for a certain rotation ratio (which varies with  $Re$ ). The question arises as to whether imposed rotation can suppress VIV of an elastically mounted sphere.

Bourguet & Lo Jacono (2014) studied computationally the effect of imposed transverse rotation on the VIV response of a circular cylinder at  $Re = 100$ . Notably, they found that the peak amplitude increases to  $\sim 1.9$  cylinder diameters, which is three times that of the non-rotating case, as the rotation ratio was increased from 0 to 3.75. An extensive experimental study by Wong *et al.* (2017) on the effect of imposed rotation on the VIV response of a circular cylinder for  $1100 \leq Re \leq 6300$  also demonstrated an increase of up to  $\sim 80\%$  in the peak oscillation amplitude over the non-rotating case for rotation rates less than 2. In contrast, Seyed-Aghazadeh & Modarres-Sadeghi (2015) studied the same problem experimentally, over the Reynolds number range  $Re = 350\text{--}1000$ . In this case, the amplitude response was found to only increase marginally with rotation rate, increasing from 0.5 to 0.6 as the rotation ratio was increased up to 2.4. Thus, even for VIV of a rotating cylinder there appear to be conflicting results on the effect of rotation on the VIV response.

One question to be addressed is whether similar features are exhibited in the case of a rotating sphere. Specifically, this paper examines the effect of the body rotation on the VIV response of an elastically mounted sphere. This study addresses the following fundamental questions: How does constant imposed transverse rotation affect the VIV response of the sphere, does it suppress or enhance the response and how does this depend on rotation rate? How does the rotation affect the flow near the sphere surface and in the wake?

The experimental method used in the current study is detailed in § 2, and a validation study based on VIV of a non-rotating oscillating sphere is given in § 3. In § 4, the results and discussion on VIV of a rotating sphere are presented. Following this, § 5 focuses on analysis of flow visualisations and finally § 6 draws conclusions for the important findings and the significance of the current study.

## 2. Experimental method

### 2.1. Fluid–structure system

A schematic showing the experimental arrangement for the problem of one-degree-of-freedom (1-DOF) transverse VIV of a rotating sphere is presented in figure 1. The elastically mounted sphere is free to oscillate in only one direction transverse to the



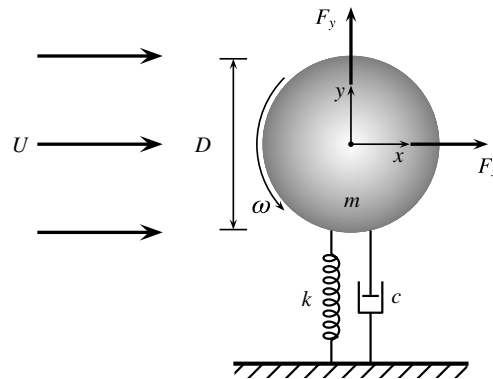


FIGURE 1. Definition sketch for the transverse vortex-induced vibration of a rotating sphere. The hydro-elastic system is simplified as a 1-DOF system constrained to move in the cross-flow direction. The axis of rotation is transverse to both the flow direction ( $x$ -axis) and the oscillation axis ( $y$ -axis). Here,  $U$  is the free-stream velocity,  $k$  the spring constant,  $D$  the sphere diameter,  $m$  the oscillating mass,  $c$  the structural damping,  $\omega$  the angular velocity.  $F_x$  and  $F_y$  represent the streamwise (drag) and the transverse (lift) force components acting on the body, respectively.

|                            |            |                         |
|----------------------------|------------|-------------------------|
| Amplitude ratio            | $A^*$      | $A/D$                   |
| Amplitude ratio            | $A_{10}^*$ | $A_{10}/D$              |
| Damping ratio              | $\zeta$    | $c/2\sqrt{k(m+m_A)}$    |
| Frequency ratio            | $f^*$      | $f/f_{nw}$              |
| Mass ratio                 | $m^*$      | $m/m_d$                 |
| Mass-damping parameter     | $\xi$      | $(m^* + C_A)\zeta$      |
| Rotation ratio             | $\alpha$   | $ \omega D/(2U)$        |
| Reduced velocity           | $U^*$      | $U/(f_{nw}D)$           |
| Reynolds number            | $Re$       | $UD/\nu$                |
| Scaled normalised velocity | $U_S^*$    | $(U^*/f^*)S = f_{vo}/f$ |
| Strouhal number            | $S$        | $f_{vo}D/U$             |

TABLE 1. Non-dimensional parameters used in this study. In the above parameters,  $A$  is the structural vibration amplitude in the  $y$  direction, and  $A_{10}$  represents the mean of the top 10 % of amplitudes.  $D$  is sphere diameter;  $f$  is the body oscillation frequency and  $f_{nw}$  is the natural frequency of the system in quiescent water.  $m$  is the total oscillating mass,  $c$  is the structural damping factor and  $k$  is the spring constant;  $U$  is the free-stream velocity, and  $\nu$  is the kinematic viscosity;  $m_A$  denotes the added mass, defined by  $m_A = C_A m_d$ , where  $m_d$  is the mass of the displaced fluid and  $C_A$  is the added-mass coefficient (0.5 for a sphere);  $\omega$  = rotational speed of the sphere;  $f_{vo}$  is the vortex shedding frequency of a fixed body.

oncoming flow. The axis of rotation is perpendicular to both the flow direction and the oscillation axis.

Table 1 presents the set of the relevant non-dimensional parameters in the current study. In studies of flow-induced vibration (FIV) of bluff bodies, the dynamics of the system is often characterised by the normalised structural vibration amplitude ( $A^*$ ) and frequency ( $f^*$ ) responses as a function of reduced velocity. Note that  $A^*$  here

is defined by  $A^* = \sqrt{2}A_{rms}/D$ , where  $A_{rms}$  is the root mean square (r.m.s.) oscillation amplitude of the body. The reduced velocity here is defined by  $U^* = U/(f_{nw}D)$ , where  $f_{nw}$  is the natural frequency of the system in quiescent water. The mass ratio, an important parameter in the fluid–structure system, is defined as the ratio of the mass of the system ( $m$ ) to the displaced mass of the fluid ( $m_d$ ), namely  $m^* = m/m_d$ , where  $m_d = \rho\pi D^3/6$  with  $\rho$  being the fluid density. The non-dimensional rotation ratio, as a measure of the ratio between the equatorial speed of the sphere to the free-stream speed, is defined by  $\alpha = |\omega|D/(2U)$ , where  $\omega$  is the angular velocity of the sphere. Physically, the rotation rate quantifies how fast the surface of the sphere is spinning relative to the incoming flow velocity. The Reynolds number based on the sphere diameter is defined by  $Re = UD/\nu$ .

The governing equation for motion characterising cross-flow VIV of a sphere can be written as

$$m\ddot{y} + c\dot{y} + ky = F_y, \quad (2.1)$$

where  $F_y$  represents fluid force in the transverse direction,  $m$  is the total oscillating mass of the system,  $c$  is the structural damping of the system,  $k$  is the spring constant and  $y$  is the displacement in the transverse direction. Using the above equation, the fluid force acting on the sphere can be calculated with the knowledge of the directly measured displacement, and its time derivatives.

## 2.2. Experimental details

The experiments were conducted in the recirculating free-surface water channel of the Fluids Laboratory for Aeronautical and Industrial Research (FLAIR), Monash University, Australia. The test section of the water channel has dimensions of 600 mm in width, 800 mm in depth and 4000 mm in length. The free-stream velocity in the present experiments could be varied continuously over the range  $0.05 \leq U \leq 0.45 \text{ m s}^{-1}$ . The free-stream turbulence level was less than 1 %. Further characterisation details of the water channel facility can be found in Zhao *et al.* (2014a,b).

A schematic of the experimental set-up is shown in figure 2. The hydro-elastic problem was modelled using a low-friction airbearing system that provided low structural damping and constrained the body motion to be in the transverse direction to the oncoming free stream. The structural stiffness was controlled by extension springs that were attached to both sides of a slider carriage. More details of the hydro-elastic facility used can be found in Zhao *et al.* (2014a,b). The sphere model was vertically supported by a thin stiff driving rod that was adapted to a rotor mechanism. The rotor mechanism was mounted to a 6-axis force sensor coupled with the carriage.

The sphere models used were solid spherical balls precision machined from acrylic plastic with a very smooth surface finish. The accuracy of the diameter was within  $\pm 20 \text{ }\mu\text{m}$ . Two sphere sizes of  $D = 70$  and  $80 \text{ mm}$  were tested in the present experiments. The spherical models were supported using a cylindrical support rod 3 mm in diameter, manufactured from hardened nitrided stainless steel for extra stiffness and to maintain straightness. This gave a diameter ratio between the sphere and the support rod of 23.3. For experiments with rotation, the 3 mm support rod was supported by two miniature roller bearings, which were covered by a non-rotating cylindrical shroud 6.35 mm in diameter manufactured from stainless steel. This set-up provided extra rigidity to the support, which in turn minimised any wobbling associated with the sphere rotation, as well as limiting undesirable wake

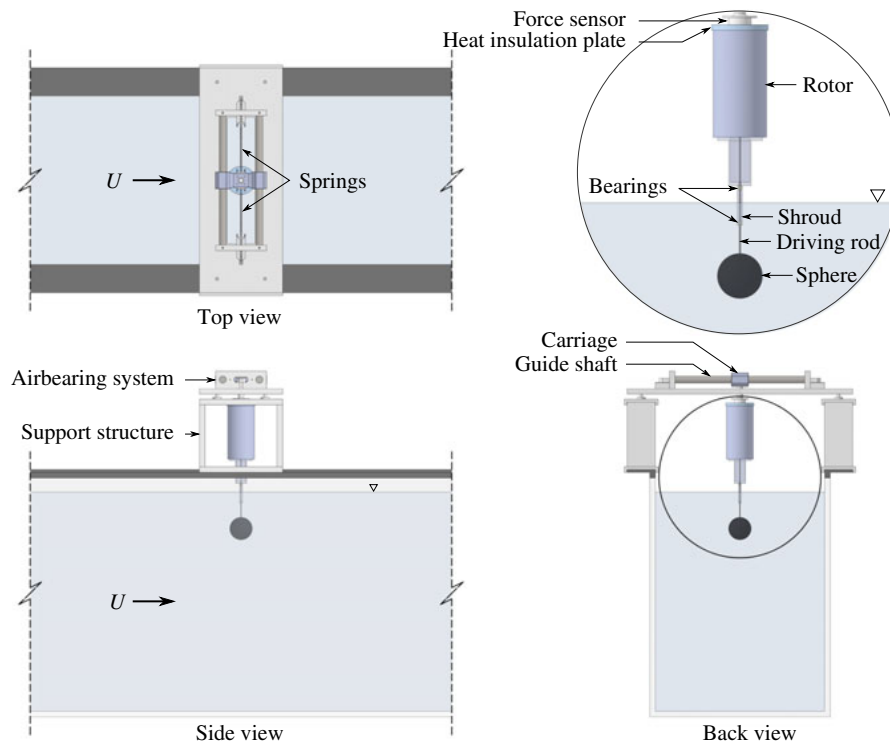


FIGURE 2. (Colour online) Schematic of the experimental set-up for the current study showing different views.

deflection that would be caused by the large Magnus force on the unshrouded rotating cylindrical rod. The immersed length of the shroud was set to approximately  $0.6D$  to minimise its influence while maintaining the structural support for the driving rod having an immersed length of  $0.5D$  exposed beyond the shroud. The total immersed length of the support set-up for the sphere was approximately  $1.1D$ . A preliminary study by Mirauda, Volpe Plantamura & Malavasi (2014) revealed that free-surface effects have an influence only when the immersion ratio (immersed length of the support rod/diameter of the sphere) is less than 0.5. Given this, an immersion ratio of  $\approx 1$  was chosen as a result of a trade-off between avoiding free-surface effects and maintaining rigidity of the support system. Furthermore, experiments were performed to determine the effect of the support rod on the amplitude response of the sphere. It was concluded that the support rod/shroud does not have any significant influence on the VIV response of the sphere for the diameter ratio (diameter of the rod/diameter of the sphere) chosen in the current study. This set-up was able to limit the wobbling deflection associated with the sphere rotation to within  $\pm 1\%D$  for the present experiments, thereby minimising undesirable perturbations to the structural dynamics and near-body wake by stabilising the sphere's rotary motion.

The rotary motion was driven using a miniature low-voltage micro-stepping motor (model: LV172, Parker Hannifin, USA) with a resolution of 25 000 steps per revolution, which was installed inside the rotor mechanism shown in figure 2. The rotation speed was monitored using a digital optical rotary encoder (model: E5-1000, US Digital, USA) with a resolution of 4000 counts per revolution. In order to reduce heat transfer from the motor to the force sensor, an insulation plate, made from acetal

plastic, was installed between the rotor rig and the force sensor. Additionally, a small fan was used to circulate the surrounding air to dissipate the heat generated by the stepper motor. These corrective actions were found to be necessary to minimise signal drifts in the force measurement signals due to thermal effects to acceptable levels.

In the current study, two methods were employed to obtain the transverse lift. In the first method, the lift was derived from the measured displacement using (2.1). For the other method, the lift was measured directly by the force sensor, although it was still necessary to subtract the inertial term accounting for the accelerating mass below the strain gauges (which includes the sphere, support structure, rotation rig and half the mass of the force sensor) to determine the actual force on the sphere. In the current paper, for cases where the signal-to-noise ratio is too low, the theoretical force has been reported instead of the directly measured force. Where necessary, this distinction is made clear in the discussion of results that follow.

The force sensor (model: Mini40, ATI-IA, USA) provided measurements of the 6-axis force and moment components ( $F_x$ ,  $F_y$ ,  $F_z$ ,  $M_x$ ,  $M_y$ ,  $M_z$ ), which in particular had a resolution of 1/200 N for  $F_x$  and  $F_y$ . This allowed accurate measurements of fluctuating lift and drag forces acting on the sphere.

The body displacement was measured using a non-contact (magnetostrictive) linear variable differential transformer (LVDT). The accuracy of the LVDT was within  $\pm 0.01\%$  of the 250 mm range available. It was observed that signal noise of the LVDT and the force sensor could be prone to the electromagnetic noise emitted by the driving motor thereby decreasing the accuracy of the force measurements. Hence, a linear encoder (model: RGH24, Renishaw, UK) with a resolution of 1  $\mu\text{m}$  was also employed to measure the displacement signal. Since the linear encoder was digital, electromagnetic noise did not affect the accuracy of the displacement signal measurement. This considerably improved accuracy and enabled reliable velocity and acceleration signals to be derived, which, in turn, enabled an accurate determination of the lift force signal as discussed above. This was tested through a direct comparison against the lift force determined by the force sensor over a wide range of  $U^*$ . It was found that the lift force measured using the force sensor matched well that derived from the linear encoder and the LVDT signals, indicating accurate measurements of the displacement and the lift force from several techniques.

The data acquisition and the controls of the flow velocity and the sphere rotation rate were automated via customised LabVIEW programs. For each data set, the signals of the displacement and force sensors were simultaneously acquired at a sampling frequency of 100 Hz for at least 100 vibration cycles.

The natural frequencies and structural damping of the system in both air and water were measured by conducting free decay tests individually in air and in quiescent water. Experiments for two mass ratios  $m^* = 7.8$  and 14.2 are reported in this paper, although only the latter was used for the rotational VIV studies because of the presence of the added motor assembly in that case. The structural damping ratio with consideration of the added mass was determined to be  $\zeta = 4.13 \times 10^{-3}$  and  $1.46 \times 10^{-3}$  for  $m^* = 7.8$  and 14.2, respectively.

To gain insight into the flow dynamics, hydrogen-bubble flow visualisations were performed in the equatorial plane of the sphere. Hydrogen bubbles were generated by an upstream platinum wire of 50  $\mu\text{m}$  in diameter and 500  $\mu\text{m}$  in length, which was powered by a potential difference of 50 VDC. A laser sheet of  $\sim 3$  mm in thickness from a continuous laser (model: MLL-N-532-5W, CNI, China), aligned parallel to the  $x$ - $y$  plane, was employed to illuminate the bubbles.

Vorticity field measurements were also performed in the central equatorial plane employing particle image velocimetry (PIV). For this purpose, the flow was seeded

with 13  $\mu\text{m}$  hollow micro-spheres having a specific weight of  $1.1 \text{ g m}^{-3}$ . The laser arrangement was the same as described above for the hydrogen-bubble visualisations. Imaging was performed using a high-speed camera (model: Dimax S4, PCO, AG) with a resolution of  $2016 \times 2016 \text{ pixels}^2$ . This camera was equipped with a 50 mm Nikon lens, giving a magnification of approximately  $7.36 \text{ pixel mm}^{-1}$  for the field of view. Velocity fields were deduced using in-house PIV software developed originally by Fouras, Lo Jacono & Hourigan (2008), using  $32 \times 32 \text{ pixel}^2$  interrogation windows in a grid layout with 50 % window overlap. All the vorticity fields shown in the current study were phase-averaged over more than 100 cycles. For each PIV measurement case, a set of 3100 image pairs were sampled at 10 Hz. Each image set was sorted into 24 phase bins based on the sphere's displacement and velocity, resulting in more than 120 image pairs for averaging at each phase. The final phase-averaged vorticity fields were smoothed slightly using an iterative Laplace filter to remove short length scale structures and to better highlight the larger-scale structures that dominate the wake.

Flow visualisations using fluorescein dye were also captured for the non-oscillating rotating sphere to better understand the effect of rotation on the near wake. For this case, the dye was injected using a thin pitot tube (1 mm in diameter) placed upstream of the sphere. Imaging was recorded using a digital camera (model: D7000, Nikon, Japan) equipped with a 50 mm lens that was positioned beneath the water channel glass floor.

In the present study, the VIV response is studied over a wide parameter space encompassing  $3 \leq U^* \leq 18$  and  $0 \leq \alpha \leq 7.5$ . The Reynolds number for the current study varies between 5000 and 30 000.

### 3. VIV response of a non-rotating sphere

#### 3.1. Vibration response measurements

The experimental methodologies used here were initially validated by comparing with previously published results of Govardhan & Williamson (2005) for transverse VIV of a non-rotating elastically mounted sphere. A sphere model of diameter 70 mm was used in this validation study. As described above, the sphere was supported from the top using a cylindrical support rod 3 mm in diameter with an immersed length of 90 mm. This gives a sphere to cylindrical support rod diameter of  $\sim 23:1$ . The mass ratio was  $m^* = 7.8$ , comparable to  $m^* = 7.0$  used in experiments by Govardhan & Williamson (2005). Free decay tests were conducted individually in air and water to determine the natural frequency in air,  $f_{na} = 0.495 \text{ Hz}$ , and in water,  $f_{nw} = 0.478 \text{ Hz}$ . Note that these values give an added-mass coefficient of  $C_A = ((f_{na}/f_{nw})^2 - 1)m^* = 0.52$ , in good agreement with the known potential added mass for a sphere. The structural damping ratio was measured as  $\zeta = 4.14 \times 10^{-3}$ , which again was comparable to the case study with  $\zeta = 4 \times 10^{-3}$  of Govardhan & Williamson (2005). For this initial study, the dynamic response of VIV was investigated over a reduced velocity range of  $2.7 \leq U^* \leq 11$ , corresponding to a Reynolds number range of  $7000 \leq Re \leq 28\,000$ . In figure 3, the amplitude response of the present study is compared directly to the response curve of Govardhan & Williamson (2005) for the similar mass ratio. The amplitude response for the higher mass ratio of  $m^* = 14.2$  used for the rotating sphere experiments is also shown for comparison, as well as a significantly higher mass ratio result for  $m^* = 53.7$  from Govardhan & Williamson (2005). Specifically, the non-dimensional amplitude of oscillations,  $A^*$ , is plotted as a function of the scaled reduced velocity,  $U_s^* = (U^*/f^*)S \equiv f_{vo}/f$ , where  $S$  is the Strouhal number for

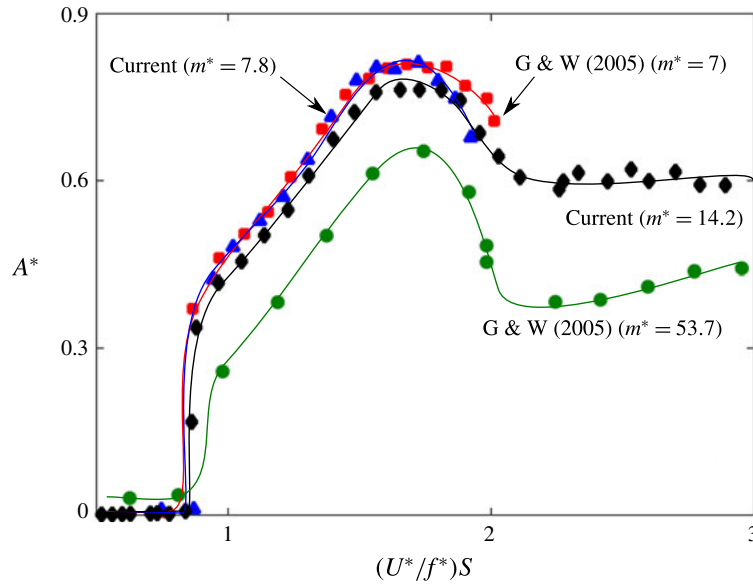


FIGURE 3. (Colour online) Comparison of the amplitude response obtained in the current study for  $m^* = 7.8$  (blue triangles) to that obtained by Govardhan & Williamson (2005) for a similar mass ratio of  $m^* = 7$  (red square). The response for  $m^* = 14.2$  (black diamonds) from the current study is also shown along with the data by Govardhan & Williamson (2005) for significantly higher mass ratio of  $m^* = 53.7$  (green circles).

the vortex shedding. Lock-in starts at  $U^* = 4\text{--}5$  for the sphere, which corresponds to  $U_S^*$  of  $0.7\text{--}0.875$ . Here, the amplitude response is plotted against  $U_S^*$  instead of  $U^*$  for the sake of direct comparison with the previous study, noting that it lines up response curves for different mass ratios. Indeed, it can be noted that using  $U_S^*$  does line up the peaks well.

It can be noted that the vibration response progresses continuously from Mode I to Mode II; indeed, the amplitude changes smoothly and continuously over the entire  $U^*$  range. This is different from the VIV response for circular cylinders, where sudden jumps are observed between the three different vibration branches. With an increase in  $m^*$  from 7.0 to 53.7, the peak amplitude in their study decreased. Similar behaviour was observed in the current study, when the mass ratio was increased, although less drastically, from 7.8 to 14.2.

For tethered spheres at higher  $U^*$ , Jauvtis *et al.* (2001) reported another vibration mode, namely Mode III. In that case, the amplitude drops to almost zero between Modes II and III, with Mode III occurring for  $U_S^* \gtrsim 3$  and extending up to  $\sim 8$ . For a 1-DOF elastically mounted sphere, the situation appears slightly different with no desynchronisation region between these modes. Instead, from the peak response in Mode II, the amplitude drops smoothly to a lower plateau that extends smoothly into Mode III as  $U_S^* \rightarrow 3$ . Thus, the lower plateau response branch for  $U_S^* \gtrsim 2$  in figure 3 might be considered to extend towards the Mode III response at the high  $U^*$  end (Govardhan & Williamson 2005). However, recall that Mode III is characterised by a vibration response at close to the natural system frequency but far from the much higher vortex shedding frequency. For the case considered here, with  $m^* = 14.2$ , the vibration frequency remains close to the natural frequency over the entire range of the lower response branch as  $f_{vo}/f$  increases beyond 2. The forcing caused by vortex



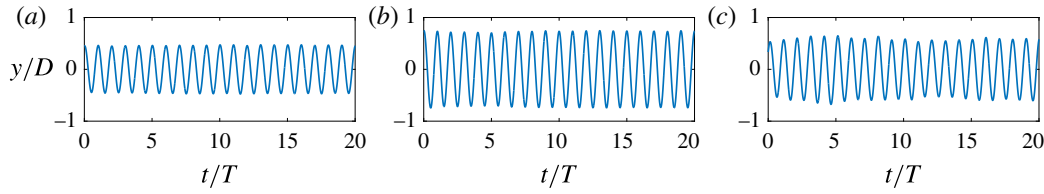


FIGURE 4. (Colour online) Strongly periodic vibrations observed for (a)  $U^* = 6.0$  (Mode I) and (b)  $U^* = 9.0$  (Mode II), and (c) slightly less periodic oscillations at the higher  $U^* = 16.0$  ( $\rightarrow$  Mode III).

shedding also remains at close to the natural frequency. This vibration response is very similar to the bifurcation region III reported by van Hout *et al.* (2010) for a heavy tethered sphere. They also observed less periodic, intermittent large oscillation amplitudes in the transverse direction for higher  $U^*$  values of  $U^* \geq 15$ . A Mode III response may occur beyond the  $U^*$  limit of these experiments, which was imposed by the strengths of the springs used.

Generally (near-)periodic vibrations are observed for the two fundamental vibration modes, as shown in figure 4. However, the vibrations are less periodic in the higher  $U^*$  range. More light will be shed on this in the following sections.

The comparison in figure 3 shows that the overall agreement with previous benchmark studies is excellent in terms of the two-mode amplitude response pattern, the amplitude peak value and the extent of the lock-in region.

### 3.2. Force measurements for a non-rotating sphere

As an approximation, it is often assumed that  $F_y(t)$  and the response displacement  $y(t)$  are both sinusoidal and represented by

$$y(t) = A \sin(2\pi ft), \quad (3.1)$$

$$F_y(t) = F_o \sin(2\pi f + \phi), \quad (3.2)$$

where  $F_o$  is the amplitude of  $F_y$ , and  $\phi$  is the phase between the fluid force and the body displacement.

Based on the suggestions of Lighthill (1986) and as performed for VIV of a tethered sphere by Govardhan & Williamson (2000), the total transverse fluid force ( $F_y$ ) can be split into a potential force ( $F_{potential}$ ), comprising the potential added-mass force, and a vortex force component ( $F_{vortex}$ ) that is due to the vorticity dynamics. From the potential theory, the instantaneous  $F_{potential}$  acting on the sphere can be expressed as

$$F_{potential}(t) = -C_A m_d \ddot{y}(t). \quad (3.3)$$

Thus, the vortex force  $F_{vortex}$  can be computed from

$$F_{vortex} = F_y - F_{potential}. \quad (3.4)$$

If all the forces are normalised by  $((1/2)\rho U^2 \pi D^2/4)$ , this reduces to

$$C_{vortex}(t) = C_y(t) - C_{potential}(t). \quad (3.5)$$

Here,  $C_{potential}$  (the potential-flow lift coefficient) can be calculated based on the instantaneous body acceleration  $\ddot{y}(t)$ . Reverting back to the dimensional forces for the moment, two equivalent forms can be written for the equation of motion

$$m\ddot{y} + c\dot{y} + ky = F_o \sin(\omega t + \phi_{total}), \quad (3.6)$$

and for vortex force

$$(m + m_A)\ddot{y} + c\dot{y} + ky = F_{vortex} \sin(\omega t + \phi_{vortex}). \quad (3.7)$$

The vortex phase  $\phi_{vortex}$ , first introduced by Govardhan & Williamson (2000), is the phase difference between  $C_{vortex}(t)$  and the body displacement  $y(t)$ . The more conventionally used total phase  $\phi_{total}$  is the phase difference between the total force  $C_y$  and the body displacement  $y(t)$ . In general, phase jumps are associated with a switch from one VIV mode to another, and have even been used to distinguish between different modes (Govardhan & Williamson 2005). The instantaneous relative phases between the two forces reported in this paper are calculated using the Hilbert transform as detailed in Khalak & Williamson (1999).

According to Govardhan & Williamson (2005), there is a vortex phase shift of approximately  $100^\circ$  when the vibration response switches from Mode I to Mode II. They observed that the vortex phase gradually increases from  $\sim 50^\circ$  in Mode I to  $\sim 150^\circ$  as the amplitude reaches the peak response in Mode II. The change in the total phase is relatively more abrupt, and it changes from  $\sim 0^\circ$  to  $\sim 150^\circ$ ; however, there is little change over the transition range between Modes I and II.

As is evident from figure 5, for the current set of experiments ( $m^* = 14.2$  and  $\zeta = 1.40 \times 10^{-3}$ ), the vortex phase and the total phase change as the vibration response switches from Mode I to Mode II, broadly following the trend of phase variations reported by Govardhan & Williamson (2005). The vortex phase starts to rise from  $\sim 50^\circ$  at the start of Mode I and reaches almost  $180^\circ$  towards the peak amplitude of Mode II, while the total phase only begins to rise from  $\sim 0^\circ$  as the response reaches close to the peak values in Mode II. Indeed, the total phase only reaches its maximum value of  $\simeq 160^\circ$  as the Mode II response transitions from its upper to lower ‘plateau’. In a sense, this appears similar to the observed behaviour for VIV of a circular cylinder. Although there are no sudden jumps or hysteresis between the branches for 1-DOF VIV of a sphere, the vortex phase and total phase transitions are broadly correlated with the initial  $\rightarrow$  upper branch cylinder transition and the upper  $\rightarrow$  lower branch cylinder transition, respectively, even though the phase jumps are much more gradual for the sphere transitions. Thus, the phase transitions suggest a sphere/cylinder mode equivalence for 1-DOF VIV of Mode I  $\equiv$  Initial Branch, Mode II (upper plateau)  $\equiv$  upper branch and Mode II (lower plateau)  $\equiv$  lower branch, although of course, for the sphere there is lock-in to the natural system frequency over a much wider range  $f_{vo}/f$  range than occurs for the circular cylinder. The phase jumps seem slightly more distinct in the current set of experiments than in those of Govardhan & Williamson (2005), possibly because of the lower mass ratio of  $m^* = 14.2$  used here (rather than  $m^* = 31.2$ ). Note that for a tethered sphere, for which the mode classification was developed, the response drops abruptly after the Mode II peak and hence there is no lower plateau.

Figure 6(a) shows the r.m.s. transverse lift coefficient as a function of  $U^*$  for  $m^* = 14.2$ . It can be noted that  $C'_{y,rms}$  jumps up at the beginning of Mode I at the onset of lock-in, and steadily decreases as the response transitions to Mode II. It remains almost constant beyond  $U^* = 10$ . Figure 6(b) shows the variation of the



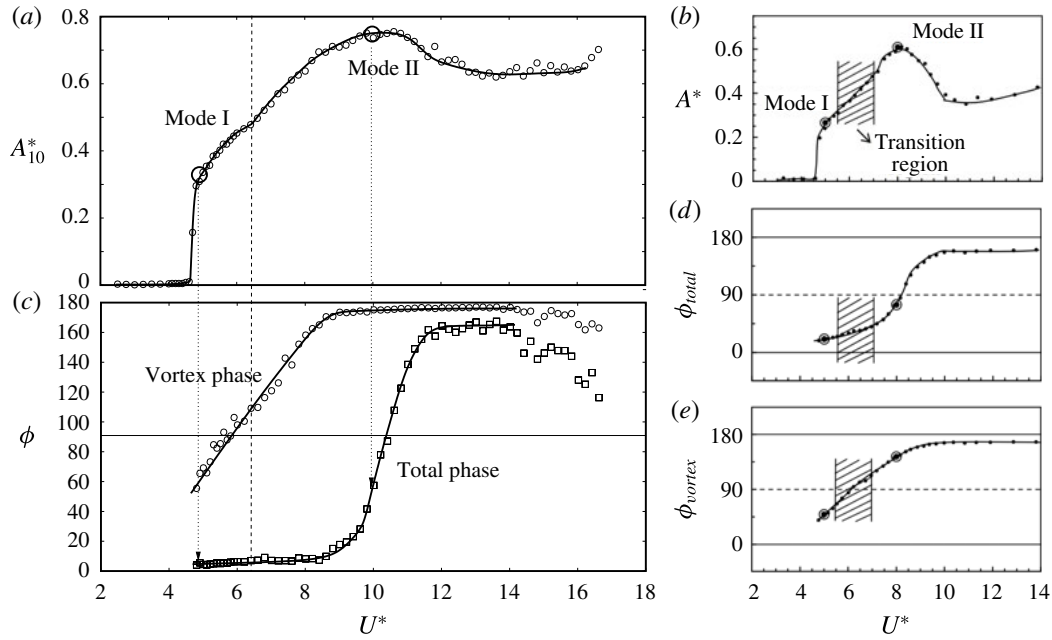


FIGURE 5. Variation of the total phase ( $\phi_{total}$ ) and the vortex phase ( $\phi_{vortex}$ ) with  $U^*$ . (a,c) measured phase variations (c) correlated with the amplitude response curve (a). The vortex phase starts to rise from  $\sim 50^\circ$  at the start of Mode I, while the total phase only begins to rise from  $\sim 0^\circ$  as the response reaches close to the peak values in Mode II. The dashed line shows the approximate boundary between Modes I and II. Here,  $A_{10}^*$  is the mean of the top 10% of amplitude peaks (as used by Hover, Miller & Triantafyllou 1997 and Morse, Govardhan & Williamson 2008). (b,d,e) comparison with previous results of Govardhan & Williamson (2005) (adapted with permission) for the higher mass ratio of  $m^* = 31.1$ .

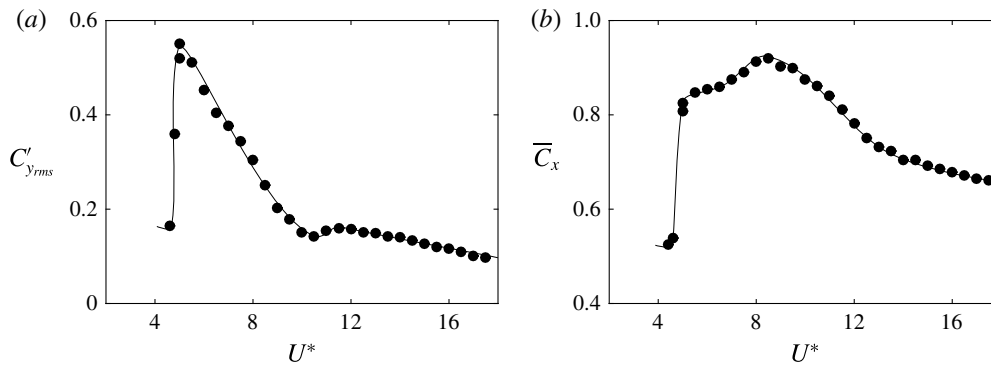


FIGURE 6. Variation of  $C'_{y,rms}$  (a) and  $\bar{C}_x$  (b) with reduced velocity.

mean drag coefficient  $\bar{C}_x$  with  $U^*$ . Note that the time-mean drag coefficient does not remain constant with increasing  $U^*$ , while the sphere is oscillating.  $\bar{C}_x$  also jumps up when the sphere locks in. These results are consistent with the previous observations of Govardhan & Williamson (2005) for an elastically mounted sphere but for a significantly different mass ratio and damping. A small jump in both the

coefficients is observed at  $U^* \sim 10$ . This is associated with the peak response in Mode II. Clear boundaries for the onset of Mode II were not known previously and  $\phi_{vortex}$  was considered to be the criterion for distinguishing Mode II from Mode I. From this study, it is found that  $\phi_{total}$  is also a useful criterion to distinguish between mode branches, as it jumps more abruptly, completing its transition to  $\sim 165^\circ$  at the start of the lower plateau beyond the main Mode II peak. Associated jumps were observed in the force coefficients as well, again demarcating the boundaries between mode branches.

#### 4. Effect of rotation on the VIV response of a sphere

This section focuses on VIV of an oscillating sphere subject to constant rotation. This set of experiments used a higher mass ratio of  $m^* = 14.2$ , because of the extra oscillating mass from the inclusion of the rotation component of the rig. The natural frequencies of the system in air and water were 0.275 Hz and 0.269 Hz, respectively, with the damping ratio of  $\zeta = 1.46 \times 10^{-3}$ . A sphere model of diameter 80 mm was attached to a 3 mm rod supported using a shroud support system as described previously in § 2.2. It was found that this support set-up closely reproduced the amplitude response previously reported by Govardhan & Williamson (2005). For each point in  $U^*-\alpha$  parameter space, more than 100 oscillation periods were recorded at an acquisition rate of 100 Hz. During these experiments, for chosen values of the rotation ratio, the flow velocity was varied in small steps to obtain a wide reduced velocity range. The Reynolds number varied between 5000 and 30 000 as the reduced velocity was increased.

To investigate the effect of  $\alpha$  on the vibration response of the sphere,  $U^*$  was varied over the range  $3 \leq U^* \leq 18$ , in increments of 0.5. For each  $U^*$  scan, the response was studied for discrete rotation ratios from the range  $0 \leq \alpha \leq 7.5$ .

##### 4.1. Effect of rotation on the vibration response

The amplitude response as a function of reduced velocity is plotted in figure 7 for different rotation rates. As discussed, for  $\alpha = 0$ , when the sphere is not rotating, the amplitude response curve (reproduced previously in figure 3) closely matches that of Govardhan & Williamson (2005), with the amplitude of vibration gradually increasing from Mode I to Mode II, and then dropping in amplitude but still maintaining a strong oscillatory response at higher  $U^*$ . When  $\alpha$  is increased slightly to 0.2, the amplitude response remains similar to the non-rotating case for  $U^* \leq 8.0$ ; however, the  $A^*$  peak in Mode II is suppressed noticeably and the amplitude response drastically drops beyond  $U^* = 14$ . For  $\alpha = 0.3$  and 0.4, a similar sudden drop in the response is seen at relatively lower  $U^*$  values. A sudden rebound in the amplitude response for  $\alpha = 0.3$  is evident at a  $U^*$  value of  $\sim 16$ –17. Such a rebound was also observed for  $\alpha = 0.25$  and  $\alpha = 0.35$ . This sudden increase in the amplitude near an  $\alpha$  value of 0.3 at higher  $U^*$  values was repeatable and was not observed for other rotation rates tested in the current study. A plausible rationale for such a rebound is discussed in § 4.3.1. For higher rotation rates ( $\alpha \geq 0.4$ ), the amplitude response drops immediately after reaching the  $A^*$  peak, rather than from a plateau, as for the cases of  $\alpha = 0.3$  and 0.4.

As  $\alpha$  is increased, the  $U^*$  range over which a synchronised VIV response characterised by highly periodic large amplitude vibrations is observed becomes progressively narrower. The end of synchronisation region decreases consistently from  $U^* > 20$  to  $U^* \sim 7$  as  $\alpha$  is increased from 0 to 4.0. Meanwhile, the magnitude of the

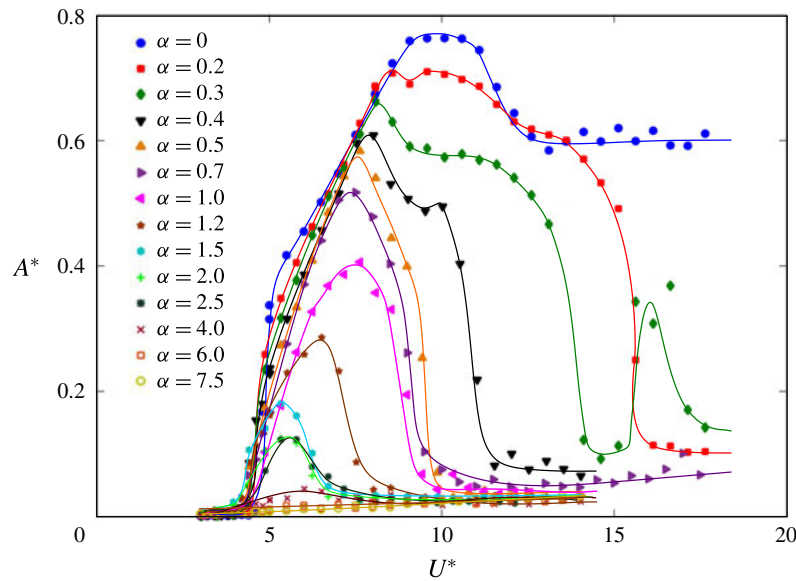


FIGURE 7. (Colour online) The vibration amplitude response as a function of reduced velocity for different rotation rates.

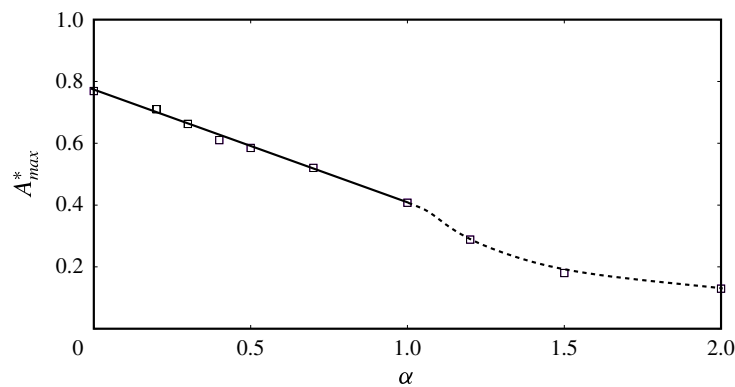


FIGURE 8. Maximum amplitude variation with rotation rate. The straight line is an approximate fit for  $\alpha \leq 1$ .

peak of amplitude response also decreases consistently from  $A^* = 0.76$  to 0.03. For higher  $\alpha$  values, no discernible peak can be detected. In addition, the peak amplitude tends to occur at a lower  $U^*$  with increasing  $\alpha$  for  $\alpha \leq 2$ . However, for higher rotation rates, the  $U^*$  value corresponding to the  $A^*$  peak increases slightly.

Figure 8 shows the variation of the  $A^*$  peak with rotation rate. It is found that the decrease in the saturation amplitude is approximately linear with increasing rotation rate for  $\alpha \lesssim 1$ , and it decreases to zero more slowly beyond that  $\alpha$  range. The overlaid straight line represents an approximate fit for the lower  $\alpha$  range.

Figure 9 shows representative time traces of the vibration amplitude for different response branches for  $\alpha = 0.5$ . Similar to the case for a non-rotating sphere, the vibration is highly periodic in regions where the sphere oscillates strongly. For regions where the VIV response was found to be suppressed, the vibration was not periodic,

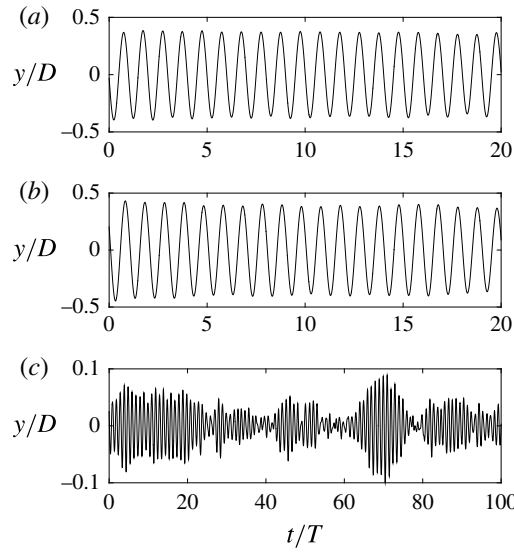


FIGURE 9. Time trace of the displacement signal at  $\alpha = 0.5$  for different values of  $U^*$ . For case (a)  $U^* = 6$ , case (b)  $U^* = 9$  and case (c)  $U^* = 12$ .

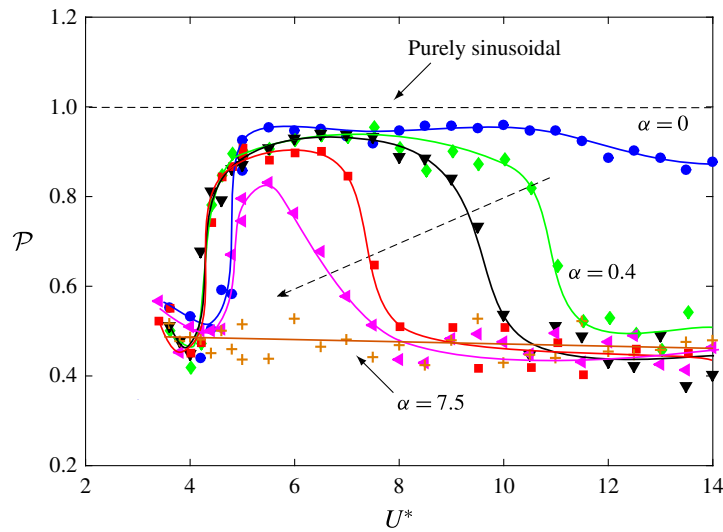


FIGURE 10. (Colour online) Variation of the periodicity,  $\mathcal{P}$ , versus reduced velocity for different rotation rates. The dashed line arrow indicates the direction of increasing  $\alpha$ . Here,  $\mathcal{P}$  is shown for a few representative cases of  $\alpha = 0, 0.4, 0.5, 1.2, 2.5$  and  $7.5$ .

and was characterised by intermittent bursts of vibrations, as shown in figure 9(c) for  $U^* = 12$  and  $\alpha = 0.5$ . This was found to be true for all rotation rates investigated.

Following Jauvtis *et al.* (2001), the periodicity of the vibration response can be quantified by defining the periodicity,  $\mathcal{P}$ , of a signal as

$$\mathcal{P} = \sqrt{2}y_{rms}/y_{max}. \quad (4.1)$$

For a purely sinusoidal signal,  $\mathcal{P}$  is equal to unity. Figure 10 shows how the periodicity varies with  $U^*$  for different values of  $\alpha$ . It is evident that the response

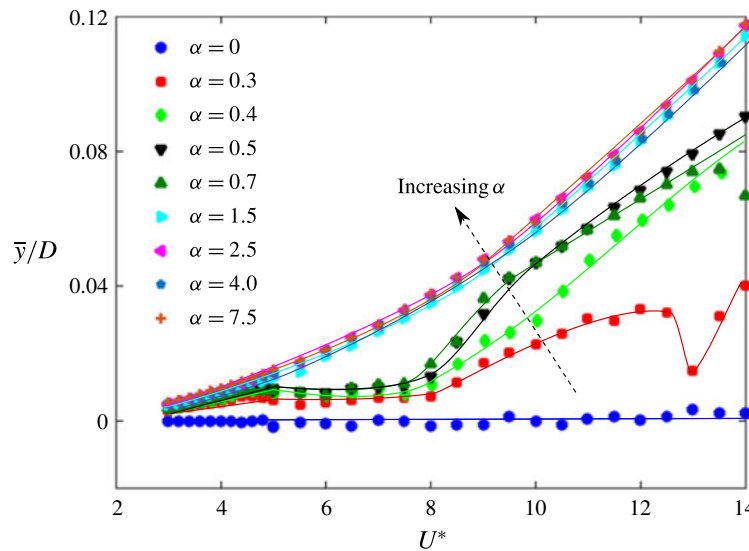


FIGURE 11. (Colour online) Variation of non-dimensional mean displacement of the sphere ( $\bar{y}/D$ ) with the reduced velocity for different rotation rates. The dashed line arrow represents the direction of increasing  $\alpha$ .

is highly periodic for the non-rotating case and it becomes relatively less periodic for the higher  $U^*$  values (beyond  $U^* = 12$ ). The sphere exhibits highly periodic oscillations for  $\alpha \leq 0.3$ , but the oscillation periodicity decreases for higher  $\alpha$  values. For higher rotation rates ( $\alpha \geq 0.4$ ), it was observed that the periodicity starts to decrease as soon as the response reaches its saturation amplitude, until it reaches a plateau value, where the vibration amplitude is negligible and no further decrease in the response is observed with any further increase in  $U^*$ . Thus it can be concluded that the rotation not only decreases the amplitude of vibration but also makes the vibration less periodic.

Figure 11 shows the non-dimensional time-averaged displacement of the sphere as a function of reduced velocity for increasing rotation rates. The time-averaged displacement remains around zero for the non-rotating case, but increases with  $\alpha$ . This is due to the rotation-induced Magnus force that exerts a one-sided fluid force acting on the sphere. It can be noted that beyond  $\alpha = 1.5$ , there is very slight increase in the time-averaged displacement, suggesting that the magnitude of the Magnus force is limited. Similar behaviour has also been observed in previous studies of rigidly mounted rotating spheres by Macoll (1928), Barlow & Domanski (2008), Kray *et al.* (2012) and Kim *et al.* (2014), showing that the increase in the lift coefficient of a sphere reaches a plateau as  $\alpha$  is increased to a certain value, which depends on the Reynolds number.

Figure 12 shows logarithmic-scale power-spectrum plots depicting the dominant oscillation frequency content ( $f^* = f/f_{nw}$ ) as a function of reduced velocity for both the non-rotating case ( $\alpha = 0$ ) and the rotating case ( $\alpha = 1$ ). The dashed line represents the value of  $f_{vo}$ , which is the vortex shedding frequency of a static sphere. Note that the power spectra were computed using fast Fourier transforms (FFTs) of the displacement time series for each  $U^*$  and then normalised by the maximum power. As can be seen in the figure, the dominant oscillation frequency remained close to

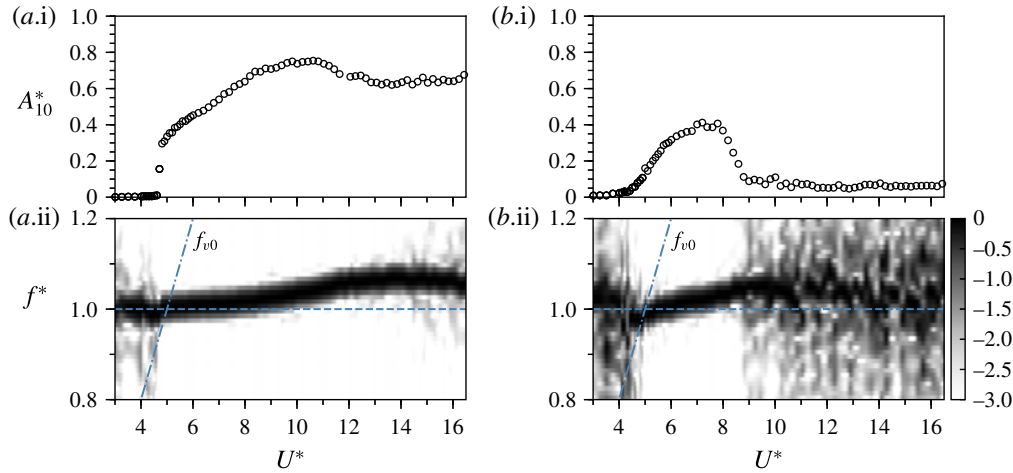


FIGURE 12. (Colour online) Frequency response as a function of  $U^*$  correlated with the amplitude response curve (above): (a.i,a.ii)  $\alpha = 0$ ; (b.i,b.ii)  $\alpha = 1$ . Here, the contour map represents a logarithmic-scale power spectrum depicting the frequency ( $f^* = f/f_{nw}$ ) content as  $U^*$  is varied. The dashed line represents the value of  $f_{v0}$ , which is the vortex shedding frequency of a static sphere.

the natural frequency of the system over the entire lock-in range for the rotating and non-rotating cases. This was found to be true for all  $\alpha$  values investigated.

Figure 13 shows phase-space plots of the measured velocity ( $\dot{y}$ ) (normalised by its maximum value) versus (normalised) fluctuating displacement ( $\tilde{y}$ ) at  $\alpha = 0.5$  for four different  $U^*$  values spanning the range from where the frequency response is near periodic to where it becomes chaotic. Figure 13(a) shows a relatively thin topologically circular structure corresponding to a strongly periodic sphere vibration response. On the other hand, as the sphere goes through the transition from a near periodic to less periodic response, as depicted in figure 13(b,d), the width of the phase-space region covered by successive orbits increases substantially. This is consistent with the frequency contour plots shown previously in figure 12), and the accompanying displacement time traces shown in this figure. Even at  $U^* = 9.5$ , where the vibration amplitude has dropped considerably from the peak response, there are signs of intermittency or mode switching, which increase at higher  $U^*$ . For an even higher  $U^*$  value of 14.0, as shown in figure 13(d), where the vibration amplitude is very small, a highly non-periodic response is observed with intermittent bursts of higher-amplitude vibrations located within an otherwise minimal response.

To add further insight to this transition, a variant of the Poincaré surface of section approach was used to further investigate the transition to non-stationary dynamics. These maps are obtained by plotting normalised sphere displacement,  $y/D$ , against its value one complete cycle previously. The points are mapped at every upward zero crossing of the sphere transverse velocity for more than 100 vibration cycles. This approach was used to explore the transition to chaos in the wake of a rolling sphere by Rao *et al.* (2012) based on numerical simulations, showing the breakdown of periodic orbits through the appearance of Kolmogorov–Arnold–Moser (KAM) tori eventually resulting in a chaotic state as the Reynolds number was further increased. Figure 14 shows such recurrence maps at  $\alpha = 0.5$  for four different  $U^*$  values. As is evident from figure 14(a), at  $U^* = 6$ , when the vibrations are highly periodic,



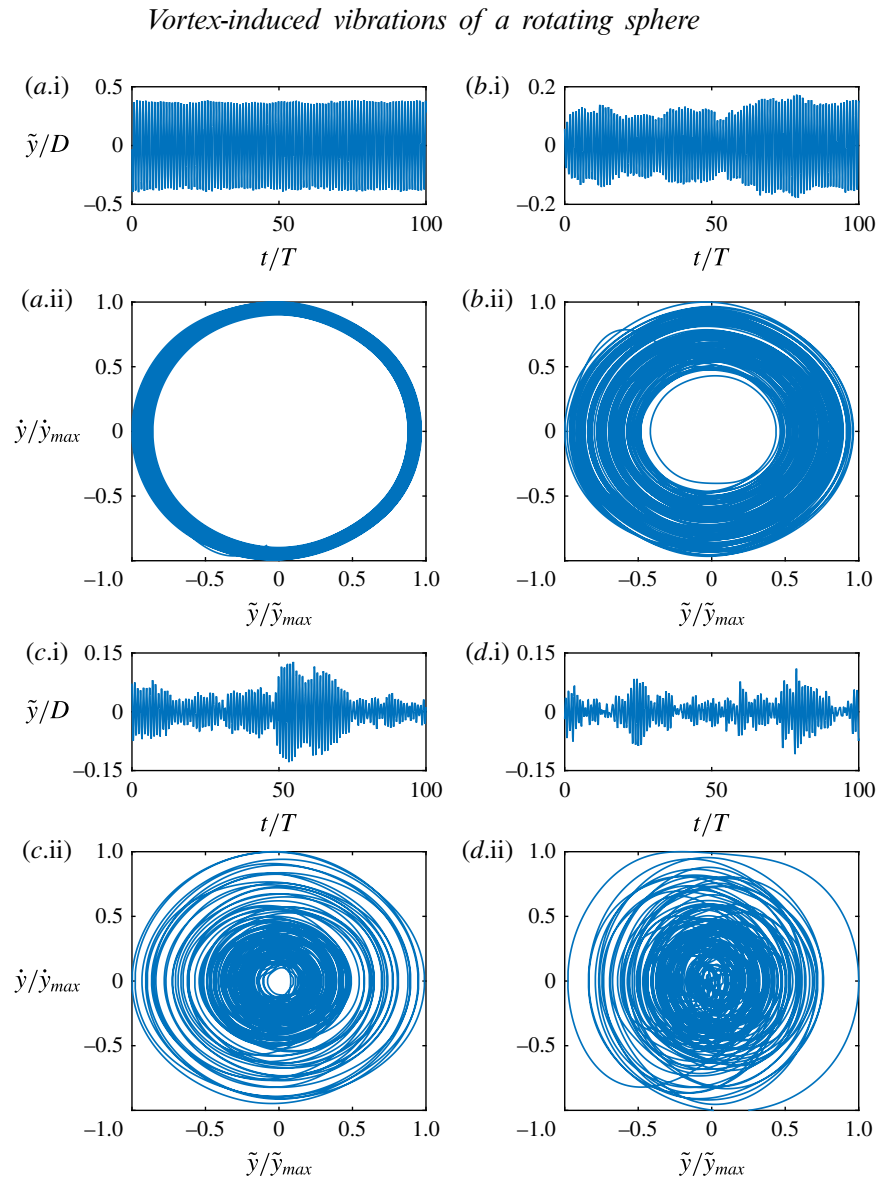


FIGURE 13. (Colour online) Phase-space plots for  $\alpha = 0.5$ , correlated with the time trace of the fluctuating displacement signal (above each map) at four different reduced velocities: (a)  $U^* = 6$ ; (b)  $U^* = 9.5$ ; (c)  $U^* = 10.5$ ; (d)  $U^* = 14.0$ .

the points are clustered over a confined region of parameter space consistent with a near-periodic system state. As the  $U^*$  value is increased to higher values of  $U^* = 9.5$  and  $U^* = 10.5$ , as shown in 14(b) and (c), respectively, the points start to spread in space, mainly along a diagonal line. For  $U^* = 14.0$ , the points now appear much more randomly distributed over a larger region. Together with the phase portraits and frequency spectra, this sequence of plots indicates that the system is undergoing a transition to chaotic oscillations.

To further explore how the vibration response evolves gradually from periodic to chaotic, figure 15 presents corresponding recurrence plots (RPs) based on the body displacement signal for the aforementioned four  $U^*$  values at  $\alpha = 0.5$ . Recurrence plots, first designed by Eckmann, Kamphorst & Ruelle (1987) to visually analyse

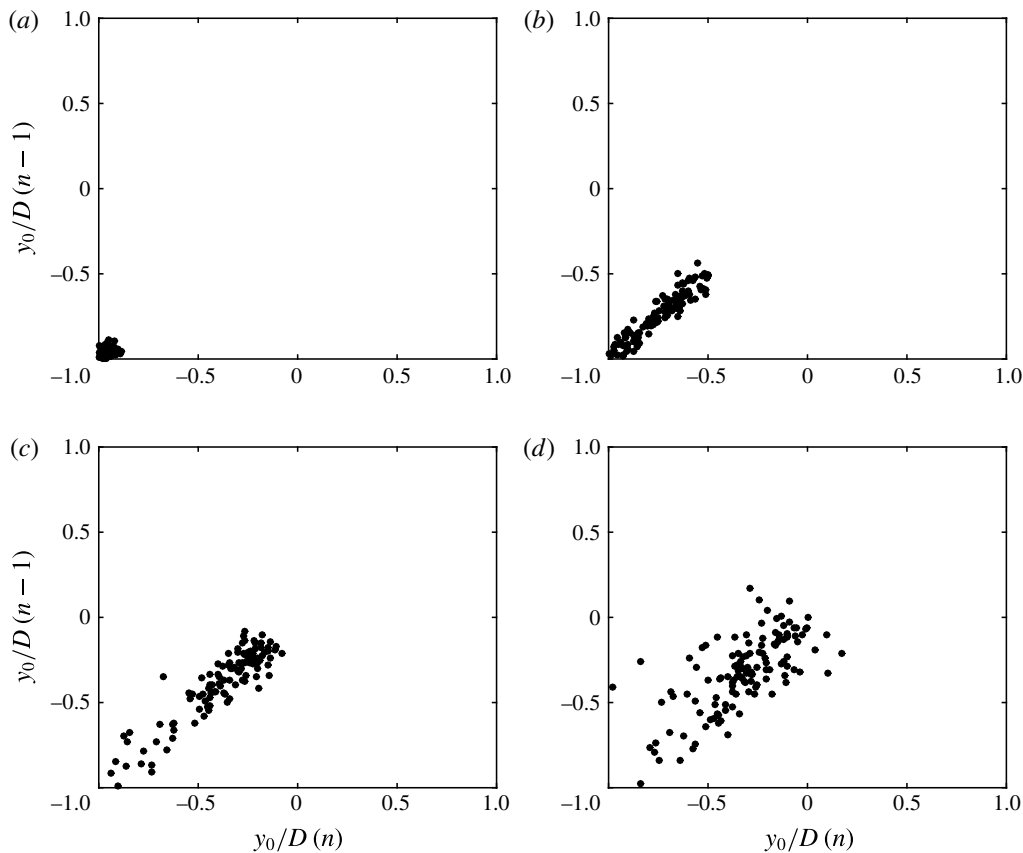


FIGURE 14. Recurrence maps for  $y_o/D$ , taken for each upward zero crossing of the sphere transverse velocity at  $\alpha = 0.5$  for various  $U^*$  values:  $U^* = 6$  (a);  $9.5$  (b);  $10.5$  (c);  $14$  (d).

the recurring patterns in time series of dynamical systems, have been utilised in a great variety of scientific areas, from physics (e.g. detection of chaos in nonlinear dynamical systems), to finance and economics, Earth science, biological systems (e.g. in cardiology, neuro-psychology), etc. A historical review of RPs has been given by Marwan (2008). The construction method for the present RPs is detailed in Marwan *et al.* (2007). As illustrated in figure 15(a), for the case of  $U^* = 6.0$ , where the body vibration is highly periodic, the RP exhibits diagonal oriented periodic checkerboard structures. These structures are symmetric about the main ( $45^\circ$ ) diagonal (also known as the line of identity (LOI)). As demonstrated in Marwan (2003) and Marwan *et al.* (2007), the diagonal lines parallel to the LOI indicate that the evolution of states of a dynamical system is similar at different epochs, while the diagonal lines orthogonal to the LOI also indicate the evolution of states of a dynamical system is similar at different epochs but with respect to reverse time. It is apparent that these diagonal lines parallel to the LOI are separated by a fixed horizontal distance matching the oscillation period, which is indicative of highly periodic recurrent dynamics with a single dominant frequency. As noted in Marwan *et al.* (2007), for a quasi-periodic system (as opposed to the current case), the distances between the diagonal lines may vary to form more complex recurrent structures. As the reduced velocity is increased to  $U^* = 9.5$  and  $10.5$  in figures 15(b) and 15(c), respectively, the periodicity of body vibration tends to reduce with less parameter space covered by



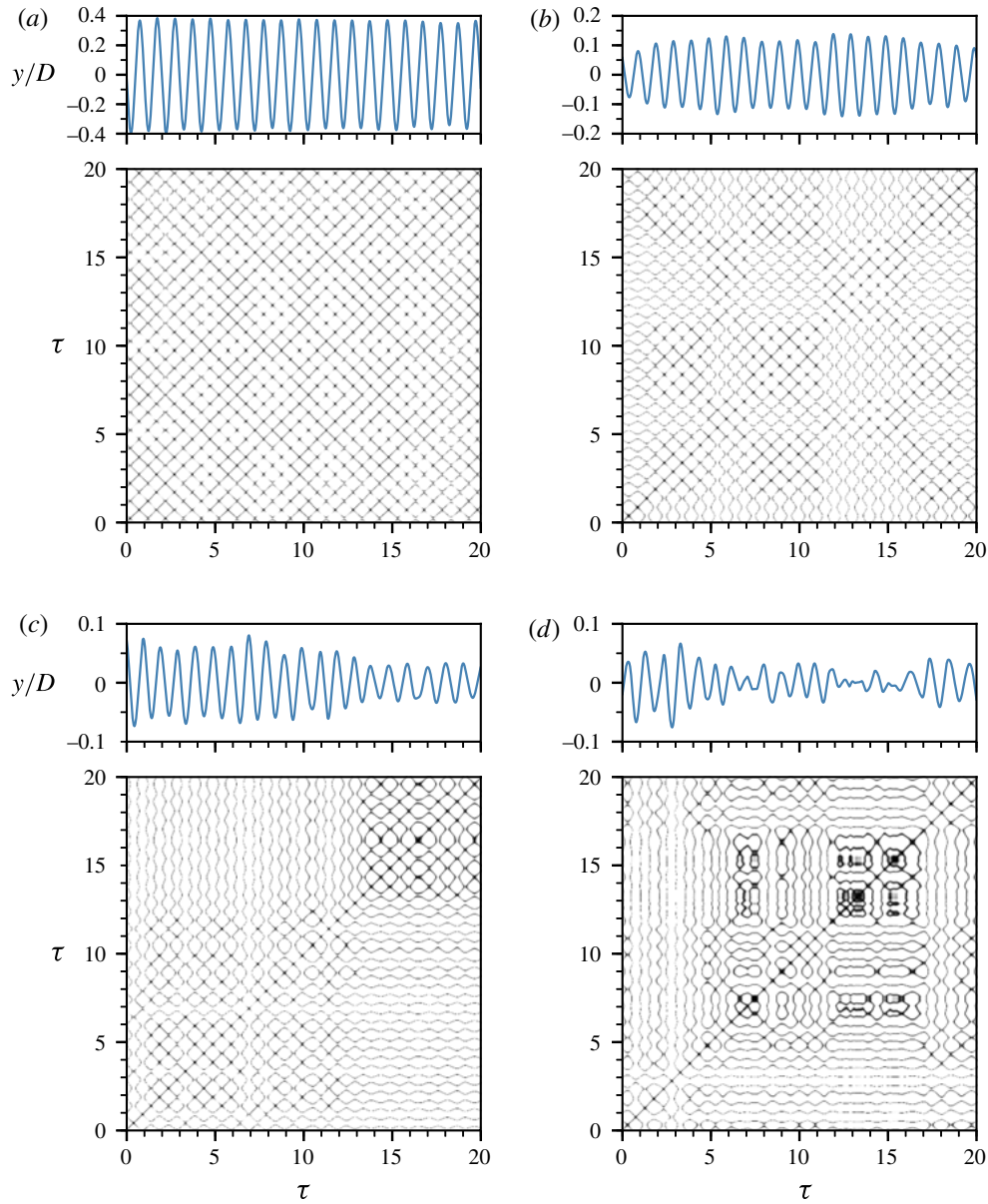


FIGURE 15. (Colour online) Recurrence plots (lower) of the time series of the normalised body displacement (upper) for  $U^* = 6.0$  (a), 9.5 (b), 10.5 (c) and 14.0 (d) at  $\alpha = 0.5$ . Note that  $\tau = t/T$  is the normalised time.

checkerboard patterns in the RPs. It should also be noted that there is an increasing trend of horizontal (and mirror vertical) curvy lines, which indicate the evolution of states of the system is similar at different epochs but with different rates; in other words, the dynamics of the system could be changing (Marwan *et al.* 2007) (e.g. a non-stationary system with time-varying frequency). As the velocity is further increased to  $U^* = 14.0$  in figure 15(d), it becomes difficult to identify any well-defined checkerboard or recurrent structures in the RP. Some horizontal curvy lines and their mirrored counterparts become flatter compared to the cases of  $U^* = 9.5$  and 10.5,

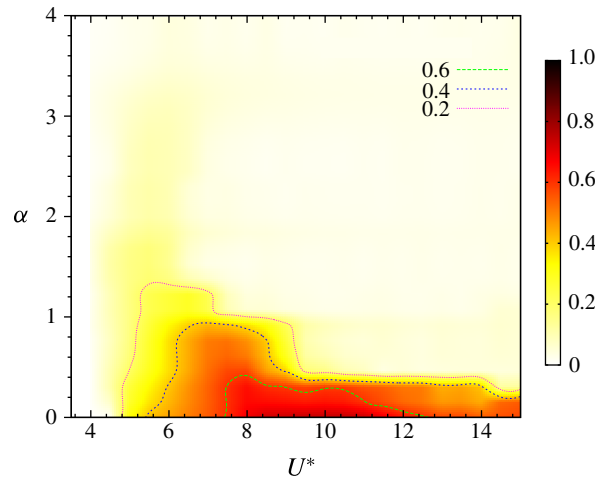


FIGURE 16. (Colour online) The VIV response contour map for a rotating sphere in  $U^*$ – $\alpha$  parameter space. Different contour lines depict different amplitude levels as shown in the figure legend.

indicating that some states do not change or change slowly for some time (e.g. for  $12 < \tau < 17$ ). Additionally, the RP exhibits some single points, indicating that the process may be an uncorrelated random or even anti-correlated (Marwan *et al.* 2007). At this point, it can be concluded that the state of the dynamical system becomes chaotic.

As an alternative depiction of the amplitude responses displayed in figure 7, figure 16 shows a response contour map of the sphere vibration in  $U^*$ – $\alpha$  parameter space. This clearly shows the shift in high-amplitude response to lower  $U^*$  values as the rotation rate is increased. Even though rotation suppresses large-amplitude oscillation as  $\alpha$  is increased towards unity, there remains a band of moderate oscillation centred at  $U^* \sim 5.5$  that decreases in amplitude much more slowly beyond this  $\alpha$  value. Perhaps also of interest is that high-amplitude oscillation is mainly limited to  $\alpha \lesssim 0.8$ . Previous studies (e.g. Giacobello, Ooi & Balachandar 2009; Kim 2009; Poon *et al.* 2014, and references therein) have shown that the onset of the shear-layer instability wake state of a non-oscillating rotating sphere occurs beyond this  $\alpha$  value. That wake state forms when fluid that passes the retreating side of the sphere is pushed towards the other side of the wake to form a distinctive one-sided separating shear layer, thus changing the characteristic formation and release of vortex loops that defines the non-rotating wake state. The nature of the wake state as a function of rotation rate is examined using flow visualisation and particle image velocimetry in § 5.

#### 4.2. The effective added-mass coefficient and critical mass ratio

Previous studies of VIV of a circular cylinder have shown the existence of a critical mass ratio,  $m_{crit}^*$ , below which large-amplitude body oscillations will persist up to infinite  $U^*$  (Govardhan & Williamson 2002; Jauvtis & Williamson 2004). The critical mass ratio can be deduced, as given by Govardhan & Williamson (2002), by evaluating the effective added-mass coefficient  $C_{EA}$  in the synchronisation regime. The effective added mass,  $m_{EA} = C_{EA}m_d$ , is (the negative of) the component of

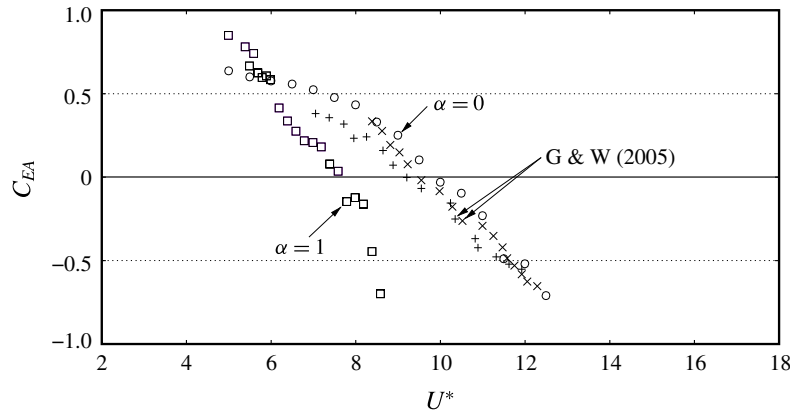


FIGURE 17. Effective added mass as a function of  $U^*$  for  $\alpha = 0$  ( $\circ$ ) and  $1$  ( $\square$ ). Data from Govardhan & Williamson (2005) for low-mass 2-DOF tethered spheres are provided for comparison ( $\times$ ,  $m^* = 1.31$ ;  $+$ ,  $m^* = 2.83$ ).

the total force in phase with the acceleration divided by the acceleration. Its significance is that from (3.2) under the condition of low damping, the system frequency depends on the sum of the system mass plus the effective added mass, i.e.  $2\pi f = \sqrt{k/(m + m_{EA})}$ , hence if  $m \rightarrow -m_{EA}$ , the system response frequency becomes unbounded. Non-dimensionalising this equation and rearranging gives an expression for  $C_{EA}$ :

$$C_{EA} = m^* \left( \frac{1 - f^{*2}}{f^{*2}} \right) + \left( \frac{C_A}{f^{*2}} \right), \quad (4.2)$$

in which  $C_A$  is the potential-flow added-mass coefficient ( $C_A = 0.5$  for a non-rotating or rotating sphere).

For low mass-damping ( $m^*\zeta$ ) systems, as proposed by Govardhan & Williamson (2002), the critical mass ratio can be evaluated by  $m_{crit}^* = \max(-C_{EA})$ . Govardhan & Williamson (2002) reported  $m_{crit}^* = 0.54$  for 1-DOF transverse VIV of a cylinder and  $m_{crit}^* = 0.52$  for the 2-DOF case, and  $m_{crit}^* \sim 0.6$  for 2-DOF VIV of a sphere. All these values were reported for very low mass-damping systems ( $m^*\zeta \leq 0.04$ ) for moderate Reynolds numbers of  $Re \sim 2000$  to  $Re \sim 20\,000$ . The mass-damping coefficient here is approximately 0.02.

Figure 17 shows the variation of  $C_{EA}$  with  $U^*$  in the synchronisation range, for the current study with  $m^* = 14.2$ , for both the non-rotating case ( $\alpha = 0$ ) and a rotating case ( $\alpha = 1$ ). The coefficient  $C_{EA}$  is computed using (4.2), in the same manner as in Govardhan & Williamson (2002). Results from the current study are directly compared to previously reported  $C_{EA}$  data for sphere vibrations with 2-DOF (tethered spheres) for relatively low mass ratios. It can be observed from the figure that  $C_{EA}$  for a non-rotating sphere ( $\alpha = 0$ ) with 1-DOF is similar to that of the 2-DOF case. The mass ratio does not seem to significantly affect  $C_{EA}$ , at least for this range of  $m^*$ . With imposed rotation,  $C_{EA}$  for sphere vibration reduces more quickly with  $U^*$ , following the shift in the response curves with rotation rate, as is evident in figure 17. However, the maximum value of  $-C_{EA}$  appears similar.

The maximum of  $-C_{EA}$  for the cases shown in figure 17 is  $\sim 0.7$ . Hence, from the above comparison, it can be concluded that the critical mass for both rotating and non-rotating sphere vibration is  $m_{crit}^* \sim 0.7$ . However, there is some scatter in the

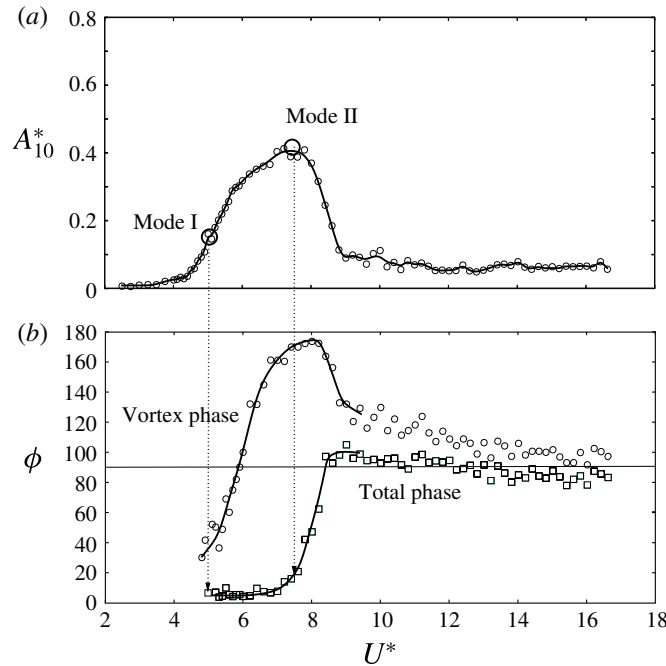


FIGURE 18. Variation of the total phase ( $\phi_{total}$ ) and the vortex phase ( $\phi_{vortex}$ ) with  $U^*$  for  $\alpha = 1$ . Measured phase variations (b), correlated with the amplitude response curve (a). The vortex phase starts to rise from low values at the start of Mode I reaching  $\sim 170^\circ$  near the peak of Mode II. In contrast, the total phase only begins to rise from  $\sim 0^\circ$  as the response reaches close to the peak values in Mode II. (Compare figure 5).

data, which is consistent with the relatively large mass ratio relative to the critical mass ratio causing the system frequency to depart only slightly from the natural frequency. Thus, the result is not inconsistent with the value of  $m_{crit}^* \simeq 0.6$  proposed by Govardhan & Williamson (2002) using much lighter spheres. Perhaps what is more interesting is that the non-rotating and rotating values are similar. The result also seems to suggest that the critical mass is not sensitive to the number of degrees of freedom of oscillation, in agreement with the finding for a circular cylinder.

#### 4.3. Effect of rotation on the force coefficients

In this section, the focus is on the effect of transverse rotation on the lift force coefficient for the first two modes within the fundamental synchronisation regime. Results are presented for a selection of rotation rates studied for the same experimental configuration used previously in § 4.1. The dimensionless fluctuating total lift coefficient  $C'_{y_{rms}}$ , and the total phase ( $\phi_{total}$ ) and the vortex phase ( $\phi_{vortex}$ ) are defined in accordance with the discussion in § 3.2.

Figure 18 shows the variation of the total phase ( $\phi_{total}$ ) and the vortex phase ( $\phi_{vortex}$ ) with  $U^*$  for  $\alpha = 1.0$ . It can be observed that the vortex phase ( $\phi_{vortex}$ ) starts to rise from low values ( $\sim 30$ – $40^\circ$ ) at the start of Mode I reaching  $\sim 170^\circ$  near the  $A_{10}^*$  peak of Mode II. In contrast, the total phase ( $\phi_{total}$ ) only starts to rise from  $\sim 0^\circ$  as the amplitude response reaches close to the peak value in Mode II. These trends were also evident in the non-rotating case shown in figure 5. However, when the vibrations

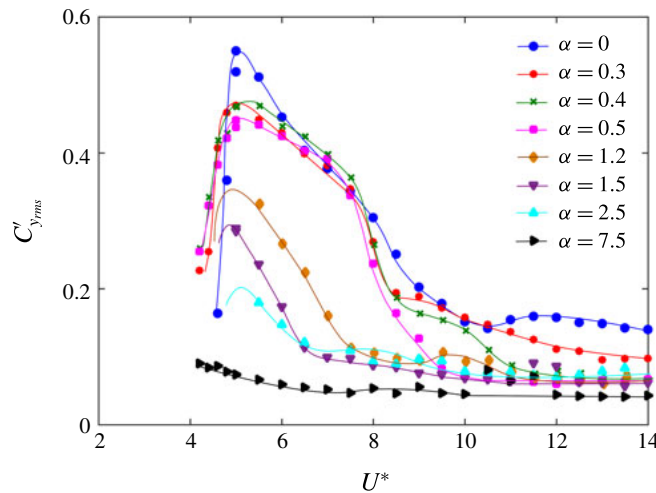


FIGURE 19. (Colour online) Variation of the  $C'_{y_{rms}}$  with reduced velocity for different rotation rates.

are suppressed, beyond  $U^* = 10$  in this case, both  $\phi_{total}$  and  $\phi_{vortex}$  settle down at approximately  $90^\circ$ . Similar behaviour was observed for other rotation rates as well.

Figure 19 shows the r.m.s. of total lift coefficient  $C'_{y_{rms}}$  versus the reduced velocity for various rotation rates. Note that for  $\alpha = 7.5$  the signal-to-noise ratio was poor in the force sensor signals due to negligible response of the sphere, hence the theoretical estimate (as discussed in § 2) has been reported for that case. For the non-rotating case ( $\alpha = 0$ ), there is a sudden jump in  $C'_{y_{rms}}$  at  $U^* \sim 5$  that is associated with the sudden increase in the amplitude response (lock-in), as shown in figure 7. For increasing  $\alpha$ , the fluctuating force coefficient decreases monotonically and gradually, in accordance with the decreasing amplitude response, as shown in figure 7. The peak value of  $C'_{y_{rms}}$  also decreases gradually with increasing  $\alpha$ . For  $\alpha = 7.5$ , no jump was observed in  $C'_{y_{rms}}$ , consistent with negligible body oscillations, as shown in figure 7. These observed behaviours of the coefficient  $C'_{y_{rms}}$  are consistent with the amplitude response. It appears that the imposed transverse rotation decreases the fluctuating component of the lift force, and in turn, that leads to a decrease in the oscillation amplitude.

Figure 20(b) shows the time trace of the total lift force coefficient,  $C_y$ , for rotation rate  $\alpha = 0.7$ , at a reduced velocity of  $U^* = 6$ , correlated with the sphere displacement (shown in figure 20a). As apparent from the figure, there is an evident asymmetry in the force signal as the sphere traverses from the advancing side to the retreating side. This is indicative of the differences in the wake shedding pattern from one half-cycle to the next as the sphere moves from one side to the other. This will be examined further in § 5.

#### 4.3.1. Competition between the Magnus force and the fluctuating lift force

The imposed rotation decreases the fluctuating component of the transverse force that drives the oscillations of the sphere. It also increases the mean component of the transverse force due to the Magnus effect. Hence, in order to better understand the dynamics of this problem, the total transverse force coefficient acting on the sphere can be split into two components, as  $C_y = \bar{C}_y + C'_{y_{rms}}$ , where  $\bar{C}_y$  is the time-averaged mean transverse force coefficient and  $C'_{y_{rms}}$  is the fluctuating transverse

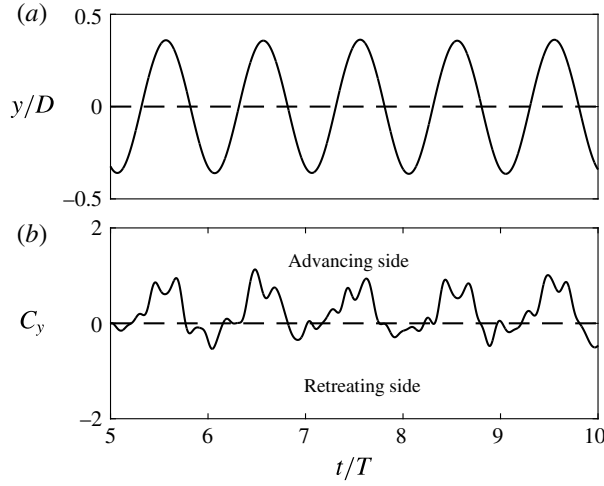


FIGURE 20. Time trace of the total lift coefficient,  $C_y$  (b), correlated with the displacement signal (a) for  $\alpha = 0.7$  at  $U^* = 6$ . Asymmetry in the force signal as the sphere traverses from the advancing to the retreating side is evident in the time trace.

force coefficient. Under resonance, where the assumption is often made that  $(U^*/f^*)$  and  $f^*$  are constant,  $A^*$  is directly correlated to  $C_y$  for a fixed mass-damping system by

$$A^* \propto \frac{C'_y \sin \phi}{(m_A + C_A)\zeta}, \quad (4.3)$$

where  $\phi$  is the phase difference between the body displacement and transverse force. This can be derived from (2.1), (3.2) and (3.1), as also shown by Williamson & Govardhan (2004). Also, the non-dimensionalised mean displacement of the sphere,  $\bar{y}/DU^{*2}$ , is directly correlated to the mean transverse force coefficient  $\bar{C}_y$  by

$$\frac{\bar{y}}{DU^{*2}} = \frac{\bar{C}_y}{2\pi^3(C_A + m^*)}. \quad (4.4)$$

Initially, for the non-rotating sphere undergoing VIV,  $\bar{C}_y$  is zero and  $C'_{y_{rms}}$  drives the oscillations. As  $\alpha$  is increased, the component of  $\bar{C}_y$  increases and the r.m.s. value of the fluctuating component  $C'_{y_{rms}}$  decreases. For lower rotation rates, the Magnus effect is not very strong, so there seems to be a competition between the increasing Magnus force and the competing fluctuating transverse force. Such a competition is evident for only lower rotation rates in the current study.

In the left column, figure 21(a–d) shows that the fluctuating oscillation amplitude,  $A^*$ , is closely correlated with the fluctuating transverse force coefficient,  $C'_{y_{rms}}$ , and the non-dimensionalised mean displacement amplitude,  $\bar{y}/DU^{*2}$ , directly correlates with the mean transverse force coefficient,  $\bar{C}_y$ , for  $\alpha = 0.4$ . The right column of figure 21(e–h) shows the same plots for  $\alpha = 2.5$ . These variations confirm the theoretical relationships given by the two equations above. The response for  $\alpha = 0.4$  can be broadly divided into three regimes for this case. In region I,  $C'_{y_{rms}}$  is large due to the resonance between the vortex shedding and body oscillation frequencies covering Mode I and the Mode II peak. For this region,  $\bar{C}_y$  is reduced



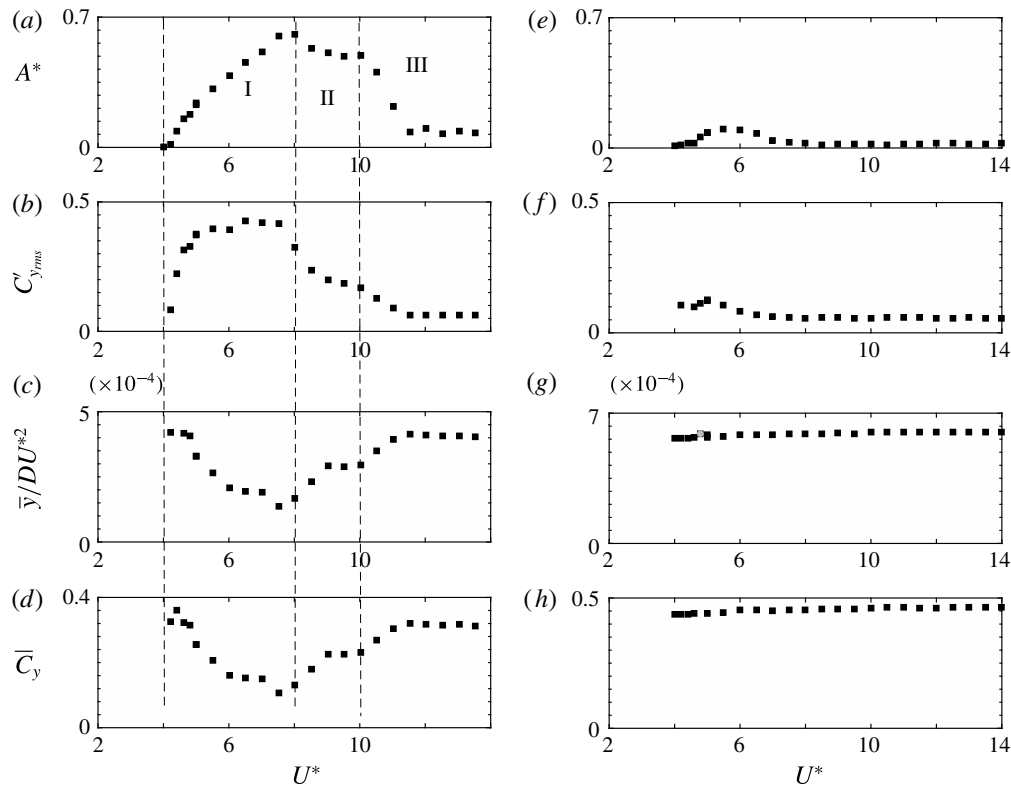


FIGURE 21. Comparison of the response characteristics for  $\alpha = 0.4$  (a–d) and  $\alpha = 2.5$  (e–h). The quantity plotted in each row is shown at the left.

with a concomitant effect in  $\bar{y}/DU^{*2}$ . In region II, which corresponds to the plateau response range after the Mode II peak, the fluctuating forcing is less and the mean force increases, leading to increased mean displacement offset. The competition between the two force components is clearly evident. In region III, the Magnus effect dominates, with  $\bar{C}_y$  again reaching a constant value close to that at low  $U^*$  before lock-in. Simultaneously, there is sudden drop in the  $A^*$  and  $C_{y'rms}$  in the desynchronisation regime at high  $U^*$ .

The sudden rebound in the amplitude response observed for a rotation rate of  $\alpha = 0.3$  at higher  $U^*$  values of  $\sim 16$ – $17$  (see figure 7) can also be explained on such grounds. A brief study by Sareen *et al.* (2016) investigated the effect of rotation on the force coefficients of a fixed rotating sphere by measuring the drag and lift coefficient for varying rotation rates ( $0 \leq \alpha \leq 6$ ) at several Reynolds numbers. They observed a sudden drop in the lift coefficient at  $\alpha = 0.3$  for a Reynolds number of  $Re = 2.75 \times 10^4$ . Interestingly, the Reynolds number where the sudden rebound is observed in the current study varies between  $2.75 \times 10^4$  and  $2.9 \times 10^4$  corresponding to the  $U^*$  range 16–17. Thus, it can be conjectured that here also there is a sudden drop in the mean lift force acting on the sphere at  $\alpha = 0.3$  for  $U^* \sim 16$ – $17$ . In lieu of the competition between the mean lift force and the fluctuating force, the fluctuating force is allowed to suddenly increase leading to a sudden rebound in the amplitude response.

However, at higher rotation rates, for example at  $\alpha = 2.5$  as shown in figure 21, the Magnus force dominates over the entire  $U^*$  range, even though there is a narrow

resonant regime. This leads to almost constant values of  $\bar{y}/DU^{*2}$  and  $\bar{C}_y$ . For this case,  $A^*$  and  $C'_{y_{rms}}$  remain at low values over the entire  $U^*$  range. How the sphere rotation affects vortex shedding and thereby leads to the attenuation of VIV will be discussed in § 5.

### 5. Modes of vortex formation

The wake of a stationary sphere at high Reynolds number ( $Re \gtrsim 1000$ ) is highly unsteady and chaotic. It is characterised by interlinked vortex rings or hairpin loops emanating from the surface of the sphere at an azimuthal location that changes from cycle to cycle. The low Reynolds number precursor structures have been observed previously in the dye visualisations of the wake of a liquid drop of Magarvey & Bishop (1961), and further experiments of Sakamoto & Haniu (1990), Leweke *et al.* (1999) and Ormières & Provansal (1999). Interlinked vortex loops have also been reported in numerical simulations concerning the wake of a static sphere by Tomboulides, Orszag & Karniadakis (1993), Johnson & Patel (1999), Mittal (1999) and Thompson, Leweke & Provansal (2001).

Similar vortex loops have also been observed in the wake of an elastically mounted sphere undergoing VIV. Previous visualisations of a rising bubble by Brücker (1999) suggested that the wake consisted of hairpin vortices. Sakamoto & Haniu (1990) also observed a similar two-sided chain of vortex loops with alternating signs. Vorticity measurements by Govardhan & Williamson (2005) showed planar symmetric vortex loops (hairpins) of opposite sign emanating from the two sides of a non-rotating sphere undergoing VIV. The central distinction between the wake behind a static sphere and an oscillating sphere is that in the case of an oscillating sphere, the loops have a preferred orientation and maintain a symmetry with the horizontal plane containing the principal transverse vibration. Lee *et al.* (2013) covered a wide range of Reynolds number  $50 \leq Re \leq 12000$  and classified the flow and response of a neutrally buoyant tethered sphere in various regimes depending on the Reynolds number. They also observed unsteady helix-shaped vortical structures in the wake at higher Reynolds number, presumably associated with the neutral buoyancy of the sphere.

But what happens if we impose a transverse rotation to the sphere while it undergoes VIV? From previous studies on rigidly mounted spheres, it is known that the transverse rotation imposes strong asymmetry in the wake, causing the loops to bend towards the advancing side (the side of the sphere moving in the direction opposite to the fluid) of the sphere due to the Magnus effect (Magnus 1853), which in consequence increases the ‘lift force’ towards the retreating side (the side of the sphere moving in the same direction as the fluid). Previous numerical studies by Giacobello *et al.* (2009), Kim (2009) and Poon *et al.* (2014) reported suppression of the vortex shedding for a certain range of rotation rates that depended on the Reynolds number. However, when  $\alpha$  was increased, the vortex shedding resumed, although it was very different to the vortex shedding at lower  $\alpha$  values that is associated with the ‘buildup and release’ of the recirculation bubbles behind the sphere. From examining the velocity and vorticity fields near the surface, they conjectured the shedding to be a shear-layer instability of the Kelvin–Helmholtz type. The flow at such high  $\alpha$  values is characterised by single-sided shedding at the advancing side of the sphere.

There have been only a few experimental studies on rigidly mounted rotating spheres at very high Reynolds numbers ( $Re \geq 6 \times 10^4$ ) (e.g. Macoll 1928; Barlow & Domanski 2008; Kim *et al.* 2014; Kray, Franke & Frank 2014). All these studies



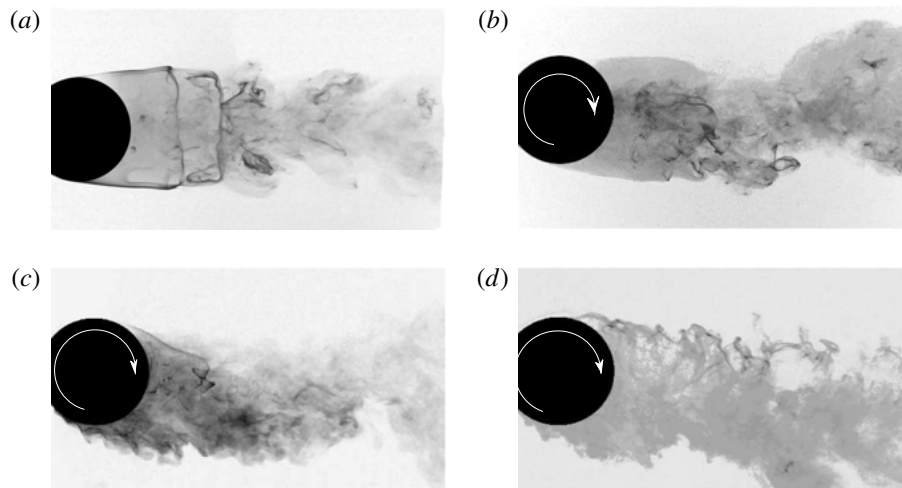


FIGURE 22. Dye visualisation images of a rigidly mounted (non-VIV case) rotating sphere at  $Re = 3510$  for (a)  $\alpha = 0$ , (b)  $\alpha = 0.2$ , (c)  $\alpha = 1.5$  and (d)  $\alpha = 3$ . Flow is from left to right. The deflection of the wake in the direction of rotation is evident from the images. For  $\alpha = 3$ , the near wake becomes wider than the smaller  $\alpha$  cases.

focused on the effect of the rotation rate on the force coefficients for understanding the inverse Magnus effect observed at such high Reynolds numbers. They found that the rotation causes asymmetry between the boundary layer separation at the retreating side and the advancing side of the sphere. There was no consensus as to whether the rotation suppresses the vortex shedding at such high Reynolds numbers or not. Figure 22 shows the effect of rotation on a rigidly mounted sphere for a Reynolds number of  $Re = 3510$ , using dye visualisation. The vectoring of the wake towards the advancing side is clearly evident. Between  $\alpha = 1.5$  and 3, the deflection does not increase further, although the near wake increases in width with the retreating side separating shear layer becoming less well defined.

The question arises, how does the transverse rotation change the wake patterns behind an elastically mounted sphere undergoing VIV? What causes the VIV response to be suppressed? In order to get an insight into the underlying flow dynamics, hydrogen-bubble visualisations were undertaken in the equatorial plane of the sphere to gauge the effect of rotation.

Figure 23 shows instantaneous hydrogen-bubble flow visualisation images for the elastically mounted rotating sphere in the equatorial plane for  $U^* = 6$  (Mode I) at  $\alpha = 0, 1, 2.5$  and 6. The flow is from left to right and the sphere is rotating anti-clockwise. The first column shows images for the instant when the sphere is at the peak of one cycle (phase of  $\pi$ ) in the  $y$  direction and the second column shows the images for the instant when the sphere reaches the peak amplitude in the opposite direction (phase of  $3\pi/2$ ). The centreline has been overlaid in the images to show the wake deflection more clearly. Some visually identified structures have been marked in red. Since the flow at high Reynolds numbers is three-dimensional and chaotic, the hydrogen bubbles do not necessarily stay in the laser plane. In spite of this, some structures are identifiable and the broad flow dynamics can be readily interpreted from these visualisations.

For  $\alpha = 0$ , in case (a), the wake is deflected upwards when the sphere reaches the peak displacement, and as the phase changes from  $\pi$  to  $3\pi/2$ , the wake changes

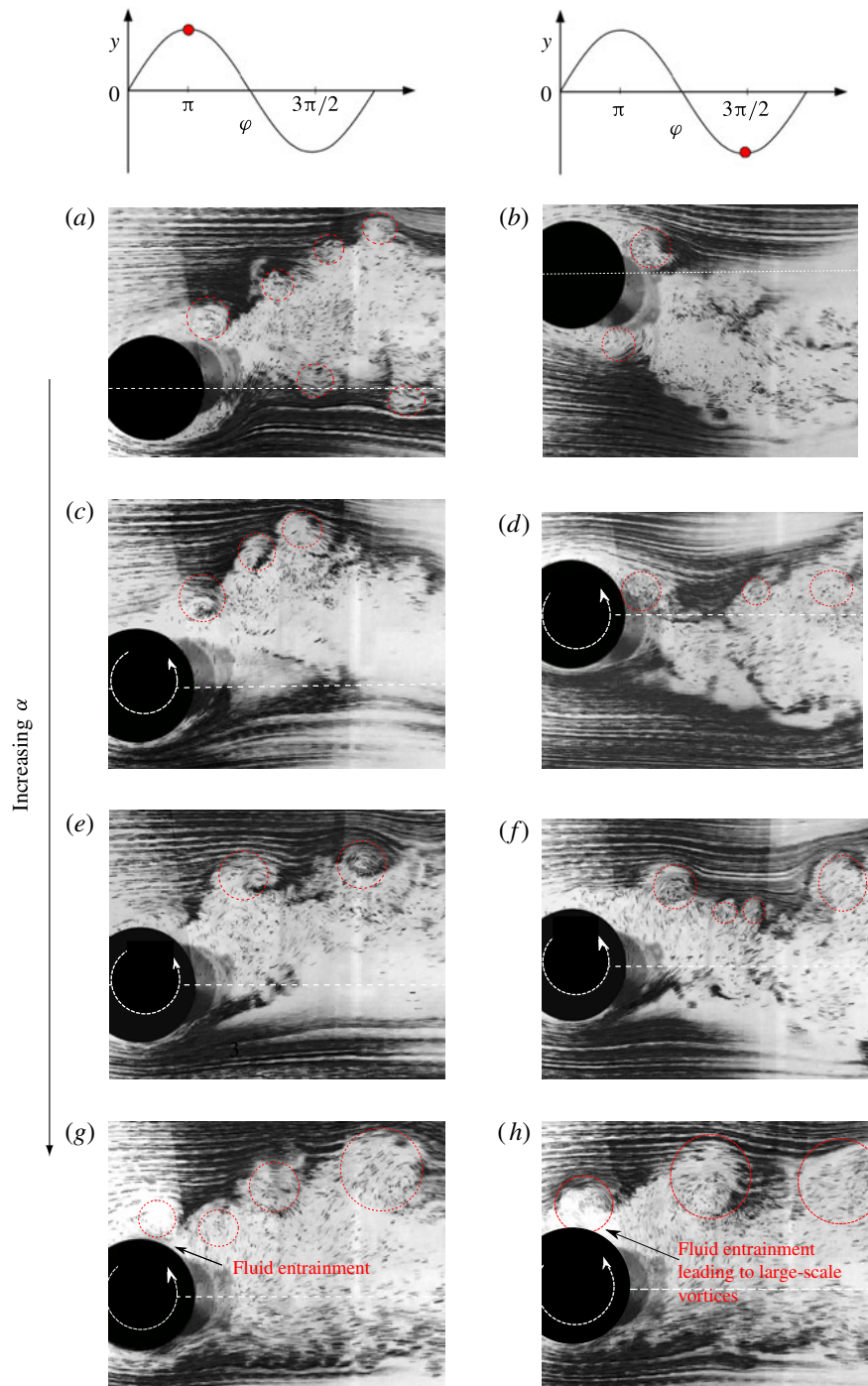


FIGURE 23. (Colour online) Instantaneous images of the hydrogen-bubble visualisation in the equatorial plane for the following cases: (a,b)  $U^* = 6$ ,  $\alpha = 0$ , (c,d)  $U^* = 6$ ,  $\alpha = 1$ , (e,f)  $U^* = 6$ ,  $\alpha = 2.5$ , (g,h)  $U^* = 6$ ,  $\alpha = 6$ . Panels (a,c,e,g) show images when the sphere is at its lowest position, and (b,d,f,h) when it is at its highest position.

orientation from upwards to downwards. The wake deflection is symmetrical, as expected for a non-rotating oscillating sphere undergoing VIV. The wake deflection and sphere displacement are in the opposite direction. Also, the roll-up of the separating shear layers just behind the sphere on both the sides can be seen, which convect downstream as vortical structures (shown in the horizontal cut through the interlinked vortex loops present in the wake).

As  $\alpha$  is increased from 0 to 6, the wake structure changes. As shown in figure 23(a,c,e,g), the deflection increases (towards the advancing side) and the wake widens due to the rotation of the sphere in the anti-clockwise direction (Magnus effect). Due to this rotation-induced forcing, the mean displacement of the sphere shifts towards the retreating side of the sphere (see § 4.1).

With increased rotation, the flow from the retreating side is vectored towards the advancing side. The flow is continuously drawn upwards by the sphere rotation; the flow structures, therefore, exhibit a large-scale shedding pattern. Case (g) clearly shows very large-scale vortices shed at the advancing side of the sphere for  $\alpha = 6$ , when the VIV is greatly suppressed.

With increased entrainment of fluid from the retreating side to the advancing side, it can be conjectured that the shear layer becomes unstable, and the vortices are shed further upstream with increasing rotation, as is evident in case (g). At high rotation rates, e.g. case (e) and case (f), the recirculation bubble is evidently mostly suppressed. This near wake is very similar to the ‘shear-layer instability’ regime reported by Giacobello *et al.* (2009), Kim (2009) and Poon *et al.* (2014) for rigidly mounted rotating spheres at low Reynolds number ( $Re \leq 1000$ ). They reported single-sided shedding on the advancing side of the rotating sphere. They also observed suppression of the recirculation bubbles and the large-scale shedding patterns with increasing rotation.

For the phase of  $3\pi/2$  (cases b,d,f,h), as  $\alpha$  increases from 0 (case b) to 1 (case d), the downward deflection of the wake decreases. For  $\alpha = 2.5$ , the wake is rather deflected slightly upwards and for  $\alpha = 6$ , the wake is highly deflected towards the advancing side. Since the wake is always deflected towards the advancing side for all shedding cycles, there is little oscillating force acting on the sphere to induce sizeable vibrations. This is also evident in measurements of the r.m.s. of the transverse fluctuating force coefficient  $C'_{y_{rms}}$  reported in § 4.3. Figure 19 shows  $C'_{y_{rms}}$  is negligible for  $U^* = 6$  at  $\alpha = 6$ . Hence, VIV is (almost) suppressed for  $\alpha = 6$  (case h) and the sphere is displaced towards the retreating side.

Owing to the fact that hydrogen-bubble visualisations provide mostly qualitative information, particle image velocimetry (PIV) was employed in the central equatorial plane (plane of symmetry) to provide more quantitative information, allowing an alternative view of the main near-wake features. Figure 24 shows representative near-wake vorticity maps, phase-averaged over more than 100 oscillation cycles, in the central equatorial plane for the same experimental conditions as shown in figure 23. As is evident from figure 24(a,b), the phase-averaged wake of a non-rotating oscillating sphere consists of a counter-rotating vortex pair downstream that represents a cut through a vortex ring, as previously reported by Govardhan & Williamson (2005). The deflections observed in the overall wake patterns in all cases are consistent with those observed earlier using the hydrogen-bubble visualisations (figure 23). For  $\alpha = 0$ , the wake deflections at opposite ends of the oscillation cycle are symmetric, but they become increasingly unsymmetric with increasing  $\alpha$ , until for  $\alpha = 6$  the vibrations are almost suppressed. The wake at  $\alpha = 6$  is considerably wider than the other cases. For the phase of  $3\pi/2$ , as the rotation rate increases from  $\alpha = 0$  to 1, it can clearly be

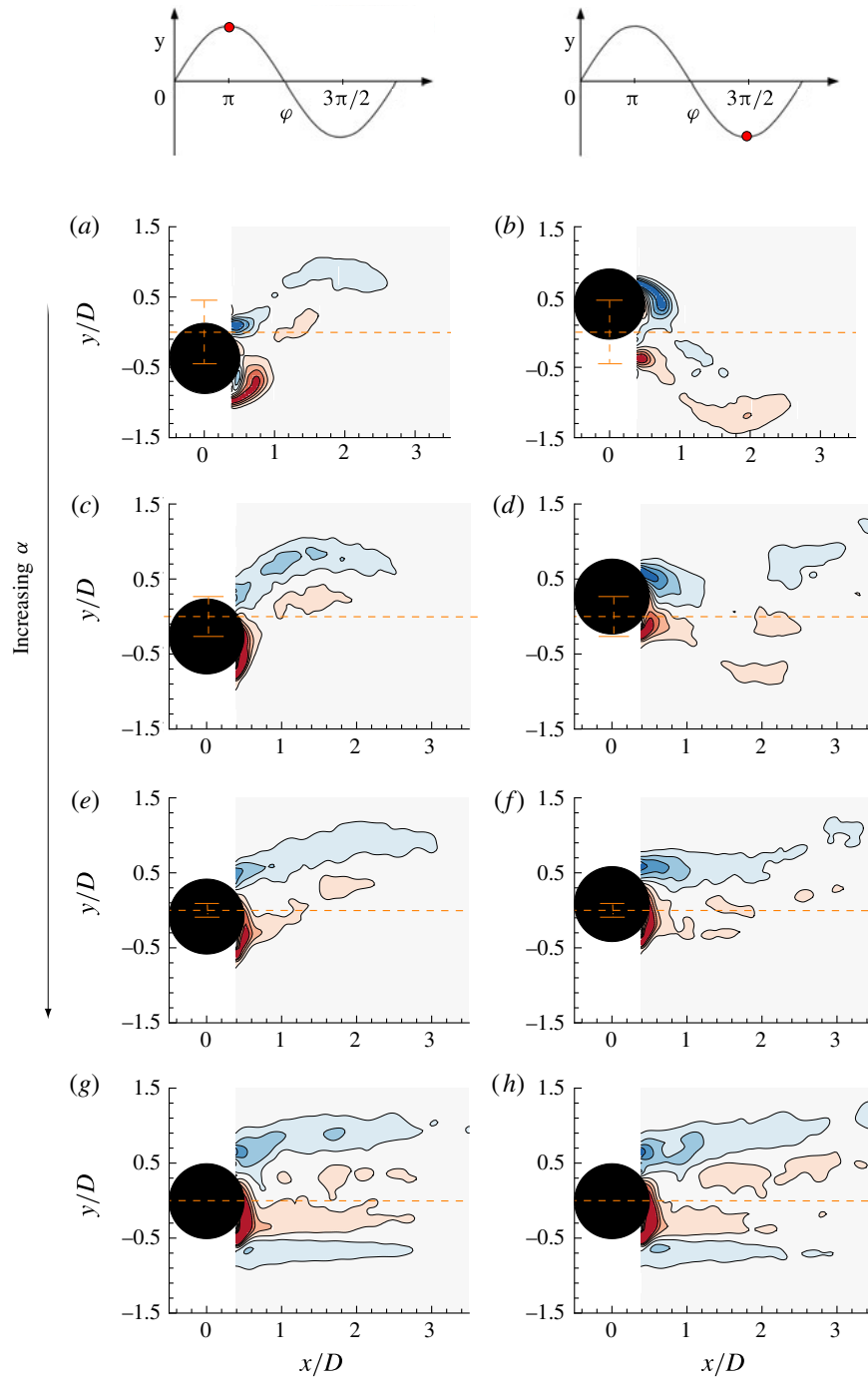


FIGURE 24. (Colour online) Equatorial near-wake vorticity maps obtained from phase-averaged PIV for the following cases: (a,b)  $U^* = 6$ ,  $\alpha = 0$ , (c,d)  $U^* = 6$ ,  $\alpha = 1$ , (e,f)  $U^* = 6$ ,  $\alpha = 2.5$  and (g,h)  $U^* = 6$ ,  $\alpha = 6$ . Panels (a,c,e,g) show images corresponding to when the sphere is at its lowest position, and (b,d,f,h) when it is at its highest position. The blue contours show clockwise vorticity and red contours show anti-clockwise vorticity. The normalised vorticity range is  $\omega^* = \omega D/U$  (where  $\omega$  is the vorticity)  $\in [-3, 3]$  for  $\alpha = 0$ ,  $[-2, 2]$  for  $\alpha = 1$  and  $\alpha = 2.5$  and  $[-1, 1]$  for  $\alpha = 6$ .

seen that the wake deflection angle towards the retreating side (downwards) decreases. When  $\alpha$  is further increased to 2.5, the downward deflection angle is almost zero. For  $\alpha = 6$ , the wake is now deflected in the opposite direction (advancing side). The presence of anti-clockwise vorticity encircling the sphere on the retreating side points towards highly vectored flow from the retreating to the advancing side. Also, the recirculation region is absent for higher rotation rates. These findings are congruous with the more qualitative hydrogen-bubble visualisations.

Although the wake of a sphere is intrinsically highly three-dimensional and chaotic at such high Reynolds numbers, the flow visualisations in the plane of symmetry (equatorial plane) still provide important insights into the underlying flow dynamics.

## 6. Conclusions

An extensive series of experiments and flow visualisations have been performed to study the effect of transverse rotation on the VIV response of a sphere. Transverse rotation was imposed such that the axis of rotation was perpendicular to the flow direction. The vibration response was studied for a wide parameter space of  $0 \leq \alpha \leq 7.5$  and  $3 \leq U^* \leq 18$ . Interestingly, unlike its two-dimensional counterpart, the cylinder, the VIV response of the sphere reduced gradually and steadily with increasing the rotation ratio, leading to an almost complete suppression for  $\alpha \geq 6.0$ . With some similarities to the non-rotating case, the amplitude response of a rotating sphere exhibited a bell-shaped curve, showing vibration Modes I and II for  $\alpha \leq 1$ . It was also found that the synchronisation regime became narrower with increasing  $\alpha$ , and also the peak amplitude response gradually decreased almost linearly for  $\alpha \lesssim 1$ . For  $\alpha \geq 0.5$ , the amplitude response dropped off rapidly with increasing  $U^*$  as soon as the peak response was reached, whereas, for lower rotation ratios of  $\alpha \leq 0.4$ , large oscillation amplitudes were still encountered at higher  $U^*$  values after the  $A^*$  peak was reached in Mode II. The oscillation frequency remained close to the natural frequency of the system for all cases.

Furthermore, it was found that oscillation amplitudes not only decreased but also the oscillations became less periodic with increasing rotation. Recurrence analysis revealed a transition from periodic to chaotic in the recurrence map complementing the occurrence of broadband frequency spectra at the onset of bifurcation. The time-averaged mean displacement increased towards the retreating side of the sphere with increasing  $\alpha$ , due to an increase in the mean Magnus force. A substantial jump in fluctuating lift force coefficient,  $C'_{y_{rms}}$ , was observed when lock-in occurred at the start of the Mode I response. The peak value of  $C'_{y_{rms}}$  as  $U^*$  was increased was found to decrease consistently with the rotation rate, following a trend similar to that of the vibration amplitude. Imposed rotation increased the mean component of the transverse force ( $\bar{C}_y$ ) due to the Magnus effect. It simultaneously decreased the fluctuating component of the transverse force ( $C'_{y_{rms}}$ ), which decreased the VIV response.

Compared to VIV of a low mass-damped cylinder, the total and vortex phase transitions are much less sharp, as the VIV mode changes. However, overall the phase transitions are similar. The vortex phase jumps as the response changes from Mode I to Mode II, and the total phase jumps from low to high values as the Mode II vibration transitions to the lower plateau, which is only observed for  $\alpha \lesssim 0.4$ .

Flow visualisations using hydrogen bubbles and the PIV techniques were performed in the equatorial plane containing the principal transverse vibration. With increased rotation, the wake deflected more and more towards the advancing side of the sphere.



The flow was continuously drawn from the retreating side to the advancing side of the sphere with increasing rotation rate, which led to entrainment of fluid at the advancing side. This entrainment gave rise to large-scale one-sided vortex shedding. This flow behaviour is very similar to the ‘shear-layer instability’ regime reported by previous studies for rigidly mounted rotating spheres. For the rotation rates where the VIV was found to be completely suppressed, the wake was found to be always deflected towards the advancing side with large-scale flow structures for all shedding cycles. A lack of an oscillating force acting on the sphere led to near suppression of the VIV. This also led to a shift in the mean displacement of the sphere towards the retreating side. Measurements of the fluctuating transverse force coefficients  $C'_{y_{rms}}$  and  $\bar{C}_y$  were also consistent with the flow visualisation observations.

### Acknowledgements

The authors would like to acknowledge the financial support from the Australian Research Council Discovery Project grants (DP150102879 and DP170100275). A.S. acknowledges the support of a Monash Graduate Scholarship (MGS) and a Monash International Postgraduate Research Scholarship (MIPRS).

### REFERENCES

- BARLOW, J. B. & DOMANSKI, M. J. 2008 Lift on stationary and rotating spheres under varying flow and surface conditions. *AIAA J.* **46** (8), 1932–1936.
- BEARMAN, P. W. 1984 Vortex shedding from oscillating bluff bodies. *Annu. Rev. Fluid Mech.* **16** (1), 195–222.
- BEHARA, S., BORAZJANI, I. & SOTIROPOULOS, F. 2011 Vortex-induced vibrations of an elastically mounted sphere with three degrees of freedom at  $Re = 300$ : hysteresis and vortex shedding modes. *J. Fluid Mech.* **686**, 426–450.
- BEHARA, S. & SOTIROPOULOS, F. 2016 Vortex-induced vibrations of an elastically mounted sphere: the effects of Reynolds number and reduced velocity. *J. Fluids Struct.* **66**, 54–68.
- BLEVINS, R. D. 1990 *Flow-Induced Vibration*, 2nd edn. Krieger Publishing Company.
- BOURGUET, R. & LO JACONO, D. 2014 Flow-induced vibrations of a rotating cylinder. *J. Fluid Mech.* **740**, 342–380.
- BRÜCKER, C. 1999 Structure and dynamics of the wake of bubbles and its relevance for bubble interaction. *Phys. Fluids* **11** (7), 1781–1796.
- ECKMANN, J., KAMPHORST, S. O. & RUELLE, D. 1987 Recurrence plots of dynamical systems. *Europhys. Lett.* **4** (9), 973–977.
- FOURAS, A., LO JACONO, D. & HOURIGAN, K. 2008 Target-free stereo PIV: a novel technique with inherent error estimation and improved accuracy. *Exp. Fluids* **44** (2), 317–329.
- GIACOBELLO, M., OOI, A. & BALACHANDAR, S. 2009 Wake structure of a transversely rotating sphere at moderate Reynolds numbers. *J. Fluid Mech.* **621**, 103–130.
- GOVARDHAN, R. & WILLIAMSON, C. H. K. 1997 Vortex-induced motions of a tethered sphere. *J. Wind Engng Indust. Aerodyn.* **375**, 69–71.
- GOVARDHAN, R. & WILLIAMSON, C. H. K. 2000 Modes of vortex formation and frequency response of a freely vibrating cylinder. *J. Fluid Mech.* **420**, 85–130.
- GOVARDHAN, R. & WILLIAMSON, C. H. K. 2002 Resonance forever: existence of a critical mass and an infinite regime of resonance in vortex-induced vibration. *J. Fluid Mech.* **473**, 147–166.
- GOVARDHAN, R. N. & WILLIAMSON, C. H. K. 2005 Vortex-induced vibrations of a sphere. *J. Fluid Mech.* **531**, 11–47.
- VAN HOUT, R., KATZ, A. & GREENBLATT, D. 2013a Acoustic control of vortex-induced vibrations of a tethered sphere. *Phys. Fluids* **25**, 077102.

- VAN HOUT, R., KATZ, A. & GREENBLATT, D. 2013*b* Time-resolved particle image velocimetry measurements of vortex and shear layer dynamics in the near wake of a tethered sphere. *Phys. Fluids* **25** (7), 077102.
- VAN HOUT, R., KRAKOVICH, A. & GOTTLIEB, O. 2010 Time resolved measurements of vortex-induced vibrations of a tethered sphere in uniform flow. *Phys. Fluids* **22** (8), 087101.
- HOVER, F. S., MILLER, S. N. & TRIANTAFYLLOU, M. S. 1997 Vortex-induced vibration of marine cables: experiments using force feedback. *J. Fluids Struct.* **11** (3), 307–326.
- JAUVTIS, N., GOVARDHAN, R. & WILLIAMSON, C. H. K. 2001 Multiple modes of vortex-induced vibration of a sphere. *J. Fluids Struct.* **15** (3–4), 555–563.
- JAUVTIS, N. & WILLIAMSON, C. H. K. 2004 The effect of two degrees of freedom on vortex-induced vibration at low mass and damping. *J. Fluid Mech.* **509**, 23–62.
- JOHNSON, T. A. & PATEL, V. C. 1999 Flow past a sphere up to a Reynolds number of 300. *J. Fluid Mech.* **378**, 19–70.
- KHALAK, A. & WILLIAMSON, C. H. K. 1999 Motions, forces and mode transitions in vortex-induced vibrations at low mass-damping. *J. Fluids Struct.* **13** (7–8), 813–851.
- KIM, D. 2009 Laminar flow past a sphere rotating in the transverse direction. *J. Mech. Sci. Technol.* **23** (2), 578–589.
- KIM, J., CHOI, H., PARK, H. & YOO, J. Y. 2014 Inverse Magnus effect on a rotating sphere: when and why. *J. Fluid Mech.* **754**, R2.
- KRAKOVICH, A., ESHBAL, L. & VAN HOUT, R. 2013 Vortex dynamics and associated fluid forcing in the near wake of a light and heavy tethered sphere in uniform flow. *Exp. Fluids* **54** (11), 1615.
- KRAY, T., FRANKE, J. & FRANK, W. 2012 Magnus effect on a rotating sphere at high Reynolds numbers. *J. Wind Engng Indust. Aerodyn.* **110**, 1–9.
- KRAY, T., FRANKE, J. & FRANK, W. 2014 Magnus effect on a rotating soccer ball at high Reynolds numbers. *J. Wind Engng Indust. Aerodyn.* **124**, 46–53.
- LEE, H., HOURIGAN, K. & THOMPSON, M. C. 2013 Vortex-induced vibration of a neutrally buoyant tethered sphere. *J. Fluid Mech.* **719**, 97–128.
- LEWEKE, T., PROVANSAL, M., ORMIERES, D. & LEBESCOND, R. 1999 Vortex dynamics in the wake of a sphere. *Phys. Fluids* **11** (9), S12.
- LIGHTHILL, J. 1986 Fundamentals concerning wave loading on offshore structures. *J. Fluid Mech.* **173**, 667–681.
- MACOLL, J. W. 1928 Aerodynamics of a spinning sphere. *J. R. Aero. Soc.* **28**, 777–798.
- MAGARVEY, R. H. & BISHOP, R. L. 1961 Transition ranges for three-dimensional wakes. *Can. J. Phys.* **39** (10), 1418–1422.
- MAGNUS, G. 1853 Ueber die Abweichung der Geschosse, und: Ueber eine auffallende Erscheinung bei rotirenden Körpern. *Annalen der Physik* **164** (1), 1–29.
- MARWAN, N. 2003 Encounters with neighbours: current developments of concepts based on recurrence plots and their applications. PhD thesis, Universität Potsdam.
- MARWAN, N. 2008 A historical review of recurrence plots. *Eur. Phys. J.* **164** (1), 3–12.
- MARWAN, N., ROMANO, M., THIEL, M. & KURTHS, J. 2007 Recurrence plots for the analysis of complex systems. *Phys. Rep.* **438** (5), 237–329.
- MIRAUDA, D., VOLPE PLANTAMURA, A. & MALAVASI, S. 2014 Dynamic response of a sphere immersed in a shallow water flow. *J. Offshore Mech. Arctic Engng* **136** (2), 021101.
- MITTAL, R. 1999 A Fourier-Chebyshev spectral collocation method for simulating flow past spheres and spheroids. *Intl J. Numer. Meth. Fluids* **30** (7), 921–937.
- MORSE, T., GOVARDHAN, R. & WILLIAMSON, C. H. K. 2008 The effect of end conditions on the vortex-induced vibration of cylinders. *J. Fluids Struct.* **24** (8), 1227–1239.
- NAUDASCHER, E. & ROCKWELL, D. 2012 *Flow-Induced Vibrations: An Engineering Guide*. Courier Corporation.
- ORMIÈRES, D. & PROVANSAL, M. 1999 Transition to turbulence in the wake of a sphere. *Phys. Rev. Lett.* **83** (1), 80.
- PAÏDOUSSIS, M. P., PRICE, S. & DE LANGRE, E. 2010 *Fluid-Structure Interactions: Cross-Flow-Induced Instabilities*. Cambridge University Press.

- POON, E. K. W., OOI, A. S., GIACOBELLO, M., IACCARINO, G. & CHUNG, D. 2014 Flow past a transversely rotating sphere at Reynolds numbers above the laminar regime. *J. Fluid Mech.* **759**, 751–781.
- PREGNATALO, C. J. 2003 Flow-induced vibrations of a tethered sphere. PhD thesis, Monash University.
- RAO, A., PASSAGGIA, P.-Y., BOLNOT, H., THOMPSON, M., LEWEKE, T. & HOURIGAN, K. 2012 Transition to chaos in the wake of a rolling sphere. *J. Fluid Mech.* **695**, 135–148.
- SAKAMOTO, H. & HANIU, H. 1990 A study on vortex shedding from spheres in a uniform flow. *J. Fluids Engng* **112** (4), 386–392.
- SAREEN, A., ZHAO, J., LO JACONO, D., SHERIDAN, J., HOURIGAN, K. & THOMPSON, M. C. 2016 Flow past a transversely rotating sphere. In *Proceedings of the 11th International Conference on Flow-Induced Vibration and Noise, The Hague, The Netherlands, 4–6 July 2016*. The Netherlands Organisation for Applied Scientific Research.
- SARPKAYA, T. 2004 A critical review of the intrinsic nature of vortex-induced vibrations. *J. Fluids Struct.* **19** (4), 389–447.
- SEYED-AGHAZADEH, B. & MODARRES-SADEGHI, Y. 2015 An experimental investigation of vortex-induced vibration of a rotating circular cylinder in the crossflow direction. *Phys. Fluids* **27** (6), 067101.
- THOMPSON, M. C., LEWEKE, T. & PROVANSAL, M. 2001 Kinematics and dynamics of sphere wake transition. *J. Fluids Struct.* **15** (3), 575–585.
- TOMBOULIDES, A., ORSZAG, S. & KARNIADAKIS, G. 1993 Direct and large-eddy simulations of axisymmetric wakes. In *31st Aerospace Sciences Meeting*, p. 546. AIAA.
- WILLIAMSON, C. H. K. & GOVARDHAN, R. 1997 Dynamics and forcing of a tethered sphere in a fluid flow. *J. Fluids Struct.* **11**, 293–305.
- WILLIAMSON, C. H. K. & GOVARDHAN, R. 2004 Vortex-induced vibrations. *Annu. Rev. Fluid Mech.* **36** (1), 413–455.
- WONG, K. W. L., ZHAO, J., LO JACONO, D., THOMPSON, M. C. & SHERIDAN, J. 2017 Experimental investigation of flow-induced vibration of a rotating circular cylinder. *J. Fluid Mech.* **829**, 486–511.
- ZHAO, J., LEONTINI, J. S., LO JACONO, D. & SHERIDAN, J. 2014a Chaotic vortex induced vibrations. *Phys. Fluids* **26** (12), 121702.
- ZHAO, J., LEONTINI, J. S., LO JACONO, D. & SHERIDAN, J. 2014b Fluid–structure interaction of a square cylinder at different angles of attack. *J. Fluid Mech.* **747**, 688–721.





## Chapter 6

# Effect of free surface on the flow-induced vibrations of a sphere

*Try not to become a man of success,  
but rather try to become a man of  
value*

---

Albert Einstein

### Overview of the chapter

In this chapter, the publication by the author entitled ‘Vortex-induced vibrations of a sphere close to a free surface’ published in the *Journal of Fluid Mechanics* (2018), vol **846**, pp. 1023-1058, has been reproduced with permission Cambridge University Press© 2018. In this paper, a comprehensive series of experiments and wake measurements have been performed to investigate the effect of proximity to a free surface on the VIV response of fully- and semi-submerged spheres. The response was studied over a wide range of reduced velocities,  $3 \leq U^* \leq 20$ , capturing the initial resonance band, and immersion ratios of  $0 \leq h^* \leq 1$  for the fully-submerged sphere and  $0 < h^* < -1$  for the semi-submerged sphere.

For a fully submerged sphere, the vibration amplitude decreased and the synchronisation region narrowed gradually with a decrease in the immersion ratio. Mode II occurred for progressively lower  $U^*$  values with decreasing  $h^*$ . In contrast, for the semi-submerged sphere, different dynamics was observed. Two regimes were identified, depending on the immersion ratio showing different characteristic responses. The amplitude response in regime II was characterised by two distinct peaks corresponding to mode I and mode II of the vibration response observed for a fully submerged sphere. The response was found to be relatively insensitive to the Froude number in the range tested,  $0.05 \leq Fr \leq 0.45$ , with the response curve shape unaffected, although increasing the Froude number did lead to a slight reduction in the peak amplitude. PIV wake measurements in the cross-plane  $1.5D$  downstream from the rear of the sphere revealed reduction in vorticity of the upper vortex of the longitudinal vortex pair that was closer to the free surface. For the piercing sphere case, only the lower vortex of the

## **Chapter 6. Effect of free surface on the flow-induced vibrations of a sphere**

---

pair was visible at  $1.5D$  downstream; it appears that the upper vortex was effectively lost through diffusion into the free surface.

# Vortex-induced vibrations of a sphere close to a free surface

A. Sareen<sup>1,†</sup>, J. Zhao<sup>1</sup>, J. Sheridan<sup>1</sup>, K. Hourigan<sup>1</sup> and M. C. Thompson<sup>1</sup>

<sup>1</sup>Fluids Laboratory for Aeronautical and Industrial Research (FLAIR), Department of Mechanical and Aerospace Engineering, Monash University, Melbourne, VIC 3800, Australia

(Received 14 November 2017; revised 7 February 2018; accepted 1 April 2018)

Results are presented from an experimental investigation into the effects of proximity to a free surface on vortex-induced vibration (VIV) experienced by fully and semi-submerged spheres that are free to oscillate in the cross-flow direction. The VIV response is studied over a wide range of reduced velocities:  $3 \leq U^* \leq 20$ , covering the mode I, mode II and mode III resonant response branches and corresponding to the Reynolds number range of  $5000 \lesssim Re \lesssim 30\,000$ . The normalised immersion depth of the sphere is varied in small increments over the range  $0 \leq h^* \leq 1$  for the fully submerged case and  $0 \leq h^* \leq -0.75$  for the semi-submerged case. It is found that for a fully submerged sphere, the vibration amplitude decreases monotonically and gradually as the immersion ratio is decreased progressively, with a greater influence on the mode II and III parts of the response curve. The synchronisation regime becomes narrower as  $h^*$  is decreased, with the peak saturation amplitude occurring at progressively lower reduced velocities. The peak response amplitude decreases almost linearly over the range of  $0.5 \leq h^* \leq 0.185$ , beyond which the peak response starts increasing almost linearly. The trends in the total phase,  $\phi_{total}$ , and the vortex phase,  $\phi_{vortex}$ , reveal that the mode II response occurs for progressively lower  $U^*$  values with decreasing  $h^*$ . On the other hand, when the sphere pierces the free surface, there are two regimes with different characteristic responses. In regime I ( $-0.5 < h^* < 0$ ), the synchronisation region widens and the vibration amplitude increases, surprisingly becoming even higher than for the fully submerged case in some cases, as  $h^*$  decreases. However, in regime II ( $-0.5 \leq h^* \leq -0.75$ ), the vibration amplitude decreases with a decrease in  $h^*$ , showing a very sharp reduction beyond  $h^* < -0.65$ . The response in regime II is characterised by two distinct peaks in the amplitude response curve. Careful analysis of the force data and phase information reveals that the two peaks correspond to modes I and II seen for the fully submerged vibration response. This two-peak behaviour is different to the classic VIV response of a sphere under one degree of freedom (1-DOF). The response was found to be insensitive to the Froude number ( $Fr = U/\sqrt{gD}$ , where  $U$  is the free-stream velocity,  $D$  is the sphere diameter and  $g$  is the acceleration due to gravity) in the current range of  $0.05 \leq Fr \leq 0.45$ , although higher Froude numbers resulted in slightly lower peak response amplitudes. The wake measurements in the cross-plane  $1.5D$  downstream of the rear of the sphere reveal a reduction in the vorticity of the upper vortex of the trailing vortex pair, presumably through diffusion of vorticity into the free surface. For the piercing sphere case, the near-surface vorticity completely diffuses into the free surface, with only the opposite-signed vortex visible in the cross-plane at this downstream position. Interestingly, this correlates with an even higher oscillation

<sup>†</sup> Email address for correspondence: [anchal.sareen@monash.edu](mailto:anchal.sareen@monash.edu)

1024 A. Sareen, J. Zhao, J. Sheridan, K. Hourigan and M. C. Thompson

amplitude than the fully submerged case. Finally, the effects of immersion ratio and diameter ratio ( $D^*$  = sphere diameter/support-rod diameter) are quantified, showing care needs to be taken with these factors to avoid unduly influencing VIV predictions.

**Key words:** flow–structure interactions, vortex shedding, wakes

## 1. Introduction

Flow past a sphere in close proximity to a free surface, or piercing it, has a number of potential practical applications, such as offshore structures, underwater vessels, buoys, submarines and especially power generation equipment using wave and tidal energy. Most floating ocean structures for offshore petroleum drilling and production operations also consist of submerged and semi-submerged structures. Despite such practical applications, the flow past a sphere close to a free surface, and also piercing it, is not well understood. Many studies have reported on the two-dimensional counterpart, the cylinder, elaborating on the effect of a free surface on the flow past that geometry. Reichl, Hourigan & Thompson (2005) studied the two-dimensional flow past a cylinder close to a free surface at  $Re = 180$ . Their major finding was that for low Froude number ( $Fr \leq 0.3$ ), where the surface deformation is minimal, the flow is largely governed by geometric constraints and behaves similarly to the flow past a cylinder close to a no-slip wall. However, for higher Froude numbers, where surface deformation becomes substantial, there is significant surface vorticity generation that can diffuse or convect into the main flow, altering the development of vortex shedding. The flow in such cases is characterised by two metastable states, which can coexist for the same system parameters. Such metastable states were previously observed in the experimental investigations by Sheridan, Lin & Rockwell (1995) and Sheridan, Lin & Rockwell (1997). The latter authors investigated experimentally the flow past a cylinder close to a free surface over the Froude number range of  $0.47 \leq Fr \leq 0.72$  and Reynolds number range  $5990 \leq Re \leq 9120$ . They reported that the flow past a cylinder close to a free surface at high Froude number gives rise to fundamental classes of near-wake structures that are distinctly different from the wake of a completely submerged cylinder located far beneath the free surface. Considering the limiting case of a piercing cylinder, Yu, Avital & Williams (2008) studied the flow past a cylinder piercing the free surface numerically for  $Re = 1 \times 10^5$  at Froude numbers up to  $Fr = 3$ . Their results showed that the free surface inhibits the vortex generation in the near wake, leading to reduced vorticity and vortex shedding. For  $Fr = 0.8$ , the vortex structures exhibited strong three-dimensional (3-D) features; however, the flow in the deep wake remained two-dimensional. Furthermore, at  $Fr = 2$ , the free-surface effect propagated throughout the wake, inhibiting regular vortex shedding past the cylinder. Similar results were observed numerically by Inoue, Baba & Himeno (1993) and Kawamura *et al.* (2002) for a piercing cylinder. The latter study reported a diverging Kelvin wave system at the free surface and observed surface fluctuations related to the shear-layer instabilities under the free surface. From all these studies, it can be inferred for a cylinder that the free surface acts like a rigid free-slip boundary for low Froude numbers of  $Fr \leq 0.5$ . For  $0.8 \leq Fr < 2$ , the free surface influences the shedding near the free surface, leading to 3-D features very close to the free surface; however, for very high Froude numbers of  $Fr \geq 2$ , the free surface was significantly deformed; there were then strong wave–wake interactions, and the periodic vortex shedding was suppressed for cylinder depths less than one diameter from the free surface.

Although the above-mentioned studies focused on fixed cylinders, significant attenuation and alteration of the vortex shedding can be expected for an elastically mounted cylinder. A very recent study by de Oliveira Barbosa *et al.* (2017) reported the effect of proximity to a solid wall boundary on the vortex-induced vibration (VIV) response of a freely vibrating cylinder. They observed a reduction in the amplitude response for gaps between 0.75 and 2 diameters and an increase in the amplitude and frequency of oscillations for gaps smaller than 0.75 diameters, when the cylinder actually impacted the boundary.

Unlike the situation for circular cylinder VIV, there are relatively few previous studies on VIV of even a fully submerged tethered sphere (Govardhan & Williamson 1997; Williamson & Govardhan 1997; Jauvtis, Govardhan & Williamson 2001; Pregalato 2003; Govardhan & Williamson 2005; van Hout, Krakovich & Gottlieb 2010; Behara, Borazjani & Sotiropoulos 2011; Krakovich, Eshbal & van Hout 2013; Lee, Hourigan & Thompson 2013; Behara & Sotiropoulos 2016). Williamson & Govardhan (1997), Govardhan & Williamson (1997) and Jauvtis *et al.* (2001) reported the existence of multiple modes of vibrations in a free stream, namely modes I, II and III. Modes I and II, which occur over a reduced velocity range of  $U^* \sim 5\text{--}10$ , are the fundamental modes of vibrations that are associated with the lock-in of the vortex-shedding frequency with the system natural frequency, similar to the 2S and 2P modes for an excited circular cylinder. Mode III occurs over a wide range at higher reduced velocities  $U^* \sim 20\text{--}40$ , where the vortex-shedding frequency is much higher than the vibration frequency. This state leads to remarkably regular vibrations with a vibration period corresponding to three to eight vortex-shedding periods. This robust mode does not have any apparent counterpart in VIV of a circular cylinder. This was later categorised as a 'movement-induced vibration' by Govardhan & Williamson (2005). Van Hout *et al.* (2010) and Lee *et al.* (2013) also observed several regimes of vibrations for a heavy tethered sphere and a neutrally buoyant tethered sphere, respectively. The former reported a response region III, which was linked to the mode III state reported by Jauvtis *et al.* (2001), and the latter reported a chaotic regime VI, which was linked to mode IV reported by Jauvtis *et al.* (2001). Both these studies reported these modes to exhibit non-stationary chaotic dynamics, where large variation in amplitude is observed. This was also reported by an extensive experimental study by Sareen *et al.* (2018).

All the above-mentioned studies focused on a fully submerged sphere located well away from a boundary. However, when a sphere is elastically mounted close to a free surface, the dynamics could be very different. There is a very brief preliminary study by Mirauda, Plantamura & Malavasi (2014) on the dynamic response of a light ( $m^* = 1.34$ , where  $m^* = \text{total oscillating mass (m)}/\text{mass of the displaced fluid (}m_d\text{)}$ ) tethered sphere in a shallow water flow. Although their study lacked any forces or vorticity measurements to support their claims, they indicated a reduction in the vibration response amplitude with the presence of a free surface. However, the main limitation of the study was that there were large variations in the blockage ratio with the immersion depth in their experimental set-up. Also, there were appreciable wall effects, as the sphere was placed close to the channel floor (3 mm from the channel wall), which were neglected. There appears to be no study so far investigating the VIV response of a semi-submerged sphere that pierces the free surface. It is still unknown if the case of a semi-submerged sphere, which is quite ubiquitous in ocean engineering, oscillates more vigorously than a fully submerged sphere or if the vibrations are greatly reduced due to the free surface. These questions remain unanswered. The current study systematically documents the effect on the VIV response of a free surface, for fully and semi-submerged spheres.

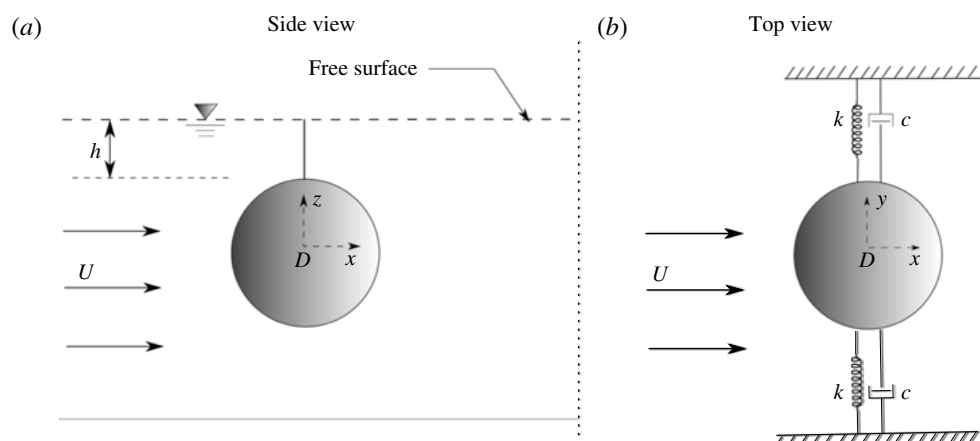


FIGURE 1. Schematic showing an overview of the experimental arrangement and definition of the geometric and flow parameters: (a) side view and (b) top view. Here,  $D$  is the sphere diameter,  $U$  is the free-stream velocity,  $k$  is the spring constant of the system and  $c$  is the structural damping;  $h$  is the distance measured from the top of the sphere to the free surface.

For these experiments, the sphere is elastically mounted in the transverse direction to the oncoming flow, where the principal VIV vibrations are observed. The VIV response is investigated experimentally over a wide range of reduced velocities and submergence depths, employing comprehensive displacement, force and vorticity measurements. To further understand the flow dynamics, various flow visualisation techniques are also employed.

In the present study, the following questions are addressed. Does the proximity to the free surface attenuate the vibrations of a sphere? What happens to the different modes of vibrations? Does the proximity to the free surface change the wake structure of the sphere? What happens in the limiting case of a piercing sphere? Does it still vibrate with analogues of the characteristic modes seen for fully submerged spheres?

The experimental method used in the current study is detailed in §2, and a validation study based on VIV of a non-rotating oscillating sphere is given in §3. In §4, the effect of a free surface on the VIV response of a fully submerged sphere is discussed. Following this, §5 focuses on the VIV response of a semi-submerged sphere piercing the free surface, §6 focuses on the effect of the support rod. In §7, the vorticity measurements are presented and discussed, supported by flow visualisations. Finally §8 draws together conclusions, summarising important findings and the significance of the current study.

## 2. Experimental details

### 2.1. Fluid–structure system

Figure 1 presents a brief schematic of the current fluid–structure interaction problem showing an overview of the experimental arrangement together with definitions of the important geometric and flow parameters. The sphere is elastically mounted in the direction transverse to the oncoming flow. The distance from the free surface is varied in terms of the parameter  $h^* = h/D$  – the immersion ratio – where  $h$  is the distance measured from the top of the sphere surface to the undisturbed free surface directly above and  $D$  is the sphere diameter.

|                            |             |                         |
|----------------------------|-------------|-------------------------|
| Amplitude ratio            | $A_{rms}^*$ | $\sqrt{2}A_{rms}/D$     |
| Damping ratio              | $\zeta$     | $c/2\sqrt{k(m+m_A)}$    |
| Diameter ratio             | $D^*$       | $D/D_r$                 |
| Frequency ratio            | $f^*$       | $f/f_{nw}$              |
| Froude number              | $Fr$        | $U/\sqrt{gD}$           |
| Mass ratio                 | $m^*$       | $m/m_d$                 |
| Mass-damping parameter     | $\xi$       | $(m^* + C_A)\zeta$      |
| Immersion ratio            | $h^*$       | $h/D$                   |
| Reduced velocity           | $U^*$       | $U/(f_{nw}D)$           |
| Reynolds number            | $Re$        | $UD/\nu$                |
| Scaled normalised velocity | $U_S^*$     | $(U^*/f^*)S = f_{vo}/f$ |
| Scruton number             | $Sc$        | $2m\zeta/\rho D^2$      |
| Strouhal number            | $S$         | $f_{vo}D/U$             |

TABLE 1. Non-dimensional parameters used in this study. In the above parameters,  $A_{rms}$  is defined as the root mean square of the structural vibration amplitude in the  $y$  direction.  $D$  is sphere diameter;  $D_r$  is the support-rod diameter,  $f$  is the body oscillation frequency and  $f_{nw}$  is the natural frequency of the system in quiescent water;  $m$  is the total oscillating mass,  $c$  is the structural-damping factor and  $k$  is the spring constant;  $U$  is the free-stream velocity, and  $\nu$  is the kinematic viscosity;  $m_A$  denotes the added mass, defined by  $m_A = C_A m_d$ , where  $m_d$  is the mass of the displaced fluid and  $C_A$  is the added-mass coefficient (0.5 for a sphere);  $f_{vo}$  is the vortex-shedding frequency of a fixed body.

Table 1 shows the set of non-dimensional parameters relevant for the current study. In problems involving flow-induced vibrations (FIV) of bluff bodies, the response dynamics of the system is often characterised by the normalised vibration amplitude ( $A^*$ ) and frequency response ( $f^*$ ) versus reduced velocity. In the current study, the normalised amplitude response is defined as  $A^* = \sqrt{2}A_{rms}/D$ , where  $A_{rms}$  is the root mean square (r.m.s.) of the oscillation amplitude of the body. The reduced velocity is defined as  $U^* = U/f_{nw}D$ , where  $U$  is the free-stream velocity and  $f_{nw}$  is the natural frequency of the system in quiescent water. Another important parameter in the current fluid–structure system is the mass ratio defined as  $m^* = m/m_d$ , where  $m$  is the total oscillating mass of the system, and  $m_d$  is the displaced fluid mass ( $m_d = \rho\pi D^3/6$  with  $\rho$  being the fluid density).

The governing equation for motion characterising cross-flow VIV of a sphere can be written as

$$m\ddot{y} + c\dot{y} + ky = F_y, \quad (2.1)$$

where  $F_y$  represents fluid force in the transverse direction,  $m$  is the total oscillating mass of the system,  $c$  is the structural damping of the system,  $k$  is the spring constant and  $y$  is the displacement in the transverse direction. Using the above equation, the fluid force acting on the sphere can be calculated from the directly measured displacement, and its time derivatives.

As a first approximation, it is often assumed that  $y(t)$  and  $F_y(t)$  are both approximately sinusoidal and can be represented by

$$y(t) = A \sin(2\pi ft), \quad (2.2)$$

$$F_y(t) = F_o \sin(2\pi ft + \phi), \quad (2.3)$$

where  $A$  is the displacement amplitude,  $F_o$  is the amplitude of  $F_y$  and  $\phi$  is the phase between the fluid force and the body displacement.



1028 A. Sareen, J. Zhao, J. Sheridan, K. Hourigan and M. C. Thompson

As done for VIV of spheres and cylinders by Govardhan & Williamson (2000), the total transverse fluid force ( $F_y$ ) can be split into a potential force  $F_{potential}$  (comprising the potential added-mass force) and a vortex force  $F_{vortex}$  that is due to the vorticity dynamics. From potential theory, the instantaneous  $F_{potential}$  acting on the sphere can be expressed as

$$F_{potential}(t) = -C_A m_d \ddot{y}(t), \quad (2.4)$$

with  $C_A$  the potential added-mass coefficient ( $C_A = 0.5$  for a sphere). Thus, the vortex force  $F_{vortex}$  can be computed from

$$F_{vortex} = F_y - F_{potential}. \quad (2.5)$$

The vortex phase is the phase difference between the vortex force and the body displacement and the total phase  $\phi_{total}$  is the phase difference between the total force and the body displacement. In general, phase jumps are associated with a switch from one VIV mode to another, and have even been used to distinguish between different modes (Govardhan & Williamson 2005). The instantaneous relative phases between the two forces are calculated using the Hilbert transform (e.g. see Khalak & Williamson 1999). For the piercing sphere cases, the potential force is calculated considering the fraction of the sphere that is submerged and assuming that the added-mass coefficient remains the same.

## 2.2. Experimental details

The experiments were conducted in the recirculating free-surface water channel of the Fluids Laboratory for Aeronautical and Industrial Research (FLAIR), Monash University, Australia. The test section of the water channel has dimensions of 600 mm in width, 800 mm in depth and 4000 mm in length. The free-stream velocity in the present experiments could be varied continuously over the range  $0.05 \leq U \leq 0.45 \text{ ms}^{-1}$ . The free-stream turbulence level was less than 1 % in the current experiments.

The current hydro-elastic problem was modelled using a low-friction air-bearing system that provided a very low structural damping and almost frictionless motion of the sphere in the transverse direction to the oncoming flow. The structural stiffness was controlled by extension springs that were attached to both sides of a slider carriage. Further details of the hydro-elastic facility can be found in Zhao *et al.* (2014a,b).

A detailed schematic of the experimental set-up is presented in figure 2, showing important components of the set-up. The sphere models used in the present study were solid spherical balls precision-machined from acrylic plastic with a very smooth surface finish. The accuracy of the diameter was within  $\pm 200 \text{ } \mu\text{m}$ . Different spheres with sizes of  $D = 40 \text{ mm}$ ,  $D = 80 \text{ mm}$  and  $120 \text{ mm}$  were used in the current experiments. The spherical models were supported using a thin cylindrical support rod 3 mm in diameter, manufactured from hardened nitrided stainless steel for extra stiffness and to maintain straightness.

The body displacement was measured using a linear encoder (model: RGH24, Renishaw, UK) with a resolution of  $1 \text{ } \mu\text{m}$ . Since the linear encoder was digital, electromagnetic noise did not affect the accuracy of the displacement signal measurement. This provided highly accurate displacement signals and allowed reliable velocity and acceleration signals to be derived. This enabled an accurate determination of the lift force signal to be derived from the displacement signal

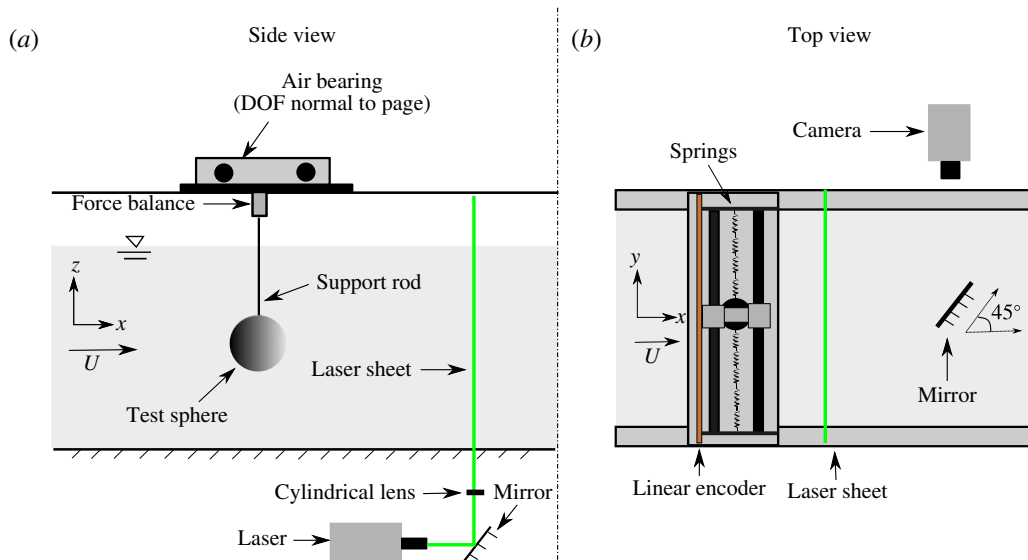


FIGURE 2. (Colour online) Experimental schematic (not to scale) showing an overview of the experimental arrangement.

using (2.1). In the experimental study by Sareen *et al.* (2018), the process was tested through a direct comparison against the lift force determined by a force sensor over a wide range of  $U^*$ . It was found that the lift force derived from the linear encoder displacement signal matched well with that measured using the force sensor, except that they were generally smoother, indicating accurate measurements of the displacement and the lift force. Zhao *et al.* (2014b) also reported such a comparison. Hence, all the force coefficients reported in the current study are derived from the measured displacement signal. It should be noted that the lift force obtained using the force sensor includes the inertial force associated with the acceleration of the mass below the force sensor (e.g. see Zhao *et al.* (2014b) and Sareen *et al.* (2018)). That term, which is derived by calculating the acceleration from the displacement signal, needs to be subtracted from the measured force to give the lift force. Hence the force sensor by itself does not enable the lift force to be measured directly. Also, the force measurements from the force sensor suffered from a greater degree of noise, presumably from electromagnetic sources; hence, the preference for the force derived from the displacement signal. Note here that this approach is appropriate only because highly accurate digital displacement measurements are possible with the current displacement encoder. Of course, one requires accurate measurements of the relevant parameters of the spring–mass system (total oscillating mass, spring constant and the structural damping).

The data acquisition and the controls of the flow velocity were automated via customised LabVIEW programs. For each data set, the displacement signal was acquired at a sampling frequency of 100 Hz for at least 100 vibration cycles.

The natural frequencies and structural damping of the system in both air and water were measured by conducting free decay tests individually in air and in quiescent water. Most of the experiments reported in this paper were performed for a mass ratio of  $m^* = 7.8$ . The structural damping ratio with consideration of the added mass was determined to be  $\zeta = 2.04 \times 10^{-3}$ . The Scruton number  $Sc$  (mass-damping parameter) for the current study was 0.00134.

1030 A. Sareen, J. Zhao, J. Sheridan, K. Hourigan and M. C. Thompson

To gain insight into the flow dynamics, velocity field measurements using particle image velocimetry (PIV) were undertaken in the cross-plane, 1.5 diameters downstream of the sphere. For this purpose, the flow was seeded with 13  $\mu\text{m}$  hollow micro-spheres having a specific weight of  $1.1 \text{ g m}^{-3}$ . A laser sheet of  $\sim 3 \text{ mm}$  thickness from a continuous laser (model: MLL-N-532-5W, CNI, China), aligned parallel to the  $y$ - $z$  plane, was employed to illuminate the laser plane. A mirror was placed at  $45^\circ$  angle to the free-stream direction towards the downstream side of the sphere. The mirror was placed more than six diameters away from the sphere. Imaging was performed using a high-speed camera (model: Dimax S4, PCO, AG) with a resolution of  $2016 \times 2016$  pixels<sup>2</sup>. This camera was equipped with a 105 mm Nikon lens, giving a magnification of approximately  $11.34 \text{ pixel mm}^{-1}$  for the field of view. Velocity fields were deduced using in-house PIV software developed originally by Fouras, Lo Jacono & Hourigan (2008), using  $32 \times 32$  pixel<sup>2</sup> interrogation windows in a grid layout with 50 % window overlap. All the vorticity fields shown in the current study were phase-averaged over more than 100 cycles. For each PIV measurement case, a set of 3100 image pairs were sampled at 10 Hz. Each image set was sorted into 24 phase bins based on the sphere's displacement and velocity, resulting in more than 120 image pairs for averaging at each phase.

In the present study, the VIV response was studied over a wide reduced velocity range of  $3 \leq U^* \leq 20$ . The immersion ratio was varied over a range of  $0 \leq h^* \leq 1$  for the first set of experiments, and  $-0.062 \leq h^* \leq -0.750$  for the next set of experiments with the piercing sphere. The Reynolds number for the current study varied between 5000 and 30 000.

### 3. VIV response of a fully submerged sphere: validation experiments

In this section, the VIV response of a fully submerged sphere is presented. For this set of experiments, the spherical model was 80 mm in diameter supported with a cylindrical support rod 3 mm in diameter. The immersed length of the support rod was one diameter (80 mm). The free decay tests were conducted individually in air and water to obtain the natural frequency in air,  $f_{na} = 0.2539$ , and in water,  $f_{nw} = 0.2455$ . The mass ratio was  $m^* = 7.8$  and the structural damping of the system was  $\zeta = 0.002$ . The response was studied for the  $U^*$  range of  $3 \leq U^* \leq 20$ , corresponding to a Reynolds number range of approximately  $5000 \leq Re \leq 30\,000$ . The signal was acquired at 100 Hz for approximately 170 cycles at each data point in this set of experiments.

In figure 3, the results from the current study are directly compared to the results reported by Govardhan & Williamson (2005) for a similar mass ratio of  $m^* = 7$ . The mass damping of the current study was  $(m^* + C_A)\zeta = 0.0169$ , compared to approximately 0.03 in their study. For comparison with their study here,  $A_{rms}^*$  is plotted against the scaled  $U_s^*$ , defined as  $U_s^* = (U^*/f^*)S \equiv f_{vo}/f$ , where  $S$  is the Strouhal number for the vortex shedding ( $\approx 0.18$  in this case).

As evident from the figure, the amplitude response of a sphere in the current study closely follows the trend reported by Govardhan & Williamson (2005). The vibrations lock in at  $U_s^* \approx 0.87$ , corresponding to a  $U^*$  value of 4.5, continuously progressing from mode I to mode II and reaching a peak saturation amplitude of 0.8 in both cases. Although, in the study by Govardhan & Williamson (2005), the response at this mass ratio is reported only until  $U_s^* = 2$ , the current study reveals that after the peak response in mode II, the amplitude response smoothly drops to a lower plateau that extends towards mode III as  $U_s^* \rightarrow 3$ . The vibrations in the 'plateau'

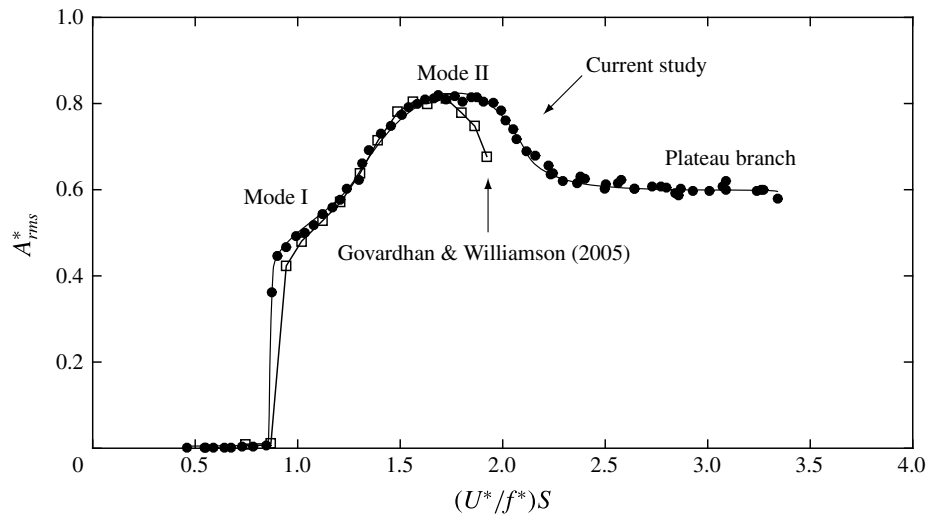


FIGURE 3. Amplitude response of a fully submerged sphere obtained in the current study compared to that reported by Govardhan & Williamson (2005). The mass damping in the current study is  $(m^* + C_A)\zeta = 0.0169$ , compared to approximately 0.03 in their study.

region exhibit slight differences to the highly periodic vibrations in mode II, even though the frequency of oscillation stays close to the natural frequency of the system over the entire  $U_s^*$  range examined in the current study.

Unlike the case of a tethered sphere with a very low mass ratio, where the two vibration modes are distinctly separated by a desynchronised region, there is no such separation between the two modes in 1-DOF hydro-elastic VIV and with higher mass ratio in this study. The transition between the modes is continuous and gradual with  $U^*$ , hence it is difficult to differentiate between the two modes by just looking at the amplitude response. The transition from one mode to the other is made clear through observations of the phase differences between the force and the sphere displacement signals for the two modes.

Figure 4 shows the variation of the total phase  $\phi_{total}$  (phase difference between the sphere displacement and the total transverse force) and the vortex phase  $\phi_{vortex}$  (phase difference between the sphere displacement and the vortex force) with  $U^*$ , correlated with the amplitude response. The results reported by (Govardhan & Williamson 2005) for a relatively higher mass ratio of  $m^* = 31.1$  are also shown for comparison. As is evident from the figure, the response in the current study undergoes a transition from mode I to mode II when  $\phi_{vortex}$  crosses through  $90^\circ$ , corresponding to the ‘inflection point’ in the amplitude response. Likewise, within the mode II regime,  $\phi_{total}$  passes continuously through  $90^\circ$ , corresponding to the peak of the amplitude response. Similar trends in the total and the vortex phases were also observed in the data reported by (Govardhan & Williamson 2005) for a higher mass ratio of  $m^* = 31.1$ .

In the current study, with the  $U^*$  range further extended beyond  $U^* = 14$ , a slight decrease in both the total phase,  $\phi_{total}$ , and the vortex phase,  $\phi_{vortex}$ , was observed as shown in the figure 4. Simultaneously a slight increase in the vibration amplitude is also evident in the figure. This corresponds to the ‘plateau branch’ mentioned above in figure 3 when  $(U^*/f^*)S \rightarrow 3$ . Jauvtis *et al.* (2001) reported the existence of another mode of vibration, mode III, for higher  $U^*$  values varying from 20 to 40 for a tethered

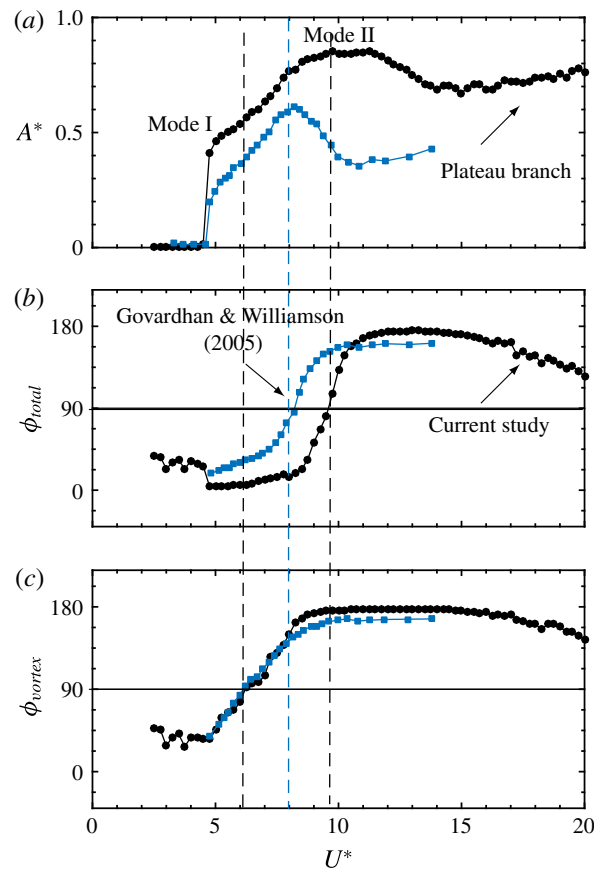


FIGURE 4. (Colour online) Variation of the total phase  $\phi_{total}$  (b) and vortex phase  $\phi_{vortex}$  (c) with  $U^*$ , correlated with the amplitude response (a). For comparison, the variations reported by Govardhan & Williamson (2005) are also presented (blue square symbols). The mass ratio of the current study is  $m^* = 7.8$  compared to 31.3 in their study.

sphere of mass,  $m^* = 80$  in wind tunnel experiments. Therefore, the vibrations in the ‘plateau branch’ can be considered to be approaching the mode III response of the sphere vibrations. A careful study of the wake in this region could shed more light on the subtle differences between the modes, which is somewhat difficult and complex to unravel for three-dimensional and chaotic flows like these. As pointed out by e.g. Govardhan & Williamson (2005), the scaled reduced velocity  $(U^*/f^*)S$  is a useful parameter to remove mass ratio effects on sphere VIV response, as it aligns the peaks of different data sets corresponding to different mass ratios. However, this scaling does not work for the current study for a sphere near or piercing a free surface, therefore, the sphere VIV response is presented as a function of  $U^*$  instead of  $(U^*/f^*)S$  in the remainder of the article.

#### 4. Effect of free surface on the VIV response of a fully submerged sphere

In this section, the effect of a free surface on the VIV response of a sphere is studied. The immersion ratio is sequentially varied from  $h^* = 1$  (fully submerged case) to  $h^* = 0$  (when the top of the sphere touches the free surface) in small increments. Note that a water-level controller is installed in the water channel to maintain a

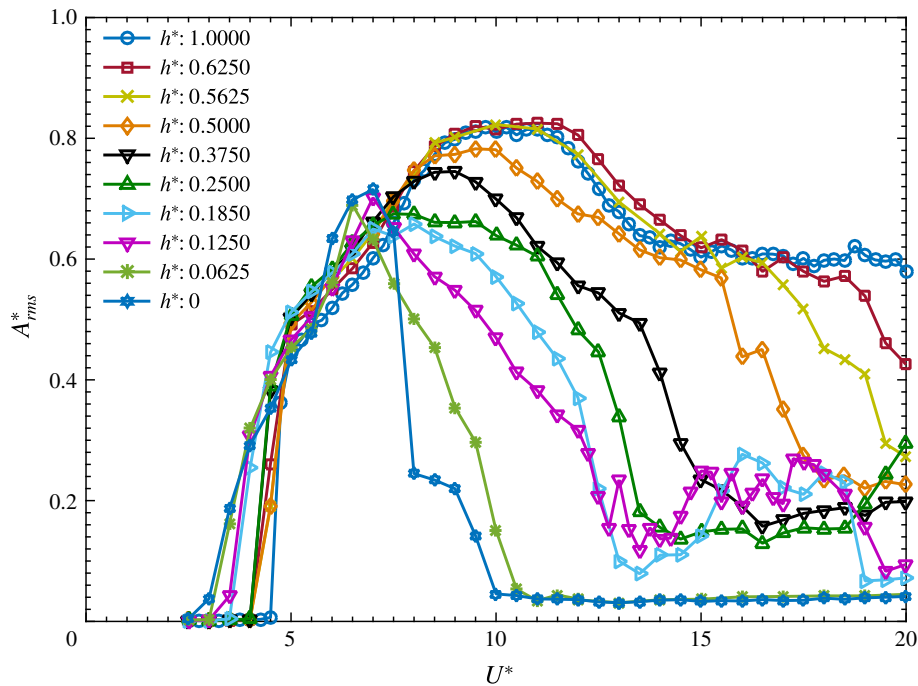


FIGURE 5. (Colour online) Variation of the amplitude response ( $A_{rms}^*$ ) with reduced velocity ( $U^*$ ) for various immersion ratios.

constant water level over time. In addition, during experiments the change in the water level was found to be less than  $\sim 1\%$  of the sphere diameter as the velocity was changed between the minimum and maximum values ( $0.05$  to  $0.45 \text{ ms}^{-1}$ ). Free decay tests in water were performed for each set of experiments to estimate  $f_{nw}$  for each case. The data were acquired generally at  $100 \text{ Hz}$  for  $120$  cycles, and for  $240$  cycles in some cases, where vibrations were not very periodic.

Figure 5 shows the variation of  $A_{rms}^*$  with  $U^*$  for various immersion ratios  $h^*$ . For  $h^* = 1$ , the response gradually progresses from mode I to mode II, approaching the plateau branch for higher  $U^*$  values ( $15 \leq U^* \leq 20$ ), as observed previously by Govardhan & Williamson (2005) and Sareen *et al.* (2018) for relatively higher mass ratios of  $m^* = 31.1$  and  $m^* = 14.2$ , respectively. At this  $h^*$ , the response is similar to the previously reported VIV responses, corroborating the negligible effect of the free surface at this submergence depth. However, when the immersion ratio was decreased to  $0.625$ , the response tapers off for  $U^* \geq 18$ . This drop becomes more prominent for  $h^* \leq 0.5$  cases, with the reduction observed for progressively smaller  $U^*$  values with decreasing  $h^*$ . It is evident that the vibration response for  $h^* \leq 0.625$  loses the ‘plateau branch’, which is typical of a fully submerged VIV response of a sphere. It can also be noticed from figure 5 that the vibrations lock in to the natural frequency at relatively lower  $U^*$  values with a decrease in  $h^*$ .

The vibrations remain fairly periodic in the synchronisation region for all immersion ratios. Figure 6 shows the time trace of the sphere vibrations for different  $U^*$  values at an immersion ratio of  $h^* = 0.25$ . For  $U^* = 6$  and  $12$  the vibrations are highly periodic, whereas for  $U^* = 15$  the vibrations are clearly non-periodic, and are characterised by sudden bursts of intermittent small vibrations. This behaviour was found to be true for all the other cases tested in this study. Consequently,  $A_{rms}^*$  may not be the best



1034 *A. Sareen, J. Zhao, J. Sheridan, K. Hourigan and M. C. Thompson*

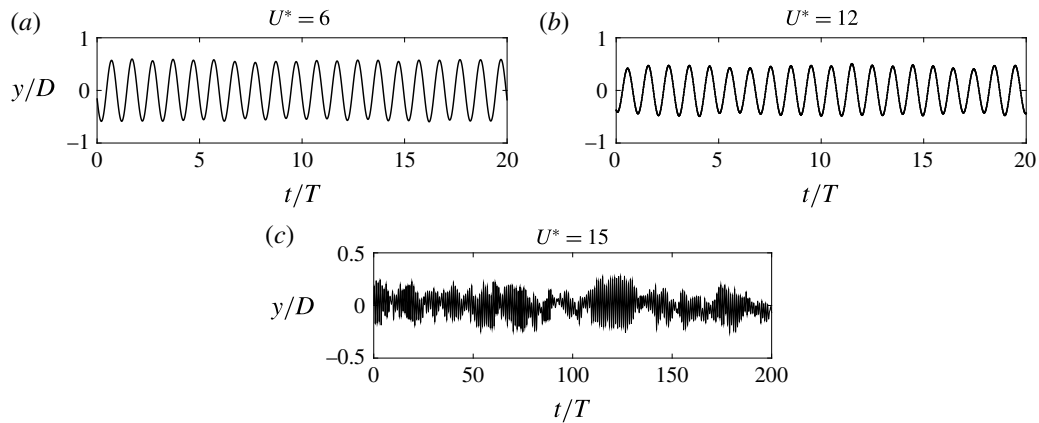


FIGURE 6. Variation of the displacement amplitude ( $y/D$ ) with dimensionless time ( $t/T$ ) for various  $U^*$  values at an immersion ratio of 0.25. Here,  $t$  is time and  $T$  is the oscillation period.

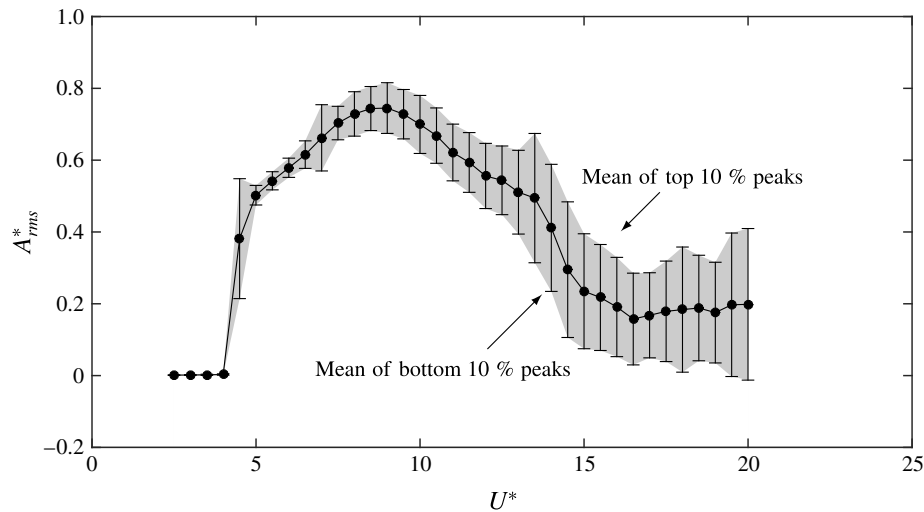


FIGURE 7. Amplitude response of a sphere for  $h^* = 0.375$ . Here, the shaded region is bounded by the mean of the top 10 % of peaks and the mean of the bottom 10 % of peaks, giving an indication of the periodicity/regularity of the signal.

representation of the response characteristics outside the synchronisation regime in this scenario, where small bursts of non-periodic vibrations are observed, as the estimated  $A_{rms}^*$  value may change substantially with the sampling time. In order to demonstrate the large variations in the amplitude, especially in this region, an alternative way of presenting VIV response is shown in figure 7, where the mean of top 10 % of the peaks and the mean of bottom 10 % of the peaks are also plotted. This also gives a good indication of the variation in the signal over the sampling time at each  $U^*$  value. This plot highlights the significant variations in the displacement amplitude for higher  $U^*$  values, and that the vibrations are much less periodic in the higher reduced velocity range. This type of response is a typical of all the  $h^*$  values investigated in the current study.

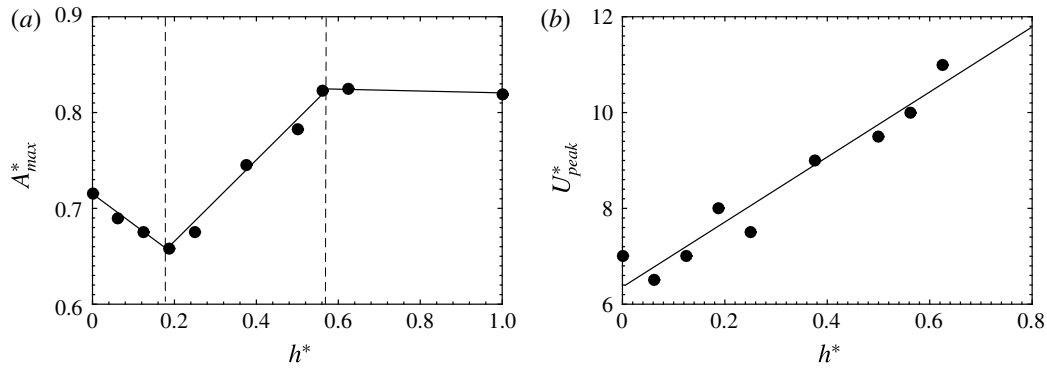


FIGURE 8. (a) Variation of the peak saturation amplitude  $A_{max}^*$  with  $h^*$ . (b) Variation of  $U_{peak}^*$  with  $h^*$ .

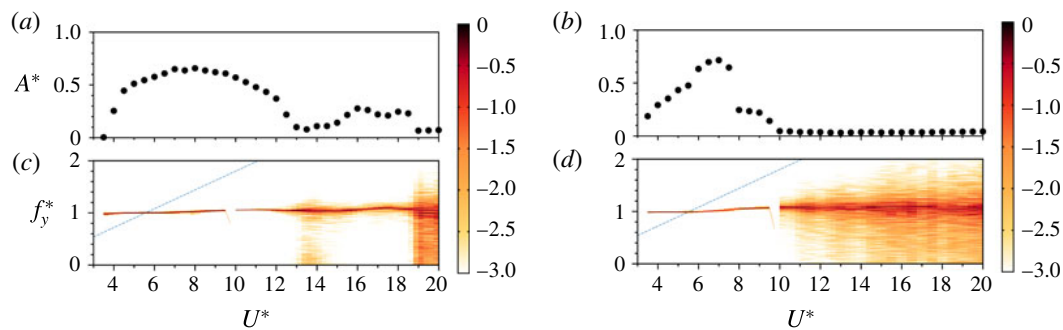


FIGURE 9. (Colour online) Frequency contour plots for  $h^* = 0.1875$  (c) and  $h^* = 0$  (d). The amplitude response curves correlated with the frequency contour plots are also shown in (a,b).

The synchronisation regime, the  $U^*$  range where large amplitude vibrations are observed, becomes narrower with decreasing  $h^*$ . The variation of the peak saturation amplitude,  $A_{max}$ , with  $h^*$  is shown in the figure 8. For  $0.5 \leq h^* \leq 1$ , the peak saturation amplitude remains almost constant; however, for  $0.185 \leq h^* \leq 0.5$ , there is a sharp linear decrease in  $A_{max}^*$  with decreasing  $h^*$ . Interestingly, when  $h^*$  is further decreased, a linear increase in the peak response amplitude is observed. In contrast, the  $U^*$  corresponding to  $A_{max}$ , which is denoted by  $U_{peak}^*$  in figure 8(b), decreases almost linearly with  $h^*$  in the range  $0 \leq h^* \leq 0.625$ .

Figure 9 shows logarithmic-scale power-spectrum plots depicting the dominant vibration frequency ( $f^* = f/f_{nw}$ ) as a function of  $U^*$  for two different immersion ratios. It is clear from the contour plots that the frequency stays close to the natural frequency (lock-in) for all  $U^*$  values. It can be observed that within the synchronisation regime the signal exhibits a clean frequency response with maximum power close to  $f_y^* = 1$ . However, a broader range of frequencies is observed outside the synchronisation regime, where small non-periodic vibrations are observed.

Figure 10 shows the variation of the r.m.s. of the transverse force coefficient,  $C_{y_{rms}}$ , with  $U^*$  for varying immersion ratios,  $h^*$ . As evident from the figure, there is a sudden jump in  $C_{y_{rms}}$  associated with the sudden increase in the amplitude response during lock-in, as shown in figure 5. The  $U^*$  corresponding to lock-in shifts to the left with



1036 A. Sareen, J. Zhao, J. Sheridan, K. Hourigan and M. C. Thompson

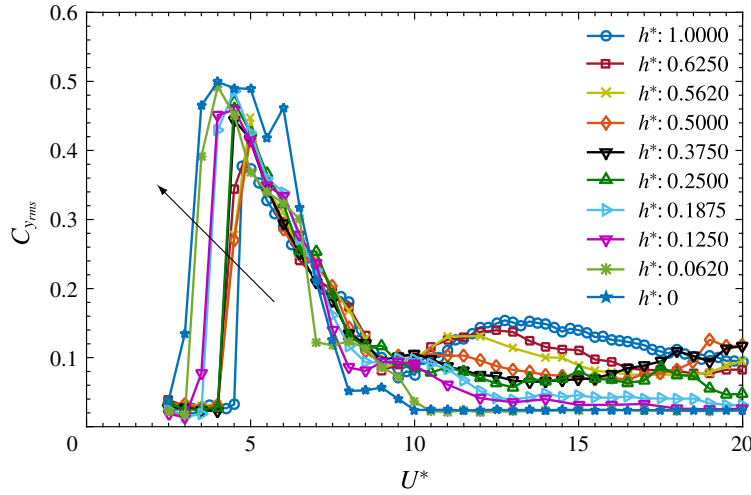


FIGURE 10. (Colour online) Variation of  $C_{y_{rms}}$  with  $U^*$  for varying immersion ratios  $h^*$ . The direction of the arrow shows the shift of the lock-in to smaller reduced velocities.

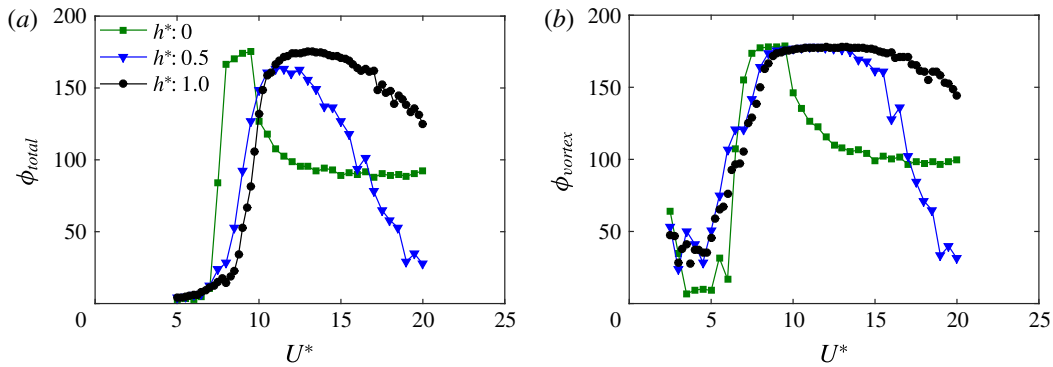


FIGURE 11. (Colour online) Variation of the total phase  $\phi_{total}$  (a) and vortex phase  $\phi_{vortex}$  (b) with  $U^*$ , for three different immersion ratios.

decreasing  $h^*$ , as indicated by the arrow in the figure. For higher  $U^*$  values of  $U^* \geq 10$ , there is a relatively larger influence of decreasing  $h^*$  in terms of decreasing the transverse fluctuating force acting on the sphere. Similar behaviour was observed for the displacement amplitudes as well, where the amplitudes were greatly influenced in the higher  $U^*$  range, as shown in figure 5. These observed behaviours of the transverse fluctuating force coefficient  $C_{y_{rms}}$  are consistent with the amplitude response.

Figure 11 shows the variation of the total phase  $\phi_{total}$  and the vortex phase  $\phi_{vortex}$  with  $U^*$  for three different immersion ratios. For  $h^* = 1$ ,  $\phi_{vortex}$  gradually increases from  $\approx 20^\circ$  to  $\approx 170^\circ$  as the sphere response continuously progresses from mode I to mode II; however,  $\phi_{total}$  only starts increasing when the response has reached the peak saturation value. This is consistent with the previously reported trends for the phases by Govardhan & Williamson (2005) and Sareen *et al.* (2018). For  $h^* = 0.5$ , both  $\phi_{total}$  and  $\phi_{vortex}$  start reducing at higher  $U^*$  values, unlike the  $h^* = 0$  case, where both phases settle down at  $\approx 90^\circ$  for higher  $U^*$  values. Another interesting point to note here is that  $\phi_{total}$  starts rising at progressively lower  $U^*$  values for decreasing  $h^*$ . This is consistent

with the linear decrease of  $U_{peak}^*$  with  $U^*$ , as discussed above in figure 8. It can be concluded here that the mode II response occurs for progressively lower  $U^*$  values with decreasing  $h^*$ .

It follows that in the parameter space studied here, as the sphere comes closer to the free surface, the transverse fluctuating force acting on the sphere decreases with a greater influence in the higher  $U^*$  range. Consequently, there is a consistent decrease in the displacement amplitude response of the sphere. For the cases where highly reduced vibrations were observed, the response was less periodic, characterised by sudden bursts of small vibrations with larger variations in amplitudes. The location of the peak saturation amplitude progressively shifts to the left with decreasing  $h^*$ , with the amplitude initially decreasing linearly but with a sudden linear increase beyond  $h^* \lesssim 0.2$ .

The response was also studied for cases where the sphere pierces the free surface. Interestingly, the dynamics are quite different. The results are discussed in detail in the following section.

## 5. VIV of a semi-submerged sphere

This section focuses on the VIV response of a semi-submerged sphere piercing the free surface. The immersion depth ratio,  $h^*$ , of the sphere was varied in small increments between 0 and  $-0.75$ , where  $h^* = 0$  denotes the case when the free surface just touches the top of the sphere. The response was studied for the reduced velocity range of  $2.5 \leq U^* \leq 20$  for all the immersion ratios. Each data point was acquired at an acquisition rate of 100 Hz, for more than  $\sim 200$  cycles for the highly periodic oscillations (at lower  $U^*$  values) and  $\sim 400$  cycles for the non-periodic vibrations (at higher  $U^*$  values).

### 5.1. Vibration response measurements

The response of a semi-submerged sphere can be divided into two regimes, one with  $0 < h^* < -0.5$ , and the other with  $-0.5 \leq h^* \leq -0.75$ , due to distinct differences in the response characteristics. Figure 12 shows the variation of  $A_{rms}^*$  with  $U^*$  for various  $h^*$  values for both these regimes. In regime I, as  $h^*$  is decreased from  $-0.062$  to  $-0.375$ , the displacement amplitude progressively increases and the synchronisation region sequentially widens.

In contrast to regime I, the displacement amplitude in regime II decreases with a decrease in  $h^*$ , as can be observed in figure 12(b). The amplitude response for  $-0.5 < h^* \leq -0.75$  is characterised by two peaks, unlike regime I, where only one peak is evident for the  $U^*$  range tested. As observed from the figure, the drop in amplitude is dramatic between  $-0.650$  and  $-0.688$ , which was found to be repeatable in follow-up experiments. The amplitudes for  $h^* = -0.688$  and  $-0.750$  are highly reduced with a suppression of vibrations for  $U^* \geq 15$ .

Figure 12(c) shows the variation of the peak amplitude,  $A_{max}^*$ , with  $h^*$ . Intriguingly, for  $h^* = -0.250$ ,  $-0.375$  and  $-0.5$ , the amplitudes become even higher than the amplitude response of a fully submerged sphere (shown with dashed horizontal line). In these cases, the vibrations corresponding to the peak amplitude remain highly periodic; however, the periodicity decreases as the response decreases at higher  $U^*$  values, as also shown in the following discussion.

In figure 13, the time trace of the displacement signal is shown at selected  $U^*$  values for  $h^* = -0.062$  (regime I) and  $h^* = -0.750$  (regime II). As evident in regime I (left column), the vibrations are highly periodic for  $U^* = 6.2$ ; however, for

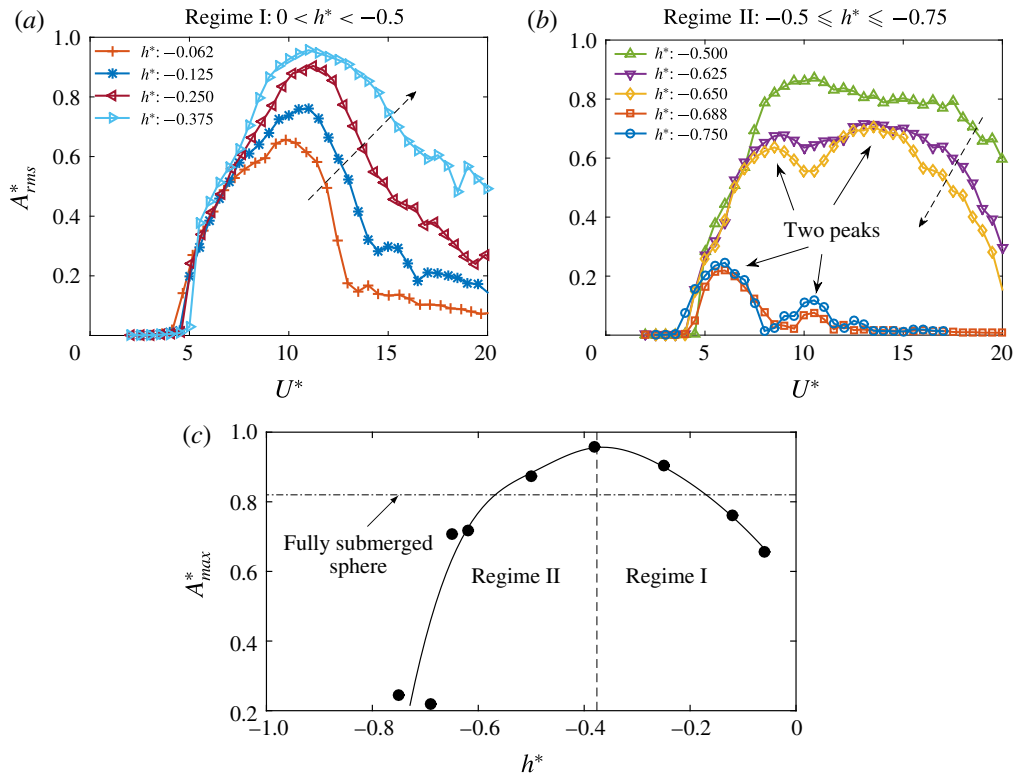


FIGURE 12. (Colour online) Amplitude response of a sphere piercing the free surface. (a) The amplitude response in regime I. (b) The amplitude response in regime II. (c) Variation of the peak amplitude,  $A^*_{max}$ , with  $h^*$ . The dashed arrow in (a,b) represents the direction of increasing  $h^*$  (in magnitude).

$U^* = 12.4$  in the decreasing amplitude branch of the response, the vibrations are of similar magnitude but the periodicity has decreased. For  $U^* = 17.1$ , the vibrations become highly non-periodic and consist of small amplitude intermittent vibrations. This behaviour was found to be typical of all other cases in regime I. In regime II on the other hand, the two peaks are separated by a transition region, where there is a sudden decrease in the amplitude; nevertheless, the vibrations are still locked in.

As evident in the frequency contours plots for these  $h^*$  values shown in figure 14, there are slight differences in the frequency spectrum as well in the two regimes. For  $h^* = -0.062$ , there is an increase in the frequency of vibration (albeit small) as the response progresses from the increasing  $A^*$  branch to the decreasing  $A^*$  branch extending towards a highly non-periodic vibration branch at higher  $U^*$ . On the contrary, for  $h^* = -0.750$ , the frequency remains constant over the entire range of  $U^*$ . The question arises, what causes two peaks in regime II? Insight into the transition between the vibration modes in this scenario can be gained through analysis of the force measurement data, as explained in detail in the following section.

## 5.2. Force measurements

For 1-DOF VIV, the transition between the principal modes of vibrations is continuous and gradual, unlike for the small mass ratio 2-DOF case. Hence, it is difficult to

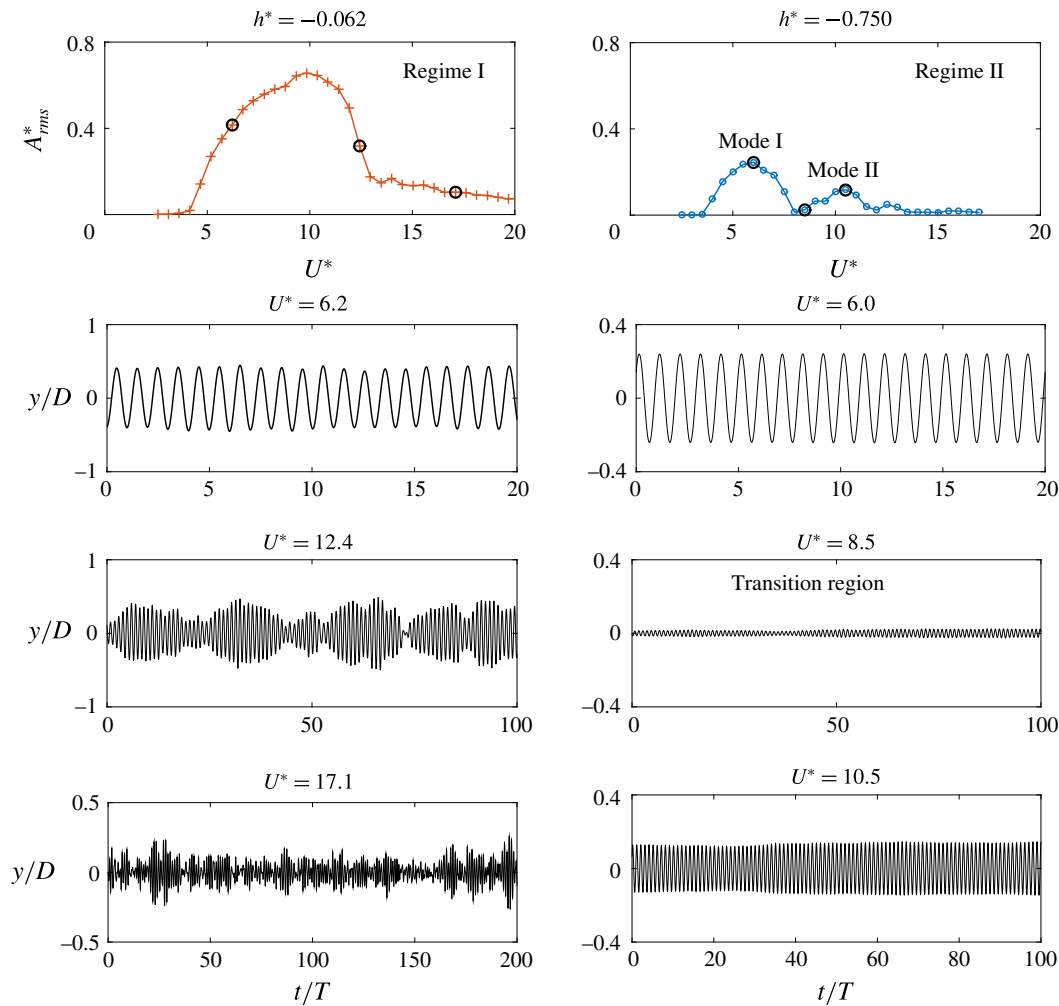


FIGURE 13. (Colour online) Variation of the displacement amplitude ( $y/D$ ) with non-dimensional time ( $t/T$ ) for various  $U^*$  values at an immersion ratio of  $h^* = -0.062$  (left) and  $h^* = -0.750$  (right). The corresponding amplitude response is shown at the top.

infer the existence of two modes and their existence boundaries from the amplitude response alone. A careful inspection of the force measurement data can provide insight into the mode transitions. Hence, the total transverse force coefficient,  $C_{ytotal}$ , and the vortex force coefficient,  $C_{vortex}$ , were derived from the displacement signal and its time derivatives. The total phase,  $\phi_{total}$ , and the vortex phase,  $\phi_{vortex}$ , were also computed to understand the mode transitions in both these regimes.

In figure 15, the variation of  $\phi_{total}$  and  $\phi_{vortex}$  with  $U^*$  is shown for three different  $h^*$  values in both the regimes. In regime I, both  $\phi_{total}$  and  $\phi_{vortex}$  increase from lower values to up to  $\sim 170^\circ$ , indicating the presence of mode I and II vibrations. In contrast,  $\phi_{vortex}$  in regime II jumps up to  $\sim 170^\circ$  during lock-in and remains constant over the entire  $U^*$  range. For  $h^* = -0.625$  and  $h^* = -0.500$ , where two peaks in the amplitude response were observed (see figure 12), the total phase crosses  $90^\circ$  twice, in line with the presence of two peaks in the amplitude response. However, it is difficult to infer

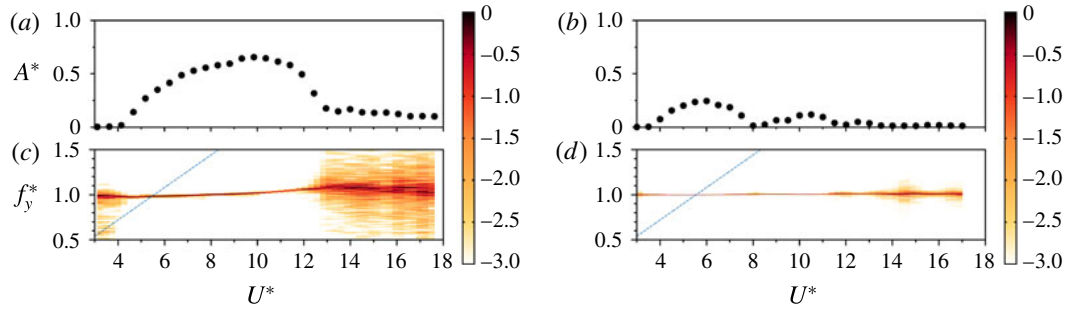
1040 *A. Sareen, J. Zhao, J. Sheridan, K. Hourigan and M. C. Thompson*


FIGURE 14. (Colour online) Variation of the frequency response (c,d) correlated with the amplitude response (a,b) for two different semi-submerged cases: (a,c)  $h^* = -0.062$ , with the sphere slightly piercing the surface; (b,d)  $h^* = -0.750$ , where only a small section of the sphere is submerged.

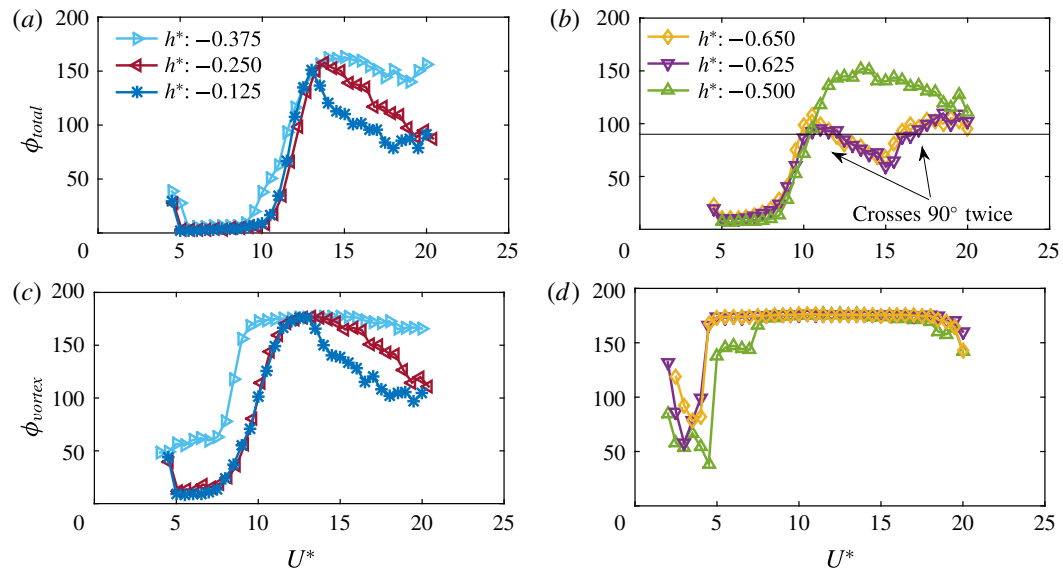


FIGURE 15. (Colour online) Variation of the total phase,  $\phi_{total}$ , (a,b) and the vortex phase,  $\phi_{vortex}$ , (c,d) for three different  $h^*$  values in regime I (a,c) and regime II (b,d).

from this what is the physical basis of the two peaks. A careful inspection of the  $C_{vortex}$  variation helps to make the picture clearer.

Figure 16 shows the variation of  $C_{vortex}$  for various immersion ratios for both the regimes. As evident in figure 16(a), the vortex force coefficient jumps up abruptly at the vibration lock-in, at approximately  $U^* \approx 5$  in these cases, and then starts decreasing. However, for  $U^* \approx 8-10$ ,  $C_{vortex}$  starts increasing again, indicating the transition to mode II of the vibration response. This trend was also observed by Govardhan & Williamson (2005) for the 1-DOF fully submerged sphere VIV case. The two peaks in the vortex force indicates these two vibration modes. On the other hand in regime II, it can be observed that the first peak is smaller than the second peak. Also, the transition from the first peak to the second occurs at lower  $U^*$  values compared to regime I for  $h^* = -0.625$  and  $-0.650$ . Beyond the transition,  $C_{vortex}$  gradually increases to a saturation value and then decreases to a lower value with

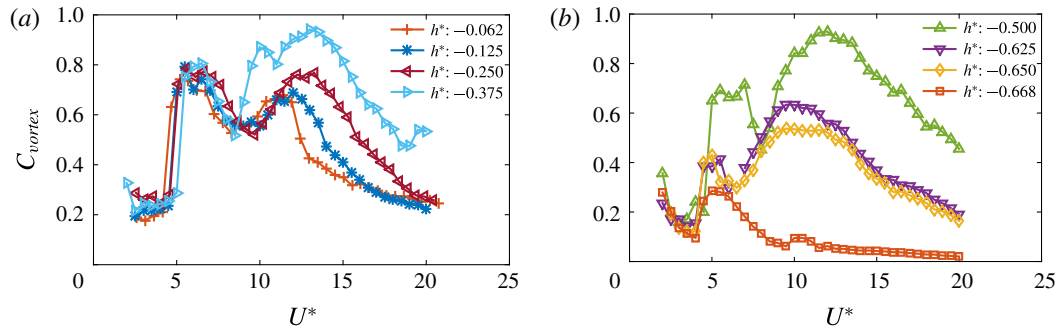


FIGURE 16. (Colour online) Variation of the vortex force coefficient ( $C_{vortex}$ ) with reduced velocity ( $U^*$ ) for various immersion ratios: (a) regime I; (b) regime II.

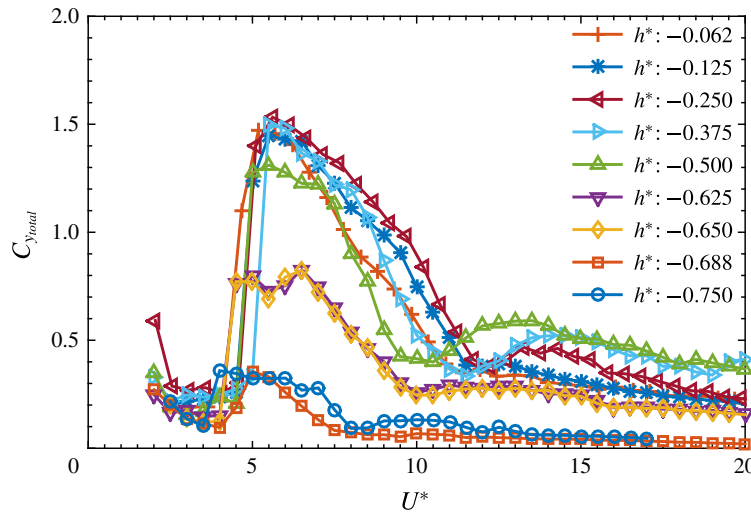


FIGURE 17. (Colour online) Variation of the total transverse force coefficient,  $C_{ytotal}$ , with  $U^*$  for varying immersion ratios  $h^*$ .

no other peak for all the cases in regime II. It can be conjectured here that there are only two fundamental modes of vibrations for all these cases and there is no mode III, at least within the  $U^*$  range studied. The two peaks in regime II indeed correspond to modes I and II.

Figure 17 shows the variation of the total transverse force coefficient,  $C_{ytotal}$ , with increasing  $U^*$  for various  $h^*$  values. The total force also follows a similar trend. However, it is not easy to demarcate the two modes and their transitions just by looking at this plot as there is no other peak evident (significantly bigger) for regime II for higher  $U^*$  values.

It is an interesting finding that although for a 1-DOF sphere VIV, there is no clear demarcation between the two modes for the fully submerged case, the VIV response of a semi-submerged sphere can show a transition region between the two where the amplitude drops, in line with the transition between the two vibration modes seen in low mass ratio tethered sphere studies.



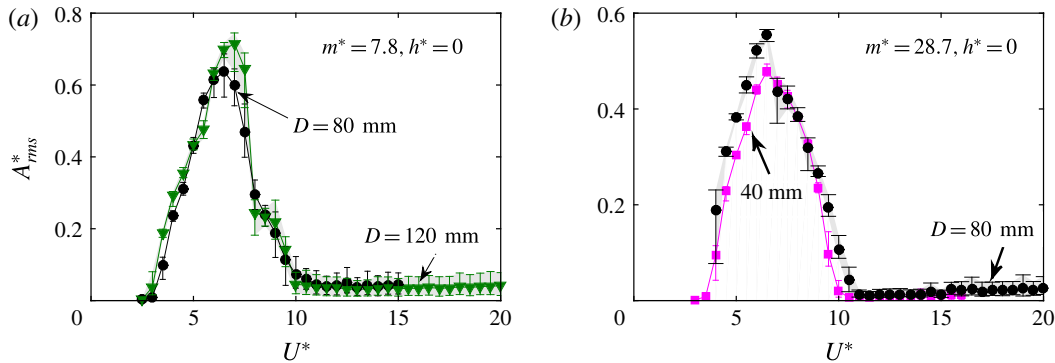


FIGURE 18. (Colour online) Effect of Froude number on the amplitude response curves for the case when the sphere is just touching the free surface. (a) Mass ratio  $m^* = 7.8$  for spheres of diameter 80 mm and 120 mm. (b) Mass ratio  $m^* = 28.7$  for spheres of diameter 40 mm and 80 mm. Note that the Froude number varies with reduced velocity as well as sphere diameter.

### 5.3. Effect of Froude number

The Froude number ( $Fr$ ) is an important parameter in problems involving proximity to a free surface. It is defined as the ratio of the inertial force to the gravitational force, and it quantifies the deformation at the free surface. In the current problem,  $Fr$  can be defined as  $Fr = U/\sqrt{gD}$  for a fixed  $h^*$  case.

In the current study, the Froude number is based on the sphere diameter, and  $Fr$  varies over the range of  $0.05 \leq Fr \leq 0.45$  for both scenarios: where the sphere is close to the free surface; and also where the sphere pierces the free surface. From previous studies with circular cylinders, it can be conjectured that in this range of Froude numbers, there will no large surface deformations at the free surface leading to any significant wave–wake interactions. Nevertheless, some tests were performed to check the sensitivity of the VIV response to a change in Froude number in this range.

The response was measured for three spheres of different sizes:  $D = 40, 80$  and  $120$  mm. Since changing the size of the sphere changes  $m^*$  due to change in the displaced fluid mass and the sphere mass, extra weights were placed on top of the air-bearing rig to maintain the same mass ratio, when possible. Figure 18(a) shows the response of a sphere of size 120 mm compared to that for a 80 mm sphere, for  $m^* = 7.8$  and  $h^* = 0$ . The Froude number range changed from  $0.06 \leq Fr \leq 0.45$  (for the 80 mm sphere) to  $0.03 \leq Fr \leq 0.2$  (for the 120 mm sphere); however, no significant change in the shape of the response curve was found. Note here that  $Fr$  scales with the  $U$  as well, so it increases with increasing  $U^*$ . Similarly, in figure 18(b), the response of a sphere of  $D = 40$  mm is shown compared to that for the 80 mm sphere, for  $m^* = 28.7$  and  $h^* = 0$ . The Froude number range in this case changed from  $0.06 \leq Fr \leq 0.45$  (for the 80 mm sphere) to  $0.11 \leq Fr \leq 0.6$  (for the 40 mm sphere); however, again no significant change in the response curve shape was seen. Despite this, these two figures do show a slight increase in peak amplitude as the diameter of the sphere is increased, or the Froude number is reduced. However, overall, it can be inferred that the VIV response is relatively insensitive to the Froude number in this Froude number range.

For a high Froude number range of  $Fr \geq 2$ , significant wave–wake interactions can be expected for the sphere. Of course, for a 3-D flow past a sphere at this higher

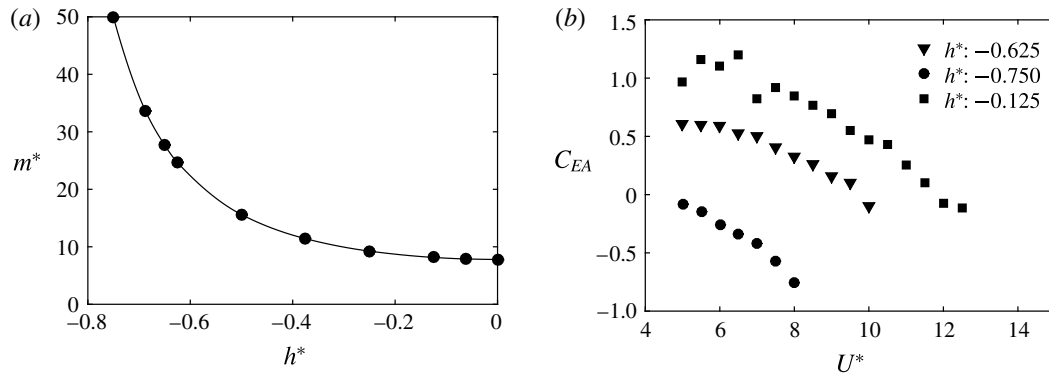


FIGURE 19. (a) Change in the mass ratio as the immersion ratio is varied for the semi-submerged sphere. (b) Variation in the effective added-mass coefficient at different immersion ratios as a function of the reduced velocity.

Reynolds number, capturing the time-varying surface deformations and their effect on the 3-D structures would be complicated and this remains open for future studies.

In summary, the current results are representative of the general problem of sphere VIV close to or piercing the free surface for a low  $Fr$  range.

### 5.3.1. Effect of mass ratio

Due to nature of the problem set-up, the displaced fluid mass changes with each immersion ratio for a semi-submerged sphere. This changes the mass ratio and the effective added-mass coefficient for the sphere with each  $h^*$  as shown in figure 19(a,b).

When the peak amplitude response of a sphere with either 1-DOF (y-only motion) or 2-DOF (x-y motion) is plotted against the mass-damping parameter, it collapses the data onto a single curve. Such a curve is known as a Griffin plot, as shown in figure 20. The open circles are data reported by Govardhan & Williamson (2005) for 1-DOF and 2-DOF cases. The peak amplitude for a fully submerged sphere in the current study, plotted as the solid diamond symbol, also falls on the same curve, noting that in practice there is a slight Reynolds number dependence (see Govardhan & Williamson 2006 for the effect on circular cylinder VIV). For the semi-submerged sphere, the mass damping changes substantially from 0.018 to 0.1 as  $h^*$  varies from  $-0.062$  to  $-0.750$ . According to figure 20, this should only result in a variation of  $A_{max}^*$  of less than 20 %. However, the situation is not quite as simple as this because the semi-submerged immersed body geometry can no longer be described as spherical once part of it lies above the waterline, and the effect of the free surface is to alter the wake, and hence the vortex forcing, considerably, as vorticity diffuses into the free surface. As can be gauged from the data presented in the previous sections, the current problem of a semi-submerged sphere shows characteristics distinct from the fully submerged case. Hence, further tests were undertaken to determine the sensitivity of the response to  $m^*$ .

Figure 21(a) shows the variation of vibration amplitude with  $U^*$  for two different  $m^*$  values at  $h^* = -0.062$  with the sphere just piercing the surface, while figure 21(b) shows the effect of the mass ratio for  $h^* = -0.25$  when the sphere has a greater proportion of its volume above the waterline. As evident from these figures, the amplitude response is more sensitive to a change in mass ratio than for the fully



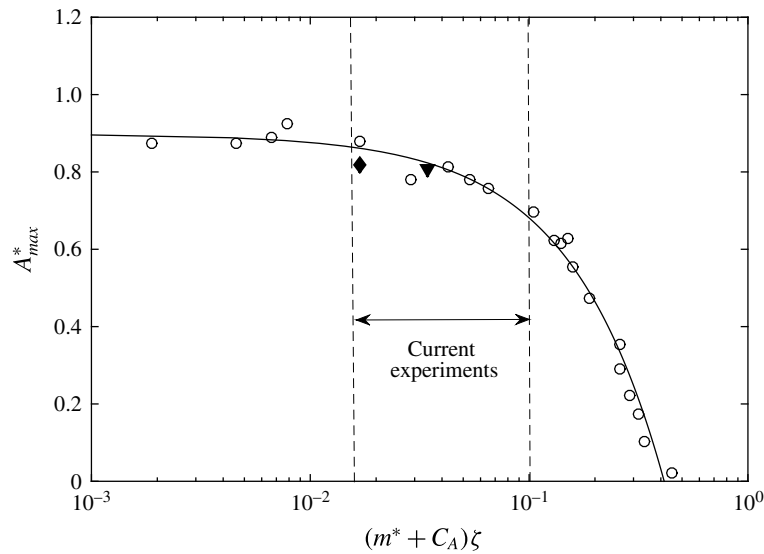


FIGURE 20. Griffin plot for the VIV of a sphere: variation of  $A_{max}^*$  with the mass-damping parameter  $(m + C_A)\zeta$ . Open circle ( $\circ$ ), the data reported by Govardhan & Williamson (2005); solid diamond,  $A_{max}^*$  for a fully submerged sphere in the current study; solid triangle,  $A_{max}^*$  reported by Sareen *et al.* (2018).

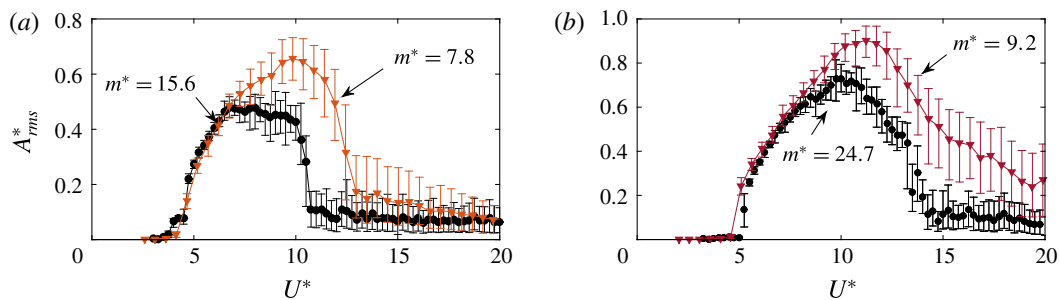


FIGURE 21. (Colour online) Variation of  $A_{rms}^*$  with  $U^*$  for different mass ratios: (a)  $h^* = -0.062$ ; (b)  $h^* = -0.25$ .

submerged case. For instance, for the case when the top of the sphere is just above the water surface at  $h^* = -0.062$ , doubling the mass ratio from  $m^* = 7.8$  to 15.6 (and hence the mass-damping ratio from 0.017 to 0.032) results in a reduction in the peak amplitude of approximately 30%. However, the predicted variation from the Griffin plot (figure 20) for a fully submerged sphere is only a few per cent. The second case, for  $h^* = 0.25$ , also shows a much greater reduction than predicted by the Griffin plot variation. Thus, the presence of the free surface has a much stronger effect on the reduction in the peak amplitude with mass-damping ratio. Despite this, the general reduction in the synchronisation range, and the reduction of amplitude at higher  $U^*$  values, is consistent with the trend observed for a fully submerged sphere. Unfortunately, limits on the weight that the air-bearing rig could support meant that it was not possible to quantify the effect further at higher mass-damping ratios. However, this clearly indicates that further future work is required in order to fully

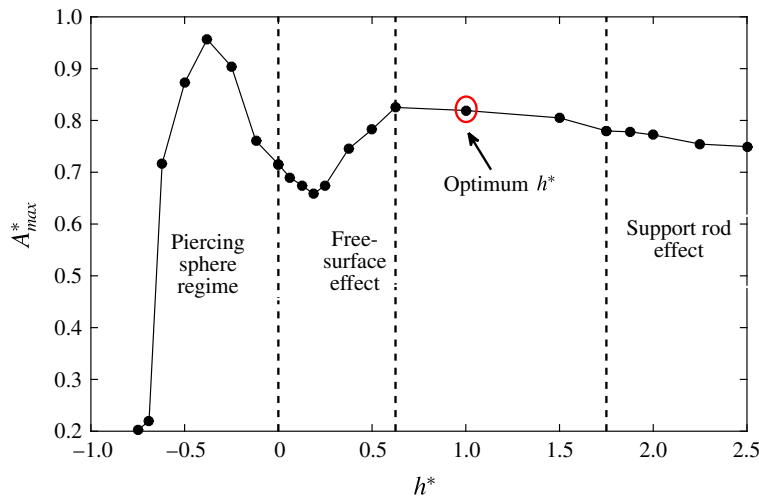


FIGURE 22. (Colour online) Variation of  $A^*_{max}$  with  $h^*$  highlighting various regimes where different effects are dominant. The marked (in red) optimum  $h^*$  denotes the suggested approximate optimum value of  $h^*$  for studying the VIV response of a fully submerged sphere if the support rod and the free-surface effects are to be minimised. The results are shown for  $D^* = 26.6$ .

understand and characterise mass-damping ratio effects on VIV of a semi-submerged sphere.

## 6. Effect of the support mechanism

In §4, the sphere VIV response was studied for immersion ratios varying in the range  $0 \leq h^* \leq 1$ . It was shown that for  $h^* = 1$ , the free-surface effect is negligible (at least in the  $U^*$  range  $0 \leq U^* \leq 20$ ), and the response matched well with the previous study of a fully submerged sphere (Govardhan & Williamson 2005) (who also used  $h^* \sim 1$ ). For higher immersion ratios ( $h^* > 1$ ), one expects to see the response of a fully submerged sphere. However, in the current study, when the immersion ratio was increased from  $1 < h^* \leq 2.5$ , another regime was found, where the support-rod effects were dominant. Mode I and mode II were found to be quite robust to the changes in immersion depths; however, the response in the ‘plateau’ branch was greatly influenced. It was found that not only the immersion ratio but also the diameter ratio ( $D^* = D/D_r$ ), with  $D_r$  being the support-rod diameter, can have significant influences on the vibration amplitude response. More detailed discussions on the support rod and submergence effects are provided in appendix A as they may be useful for future studies.

### 6.1. Peak response variation with submergence ratio

Figure 22 shows the variation of peak amplitude,  $A^*_{max}$ , with the immersion ratio,  $h^*$ , summarising the results in the current and previous sections. Based on the current study, the response can be conveniently categorised into several regimes where certain effects are dominant. Amongst other things, this figure highlights that the suggested optimum  $h^*$  for studying the response of a fully submerged sphere, if free surface and support-rod effects are to be minimised, corresponds to  $h^* \approx 1D$ . However, there are

1046 A. Sareen, J. Zhao, J. Sheridan, K. Hourigan and M. C. Thompson

also strong effects of  $D^*$  on the peak response, and both  $h^*$  and  $D^*$  strongly affect the amplitude response at higher reduced velocities beyond where the peak response occurs.

## 7. Wake measurements

### 7.1. Vorticity measurements in the cross-plane

In terms of VIV wake dynamics, the central distinction between a three-dimensional body like a sphere, and its two-dimensional counterpart, the cylinder, is that VIV of a sphere is induced by streamwise vorticity. This is in contrast to the cylinder whose dynamics are mainly induced by spanwise vortex structures in the wake. The generation of lift from the presence of streamwise vortex structures in the former case is analogous to the induced force on an aircraft wings due to counter-rotating trailing tip vortices. Govardhan & Williamson (2005) demonstrated this by comparing the direct force measurements from a force sensor to the vortex force calculated using the knowledge of strength and spacing of the streamwise vortices. Therefore, the principal conclusion one may draw is that most of the transverse force on the sphere is associated with the streamwise vorticity, and with the knowledge of the strength of the upper vortex and the spacing between the vortex pair, one may deduce the vortex force acting on the sphere. As performed for a sphere undergoing VIV with 1-DOF by Govardhan & Williamson (2005), the vortex force (or the lift force) acting on the sphere in this case can be given by the expression

$$F_{\text{vortex}} = -\rho U_v \tau b, \quad (7.1)$$

where  $U_v$  is the convection speed of the trailing vortices,  $\tau$  is the strength of the upper vortex and  $b$  is the spacing between the vortices.

Particle image velocimetry (PIV) measurements in a plane normal to the flow can reveal important insights into the temporal evolution of streamwise vorticity as the vortex loops pass through the cross-plane. Hence, in the current study, the measurement of the streamwise vorticity has been carried out in a cross-plane at a distance of  $1.5D$  from the sphere rear surface similar to the vorticity measurements by Govardhan & Williamson (2005). Figure 23 shows the vorticity contour plots phase-averaged (over more than 100 cycles) at two different phases of the oscillation cycle for a fully submerged sphere ( $h^* = 1$ ). The plots are shown for a reduced velocity of  $U^* = 10$ , which corresponds to the peak amplitude in the VIV response (the heart of mode II). The top boundary in all the contour plots reported in the paper marks the free-surface boundary.

As clearly observed from figure 23(a,b), the streamwise vorticity consists of a dominant counter-rotating vortex pair symmetric across the horizontal plane, which is consistent with the formation of vortex loops on both the sides of the wake (Sakamoto & Haniu 1990; Brücker 1999; Govardhan & Williamson 2005). Streamwise vorticity measurements by Govardhan & Williamson (2005) also revealed a counter-rotating streamwise vortex pair similar to the current study. As the sphere oscillates from one side to the other, the observed vorticity changes sign. In figure 23(a), the blue vortex (anticlockwise vorticity) is above the red vortex (clockwise vorticity). On the other hand, when the sphere traverses towards the opposite side, the vorticity changes sign with the red vortex now above the blue vortex. This is congruent with the fact that as the sphere oscillates from one side to the other, hairpin loops from opposite sides are shed downstream into the wake. Vorticity measurements in a cross-plane,  $1.5D$

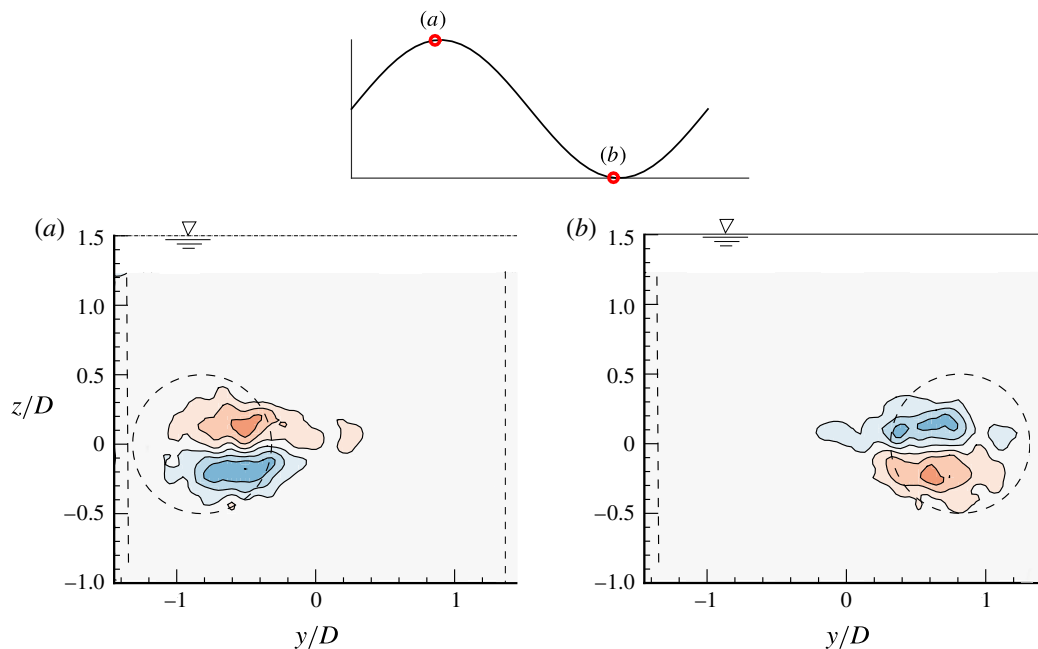


FIGURE 23. (Colour online) Streamwise vorticity plots for a fully submerged sphere VIV at  $U^* = 10$  taken  $1.5D$  downstream of the sphere. The above phase-averaged plots from cross-sectional digital particle image velocimetry (DPIV) measurements show mean vorticity contours at approximately the two opposite extremes of the displacement cycle. The position of the sphere is shown by the dashed circle. Blue contours show anticlockwise vorticity and red contours show clockwise vorticity. Contour levels vary in eight steps in the range  $\omega D/U \in [-3.33, 3.33]$ . The top boundary indicates the location of the free surface.

downstream of the sphere by Govardhan & Williamson (2005), also reported similar findings for a fully submerged sphere.

The question arises: how do these counter-rotating vortex pairs (depicting propagating streamwise vortex pairs) change when the sphere moves closer to the free surface? In order to answer this question, similar streamwise vorticity measurements at  $1.5D$  downstream were undertaken for several different immersion ratios. Figure 24(a–d) shows vorticity contour plots at several phases of the oscillation cycle for a sphere close to a free surface, in this case for an immersion ratio of  $h^* = 0.125$ . As evident from the figure, the orientation of the vortex pair has changed dramatically due to proximity to the free surface, indicating that the vortex loops change orientation and the horizontal plane through the sphere centre no longer acts as a plane of symmetry.

In figure 24 when the sphere traverses to one side, the vortex closer to the free surface (red) is reduced in size remarkably; however, as the sphere returns to the other side, the red vortex is seemingly restored and instead the size of the blue vortex is reduced substantially. This means that the anticlockwise (blue) vorticity is the dominant vorticity during the first half of the cycle and the clockwise (red) vorticity is dominant in the next half. These observations of vorticity transformation via turning, stretching and diffusion in the current results are perhaps related to the case of a vortex ring approaching a free surface as reported by Zhang, Shen & Yue

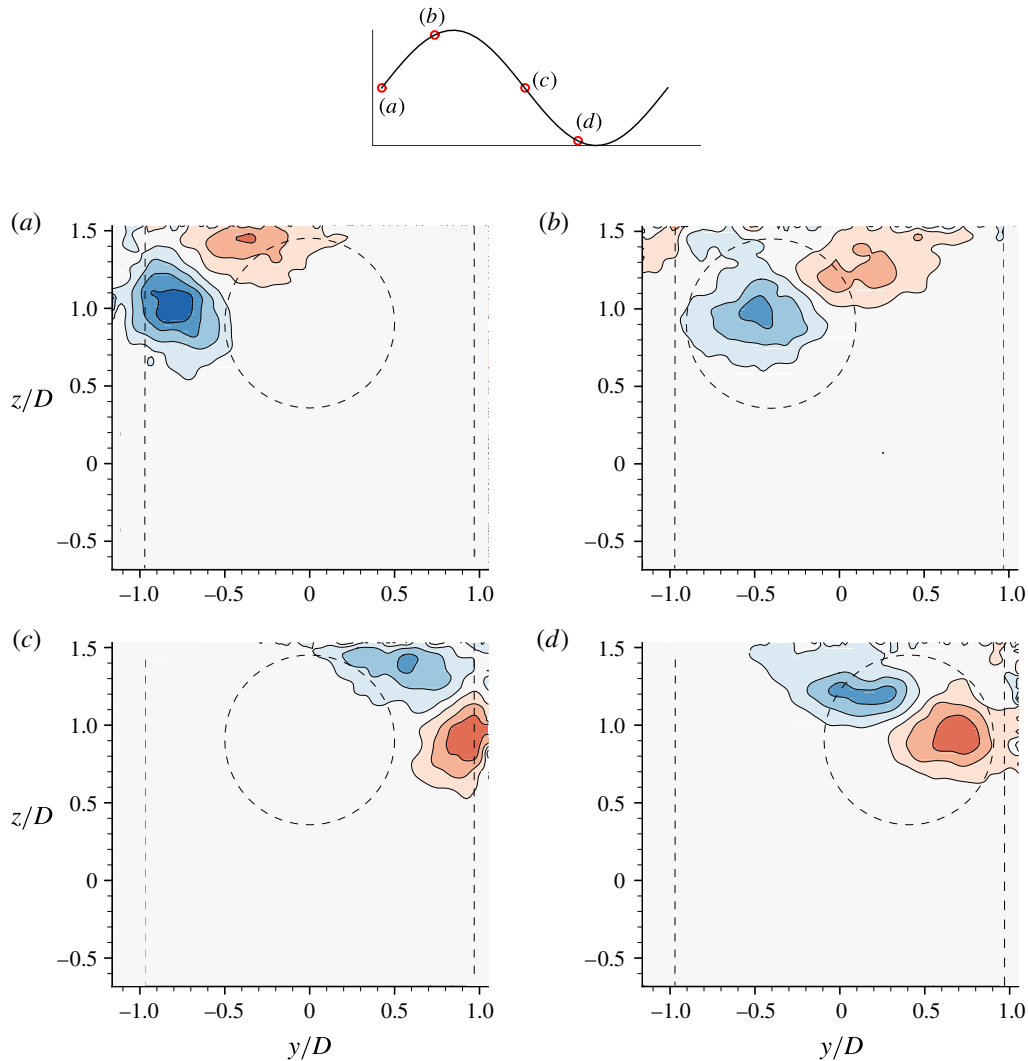


FIGURE 24. (Colour online) Streamwise vorticity measurements (phase-averaged) for  $U^* = 10$  for a sphere with an immersion ratio of  $h^* = 0.125$  at marked phases over a displacement cycle. The corresponding displacement phases are depicted in the plot above. See figure 23 for further information.

(1999). They demonstrated that the mechanisms of vorticity transformation via turning, stretching and diffusion take on distinct roles in the two surface layers, i.e. an inner viscous layer and an outer blockage layer. Similar observations of disconnection and termination of vortex lines at the free surface have been made previously by several studies, e.g. Bernal & Kwon (1989), Gharib & Weigand (1996) and Zhang *et al.* (1999) for the case of an approaching vortex ring near a free surface, Reichl *et al.* (2005) for the case of a fixed cylinder near a free surface, Ohring & Lugt (1991) for a vortex pair near a free surface and also in the review study by Sarpkaya (1996) on the vorticity and free-surface interactions.

In the current case, where the vortex pair is streamwise orientated during the initial evolution, the dynamics may be even simpler. As the upper vortex of the pair advects

downstream, the stress-free free-surface condition means that a velocity gradient cannot be maintained, i.e. the vortex diffuses into the free surface (e.g. Wu 1995; Brøns, Thompson & Leweke 2014). Thus, the pair becomes unequal in strength. This causes rotation in the cross-plane through mutual induction, allowing the lower vortex of the pair to move outwards and upwards. During the second half of the cycle, the newly formed vortex pair originating from the opposite side experiences the same dynamics, except with the signs swapped and positions reversed. One can also notice asymmetric deformation of the vortex pair due to unequal induced strains due to the presence of the free surface.

It can be concluded here that as the sphere traverses from one side to the other (in one displacement cycle), the strength of the upper vortex decreases in the cross-plane. This reduction in the strength of the upper vortex suggests a reduction in the vortex force (or lift) acting on the sphere (see (7.1)). Since the transverse force acting on the sphere decreases in this case, the vibration amplitude could be expected to decrease. This is consistent with the amplitude response measurements shown earlier in figure 5. There is considerable reduction in the amplitude response of the sphere for  $h^* = 0.125$  at  $U^* = 10$  compared to the fully submerged sphere.

An interesting case is where the sphere pierces through the free surface. Figure 25(a–d) shows cross-stream vorticity contour plots for  $h^* = -0.25$  at  $U^* = 10$ . Notably, at a distance  $1.5D$  downstream, the upper vorticity has completely disappeared. In contour panels (a) and (b), only anticlockwise vorticity is present in the cross-plane. For panels (c,d), only clockwise vorticity is present. Of course, there may still be some vorticity of opposite sign in the region (in the same plane) not captured by the PIV imaging plane. Also, these observations indicate that the formation length of the vortices is significantly longer compared to a fully submerged case, and large elliptic deformation is evident. From these vorticity contour plots, it seems likely that there are no hairpin vortex loops that develop in the wake past the sphere for a piercing sphere case. Hence, the VIV dynamics in this case are very different to that of the fully submerged case. For a partially submerged sphere (in this case,  $h^* = -0.25$ , i.e. only 75 % of the sphere is submerged), as the sphere traverses from one side to the other, only one streamwise vortex is seen in the cross-plane with alternate signs, in contrast to the fully submerged sphere, where a counter-rotating vortex pair is seen with alternate signs. However, for this case, the vibrations are larger compared to the fully submerged case, as shown in the amplitude response measurements in figure 12. To obtain the full picture of the vortex dynamics for this case, with implications for the sphere forcing, would seem to require capturing the vorticity formation closer to the sphere. This is difficult to capture with the current PIV imaging set-up.

In order to obtain a better perspective of the wake structures, spatio-temporal reconstructions of the sphere wake at a Reynolds number of  $\sim Re = 1.5 \times 10^4$  are shown in figure 26, employing 24 cross-stream vorticity fields, each phase-averaged over more than 100 sphere oscillation cycles. A convection velocity of  $U$  (free-stream velocity of  $0.196 \text{ ms}^{-1}$ ) was assumed to build the three-dimensional images. As is evident in figure 26(a), the wake comprises a two-sided chain of streamwise vortex loops. Govardhan & Williamson (2005) also reported similar wake structures for the sphere wake, but at a lower Reynolds number of  $Re = 3000$ . On the other hand, for the case when the sphere is much closer to the free surface, at  $h^* = 0.125$  in figure 26(bi), the loops twist to attach to (and diffuse into) the free surface alternatively. This observation is clearer in figure (bii), which shows the same structures but from a different perspective view (zoomed in view from the bottom).

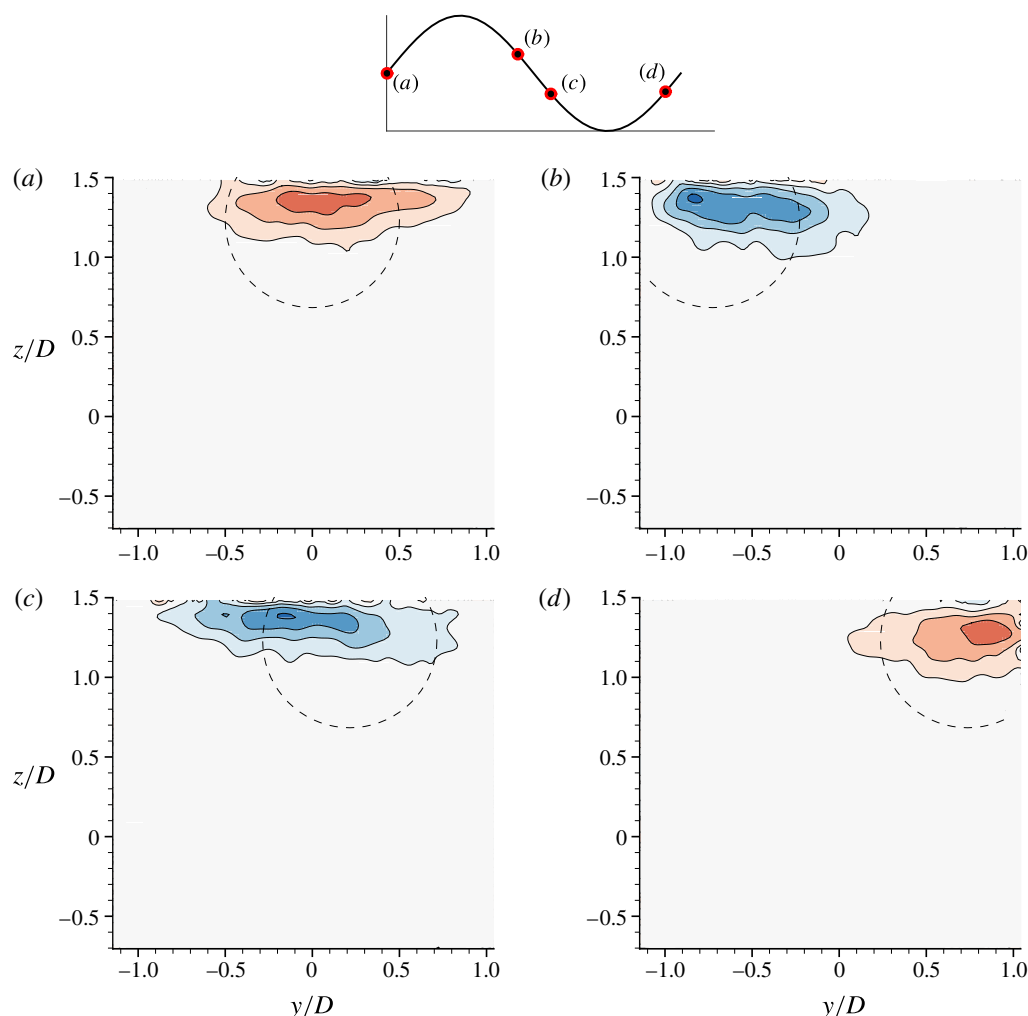


FIGURE 25. (Colour online) Streamwise vorticity measurements (phase-averaged) for  $U^* = 10$  for a sphere with an immersion ratio of  $h^* = -0.25$  at several phases through a displacement cycle. See figure 23 for further details.

### 7.2. Some comments on surface patterns and deformations

In order to gain some qualitative insight into the free-surface deformation patterns, an ultraviolet lamp was placed just above the water channel facing downwards towards the wake. A Nikon D7000 camera was placed upstream to capture the free-surface patterns. In quiescent water, the UV lamp reflection appeared as a straight horizontal band, and as the free surface deforms, this deformation can be captured by visualising the UV reflection patterns.

Figure 27(a) shows the UV lamp pattern for  $h^* = 0$  and  $U^* = 5$ . In this case, there is minimal free-surface deformation, hence the UV reflection appears as a horizontal band with little distortion that would be caused by surface waves. However, at a relatively higher  $U^*$  value of 12 (figure 27b), small surface ripples are clearly visible with a standing wave at the front of the surface. On the other hand, for  $h^* = 0.25$ , as shown in figure 27(c), there is very small deformation (unlikely to be significant); however, patterns resembling Kelvin-type waves are visible on the surface, which are



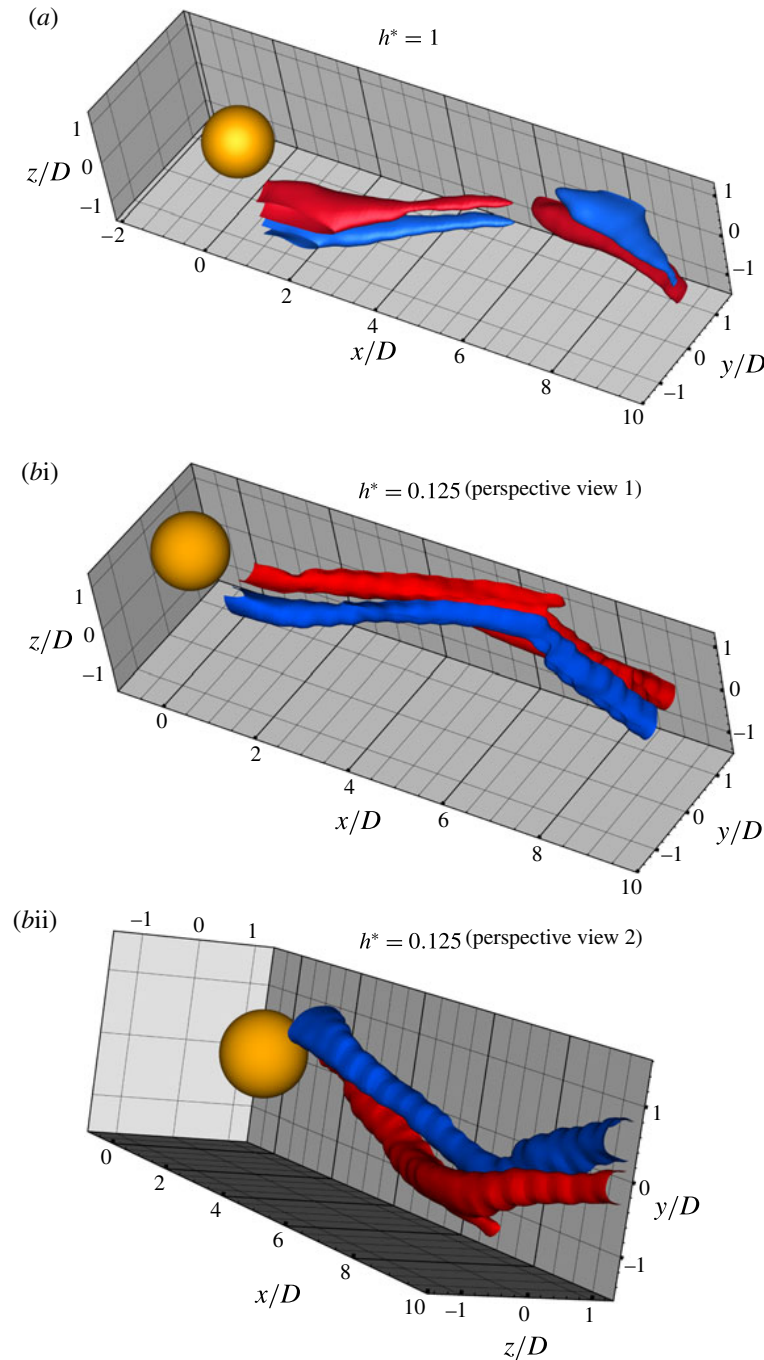


FIGURE 26. (Colour online) Spatio-temporal reconstructions of the streamwise vorticity crossing the transverse plane at a distance  $1.5D$  from the sphere rear surface for (a)  $h^* = 1$ , and (b)  $h^* = 0.125$ , based on the phase-averaged streamwise vorticity. Figures (bi) and (bii) show two different perspective views of the same case,  $h^* = 0.125$ . The wake is shown for  $U^* = 10$ , corresponding to a Reynolds number of  $\sim 1.5 \times 10^4$ . Blue indicates anticlockwise vorticity, and red clockwise vorticity (both in the  $x$ - $y$  plane). The  $x$ - $y$  plane at the  $z/D = 1.5$  boundary of the visualisation box indicates the location of the free surface. A convection velocity of  $U$  (free-stream velocity) of  $0.196 \text{ ms}^{-1}$  was used for the reconstructions.



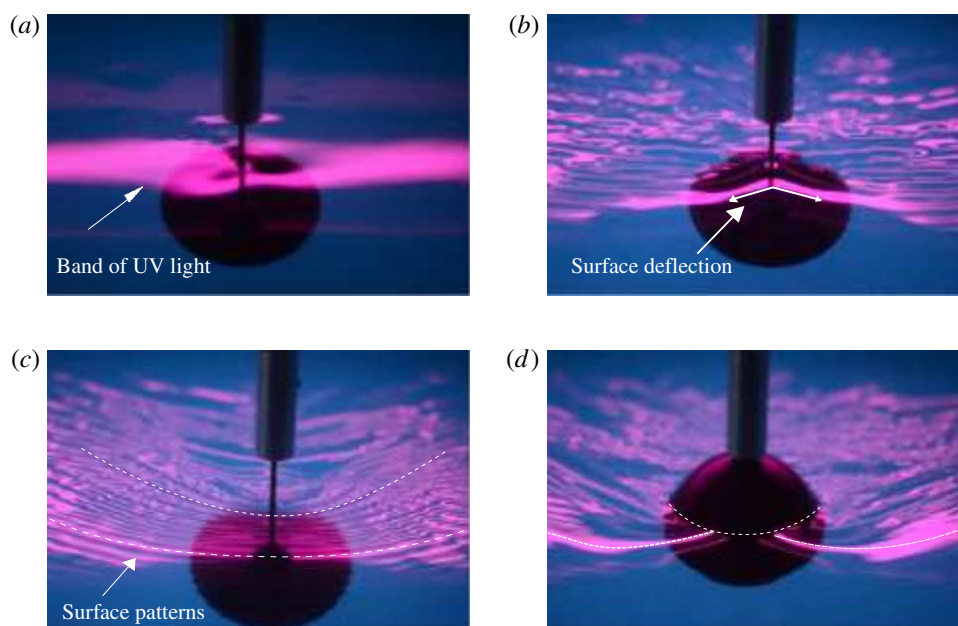
1052 *A. Sareen, J. Zhao, J. Sheridan, K. Hourigan and M. C. Thompson*

FIGURE 27. (Colour online) Images showing the surface distortion for  $h^* = 0$  at  $U^* = 5$  (a) and  $U^* = 12$  (b), and for  $h^* = 0.25$  (c) and  $h^* = -0.25$  (d) at  $U^* = 15$ . The UV lamp was placed above the water channel facing downwards towards the wake. The free-surface patterns were viewed using a Nikon camera placed upstream.

probably due to the piercing support rod. For a piercing sphere case, as shown in figure 27(d), the patterns are very different, with appreciable surface deformation seen as a standing wave structure.

In most of these cases, the surface wave structures are of low amplitude of less than two per cent of the sphere diameter. However, for  $h^* = 0.125$ , they exceeded  $\sim 4\%$  for  $U^* \gtrsim 15$ . The limiting case of  $h^* = 0$  had deformations in the vicinity of the submerged sphere of  $\sim 10\%$  at  $U^* \gtrsim 15$ . The surface deformations were estimated by measuring the approximate dip in the free surface in close proximity to the sphere using scaled images similar to those shown in figure 27. The observation of generally small surface deformation over most of the parameter space investigated is consistent with the relatively small effect of Froude number observed in § 5.3. Much higher Froude numbers are expected to lead to significantly larger surface deformations, in turn leading to nonlinear wave–wake interactions and complicated dynamics; however, even for the small Froude numbers examined in this paper, the proximity to the free surface has a strong effect on the VIV and the wake dynamics.

## 8. Conclusions

A comprehensive series of experiments and wake measurements have been performed to investigate the effect of proximity to the free surface on the VIV response of fully and semi-submerged spheres. The response was studied over a wide range of reduced velocities,  $3 \leq U^* \leq 20$ , capturing the initial resonance band, and immersion ratios of  $0 \leq h^* \leq 1$  for the fully submerged sphere and  $0 < h^* < -1$  for the semi-submerged sphere. For a fully submerged sphere, the vibration amplitude decreased and the synchronisation region narrowed gradually with the decrease

in the immersion ratio. Mode II occurred for progressively lower  $U^*$  values with decreasing  $h^*$ .

In contrast, for the semi-submerged sphere, different dynamics was observed. Two regimes were identified, depending on the immersion ratio showing different characteristic responses. In regime I, covering  $(-0.5 < h^* < 0)$ , the synchronisation region widened and the vibration amplitude increased. However, in regime II, the vibration amplitude decreased with a decrease in  $h^*$ , accompanied with a very sharp reduction beyond  $h^* < -0.65$ . The amplitude response in regime II was characterised by two distinct peaks corresponding to mode I and mode II of the vibration response observed for a fully submerged sphere.

The response was found to be relatively insensitive to the Froude number in the range tested,  $0.05 \leq Fr \leq 0.45$ , with the response curve shape unaffected, although increasing the Froude number did lead to a slight reduction in the peak amplitude. It was also found that the immersion ratio and the diameter ratio ( $D^* = \text{sphere diameter/support-rod diameter}$ ) of the support can have significant influences on the VIV response of a sphere. These effects were quantified.

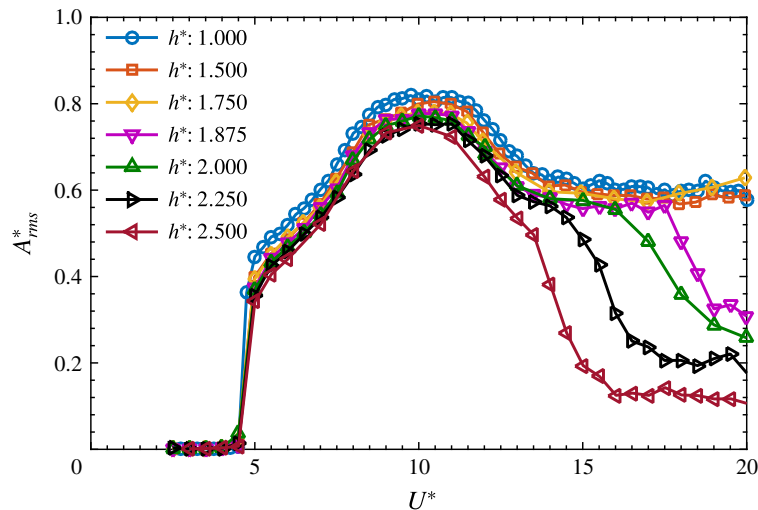
PIV wake measurements in the cross-plane  $1.5D$  downstream from the rear of the sphere revealed reduction in vorticity of the upper vortex of the longitudinal vortex pair that was closer to the free surface. This is consistent with vorticity diffusion into the free surface. Since this reduces the circulation in the upper vortex, the vortex pair twists towards the free surface as it propagates downstream due to mutual induction. For the piercing sphere case, only the lower vortex of the pair was visible at  $1.5D$  downstream; it appears that the upper vortex was effectively lost through diffusion into the free surface. This changes the wake dynamics substantially and indeed a larger oscillation amplitude than the fully submerged case is observed. Surface flow visualisations of the free surface revealed different surface patterns for the fully submerged and the semi-submerged cases; however, the total surface distortion was relatively minor, in line with the lower Froude numbers covered by this study.

### Acknowledgements

A.S. acknowledges the support of a Monash Graduate Scholarship (MGS) and Monash International Postgraduate Research Scholarship (MIPRS). The research was supported by Australian Research Council Discovery Project grants: DP150102879 and DP170100275. J.Z. also acknowledges post-doctoral salary support through the latter grants.

### Appendix A

The presence of a sting or trip wire near the boundary layer of a bluff body is known to alter the boundary layer transitions and hence the wake and its size. This leads to changes in the drag coefficient and heat transfer measurements. Mostly, previous experimental studies on the flow past spheres were performed with spheres supported using either tethers or stings. The location of the sphere support systems can also have remarkable influences. Raithby & Eckert (1968) studied the effect of the support position on the flow near the surface of a sphere using flow visualisation techniques. They concluded that in the case of a cross-flow support position, the boundary layer is still attached when it meets the support rod with ensuing violent interactions, leading to an altered wake near the sphere. However, at subcritical Reynolds numbers, the boundary layer is already separated when it encounters the support. It was shown that no significant general disturbance was produced for

FIGURE 28. (Colour online) Variation of  $A_{rms}^*$  with  $U^*$  for various immersion ratios.

these Reynolds numbers. In the current study, the Reynolds number regime is well below the critical  $Re_c$ , i.e. in the subcritical regime, and the sphere is supported at the cross-flow support position. Although significant changes in the wake are not expected in the current study, it is shown by systematic experiments that the immersion ratio ( $h^*$ ) and the diameter ratio ( $D^* = D/D_r$ ), with  $D_r$  the support-rod diameter, can have significant influences on the vibration amplitude response.

This short study essentially follows on from the work of Govardhan & Williamson (2005), who found that a support rod with a diameter ratio of 1 : 30 was sufficiently thin not to strongly affect the amplitude response curve. However, the selection of the rod diameter and submergence depth involves a compromise between a number of competing factors: providing sufficient structural stiffness, minimising the direct effect on the sphere wake, reducing the resonant response of the rod, reducing sphere and cylinder wake interaction, avoiding free-surface effects; it was therefore decided that documenting these influences would be worthwhile.

#### A.1. Effect of the immersion ratio

Figure 28 shows the response curves for a sphere supported with a circular cross-section cylindrical rod for various immersion ratios  $h^*$ . In this case, the sphere of diameter  $D = 80$  mm is supported with a rod of  $D_r = 3$  mm, equating to a diameter ratio of  $D^* = 26.6$ . Also, the change in damping with the change in the support-rod length was found to be negligible.

When the immersion ratio was increased from 1 to 1.75, there were no significant changes in the responses. On the other hand, increasing  $h^*$  to 1.875 led to a sudden drop in the amplitude at higher  $U^*$  values. This trend was observed for  $h^* \geq 1.875$ . The  $U^*$  value at which the sudden drop is observed, decreased progressively with increasing  $h^*$ . Nonetheless, for  $U^* \leq 10$ , the response shape remained similar, although there was a not insignificant decrease in the peak amplitude, by approximately 10%, as  $h^*$  was increased from 1 to 2.5. Also, it is evident from the figure that increasing  $h^*$  does not shift the position of the peak to the left; they are aligned for all cases examined. However, the peak vibration amplitude  $A_{max}^*$  decreases almost linearly with the immersion ratio  $h^*$ , as shown in figure 29.

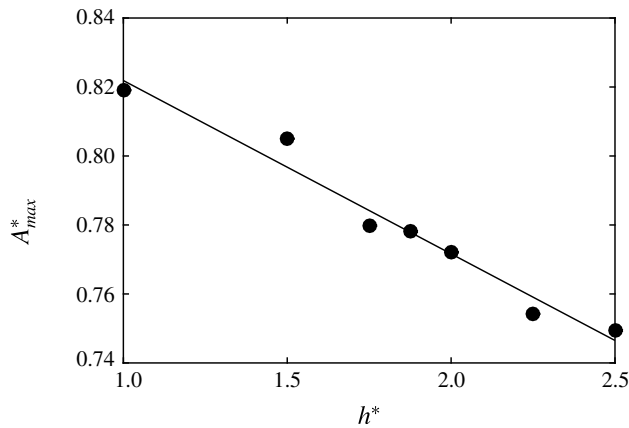


FIGURE 29. Variation of the peak saturation amplitude  $A_{max}$  with  $h^*$ .

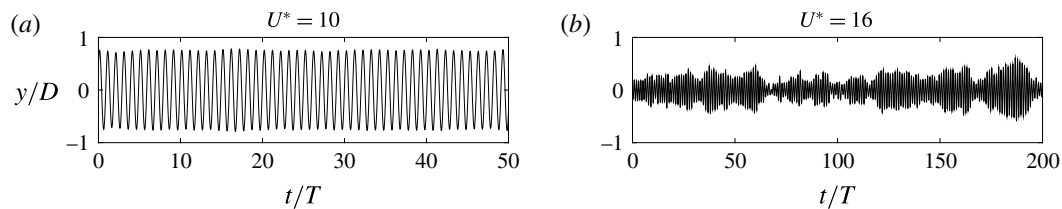


FIGURE 30. Variation of the displacement amplitude ( $y/D$ ) with non-dimensional time ( $t/T$ ) for two  $U^*$  values at an immersion ratio of 2.25.

The displacement time trace for one of the  $h^*$  values ( $h^* = 2.25$  in this case), for which the amplitude is strongly affected at higher  $U^*$  values, is shown in figure 30. At  $U^* = 10$ , the signal is highly periodic; on the other hand, at  $U^* = 16$ , where the amplitude has dropped substantially, the signal is no longer periodic and instead consists of intermittent small bursts of vibration. Figure 31 shows that there is an associated drop in the transverse force coefficient with the corresponding decrease in the amplitude response shown in the figure 28. The vortex and the total phases for all the  $h^*$  values follow a similar trend in mode I; however, in mode II, both the phases drop to lower values at  $U^*$  values, progressively decreasing with the increasing  $h^*$ , as shown in figure 32.

#### A.2. Effect of the diameter ratio

For all the above cases, the diameter ratio,  $D^*$ , was fixed at 26.6 and only the immersion ratio was varied.  $D^*$  is another important parameter that can influence the amplitude response. Hence, the effect of  $D^*$  was studied by keeping the immersion ratio fixed at unity (where free-surface effects are insignificant) while varying the diameter ratio. Figure 33(a) shows the amplitude response of a sphere supported by a rod with  $D^*$  varying in small steps from 26.6 to 7. Figure 33(b) shows the fluctuation in the amplitude response for  $D^* = 11$ . Note here that the error bars are delimited by the mean of the top 10% of the peaks and the mean of the bottom 10% of the peaks of the displacement signal. It can be clearly seen that there are large fluctuations

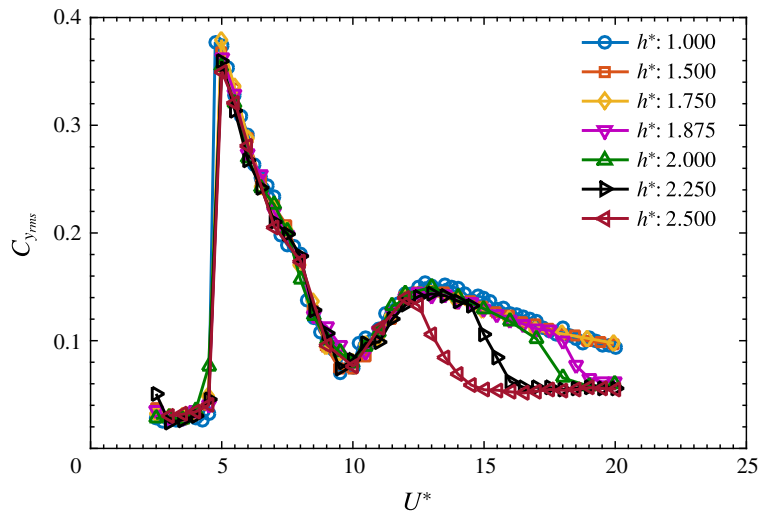
1056 *A. Sareen, J. Zhao, J. Sheridan, K. Hourigan and M. C. Thompson*


FIGURE 31. (Colour online) Variation of the r.m.s. cross-stream force coefficient  $C_{y_{rms}}$  with reduced velocity  $U^*$  for varying immersion ratios  $h^*$ .

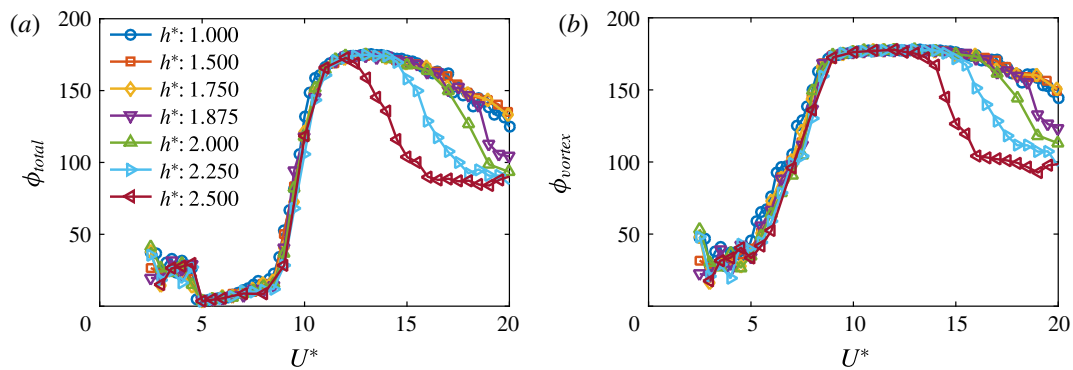


FIGURE 32. (Colour online) Variation of the total phase  $\phi_{total}$  (a) and the vortex phase  $\phi_{vortex}$  (b) with  $U^*$  for a series of different immersion ratios.

in the displacement signal, i.e. the displacement signal is highly non-periodic, for higher  $U^*$  values. This behaviour was typical of all the cases tested in the current study.

Another interesting point to note is that, unlike the previous case discussed above where all the response curves were essentially aligned, the peak responses here shift to the left gradually with increasing  $D^*$ . In fact, the initial part of the response curve seems almost the same for each case, but the amplitude begins to be reduced at a smaller reduced velocity as the diameter ratio is lower. This suggests different underlying dynamics compared to the previous one. Although not undertaken here, a study of the wake interactions from the cylindrical rod and the sphere would be informative, and help to determine the physical basis of this substantial effect. Nevertheless, the current investigations quantify substantial effects on the amplitude response, and suggest some care is necessary with body mounting and positioning for sphere VIV experiments.

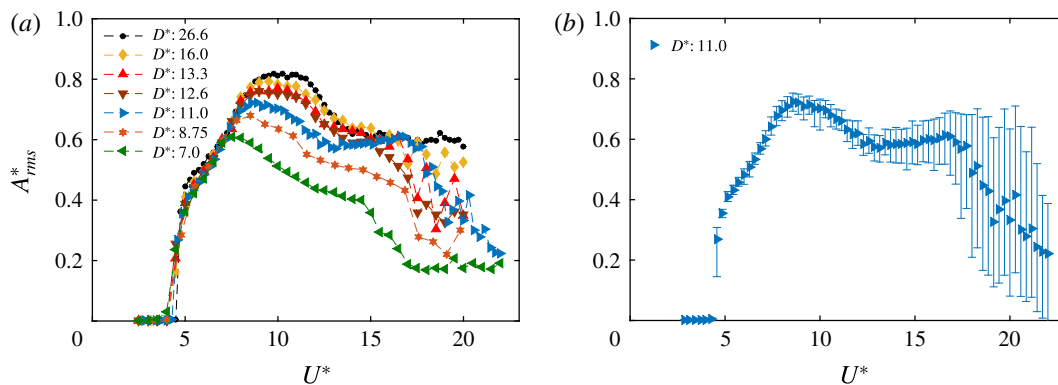


FIGURE 33. (Colour online) (a) Variation of  $A_{rms}^*$  with  $U^*$  for a range of support-rod diameter ratios. (b) Example of the fluctuations in the oscillation amplitude for the case of  $D^* = 11.0$  through error bars delimiting the range of amplitude variation from cycle to cycle.

#### REFERENCES

- BEHARA, S., BORAZJANI, I. & SOTIROPOULOS, F. 2011 Vortex-induced vibrations of an elastically mounted sphere with three degrees of freedom at  $Re = 300$ : hysteresis and vortex shedding modes. *J. Fluid Mech.* **686**, 426–450.
- BEHARA, S. & SOTIROPOULOS, F. 2016 Vortex-induced vibrations of an elastically mounted sphere: the effects of Reynolds number and reduced velocity. *J. Fluids Struct.* **66**, 54–68.
- BERNAL, L. P. & KWON, J. T. F. 1989 Vortex ring dynamics at a free surface. *Phys. Fluids A* **1** (3), 449–451.
- BRØNS, M., THOMPSON, M. C., LEWEKE, T. & HOURIGAN, K. 2014 Vorticity generation and conservation for two-dimensional interfaces and boundaries. *J. Fluid Mech.* **758**, 63–93.
- BRÜCKER, C. 1999 Structure and dynamics of the wake of bubbles and its relevance for bubble interaction. *Phys. Fluids* **11** (7), 1781–1796.
- FOURAS, A., LO JACONO, D. & HOURIGAN, K. 2008 Target-free stereo PIV: a novel technique with inherent error estimation and improved accuracy. *Exp. Fluids* **44** (2), 317–329.
- GHARIB, M. & WEIGAND, A. 1996 Experimental studies of vortex disconnection and connection at a free surface. *J. Fluid Mech.* **321**, 59–86.
- GOVARDHAN, R. & WILLIAMSON, C. H. K. 1997 Vortex-induced motions of a tethered sphere. *J. Wind Engng Ind. Aerodyn.* **69**, 375–385.
- GOVARDHAN, R. & WILLIAMSON, C. H. K. 2000 Modes of vortex formation and frequency response of a freely vibrating cylinder. *J. Fluid Mech.* **420**, 85–130.
- GOVARDHAN, R. N. & WILLIAMSON, C. H. K. 2005 Vortex-induced vibrations of a sphere. *J. Fluid Mech.* **531**, 11–47.
- GOVARDHAN, R. N. & WILLIAMSON, C. H. K. 2006 Defining the ‘modified Griffin plot’ in vortex-induced vibration: revealing the effect of Reynolds number using controlled damping. *J. Fluid Mech.* **561**, 147–180.
- VAN HOUT, R., KRAKOVICH, A. & GOTTLIEB, O. 2010 Time resolved measurements of vortex-induced vibrations of a tethered sphere in uniform flow. *Phys. Fluids* **22** (8), 087101.
- INOUE, M., BABA, N. & HIMENO, Y. 1993 Experimental and numerical study of viscous flow field around an advancing vertical circular cylinder piercing a free-surface. *J. Kansai Soc. Naval Arch.* **220**, 57–64.
- JAUVTIS, N., GOVARDHAN, R. & WILLIAMSON, C. H. K. 2001 Multiple modes of vortex-induced vibration of a sphere. *J. Fluids Struct.* **15** (3–4), 555–563.
- KAWAMURA, T., MAYER, S., GARAPON, A. & SORESENSEN, L. 2002 Large eddy simulation of a flow past a free surface piercing circular cylinder. *Trans. ASME J. Fluids Engng* **124** (1), 91–101.



1058 A. Sareen, J. Zhao, J. Sheridan, K. Hourigan and M. C. Thompson

- KHALAK, A. & WILLIAMSON, C. H. K. 1999 Motions, forces and mode transitions in vortex-induced vibrations at low mass-damping. *J. Fluids Struct.* **13**, 813–851.
- KRAKOVICH, A., ESHBAL, L. & VAN HOUT, R. 2013 Vortex dynamics and associated fluid forcing in the near wake of a light and heavy tethered sphere in uniform flow. *Exp. Fluids* **54** (11), 1615.
- LEE, H., HOURIGAN, K. & THOMPSON, M. C. 2013 Vortex-induced vibration of a neutrally buoyant tethered sphere. *J. Fluid Mech.* **719**, 97–128.
- MIRAUDA, D., PLANTAMURA, A. V. & MALAVASI, S. 2014 Dynamic response of a sphere immersed in a shallow water flow. *J. Offshore Mech. Arctic Engng* **136** (2), 021101.
- OHRING, S. & LUGT, H. J. 1991 Interaction of a viscous vortex pair with a free surface. *J. Fluid Mech.* **227**, 47–70.
- DE OLIVEIRA BARBOSA, J. M., QU, Y., METRIKINE, A. V. & LOURENS, E. 2017 Vortex-induced vibrations of a freely vibrating cylinder near a plane boundary: experimental investigation and theoretical modelling. *J. Fluids Struct.* **69**, 382–401.
- PREGNALATO, C. J. 2003 Flow-induced vibrations of a tethered sphere. PhD thesis, Monash University.
- RAITHBY, G. D. & ECKERT, E. R. G. 1968 The effect of support position and turbulence intensity on the flow near the surface of a sphere. *Heat Mass Transfer* **1** (2), 87–94.
- REICHL, P., HOURIGAN, K. & THOMPSON, M. C. 2005 Flow past a cylinder close to a free surface. *J. Fluid Mech.* **533**, 269–296.
- SAKAMOTO, H. & HANIU, H. 1990 A study on vortex shedding from spheres in a uniform flow. *Trans. ASME J. Fluids Engng* **112**, 386–392.
- SAREEN, A., ZHAO, J., LO JACONO, D., SHERIDAN, J., HOURIGAN, K. & THOMPSON, M. C. 2018 Vortex-induced vibration of a rotating sphere. *J. Fluid Mech.* **837**, 258–292.
- SARPKAYA, T. 1996 Vorticity, free surface, and surfactants. *Annu. Rev. Fluid Mech.* **28** (1), 83–128.
- SHERIDAN, J., LIN, J. C. & ROCKWELL, D. 1995 Metastable states of a cylinder wake adjacent to a free surface. *Phys. Fluids* **7** (9), 2099–2101.
- SHERIDAN, J., LIN, J. C. & ROCKWELL, D. 1997 Flow past a cylinder close to a free surface. *J. Fluid Mech.* **330**, 1–30.
- WILLIAMSON, C. H. K. & GOVARDHAN, R. 1997 Dynamics and forcing of a tethered sphere in a fluid flow. *J. Fluids Struct.* **11** (3), 293–305.
- WU, J. Z. 1995 A theory of three-dimensional interfacial vorticity dynamics. *Phys. Fluids* **7** (10), 2375–2395.
- YU, G., AVITAL, E. J. & WILLIAMS, J. J. 2008 Large eddy simulation of flow past free surface piercing circular cylinders. *Trans. ASME J. Fluids Engng* **130** (10), 101304.
- ZHANG, C., SHEN, L. & YUE, D. K. P. 1999 The mechanism of vortex connection at a free surface. *J. Fluid Mech.* **384**, 207–241.
- ZHAO, J., LEONTINI, J. S., LO JACONO, D. & SHERIDAN, J. 2014a Chaotic vortex induced vibrations. *Phys. Fluids* **26** (12), 121702.
- ZHAO, J., LEONTINI, J. S., LO JACONO, D. & SHERIDAN, J. 2014b Fluid–structure interaction of a square cylinder at different angles of attack. *J. Fluid Mech.* **747**, 688–721.

## Chapter 7

# Flow-induced Vibration of a Rotary Oscillating Sphere

*If I have the belief that I can do it, I shall surely acquire the capacity to do it even if I may not have it at the beginning*

---

Mahatma Gandhi

### 7.1 Overview of the chapter

In this chapter, the publication titled ‘The effect of imposed rotary oscillation on the flow-induced vibration of a sphere’ published in the *Journal of Fluid Mechanics* (2018), vol **855**, pp. 703–735, has been reproduced with permission Cambridge University Press© 2018. In this paper, a comprehensive series of experiments and wake measurements were performed to examine the effect of imposed rotary oscillation on the FIV of a sphere that is elastically mounted in the cross-flow direction. The response was investigated for a wide range of forcing parameters, non-dimensional forcing frequency,  $f_R$ , in the range  $0 \leq f_R \leq 5$ , forcing amplitude,  $\alpha_R$ , in the range  $0 \leq \alpha_R \leq 2$ , and reduced velocity  $U^*$  between  $0 \leq U^* \leq 20$ .

It was found that when the forcing frequency  $f_r$  was in close proximity to the natural frequency  $f_{nw}$ , the vibrations locked-on to  $f_r$  instead of  $f_{nw}$  inhibiting the resonance response. The vibrations were greatly suppressed in the lock-on region, except for the case when  $f_R = f_{nw}$ , where an ‘enhanced resonance’ response was observed leading to very large amplitudes, even greater than those observed for the non-rotating sphere in some cases. In the lock-on region, a sudden jump in the total phase was observed from  $0^\circ$  to  $180^\circ$ . The displacement signal was highly modulated in the non lock-on regions. Near the lock-on boundaries, a wide spectrum of frequencies was observed. Interestingly, suppression was also observed in the non lock-on regions for very high  $f_R$  and  $\alpha_R$  values. Mode I was found to be quite resistant to control requiring very high velocity ratios for the suppression of vibrations. On the other hand, control (suppression) was most effective for mode III. Overall, relatively high velocity ratios were required to suppress the vibrations. The width of the RLO region increased with an increase in  $\alpha_R$  for all three modes. When the reduced velocity was increased progressively, several types of responses with different characteristic behaviours were observed. For some cases, the



vibration amplitudes increased monotonically with an increase in  $U^*$ . Such vibrations have been termed ‘*Rotary induced vibrations*’. The phase difference between the rotary oscillations and the sphere displacement  $\phi_{rot}$  was found to be crucial in determining the response. Monotonically decreasing  $\phi_{rot}$  values were always associated with the monotonically increasing responses. Wake measurements performed in the cross-plane revealed structures similar to those for an oscillating sphere without imposed rotation; however, there was a change in the timing of vortex formation. For a high frequency ratio of  $f_R = 3$ , there was a clear reduction in the streamwise vorticity consistent with a reduced amplitude response.

## The effect of imposed rotary oscillation on the flow-induced vibration of a sphere

A. Sareen<sup>1,†</sup>, J. Zhao<sup>1</sup>, J. Sheridan<sup>1</sup>, K. Hourigan<sup>1</sup> and M. C. Thompson<sup>1</sup>

<sup>1</sup>Fluids Laboratory for Aeronautical and Industrial Research (FLAIR), Department of Mechanical and Aerospace Engineering, Monash University, Melbourne, VIC 3800, Australia

(Received 6 February 2018; revised 27 June 2018; accepted 11 August 2018;  
first published online 19 September 2018)

This experimental study investigates the effect of imposed rotary oscillation on the flow-induced vibration of a sphere that is elastically mounted in the cross-flow direction, employing simultaneous displacement, force and vorticity measurements. The response is studied over a wide range of forcing parameters, including the frequency ratio  $f_R$  and velocity ratio  $\alpha_R$  of the oscillatory forcing, which vary between  $0 \leq f_R \leq 5$  and  $0 \leq \alpha_R \leq 2$ . The effect of another important flow parameter, the reduced velocity,  $U^*$ , is also investigated by varying it in small increments between  $0 \leq U^* \leq 20$ , corresponding to the Reynolds number range of  $5000 \lesssim Re \lesssim 30\,000$ . It has been found that when the forcing frequency of the imposed rotary oscillations,  $f_r$ , is close to the natural frequency of the system,  $f_{nw}$ , (so that  $f_R = f_r/f_{nw} \sim 1$ ), the sphere vibrations lock on to  $f_r$  instead of  $f_{nw}$ . This inhibits the normal resonance or lock-in leading to a highly reduced vibration response amplitude. This phenomenon has been termed ‘rotary lock-on’, and occurs for only a narrow range of  $f_R$  in the vicinity of  $f_R = 1$ . When rotary lock-on occurs, the phase difference between the total transverse force coefficient and the sphere displacement,  $\phi_{total}$ , jumps from  $0^\circ$  (in phase) to  $180^\circ$  (out of phase). A corresponding dip in the total transverse force coefficient  $C_{y(rms)}$  is also observed. Outside the lock-on boundaries, a highly modulated amplitude response is observed. Higher velocity ratios ( $\alpha_R \geq 0.5$ ) are more effective in reducing the vibration response of a sphere to much lower values. The mode I sphere vortex-induced vibration (VIV) response is found to resist suppression, requiring very high velocity ratios ( $\alpha_R > 1.5$ ) to significantly suppress vibrations for the entire range of  $f_R$  tested. On the other hand, mode II and mode III are suppressed for  $\alpha_R \geq 1$ . The width of the lock-on region increases with an increase in  $\alpha_R$ . Interestingly, a reduction of VIV is also observed in non-lock-on regions for high  $f_R$  and  $\alpha_R$  values. For a fixed  $\alpha_R$ , when  $U^*$  is progressively increased, the response of the sphere is very rich, exhibiting characteristically different vibration responses for different  $f_R$  values. The phase difference between the imposed rotary oscillation and the sphere displacement  $\phi_{rot}$  is found to be crucial in determining the response. For selected  $f_R$  values, the vibration amplitude increases monotonically with an increase in flow velocity, reaching magnitudes much higher than the peak VIV response for a non-rotating sphere. For these cases, the vibrations are always locked to the forcing frequency, and there is a linear decrease in  $\phi_{rot}$ . Such vibrations have been termed ‘rotary-induced vibrations’. The wake measurements in the cross-plane 1.5D downstream of the sphere position reveal that the sphere wake consists of vortex loops, similar to the wake of a sphere without any imposed rotation; however, there

<sup>†</sup> Email address for correspondence: [anchal.sareen@monash.edu](mailto:anchal.sareen@monash.edu)

704 *A. Sareen, J. Zhao, J. Sheridan, K. Hourigan and M. C. Thompson*

is a change in the timing of vortex formation. On the other hand, for high  $f_R$  values, there is a reduction in the streamwise vorticity, presumably leading to a decreased total transverse force acting on the sphere and resulting in a reduced response.

**Key words:** flow–structure interactions, vortex streets, wakes

## 1. Introduction

Vortex-induced vibration (VIV) of structures is encountered in a variety of engineering situations, such as for flows past offshore structures, bridges, heat exchangers, aircraft, pipelines and other hydrodynamic applications. The practical significance of VIV has led to numerous studies focusing on understanding the underlying physics, including the comprehensive reviews by Bearman (1984), Blevins (1990), Sarpkaya (2004), Williamson & Govardhan (2004), Paidoussis, Price & De Langre (2010) and Naudascher & Rockwell (2012). Most of the previous studies, however, were focused on two-dimensional (2-D) bluff bodies like cylinders. There are relatively fewer studies on the VIV of elastically mounted or tethered spheres despite their ubiquitous practical significance, such as marine buoys, underwater mines, other offshore structures and tethered or towed spheroidal objects. Govardhan & Williamson (1997), Williamson & Govardhan (1997) and Jauvtis, Govardhan & Williamson (2001) were among the first to report on the VIV response of a sphere identifying three fundamental modes of vibration, namely modes I, II and III. Since then, a number of systematic studies have investigated the VIV response of spheres, e.g. Pregalato (2003), Govardhan & Williamson (2005), van Hout, Krakovich & Gottlieb (2010), Behara, Borazjani & Sotiropoulos (2011), Krakovich, Eshbal & van Hout (2013), Lee, Hourigan & Thompson (2013), Behara & Sotiropoulos (2016) and Sareen *et al.* (2018a).

Large-amplitude vibration caused by VIV over a wide range of Reynolds number is a common cause of serious structural fatigue and damage, which has led to a plethora of research studies focusing on suppressing VIV over last four decades. For this reason, several active and passive control methods have been studied previously for 2-D bluff bodies. Choi, Jeon & Kim (2008) provide a review of various control methods employed for flow over bluff bodies. Although passive control methods do not consume external energy and are fairly insensitive to changes in the flow direction, it tends to be difficult to dramatically reduce VIV, and the drag often increases. In contrast, active control methods such as moving-surface boundary-layer control (MSBC) (Mittal 2001) and windward suction leeward blowing (WSLB) (Dong, Triantafyllou & Karniadakis 2008) reduce VIV to a much lower level; however, the efficacy of both these active methods depends on the flow direction.

The control of VIV by rotary motion has received increased attention recently due to its insensitivity to flow direction, efficacy over a broader range of flow parameters and the greater extent of VIV reduction. A recent experimental study by Sareen *et al.* (2018a) reported suppression of VIV of a sphere by means of an imposed transverse rotation for a wide range of Reynolds numbers and reduced velocities. They reported a reduction in the strength of the vortex street, which can be associated with a reduction of the transverse force acting on the sphere. VIV can also be suppressed by forced sinusoidal rotary oscillations of the bluff body, to prohibit the phenomenon of resonance or ‘lock-in’ by deviating the vortex shedding frequency from the natural frequency of the system towards the forcing frequency (also known as ‘lock-on’).

This approach has been extensively investigated on a fixed cylinder over the last four decades. Taneda (1978) was the first to examine this experimentally for a rotary oscillating cylinder, and reported the disappearance of vortex shedding for very high forcing frequencies. Later, Tokumaru & Dimotakis (1991) reported a drag reduction of up to 80 % for a certain range of forcing frequencies and amplitudes of sinusoidal rotary oscillations. This pioneering study inspired a number of systematic numerical studies aimed at understanding this wake control and the underlying dynamics, such as Tokumaru & Dimotakis (1991), Lu & Sato (1996), Chou (1997), Baek & Sung (2000), Mahfouz & Badr (2000), Cheng, Chew & Luo (2001), Shiels & Leonard (2001), Choi, Choi & Kang (2002), Lee & Lee (2006) and Kumar *et al.* (2013). It is known for the case of a fixed cylinder that for a certain range of forcing frequency ratios encompassing the natural frequency of the system, the vortex shedding locks to the forcing frequency, leading to the ‘lock-on’ phenomenon (Chou 1997; Baek & Sung 2000). The state is accompanied by a significant drag reduction (Tokumaru & Dimotakis 1991; Lu & Sato 1996; Chou 1997). The lock-on region widens with increasing rotational speed (Mahfouz & Badr 2000). The boundaries of lock-on and non-lock-on regions are associated with the modulation of the drag, lift and velocity (Choi *et al.* 2002), and the non-lock-on regions exhibit quasi-periodicity (Baek & Sung 2000). Several studies have focused on understanding the underlying dynamics. It was found that the lock-on region is associated with enhanced separation and vortex coalescence in the wake (Cheng *et al.* 2001; Shiels & Leonard 2001; Lee & Lee 2006). The experimental investigation by Thiria, Goujon-Durand & Wesfreid (2006) also revealed that the phase lag between the vortex shedding and the rotary motion of the cylinder effectively gives either a constructive or destructive contribution to the wake, leading to a global decrease or increase in fluctuations in the wake.

Recently, Du & Sun (2015) investigated numerically the potential of rotary oscillations to suppress VIV of an elastically mounted cylinder at  $Re = 350$ . They found ‘lock-on’ for the elastically mounted cylinder, which led to switching of vortex shedding from the natural frequency to the forcing frequency, inhibiting resonance or VIV. They observed effective control only for large enough velocity ratios, and the lock-on regime became narrower with an increase in reduced velocity. They observed no significant reduction in the strength of vortices in the wake.

The papers discussed so far report on rotational control of 2-D bluff bodies. However, there do not appear to be studies investigating the potential of rotary oscillations in wake control for 3-D bluff bodies, such as spheres. However, a sphere is the most basic 3-D body shape; certainly the one with the most symmetry, and clearly spheres can undergo significant amplitude VIV. A sphere provides a starting framework to comprehend VIV control of more complex three-dimensional bluff bodies. The current study aims at producing an understanding of the effect of imposed rotary oscillations on the VIV response of a sphere for a wide range of forcing and flow parameters. One question to be addressed is whether similar features (as discussed above for a fixed cylinder) are exhibited in the case of an elastically mounted sphere. Specifically, this study addresses the following fundamental questions: Is ‘lock-on’ also observed for a sphere exhibiting a 3-D wake? If so, how does the lock-on range depend on various forcing and flow parameters? How does this phenomenon affect the 3-D wake structures of the flow past a sphere?

The outline of the article is as follows. The experimental methodology for the current experiments is detailed in § 2. The VIV response of a non-rotating oscillating sphere is briefly presented in § 3. Section 4.1 discusses in detail the effect of frequency ratio on the VIV response of a sphere, followed by § 4.2 on the effect of velocity ratio.

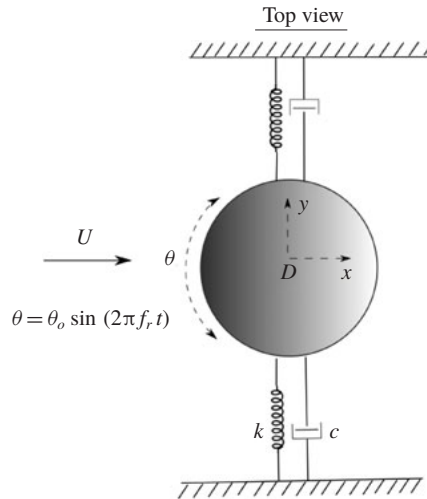


FIGURE 1. Definition sketch for the transverse vortex-induced vibration of a sphere undergoing forced rotary oscillations. The hydro-elastic system is simplified as a one-degree-of-freedom (1-DOF) system constrained to move only in the cross-flow direction. The axis of rotation ( $z$ ) is transverse to both the flow direction ( $x$ -axis) and the oscillation axis ( $y$ -axis). Here,  $U$  is the free-stream velocity,  $k$  the spring constant,  $D$  the sphere diameter,  $c$  the structural damping and  $\theta$  the imposed angular displacement.

§ 4.3 focuses on the effect of the reduced velocity on the VIV response. Section 5 discusses the effect on the wake structures, and finally § 6 draws conclusions, and summarises the important findings and significance of the current study. To be clear, in this article, if the vibrations are locked to the natural frequency, the phenomenon is termed ‘lock-in’ or ‘resonance’, and if they are locked to the forcing frequency instead, it is termed ‘lock-on’ or, in this case, ‘rotary lock-on’.

## 2. Experimental method

A schematic showing the experimental arrangement of the current fluid–structure interaction problem is presented in figure 1. The sphere is elastically mounted in the direction transverse to the incoming flow. The axis of the sinusoidal rotary oscillations imposed on the sphere is transverse to the flow direction and the free vibration axis.

The two important parameters characterising the rotary oscillation motion of the sphere are  $f_R$  and  $\alpha_R$ . Here,  $f_R$  is the forcing frequency ratio, expressed as the ratio of forcing frequency,  $f_r$ , and the natural frequency of the system,  $f_{nw}$ , as

$$f_R = f_r / f_{nw}. \quad (2.1)$$

Alternatively, sometimes the non-dimensional forcing Strouhal number is used to characterise the forcing

$$S_f = \frac{f_r D}{U}. \quad (2.2)$$

The other key parameter,  $\alpha_R$ , is the forcing velocity ratio expressed as the ratio of the maximum tangential velocity of the sphere surface and the free-stream velocity  $U$  as

$$\alpha_R = \frac{D \dot{\theta}_{max}}{2U}, \quad (2.3)$$

|                              |              |                                     |
|------------------------------|--------------|-------------------------------------|
| Amplitude ratio              | $A_{rms}^*$  | $\sqrt{2}A_{rms}/D$                 |
| Damping ratio                | $\zeta$      | $c/\sqrt{k(m+m_A)}$                 |
| Forcing frequency ratio      | $f_R$        | $f_r/f_{nw}$                        |
| Frequency ratio              | $f^*$        | $f/f_{nw}$                          |
| Forcing Strouhal number      | $S_f$        | $f_r D/U$                           |
| Mass ratio                   | $m^*$        | $m/m_d$                             |
| Mass-damping parameter       | $\xi$        | $(m^* + C_A)\zeta$                  |
| Reduced velocity             | $U^*$        | $U/(f_{nw}D)$                       |
| Reynolds number              | $Re$         | $UD/\nu$                            |
| Scaled normalised velocity   | $U_S^*$      | $(U^*/f^*)S = f_{vo}/f$             |
| Strouhal number              | $S$          | $f_{vo}D/U$                         |
| Transverse force coefficient | $C_{y(rms)}$ | $F_y/(\frac{1}{8}\rho U^2 \pi D^2)$ |
| Velocity ratio               | $\alpha_R$   | $D\dot{\theta}_{max}/(2U)$          |

TABLE 1. Non-dimensional parameters used in this study. In this table:  $A_{rms}$  is the root-mean-square (r.m.s.) value of the vibration amplitude in the  $y$  direction;  $D$  is the sphere diameter;  $f$  is the body oscillation frequency;  $f_r$  is the frequency of the imposed rotary oscillation; and  $f_{nw}$  is the natural frequency of the system in quiescent water. In addition,  $m$  is the total oscillating mass;  $c$  is the structural damping factor with  $k$  the spring constant;  $U$  is the free-stream velocity;  $\nu$  is the kinematic viscosity;  $m_A$  denotes the added mass, defined by  $m_A = C_A m_d$ , where  $m_d$  is the mass of the displaced fluid and  $C_A$  is the added mass coefficient (0.5 for a sphere);  $\dot{\theta}_{max}$  = maximum angular velocity of the sphere;  $f_{vo}$  is the vortex shedding frequency of a fixed body and  $F_y$  is the fluid force acting on the sphere in the transverse direction.

where  $\dot{\theta}_{max}$  is the maximum angular velocity of the sphere. All other relevant non-dimensional parameters for the current study are listed in table 1.

The governing equation of motion describing the cross-flow motion of the sphere can be written as

$$m\ddot{y} + c\dot{y} + ky = F_y, \quad (2.4)$$

where  $F_y$  is the fluid force in the transverse direction,  $m$  is the total oscillating mass of the system,  $y$  is the displacement in the transverse direction,  $c$  is the structural damping of the system and  $k$  is the spring constant. Using the above equation, the total fluid force in the transverse direction can be calculated with the knowledge of the directly measured displacement, and its time derivatives. The sinusoidal rotation imposed on the sphere can be expressed as

$$\theta(t) = \theta_o \sin(2\pi f_r t), \quad (2.5)$$

where  $\theta$  is time-dependent imposed angular displacement,  $\theta_o$  is maximum angular displacement and  $f_r$  is the forcing frequency. In terms of the angular velocity, the imposed rotation can be represented as

$$\dot{\theta} = 2\pi f_r \theta_o \cos(2\pi f_r t). \quad (2.6)$$

The velocity ratio  $\alpha_R$  given in (2.3) can thus be written as

$$\alpha_R = \frac{\pi f_r \theta_o D}{U}. \quad (2.7)$$

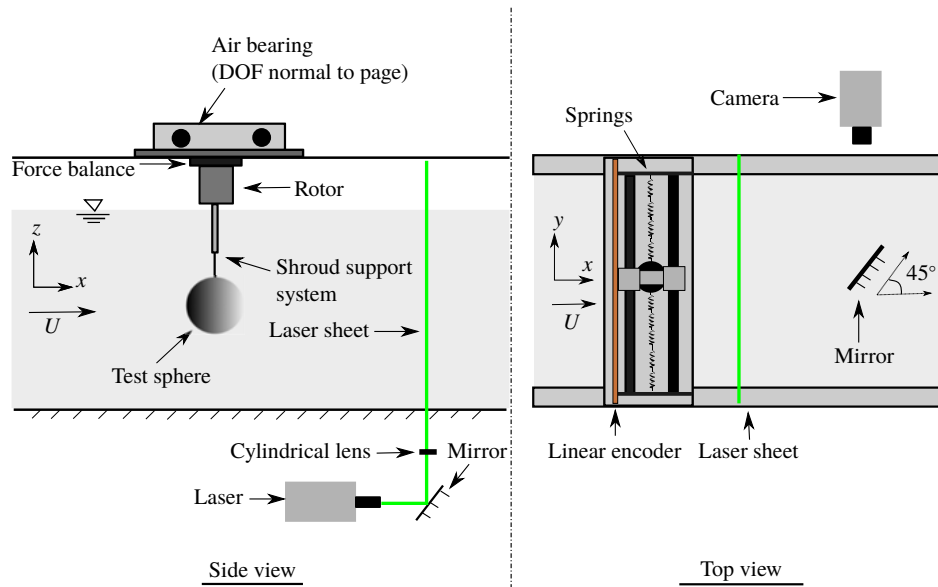


FIGURE 2. (Colour online) Schematic of the experimental set-up for the current study showing the side and top-down views.

### 2.1. Experimental details

The experiments were conducted in the recirculating free-surface water channel of the Fluids Laboratory for Aeronautical and Industrial Research (FLAIR), Monash University, Australia. The test section of the water channel is 600 mm in width, 800 mm in depth and 4000 mm in length. The free-stream velocity can be varied continuously over a range of  $0.05 \leq U \leq 0.45 \text{ m s}^{-1}$ . The free-stream turbulence level for the current experiments was less than 1% at intermediate flow speeds.

Figure 2 shows a schematic of the current experimental set-up. The sphere was elastically mounted in the transverse direction using a low-friction air-bearing system that provides low structural damping. The structural stiffness was controlled by extension springs. More details of the hydro-elastic facility can be found in Zhao *et al.* (2018). A solid spherical ball of diameter  $D = 80 \text{ mm}$  (accuracy within  $\pm 0.200 \text{ mm}$ ) precision-machined from acrylic plastic was used in the current experiments. The sphere model had a smooth polished surface finish. It was supported with a cylindrical shroud support system. The immersed length of the total support set-up for the sphere was one diameter. A more complete description of the current experimental set-up can be found in Sareen *et al.* (2018a).

The rotary motion was driven using a miniature low-voltage micro-stepping motor (model: LV172, Parker Hannifin, US) with a resolution of 25 000 steps/revolution. The rotary oscillations were monitored using a digital optical rotary encoder (model: E5-1000, US Digital, US) with a resolution of 4000 counts/revolution. The sphere displacement was measured using a linear encoder (model: RGH24, Renishaw, UK) with a resolution of  $1 \mu\text{m}$ . The data acquisition and the controls of the flow velocity and the sphere oscillations were automated via customised LabVIEW programs. For each data set, the signal was acquired at a sampling frequency of 100 Hz for more than 100 vibration cycles. The natural frequencies and structural damping of the system in both air and water were measured by conducting free decay tests



individually in air and in quiescent water. The natural frequencies in air and water were found to be  $f_{na} = 0.208 \pm 0.005$  and  $f_{nw} = 0.200 \pm 0.005$ , respectively. The structural damping ratio with consideration of the added mass was determined to be  $\zeta = 4.3 \times 10^{-3} \pm 0.0006$ . The results in the current study are reported for a mass ratio of  $m^* = 12.116 \pm 0.004$ .

To gain better insight into the flow dynamics, particle image velocimetry (PIV) measurements were employed in the cross-plane, 1.5 diameters downstream of the sphere. The flow was seeded with 13  $\mu\text{m}$  hollow micro-spheres having a specific weight of 1.1  $\text{g m}^{-3}$ . A continuous laser (model: MLL-N-532-5W, CNI, China) was used to illuminate a laser plane of  $\sim 3$  mm thickness aligned parallel to the  $y$ - $z$  plane. A mirror was placed at  $45^\circ$  angle to the free-stream direction towards the downstream side of the sphere. The mirror was placed more than 6 diameters downstream of the sphere to limit any upstream disturbance. A distance of  $\approx 2$  diameters is sufficient to avoid any upstream effect of the mirror in this set-up (see Venning 2016). Imaging was performed using a high-speed camera (model: Dimax S4, PCO, AG) with a resolution of  $2016 \times 2016$  pixels<sup>2</sup>. The camera was equipped with a 105 mm Nikon lens, giving a magnification factor of 10.73 pixel  $\text{mm}^{-1}$  for the field-of-view. Velocity fields were deduced using in-house PIV software developed originally by Fouras, Lo Jacono & Hourigan (2008), using  $32 \times 32$  pixel<sup>2</sup> interrogation windows in a grid layout with 50% window overlap. All the vorticity fields shown in the current study were phase-averaged over more than 100 cycles. For each PIV measurement case, a set of 3100 image pairs were collected by sampling at 10 Hz. Each image set was sorted into 24 phase bins based on the sphere's displacement and velocity, resulting in more than 120 image pairs for averaging at each phase. The final phase-averaged vorticity fields were smoothed slightly using an iterative Laplace filter to remove small length-scale structures and to better highlight the larger-scale structures that dominate the wake.

### 3. VIV response of a sphere without control

In this section, we provide a brief overview of what is already known for an elastically mounted sphere undergoing VIV. A more detailed validation study based on the VIV response of an elastically mounted sphere without imposed rotation can be found in Sareen *et al.* (2018a,b).

The VIV response of an elastically mounted sphere (1-DOF) without imposed rotation consists of two fundamental modes of vibration, modes I and II, in the synchronisation region followed by a 'plateau branch', which appears to be a precursor to mode III, seen at higher reduced velocities (Govardhan & Williamson 2005; Sareen *et al.* 2018a,b). The vibrations in the plateau region are not as highly periodic as the vibrations in mode II, albeit that the frequency of oscillation stays close to the natural frequency of the system for the entire  $U^*$  range. Although the vortex shedding remains similar in all three modes of vibration, there is a change in the timing of the vortex formation. Govardhan & Williamson (2005) and Sareen *et al.* (2018a,b) showed that the sphere vibration response transitions from mode I to mode II when the phase difference between the vortex force and the sphere displacement,  $\phi_{\text{vortex}}$ , crosses through  $90^\circ$ , corresponding to an inflection point in the amplitude response. Similarly, within mode II, the phase difference between the total transverse force and sphere displacement,  $\phi_{\text{total}}$ , passes through  $90^\circ$ , corresponding to the peak of the amplitude response. The variations of  $\phi_{\text{total}}$  and  $\phi_{\text{vortex}}$  for the current experimental set-up can be found in Sareen *et al.* (2018a,b).



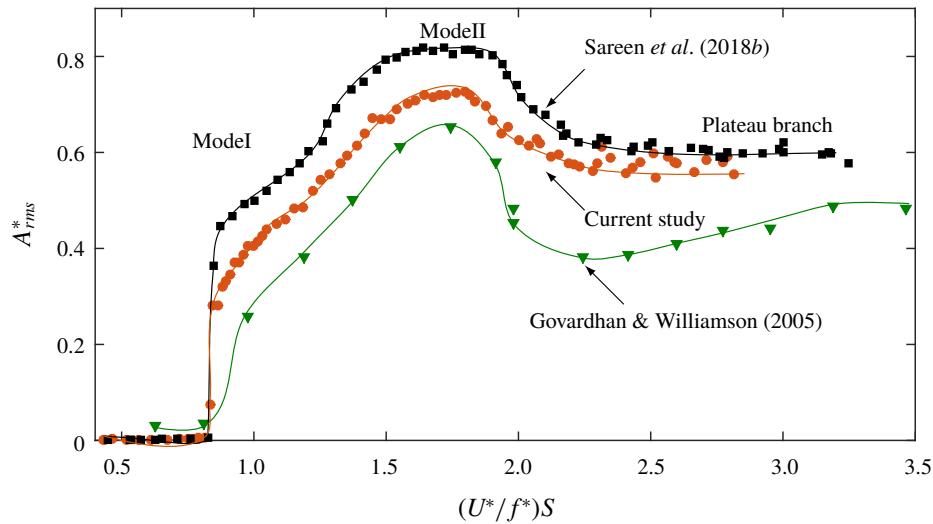


FIGURE 3. (Colour online) Amplitude response of an elastically mounted sphere (1-DOF) obtained in the current study (●) with a mass damping of  $(m^* + C_A)\zeta = 0.03$  compared to previous studies by Govardhan & Williamson (2005) (▼) with a mass damping approximately 0.92 and Sareen *et al.* (2018b) (■) with a mass damping of 0.0169.

Unlike the case of a tethered sphere with 2-DOF, where the modes are separated by a desynchronised reduced velocity range (Jauvtis *et al.* 2001; Govardhan & Williamson 2005), the vibration amplitude for a sphere in the 1-DOF case increases gradually and continuously from mode I to mode II ( $4.5 \lesssim U^* \lesssim 15$ ) leading to an almost constant amplitude in the plateau branch ( $15 \leq U^* < 30$ ). Although it is difficult to demarcate the two modes in the 1-DOF case, there are considerable changes in the phase difference between the sphere displacement and the total transverse force  $\phi_{total}$ , and the phase difference between the sphere displacement and the vortex force,  $\phi_{vortex}$ . The response transitions from mode I to mode II when  $\phi_{vortex}$  crosses through  $90^\circ$ , corresponding to the ‘inflection point’ in the amplitude response. Likewise, within the mode II regime,  $\phi_{total}$  passes continuously through  $90^\circ$ , corresponding to the peak of the amplitude response (Govardhan & Williamson 2005; Sareen *et al.* 2018a,b). Lowering the mass-damping parameter  $(m^* + C_A)\zeta$  leads to greater vibration amplitudes and a widened synchronisation regime, as shown in figure 3. The mass damping of the current study is  $(m^* + C_A)\zeta = 0.03$ , compared to approximately 0.92 in the study by Govardhan & Williamson (2005) and 0.0169 in the study by Sareen *et al.* (2018b). When plotted against the scaled  $U_S^*$ , defined as  $U_S^* = (U^*/f^*)S \equiv f_{vo}/f$ , where  $S$  is the Strouhal number for vortex shedding ( $\approx 0.18$  in this case), the saturation amplitudes (peaks) line up for all the results with different mass-damping parameters, as was demonstrated by Govardhan & Williamson (2005).

#### 4. Effect of rotary oscillations on the vibration response

##### 4.1. Effect of the forcing frequency ratio

In this section, the effect of forcing frequency ratio,  $f_R$ , on the sphere VIV response is discussed. The response is studied for a wide range of frequency ratios varying from 0 to 5 in small increments at several fixed velocity ratios; however, only a few of the representative cases are discussed in detail here. The results are presented for three  $U^*$

values of  $U^* = 6, 10$  and  $15$ , corresponding to modes I, II and mode III, respectively, of the sphere VIV response.

#### 4.1.1. Mode I

Figure 4(a) shows the variation of the r.m.s. of the amplitude of the sphere oscillations,  $A_{rms}^*$ , with  $f_R$ . Figures 4(b) and 4(c) present the frequency power spectral density (PSD) contours of the sphere displacement and the total transverse force, respectively. Figures 4(d) and (e) show the variation of the coefficient of the total transverse force,  $C_{y(rms)}$ , and the total phase difference,  $\phi_{total}$ , respectively.

As evident in figure 4(a), when  $f_R$  is gradually increased from 0 to  $\sim 0.5$ ,  $A_{rms}^*$  progressively decreases in magnitude. The vibrations remain locked to the natural frequency of the system, i.e.  $f^* = 1$ , as shown in figure 4(b). Although the frequency response shows a clear dominant frequency at  $f^* = 1$ , the displacement is modulated in the presence of the forcing, as is clear from the time trace of the sphere displacement shown in figure 5(a). As is also evident from figure 4(c), unlike the frequency contour plot of the sphere displacement, the PSD of the total transverse force does not show a single frequency in this region. Previous studies on rotationally oscillating cylinders have also noted highly modulated states in the non-lock-on regions (Choi *et al.* 2002).

When  $f_R$  is further increased to higher values beyond 0.5, the vibrations start to lock on to  $f_R$  instead of  $f_{nw}$ , as is clearly discernible in figure 4(b). Figure 4(c) shows that the total lift force also locks on to  $f_R$ . This marks the start of the rotary lock-on (RLO) region that extends from  $0.5 \lesssim f_R \lesssim 1.5$  (bounded by dashed vertical lines). In the RLO region, the vibrations and the total transverse force are locked to the forcing frequency instead of the natural frequency, which prohibits the fluid–structure energy transfer. The vibrations are highly suppressed in this range except the case when all the characteristic frequencies of the system are equal, i.e.  $f_R = f^* = f_{nw}$ ; here, the vibration amplitude is close to that of a sphere without imposed rotation, and the displacement signal is highly periodic as shown in figure 5(c). In the RLO region,  $C_{y(rms)}$  drops to lower values with a sudden dip for the  $f_R = f^* = f_{nw}$  case (shown in figure 4d). Also, figure 4(e) shows that there is a sudden jump in the total phase difference,  $\phi_{total}$ , from almost  $0^\circ$  (in phase) to  $180^\circ$  (out of phase). Such a sudden jump in  $\phi_{total}$  is associated with the change in the timing of vortex formation, as will be shown later in § 5 through wake measurements. Such a region of rotary lock-on, where the sphere displacement locks on to the forcing frequency, has also been observed recently for an elastically mounted cylinder under imposed rotary oscillation in the experimental study by Wong *et al.* (2018). They also observed a sudden jump in  $\phi_{total}$  from  $0^\circ$  to  $180^\circ$  for a cylinder in the rotary lock-on region.

One can also note a transition region near the lock-on boundaries in figure 4(b). This region has a richness in frequency content and relatively broadened spectral densities that appear to be caused by competing  $f_{nw}$  and  $f_r$ . This is clearer for higher  $U^*$  responses shown later in this section. The time traces of the displacement signal near the boundaries (shown in figures 5b and 5d) indicate a quasi-periodic state. Baek & Sung (2000) previously reported quasi-periodic states near the lock-on boundaries for a cylinder. When  $f_R$  is further increased to higher values,  $f_R > 2$ , the vibrations again start to lock in to the natural frequency of the system instead of the forcing frequency. For  $2 < f_R \leq 5$ , the vibration amplitudes and  $\phi_{total}$  recover and become close to their initial values without imposed rotation (shown in a and d). The time trace of the sphere displacement (figure 5e) shows a highly periodic response in this range.

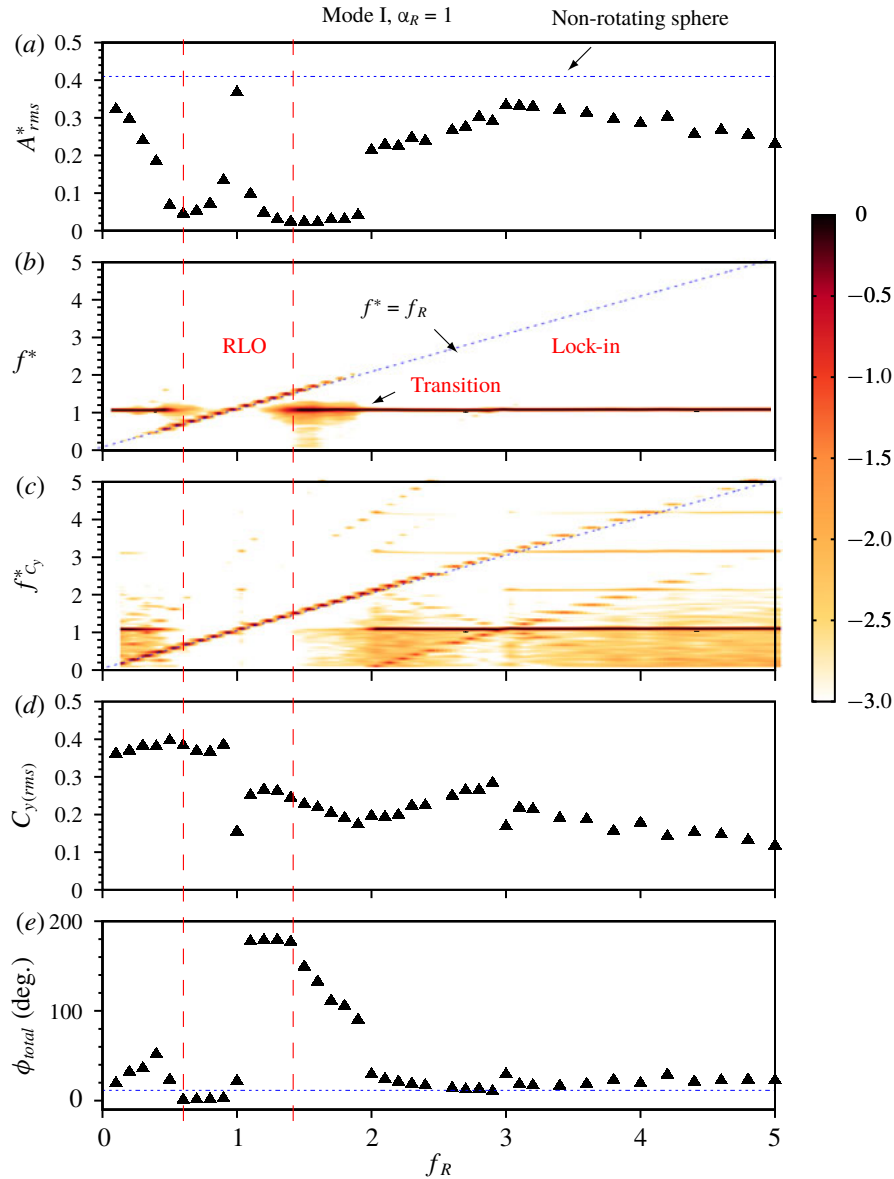


FIGURE 4. (Colour online) The response of an elastically mounted sphere under imposed rotary oscillation is presented as a function of forcing frequency ratio,  $f_R$ , at a fixed velocity ratio of  $\alpha_R = 1$  for the mode 1 response ( $U^* = 6$ ). (a) The variation of r.m.s. of the oscillation amplitude ( $A_{rms}^*$ ). The dotted line represents the amplitude of a sphere with no imposed rotation. (b,c) Power spectral density (PSD) contour plots of the sphere displacement signal and the total transverse force (coefficient), respectively. The dotted line represents where the normalised frequency response,  $f^*$ , equals the forcing frequency ratio  $f_R$ . (d) The variation of the r.m.s. force coefficient of the total transverse lift  $C_{y(rms)}$ . (e) The variation of the total phase difference,  $\phi_{total}$ . The horizontal dotted line shows  $\phi_{total}$  for a non-rotating sphere. The dashed vertical lines indicate the approximate lock-on boundaries. Note that the colour bar applies to the frequency plot, indicating the normalised spectral power on a  $\log_{10}$  scale.

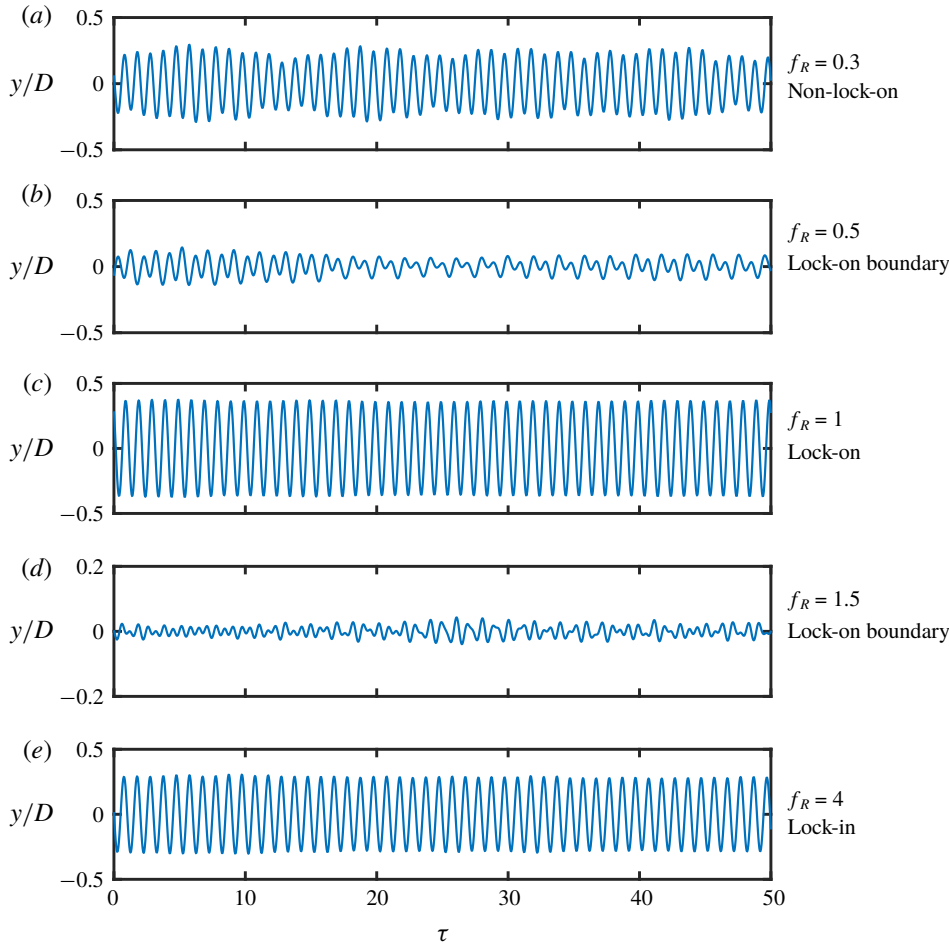


FIGURE 5. (Colour online) Time traces of the sphere displacement in mode I for different frequency ratios of (a)  $f_R = 0.3$ , (b)  $f_R = 0.5$ , (c)  $f_R = 1$ , (d)  $f_R = 1.9$  and (e)  $f_R = 4$ . The velocity ratio is fixed at  $\alpha_R = 1$ .

Figure 6 shows the response characteristics, similar to those shown previously, but for a relatively higher velocity ratio of  $\alpha_R = 1.5$  in mode I. One can clearly see the difference that the transition region (or the non-lock-on region, where the flow is neither locked in nor locked on), where a wide spectrum of frequencies is observed, now extends for a wider range of  $f_R$  values between  $1.5 \lesssim f_R \lesssim 3$ . Also, the lock-in region is observed for a narrow range of high  $f_R$  values in the range  $3 < f_R < 5$ . The vibration amplitude in the lock-in region does not recover to the values close to the non-rotating case but rather remains  $< 0.2D$ . So, as the velocity ratio is increased to  $\alpha_R = 1.5$ , the transition region becomes wider, and lock-in occurs for a narrow range of  $f_R$  values. For even higher velocity ratio of  $\alpha_R = 2$  (not discussed here), the lock-in region disappears, and the transition range extends until the maximum  $f_R$  tested in the current study.

#### 4.1.2. Mode II

Figure 7 shows the response quantities for  $U^* = 10$ , (in the heart of mode II) at a fixed velocity ratio of  $\alpha_R = 0.5$ . One can note here that unlike mode I, the vibration

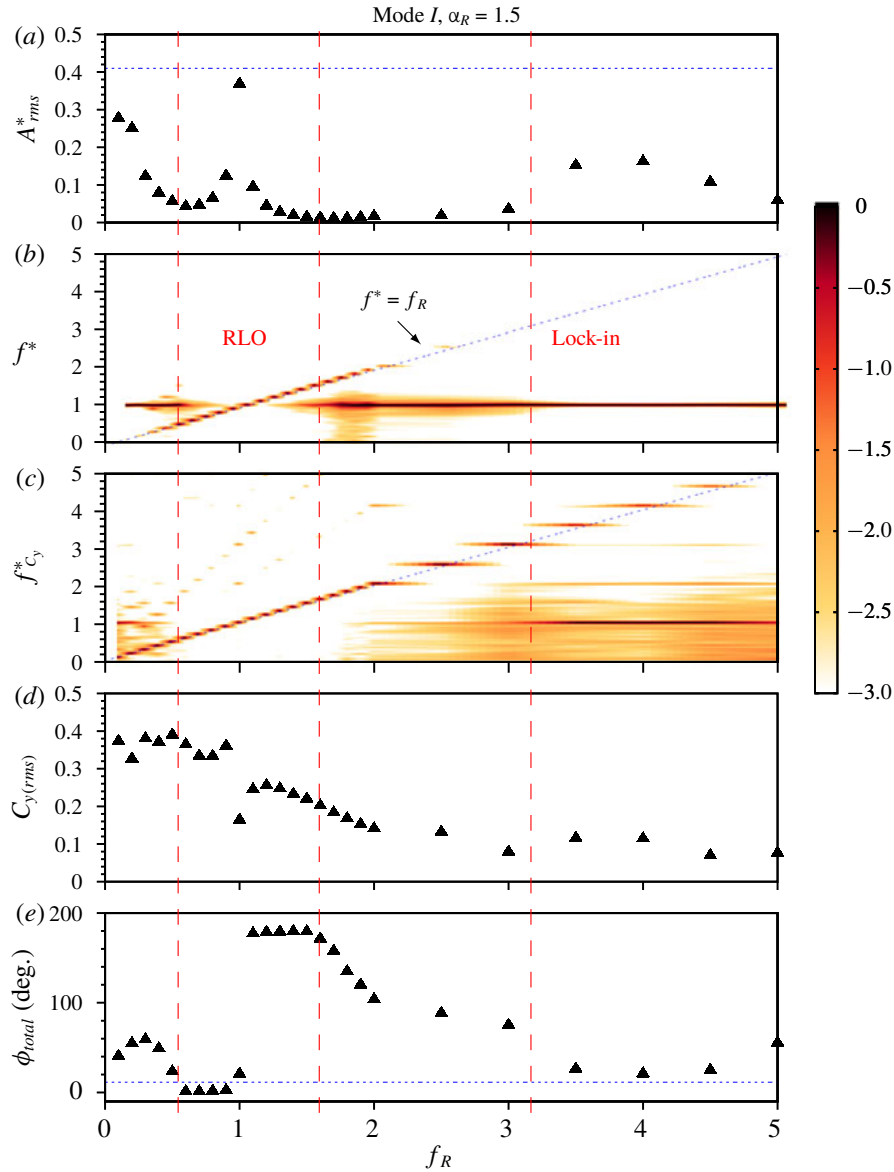


FIGURE 6. (Colour online) The response of an elastically mounted sphere under imposed rotary oscillation is presented as a function of forcing frequency ratio,  $f_R$ , at the fixed velocity ratio of  $\alpha_R = 1.5$  in the mode I region ( $U^* = 6$ ). Refer to figure 4 for further details.

amplitudes do not drop at all before entering the RLO region. However, as the sphere response enters the RLO region, the response characteristics are similar to mode I, with a sudden jump in  $A_{rms}^*$  for  $f_R = 1$  and a corresponding drop in  $C_{y(rms)}$  and  $\phi_{total}$ . Immediately past  $f_R = 1$ , the vibrations become out of phase with the total transverse force, and the vibration amplitudes drop to highly reduced values. A transition region with a wide spectrum of frequencies and highly modulated vibration amplitudes (see figure 8b) is also evident in the frequency contour plot as the response exits the RLO region. For  $2 \lesssim f_R \lesssim 3$ , the vibrations lock back to  $f_{nw}$  and the vibration amplitudes

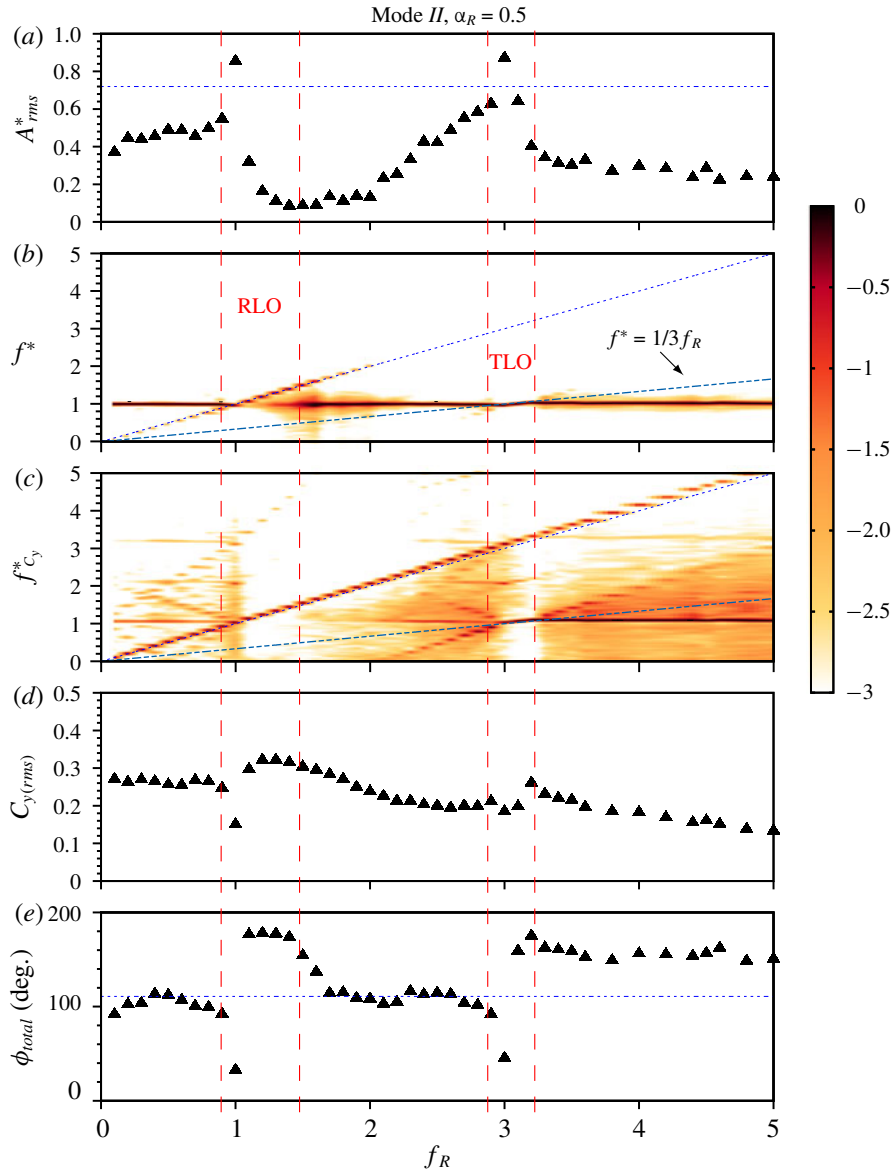


FIGURE 7. (Colour online) The response quantities of an elastically mounted sphere with imposed rotary oscillations is presented as a function of forcing frequency ratio,  $f_R$ , at a fixed velocity ratio of  $\alpha_R = 0.5$  in mode II ( $U^* = 10$ ). Refer to figure 4 for further details.

start to recover. The dominant frequency of the transverse force, however, remains the forcing frequency (see figure 7c). As the response approaches the vicinity of  $f_R = 3$ , the vibrations lock on to the third subharmonic of the forcing frequency,  $f^* = f_R/3$ , although the effect is localised to a small  $f_R$  range. Figure 7(c) shows that the transverse force locks on simultaneously to the third harmonic as well. This is termed ‘tertiary lock-on’ (TLO). Such a region of tertiary lock-on has also been observed previously for a cylinder allowing 1-DOF transverse movement under imposed rotary oscillation (Wong *et al.* 2018), and also for a rigidly mounted cylinder (Choi *et al.* 2002; Thiria *et al.* 2006). The TLO region is also characterised by a sudden jump

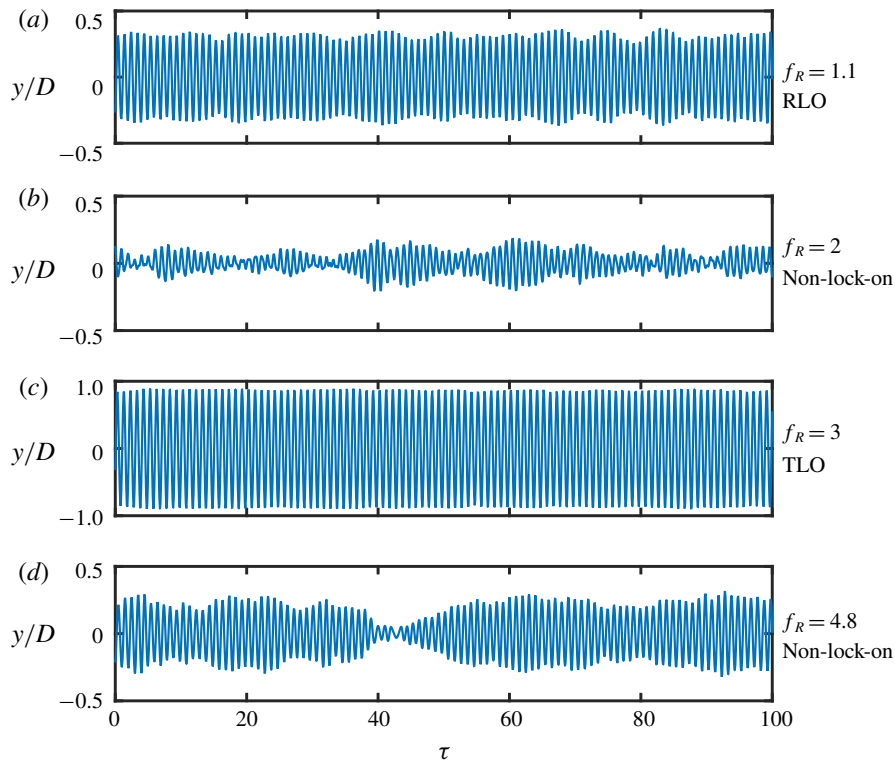
716 *A. Sareen, J. Zhao, J. Sheridan, K. Hourigan and M. C. Thompson*


FIGURE 8. (Colour online) Time traces of the sphere displacement in mode II for different frequency ratios of (a)  $f_R = 1.1$ , (b)  $f_R = 2$ , (c)  $f_R = 3$  and (d)  $f_R = 4.8$ . The velocity ratio is fixed at  $\alpha_R = 0.5$ .

in  $\phi_{total}$  and  $C_{y(rms)}$ , as evident from figures 7(e) and (d), respectively. The time trace of the sphere displacement reveals a highly periodic response in the TLO region (see figure 8c). As the sphere exits the TLO region, the dominant frequency again becomes  $f_{nw}$ ; however, unlike standard lock-in, there is no clean single frequency response. The vibrations exhibit amplitude modulation, as evident from figure 8(d). The vibration amplitude drops to lower values,  $\sim 0.2$ , and remains almost constant until  $f_R = 5$ .

It is interesting to see how the response changes as the velocity ratio is increased to  $\alpha_R = 1$ . Figure 9 shows the observed response for a higher velocity ratio of  $\alpha_R = 1$  in mode II. The lock-in and the tertiary lock-on regions are absent for  $\alpha_R = 1$ , unlike the  $\alpha_R = 0.5$  case. Again, the vibration amplitude for the  $f_R = f^* = f_{nw}$  case in the mode II region is even higher than the non-rotating case (shown as a dashed line in a). An interesting point to note here is that for  $f_R > 2$ , although  $\phi_{total}$  recovers to its initial non-rotating values, the vibration amplitude does not recover to its initial value as observed in mode I. Near the lock-on boundaries, a rich frequency content is observed, however; it extends until  $f_R = 3$ . For  $f_R > 3$ , the frequency no longer follows the  $f_R$  line and the vibration is highly reduced. In this case, the vibration is neither locked in (as characterised by a single frequency response at  $f^* = 1$ ) nor locked on (as characterised by a single frequency response at  $f^* = f_R$ ). Interestingly, the dominant frequency of the lift force remains  $f_R$  for  $f_R > 3$ . Overall, the characteristics of the RLO region remain the same with a sudden jump in  $\phi_{total}$  from  $0^\circ$  to  $180^\circ$ , and a drop in  $C_{y(rms)}$  correlated with the jump in  $A_{rms}^*$ .



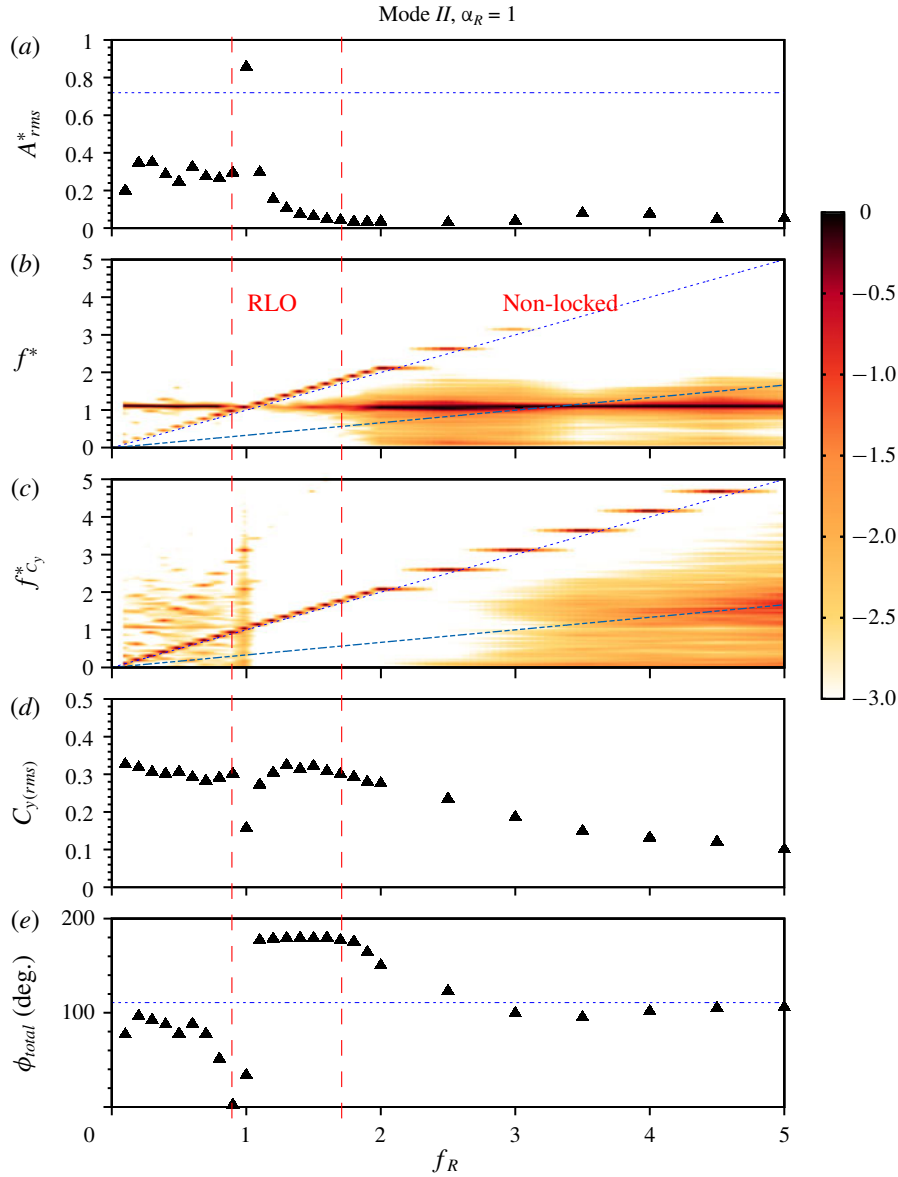


FIGURE 9. (Colour online) The response of an elastically mounted sphere with imposed rotary oscillations is presented as a function of forcing frequency ratio,  $f_R$ , at a fixed velocity ratio of  $\alpha_R = 1$  in mode II ( $U^* = 10$ ). Refer to figure 4 for further details.

#### 4.1.3. Mode III

Figure 10 shows the response curves at even higher  $U^*$  values towards the mode III region. As evident from the figure, the width of rotary lock-on region is decreased in mode III, extending only between  $0.8 < f_R < 1.4$ . Another interesting point to note is that for the  $f_R = f^* = f_{nw}$  case, the vibration amplitude reaches a value of more than one sphere diameter, which is  $\sim 66\%$  higher than for the non-rotating case. The imposed rotation is very effective in mode III in suppressing vibration for the entire range of  $f_R$  tested in the current study (except of course the  $f_R = f_{nw}$  resonant case). The response



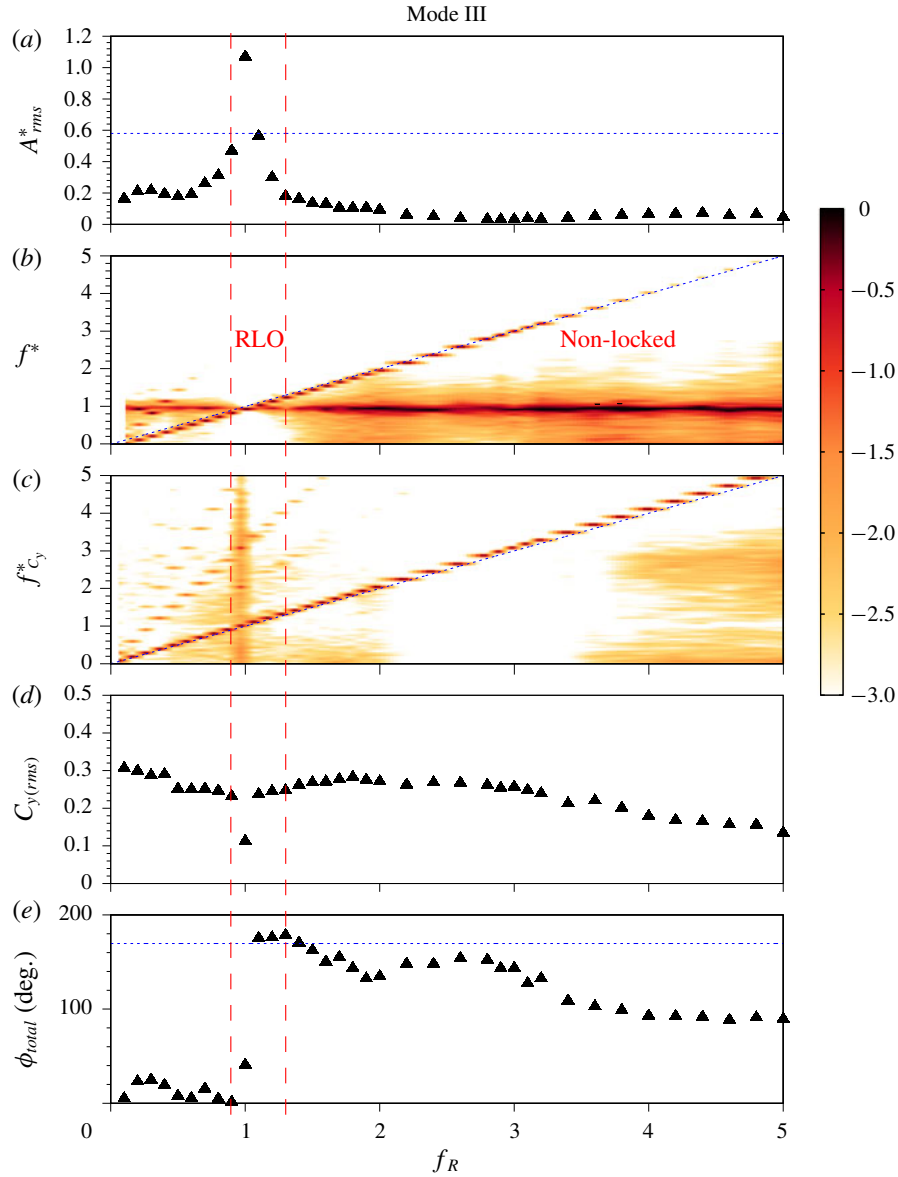


FIGURE 10. (Colour online) The response of an elastically mounted sphere with imposed rotary oscillations is presented as a function of forcing frequency ratio,  $f_R$ , at a fixed velocity ratio of  $\alpha_R = 1$  in mode III ( $U^* = 15$ ). Refer to figure 4 for further details.

characteristics in mode III are quite similar to mode II (the  $\alpha_R = 1$  case), where the vibrations do not recover to higher values after exiting the rotary lock-on region, and a broad frequency spectrum is observed for higher  $f_R$  values. However, in mode III, the vibration frequency and the lift frequency follows the  $f^* = f_R$  line for the entire range of  $f_R$  tested, unlike in the case of mode II. It appears that the transition region extends until  $f_R = 5$  in this case. Interestingly, a clean single frequency response is observed for the lift force for  $2 \lesssim f_R \lesssim 4$ , as seen in figure 10(c).

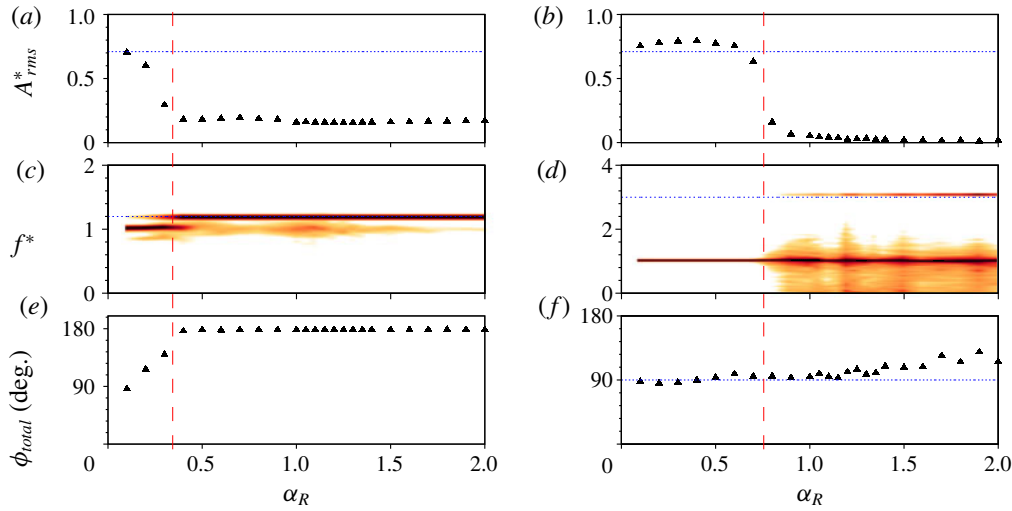


FIGURE 11. (Colour online) The response quantities of an elastically mounted sphere with imposed rotary oscillations is presented as a function of velocity ratio,  $\alpha_R$ , at fixed frequency ratios of  $f_R = 1.2$  (a,c,e) and  $f_R = 3$  (b,d,f) in mode II. The dashed red line demarcates the two regions obtained as the velocity ratio is varied in the above cases. The vibrations are greatly suppressed beyond the dashed line for both the frequency ratios shown above.

#### 4.2. Effect of velocity ratio

In this section, the effect of another important forcing parameter on the sphere vibration response, the velocity ratio  $\alpha_R$ , is investigated. The velocity ratio was varied over the range  $0 \leq \alpha_R \leq 2$  in small increments, keeping constant values of  $U^*$  and  $f_R$ . The response was studied for  $U^* = 10$  (heart of mode II) and frequency ratios of  $f_R = 1$  (resonance),  $f_R = 1.2$  (lock-on) and  $f_R = 3$  (non-lock-on).

Figure 11(a) shows the response as a function of  $\alpha_R$  at a constant value of  $f_R = 1.2$  in mode II. It can be seen that when the velocity ratio is increased gradually to  $\alpha_R = 0.5$ , there is a progressive decrease in  $A_{rms}^*$ . The dominant frequency remains as  $f_{nw}$  (see figure 11(c)). However, when  $\alpha_R$  is increased beyond 0.5, the oscillation frequency locks on to the forcing frequency ( $f^* = 1.2$ ), as shown in figure 11(c), and the displacement becomes out of phase with the total transverse force, as shown in figure 11(e). The vibrations are highly suppressed for  $\alpha_R \geq 0.5$  with  $\sim 77.7\%$  reduction in the vibration amplitude compared to the case of a sphere without imposed rotation. This demonstrates that values of  $\alpha_R \geq 0.5$  are desirable for effective suppression of VIV in mode II, at least for  $f_R = 1.2$ . An obvious question is that when  $f_R$  is outside the lock-on range, what velocity ratios are favourable for reducing the amplitude of oscillations?

To answer this question, another frequency ratio was chosen in the non-lock-on range and the response was investigated. Figure 11(b,d,f) shows the response quantities for  $f_R = 3.0$  in mode II. Initially, when  $\alpha_R$  is increased, there are no significant changes in the vibration amplitude compared to the case of the sphere without any imposed forcing. The oscillations are locked to the natural frequency of the system, as shown in figure 11(d). However, there is a sharp reduction in  $A_{rms}^*$  beyond  $\alpha_R \gtrsim 0.7$ . For higher  $\alpha_R$  values, the vibrations are suppressed completely. In the frequency spectrum plot figure 11(d), a wide spectrum of frequencies is evident

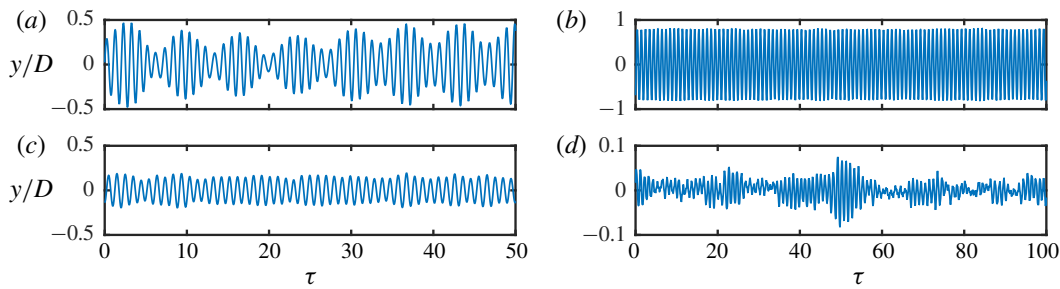
720 *A. Sareen, J. Zhao, J. Sheridan, K. Hourigan and M. C. Thompson*


FIGURE 12. (Colour online) Time traces of the sphere displacement for frequency ratios  $f_R = 1.2$  (a,c) and  $f_R = 3$  (b,d) at two different velocity ratios of  $\alpha_R = 0.3$  and  $\alpha_R = 1.3$ .

for  $\alpha_R \geq 0.7$ . The forcing frequency  $f_R = 3$  is also present; however,  $f_{nw}$  remains the dominant frequency. For this case, the sphere vibrations are neither locked in (single frequency response at  $f^* = 1$ ) nor locked on (single frequency response at  $f^* = f_R$ ) and the frequency contour map is characterised by a wide spectrum of frequencies.  $\phi_{total}$  remain close to  $90^\circ$  for the entire range of  $\alpha_R$  (except the higher  $\alpha_R$  values, where small deviation can be observed). An interesting thing to note here is that suppression of vibrations can be observed for a sphere even in the non-lock-on range for high enough  $\alpha_R$  values.

Figure 12(a,c) shows the time trace of the sphere displacement at  $f_R = 1.2$  for the two different velocity ratios of  $\alpha_R = 0.3$  (a) and  $\alpha_R = 1.3$  (c). For  $\alpha_R = 0.3$ , a pulsating signal is evident with a beating frequency  $\sim |f_r - f_{nw}|$ . For  $\alpha_R = 1.3$ , on the other hand, beating is not clear and the vibrations are not very periodic. Figure 12(b,d) shows the time trace of the sphere displacement at  $f_R = 3$  for two different velocity ratios  $\alpha_R = 0.3$  (b) and  $\alpha_R = 1.3$  (d). For  $\alpha_R = 0.3$ , the vibrations are highly periodic without any signs of amplitude modulation. On the contrary, at  $\alpha_R = 1.3$ , where highly reduced vibrations are observed ( $A_{rms}^* < 0.08$ ), the displacement signal is highly non-periodic with chaotic intermittent vibrations similar to the ones reported by Sareen *et al.* (2018a) in their experimental study on an elastically mounted sphere with imposed constant rotation.

Another interesting case to examine is  $f_R = 1$ , where vibration amplitudes higher than the non-rotating case can be observed, depending on the  $U^*$  and  $\alpha_R$ , as was shown in § 4.1. Figure 13 shows the response quantities for  $f_R = 1$  for varying velocity ratios in mode II. As  $\alpha_R$  increases from  $0 \leq \alpha_R \leq 0.5$ ,  $\phi_{total}$  decreases almost linearly from  $90^\circ$  to  $0^\circ$  but the vibration amplitudes remain close to the non-rotating sphere case. In this range, the sphere displacement has modulation over a very large period of  $\sim 40$  cycles, as is clear from the time trace of the sphere displacement shown in figure 13(b). The degree of modulation decreases for  $\alpha_R = 0.6$  (see figure 13(d)). For  $0.5 < \alpha_R \leq 2$ , the vibration amplitudes increase by  $\sim 94\%$  compared to the non-rotating sphere case. In this range, the displacement is always in phase with the total transverse force acting on the sphere, and the vibrations become highly periodic without any signs of amplitude modulation (see figure 13(f)).

To summarise the discussions so far on the effect of the two main forcing parameters on the vibration response of a sphere, all the results are synthesised and presented as contour plots in Figure 14. Figure 14(a–c) shows the amplitude response ( $A_{rms}^*$ ) contours over the  $f_R - \alpha_R$  parameter space for all three modes of sphere vibrations. The contour plots show there are two observed lock-on regions: rotary lock-on (RLO) and tertiary lock-on (TLO). These regimes are determined by examining the body vibration frequency response as a function of  $f_R$  for each fixed  $\alpha_R$ . Such regions have also been recently identified for an elastically mounted

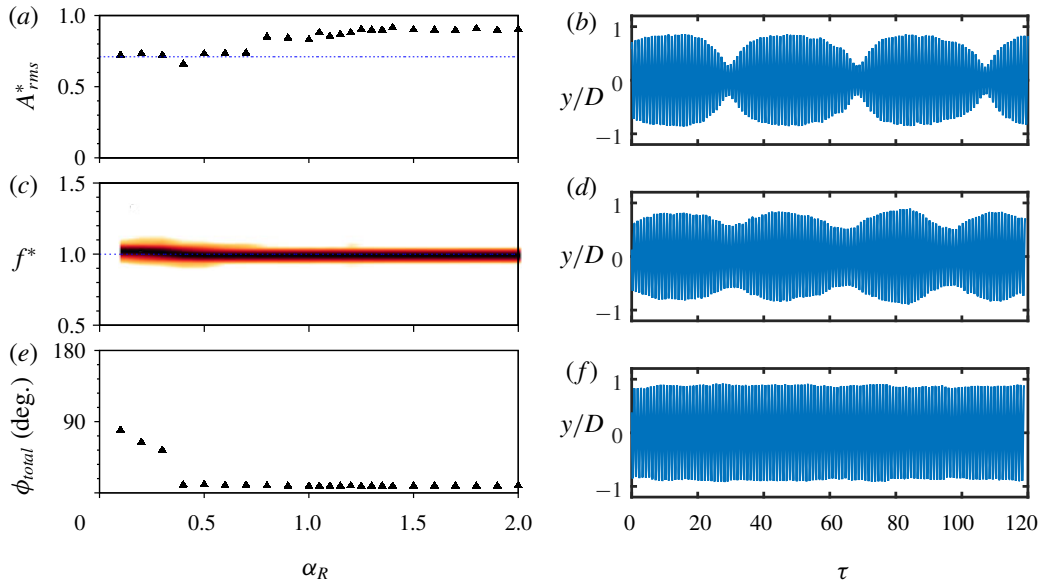


FIGURE 13. (Colour online) The response quantities of an elastically mounted sphere with the imposed rotary oscillations is presented as a function of velocity ratio,  $\alpha_R$ , at a fixed frequency ratio of  $f_R = 1$  (a,c,e) for mode II. (b,d,f) The time traces of the sphere displacement for  $\alpha_R = 0.3$  (d),  $\alpha_R = 0.6$  (d) and  $\alpha_R = 1.2$  (f).

cylinder by Wong *et al.* (2018). Evidently, these lock-on regions are a function of all three forcing parameters:  $f_R$ ,  $\alpha_R$  and  $U^*$ . For all three sphere vibration modes, the RLO region exists over a narrow window in the vicinity of  $f_R = 1$ . For  $\alpha_R < 1$ , the RLO region occurs in a narrow band around  $f_R = 1$  but becomes considerably wider for higher velocity ratios, resulting in an inverted pear-shaped region. A tertiary lock-on region (TLO) was also observed in mode II in the vicinity of  $f_R = 3$  for very low velocity ratios of  $\alpha_R \leq 0.5$ . The RLO region remains fairly similar in mode I and mode II. However, for mode III, the RLO region becomes narrower for  $\alpha_R \leq 1$  and considerably wider for higher velocity ratios of  $\alpha_R > 1.5$ . As evident from the contour plots, the reduced velocity can also influence the lock-in and TLO regions. The lock-in region becomes significantly smaller for mode II ( $U^* = 10$ ) compared to mode I ( $U^* = 6$ ), and vanishes completely for mode III ( $U^* = 15$ ). TLO, however, was only observed for  $f_R = 3$  at very low velocity ratios ( $\alpha_R \leq 0.5$ ) in mode I and mode III.

In general, mode I was found to be quite robust, requiring high velocity ratios for the suppression of vibrations. The control was highly effective in mode III, with a highly reduced response obtained over the entire parameter space studied (except for the  $f_R = f_{nw}$  case). For the  $f_R = f_{nw}$  case, the sphere exhibited an ‘enhanced resonance’, where vibrations increased to much higher values compared to the non-rotating case. Overall, higher velocity ratios of  $\alpha_R \geq 1$  were effective in suppressing the vibrations. Suppression of vibration was observed even in the non-lock-on region at high  $f_R$  and  $\alpha_R$  values.

#### 4.3. Effect of reduced velocity

In this section, the effect of another important flow parameter, the reduced velocity,  $U^*$ , is discussed. In order to systematically investigate the effect of  $U^*$ , both the

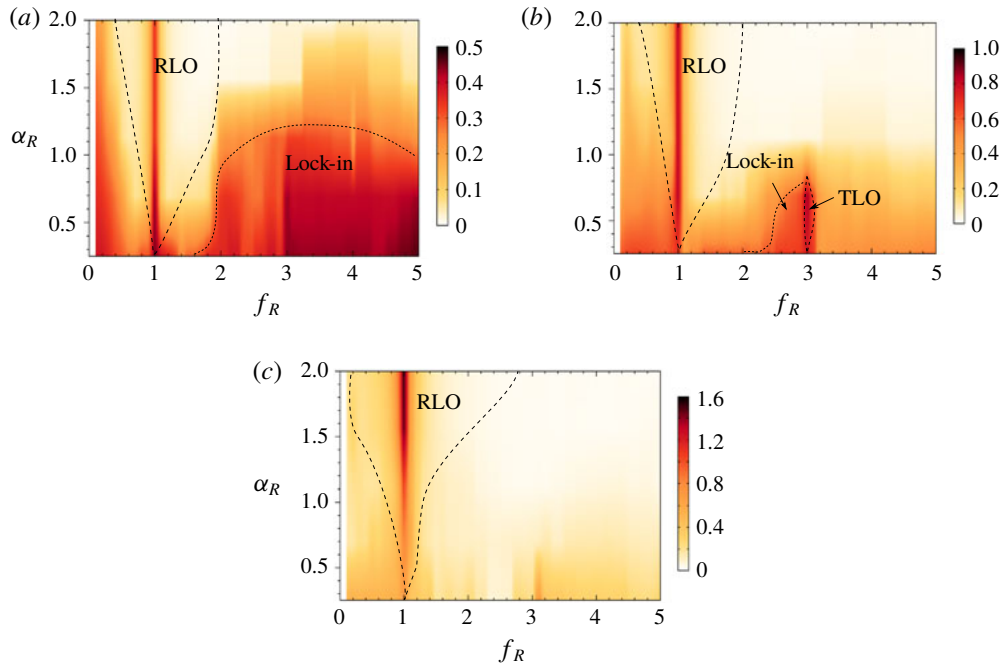
722 *A. Sareen, J. Zhao, J. Sheridan, K. Hourigan and M. C. Thompson*


FIGURE 14. (Colour online) Plots showing the contours of  $A_{rms}^*$  as a function of  $\alpha_R$  and  $f_R$  in mode I (a), mode II (b) and mode III (c). Different regions highlighted with dashed lines.

other forcing parameters ( $\alpha_R$  and  $f_R$ ) were kept constant and  $U^*$  was varied in small increments from 0 to 20. The results are presented for  $\alpha_R = 1$  at several representative  $f_R$  values.

Figure 15 shows the response quantities for  $f_R = 0.3$  (a) and  $f_R = 0.9$  (b) at a fixed velocity ratio of  $\alpha_R = 1$ . In the plots depicting the phases, the phase difference between the imposed rotary oscillation and the sphere displacement,  $\phi_{rot}$ , is also shown along as  $\phi_{total}$ . It is found that  $\phi_{rot}$ , i.e. the phase difference between the imposed rotary oscillation and the sphere displacement is an important parameter affecting the response of the sphere to the imposed rotation during lock-on conditions. Readers should note here that  $\phi_{rot}$  is only useful in lock-on regions, where the sphere displacement is locked to the forcing frequency. As evident from panel (a), for  $U^*$  varying from  $\sim 4.5$  to  $\sim 12$ , the vibrations are locked to the natural frequency. There is an increase in the displacement amplitude with a corresponding increase in the transverse force coefficient. The displacement is in phase with the total transverse force (or  $\phi_{total} = 0$ ). The time trace of the sphere displacement shows a highly periodic response in this region (see figure 16a). This indicates the occurrence of lock-in over this range. However, for higher values of  $U^* > 12$ ,  $\phi_{rot}$  drops to almost zero. In this region, the vibrations are locked to  $f_R$  and the frequency at  $f_{nw}$  becomes weaker in power. There is no significant increase in the amplitude response up to  $U^* = 20$ . This region cannot be termed lock-in. The time trace shows amplitude and frequency modulation in this range (see figure 16c). In this region, the two frequencies compete with each other; such a region is termed the ‘lock-in + RIV’ region in the text.

For  $f_R = 0.9$ , the response clearly has two regions with different characteristic behaviours. For  $0 \leq U^* \lesssim 8$ , the vibrations are locked to  $f_R$  instead of  $f_{nw}$ , and there

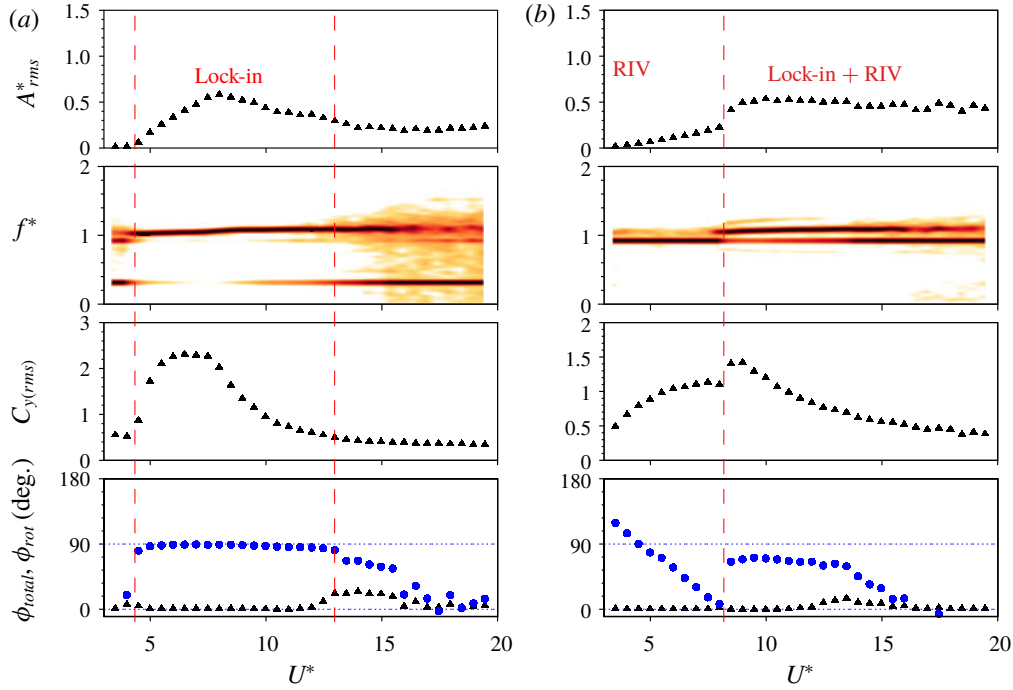


FIGURE 15. (Colour online) The response of an elastically mounted sphere with imposed rotary oscillations is presented as a function of reduced velocity for a fixed frequency ratio of  $f_R = 0.3$  (a) and  $f_R = 0.9$  (b) at  $\alpha_R = 1$ . See figure 4 for a detailed description of the figures. The blue-filled circular symbols in the phase plots represent the phase difference between the rotary oscillations and the displacement. The ‘Lock-in + RIV’ region highlighted for  $f_R = 0.9$  indicates the  $U^*$  values for which the two frequencies compete with each other.

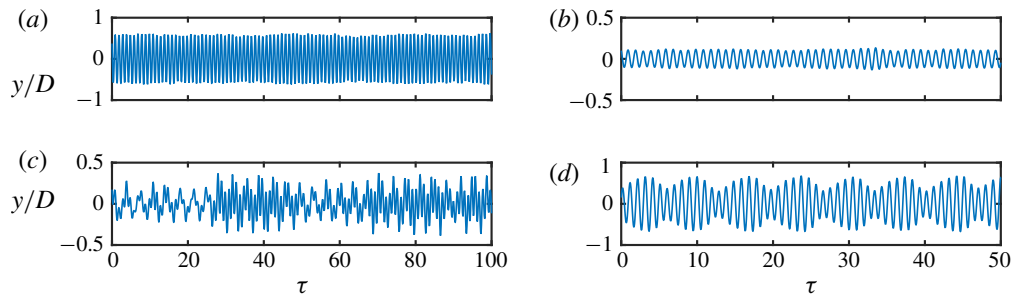


FIGURE 16. (Colour online) Time traces of the sphere displacement for  $f_R = 0.3$  (a,c) and  $f_R = 0.9$  (b,d) for a velocity ratio of  $\alpha_R = 1$ . (a,c) Time traces for  $U^* = 8$  and 15, respectively. (b,d) Time traces for  $U^* = 6$  and  $U^* = 10$ , respectively.

is a linear decrease in  $\phi_{rot}$  from  $\sim 130^\circ$  to  $0^\circ$ . This is clearly not lock-in. It will be shown later in the text that such a region corresponds to the rotary-induced vibrations (RIV). Nevertheless, the time trace shows highly periodic vibrations in this range. For  $8 < U^* < 14$ , on the other hand, the behaviour is similar to lock-in. The vibrations are locked to  $f_{nw}$ , there is a jump in  $C_{y(rms)}$ , and  $\phi_{total}$  remains close to  $0^\circ$ . However,



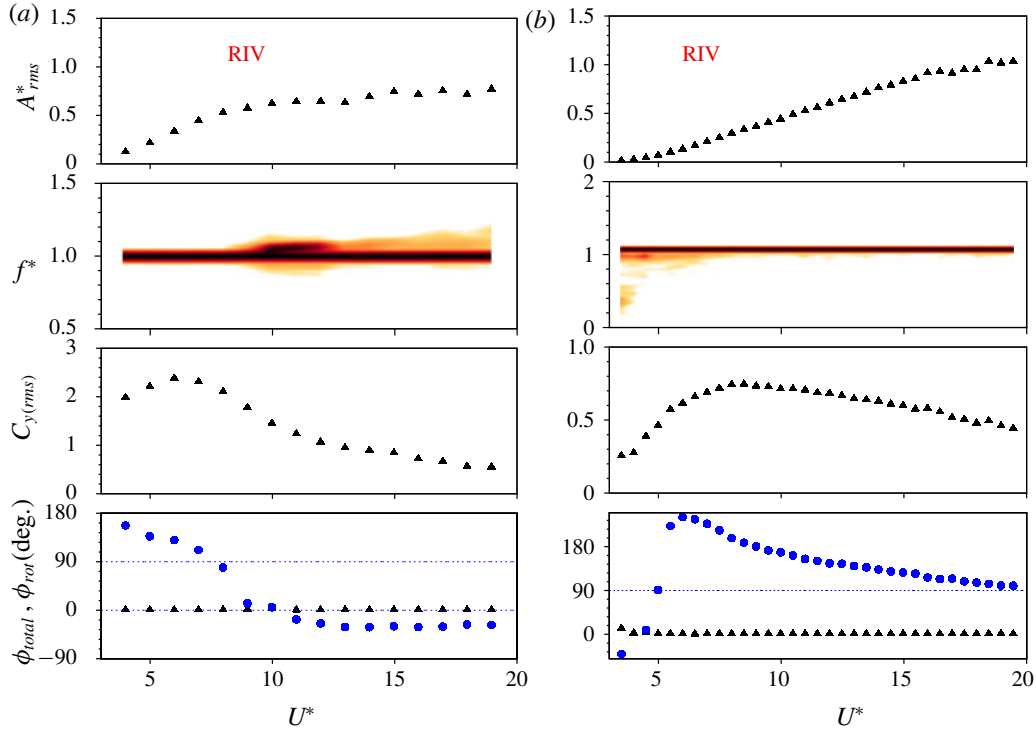
724 *A. Sareen, J. Zhao, J. Sheridan, K. Hourigan and M. C. Thompson*


FIGURE 17. (Colour online) The response of an elastically mounted sphere with imposed rotary oscillations is presented as a function of reduced velocity for a fixed frequency ratio of  $f_R = 1.0$  (a) and  $f_R = 1.1$  (b) at a value of  $\alpha_R = 1$ . Refer to figure 4 for further details.

the time trace of the displacement signal shows beating in this range due to  $f_r$  being very close to  $f_{nw}$ . When  $U^*$  is increased beyond  $U^* \geq 15$ , the vibrations lock to  $f_R$  again. In this range, both  $\phi_{total}$  and  $\phi_{rot}$  approach  $0^\circ$ . In this region, extending from  $8 < U^* < 20$ , it can be conjectured that the two frequencies compete with each other and there is no clear lock-in or lock-on region.

Therefore, depending on the  $U^*$  value, the vibrations may lock to  $f_{nw}$  or  $f_R$ . If vibrations lock to  $f_{nw}$  in the synchronisation region, lock-in or resonance is observed; however, if they lock to  $f_R$ , the response is reflected in  $\phi_{rot}$ . Monotonically decreasing  $\phi_{rot}$  values coincide with monotonically increasing  $A_{rms}^*$  (that lead to RIV response) and constant  $\phi_{rot}$  values coincide with constant amplitudes. This behaviour will be further clarified in later discussions.  $\phi_{rot}$  was plotted here to highlight its correlation with the amplitude response in the lock-on regions. During lock-in, however,  $\phi_{rot}$  does not signify anything as the displacement and rotary oscillation do not exhibit the same frequency:  $\phi_{rot}$  is fixed at  $90^\circ$  in lock-in regions.

#### 4.3.1. Rotary-induced vibrations

Figure 17 shows the response for  $f_R = 1$  (a) and  $f_R = 1.1$  (b). Overall, it is evident that neither frequency ratio exhibits the typical bell-shaped response known for a non-rotating sphere VIV over this  $U^*$  range. Unlike the non-rotating case,  $\phi_{total}$  remains at  $0^\circ$  for the entire range of  $U^*$  tested. Also, the vibrations are locked to the forcing frequency. Clearly, this is not a lock-in phenomenon.

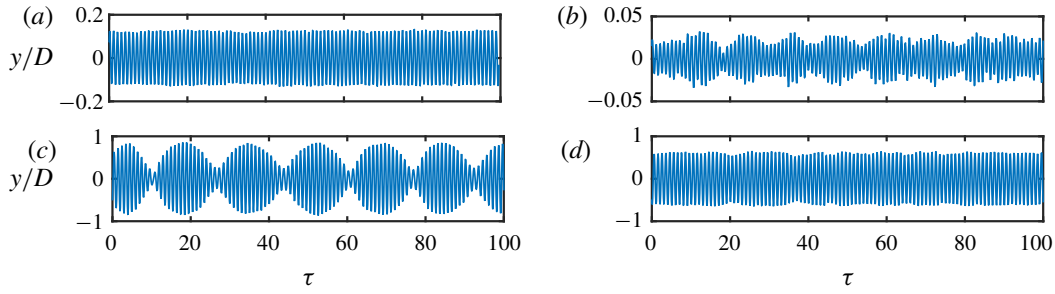


FIGURE 18. (Colour online) Time traces of the sphere displacement for  $f_R = 1$  (a,c) and  $f_R = 1.1$  (b,d) for reduced velocities of  $U^* = 4$  and  $U^* = 12$ .

For  $f_R = 1$ , initially the vibration amplitude increases almost linearly in the range  $0 < U^* < 10$ . In this range,  $\phi_{rot}$  is not fixed at  $\sim 90^\circ$ , as was previously found for lock-in, but decreases monotonically from  $\sim 170^\circ$  to lower values. The vibrations are highly periodic as clear from figure 18(a), and the frequency contour plot shows a clean single frequency response at  $f^* = 1$ . Interestingly, a ‘kink’ can be observed in the frequency response when  $\phi_{rot}$  crosses zero at  $U^* = 10$ . Beyond this point in  $U^*$ , there are large modulations in the sphere displacement signal (at a low frequency) as evident from the time trace shown in figure 18(c). Also,  $\phi_{rot}$  and  $A_{rms}^*$  remain almost constant.

For  $f_R = 1.1$ , initially the vibrations are not very periodic in the range  $0 < U^* < 6$  (see figure 18b) but as the reduced velocity is increased further ( $U^* \geq 6$ ), the vibrations become periodic (see figure 18d). For  $U^* \geq 6$ , the frequency plot shows a clean frequency at  $f^* = f_R = 1.1$ . Also,  $\phi_{rot}$  decreases monotonically from  $\sim 260^\circ$  to  $90^\circ$ , and correspondingly, the vibration amplitude increases monotonically (almost linearly) with the increase in reduced velocity for the entire range of  $U^*$  tested in the current study.

The vibration response observed in the above cases show some similarities to the ‘wake-induced vibration (WIV)’ reported by Assi, Bearman & Meneghini (2010), or called ‘wake-induced galloping’ by Bokaian & Geoola (1984) and Brika & Laneville (1999) for an elastically mounted cylinder placed downstream of a fixed cylinder. The latter studies reported that for a fixed structural damping, the downstream cylinder can exhibit vortex resonance, WIV, combined vortex resonance and WIV, or separately vortex resonance and WIV depending on the cylinders’ separation. Assi *et al.* (2010) suggested that wake-induced vibration (WIV) requires a frequency input such as upstream vortex shedding to occur. They also highlighted that the upstream vortices interfering with the downstream cylinder induce fluctuations in the fluid force. A favourable phase lag between the fluid force and the displacement ensures a positive energy transfer from the flow to the structure that sustains the oscillations. One may infer here that the wake of the fixed cylinder placed upstream provides an oscillating forcing to the elastically mounted cylinder placed downstream. In the current study, however, the forcing is imposed on the sphere itself in contrast to the less controlled forcing of their study. The vibrations are not generated by a wake upstream but rather by rotary oscillations imposed on the sphere. Thus, it makes sense to describe such vibrations as ‘rotary-induced vibrations (RIV)’. Similar vibrations have also been observed recently for an elastically mounted cylinder with imposed rotary oscillation by Wong *et al.* (2018). They reported vibration increasing monotonically with  $U^*$  for  $f_R = 1$  and  $\alpha_R = 1$ .



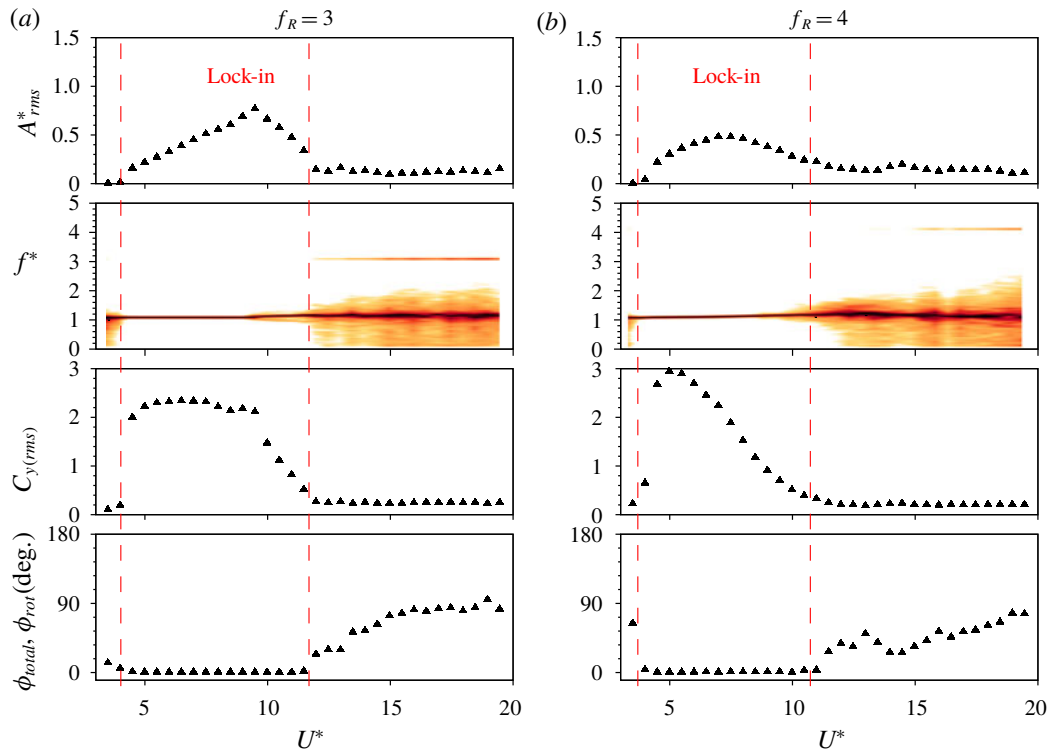


FIGURE 19. (Colour online) The response characteristics of an elastically mounted sphere with imposed rotary oscillations is presented as a function of reduced velocity for a fixed frequency ratio of  $f_R = 3$  (a) and  $f_R = 4$  (b) at a  $\alpha_R$  value of  $\alpha_R = 1$ . Refer to figure 4 for further details.

Nevertheless, it should be mentioned here that the vibrations observed in the current study are very different to the galloping response known for isolated non-circular bluff bodies, that is, a low frequency phenomenon observed at very high flow velocities (Blevins 1990; Zhao *et al.* 2014b). In contrast, in the current study, vibrations exhibiting RIV were always locked to the forcing frequency. It was also evident that monotonic increasing amplitudes were associated with the monotonic decreasing  $\phi_{rot}$  values (from  $\sim 180^\circ$  to lower values). It can be conjectured here based on this evidence that RIV will only occur in the  $U^*$  range where lock-on is observed. The case of monotonically decreasing  $\phi_{rot}$  values from  $\sim 180$  to lower values leads to monotonically increasing amplitude. In cases where  $\phi_{rot}$  remains constant, there is no appreciable increase in the vibration amplitude. In § 4.1, it was shown that the lock-on range varies with  $U^*$ , becoming narrower with increasing  $U^*$ . This leaves a very narrow window of  $f_R$  values where lock-on, and hence RIV, can be observed for the entire range of  $U^*$  tested in the current study.

In § 4.1, the results showed suppression of vibrations for very high frequency ( $f_R \geq 3$ ) and velocity ratios ( $\alpha_R \geq 1$ ), even in non-lock-on regions. The question arises as to whether a specific set of parameters leads to RIV or VIV, or both? To investigate this, high frequency ratios of  $f_R = 3$  and  $f_R = 4$  were also investigated. Figure 19 shows the response characteristics for  $f_R = 3$  (a) and  $f_R = 4$  (b). A wide lock-in region is evident for both the frequencies extending from  $\sim 4.5$  to  $\sim 11$ , with a corresponding jump in the  $C_{y(rms)}$ . As previously,  $\phi_{total}$  is fixed at  $0^\circ$  in the lock-in

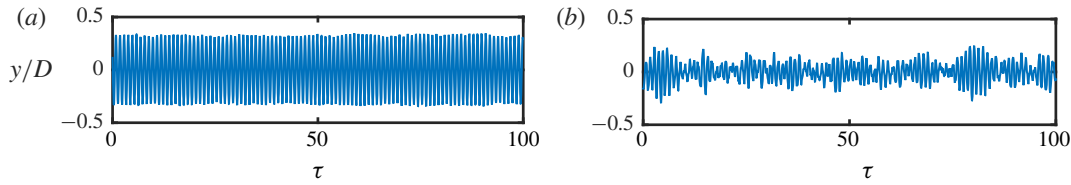


FIGURE 20. (Colour online) Time traces of the sphere displacement for  $U^* = 6$  (a) and  $U^* = 18$  (b) for  $f_R = 3$ .

region, and the time trace of the displacement signal is highly periodic, as shown in figure 20 (a). When  $U^*$  is increased beyond the lock-in region, the frequency contour plot shows a wide spectrum of frequencies. The frequency does not lock on to  $f_R$ , and nor is there a clean single frequency response at  $f^* = 1$ , as observed for lock-in. Interestingly,  $\phi_{total}$  approached  $90^\circ$  in this region. The time trace of the displacement signal shows a non-periodic signal in this range (see figure 20b).

### 5. Wake measurements

The VIV of a sphere is induced by streamwise vorticity, in contrast to its two-dimensional counterpart, the cylinder, whose dynamics is mainly induced by spanwise vorticity. PIV measurements in a plane normal to the flow can reveal important insights into the temporal evolution of the streamwise vorticity as the vortex loops pass through a cross-plane. Hence, the current study employs PIV measurements in the cross-plane at a distance of  $1.5D$  from the sphere's downstream surface, similar to that employed by Govardhan & Williamson (2005) and Sareen *et al.* (2018b). Figure 21 shows the vorticity contour plots, phase-averaged over more than 100 cycles, at four different phases of the oscillation cycle, separated by a quarter period, for a sphere without any imposed rotary oscillation. The plots are shown for a reduced velocity of  $U^* = 6$  (mode I). As evident from figure 21, the streamwise vorticity consists of a dominant counter-rotating vortex pair consistent with the legs of vortex loops forming on both the sides of the sphere wake (Sakamoto & Haniu 1990, Govardhan & Williamson 2005 and Sareen *et al.* 2018b). As the sphere traverses from one side to the other, the vorticity changes sign, corresponding to hairpin loops being shed downstream into the wake from opposite sides.

To understand how the wake structures differ in the lock-on region compared to the lock-in region, some representative cases were chosen in mode I to give an overview of the underlying associated wake dynamics. PIV measurements were also performed for a fixed velocity ratio of  $\alpha_R = 1$  at  $U^* = 6$  in mode I for four different  $f_R$  values. Considering the limitation of the present experimental set-up, measurements were not performed for very high  $U^*$  values, where very large vibration amplitudes are observed. Moreover, studying the wake in mode I should be sufficient to highlight some of the main features of the lock-on phenomenon. The chosen  $f_R$  values are as follows:  $f_R = 1$ , where all the dominant frequencies are equal, leading to amplitudes higher than for the non-rotating sphere;  $f_R = 0.9$  corresponding to a lock-on frequency just under  $f_R = 1$ ;  $f_R = 1.1$  corresponding to lock-on frequency just past  $f_R = 1$ ; and  $f_R = 3$ , corresponding to the lock-in region, where the amplitudes recover after the lock-on region.

Figure 22 shows the streamwise vorticity plots for four different phases, separated by a quarter period of the oscillation cycle, for  $f_R = 0.9$  at a velocity ratio of  $\alpha_R = 1$

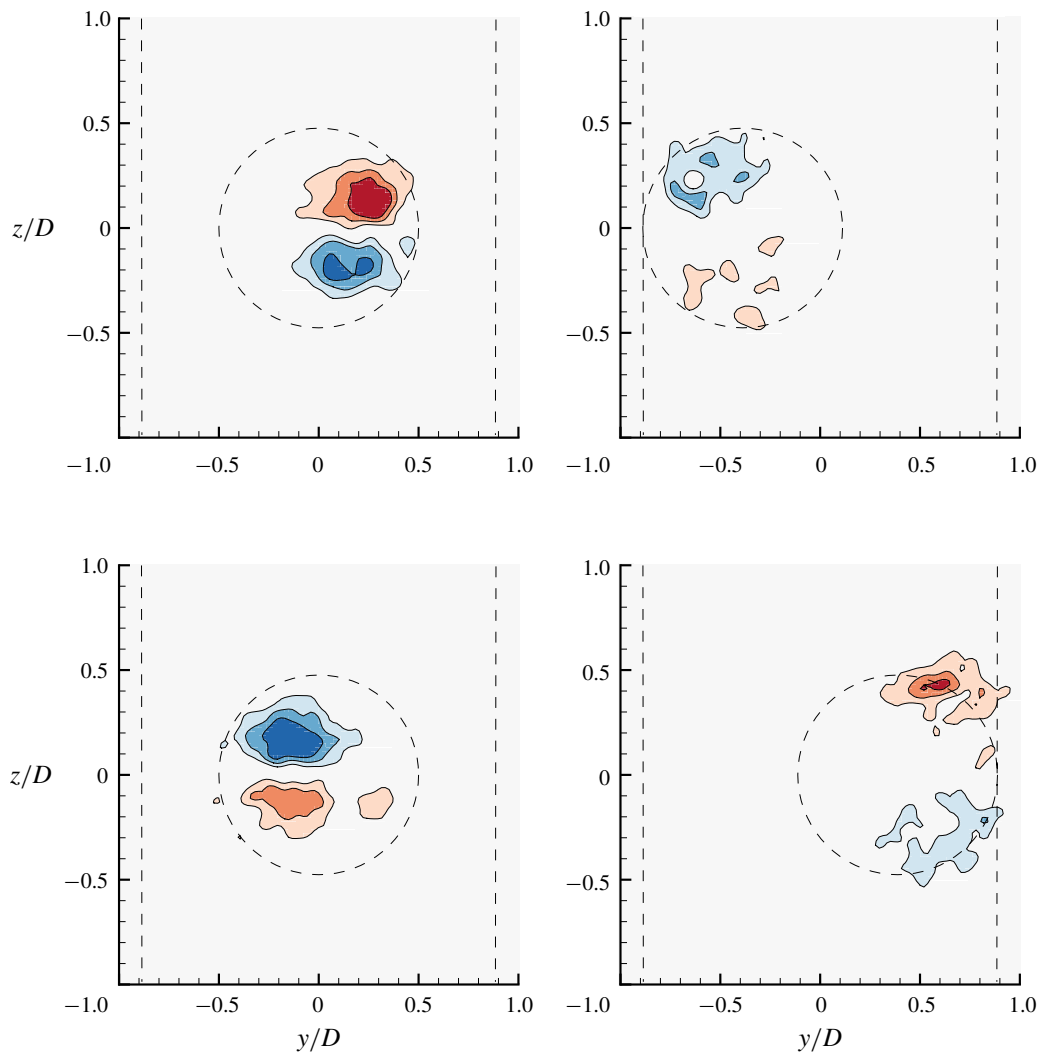


FIGURE 21. (Colour online) Streamwise vorticity plots showing the dominant counter-rotating vortex pair in mode I ( $U^* = 6$ ) without any imposed rotation. Each of these plots are separated by a quarter period, and were measured at a distance of  $x/D = 1.5$  from the sphere. The dashed lines show the maximum displacement of the sphere and the sphere location. Blue contours show clockwise vorticity, red anti-clockwise vorticity. The normalised vorticities vary in eight steps in the range  $\omega^* = \omega D/U \in [-3, 3]$ , where  $\omega$  is the vorticity.

in mode I. The position of the sphere (placed upstream) and the maximum extent of the sphere vibration have been marked in dashed lines. As evident from the plots, the wake consists of a counter-rotating vortex pair similar to the wake of a sphere without any imposed rotation. However, there is a slight change in the timing of the vortex formation. This finding is consistent with the fact that as the vibrations lock to the forcing frequency, there is a slight change in  $\phi_{total}$  as shown in figure 4.

When the streamwise vorticity for another lock-in frequency of  $f_R = 1.1$  is examined as shown in figure 23, a drastic change in the vortex formation timing is clearly evident. The plots are exactly  $180^\circ$  out of phase with the plots shown in figure 21

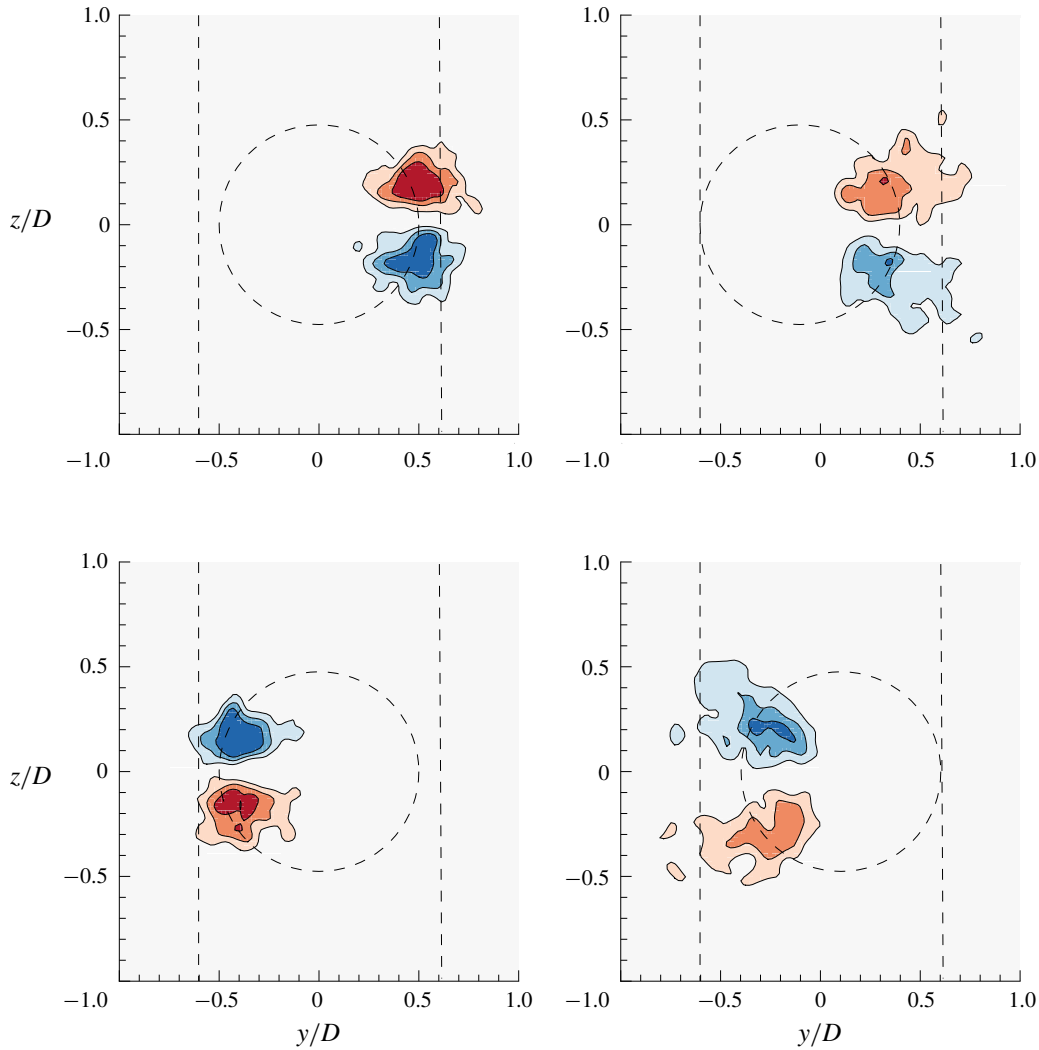


FIGURE 22. (Colour online) Streamwise vorticity plots showing the dominant counter-rotating vortex pair in mode I ( $U^* = 6$ ) for the frequency ratio of  $f_R = 0.9$  under lock-on. Refer to figure 21 for further details.

for a non-rotating sphere. This is congruent with the data reported in figure 4, where one can clearly see that  $\phi_{total}$  jumps from  $\sim 0^\circ$  to  $180^\circ$  as  $f_R$  increases from  $f_R = 1$  to  $f_R = 1.1$  in the lock-on range. To provide a better perspective on the wake structures, spatio-temporal reconstructions of the sphere wake were generated for the  $f_R = 1.1$  case and compared to the  $f_R = 0$  case, as shown in figure 24(b) and figure 24(a). The spatio-temporal reconstruction was generated from 24 cross-stream vorticity fields, each phase-averaged for more than 100 cycles. A convection velocity of  $U$  (free-stream velocity) was assumed to build the 3-D image. As evident in this case, the wake consists of an alternating two-sided chain of vortex loops, similar to the wake of an oscillating sphere with no imposed rotation reported by Govardhan & Williamson (2005) and Sareen *et al.* (2018b). Of course, this reconstruction should not be viewed as a typical image of the wake, since it is only representative of the average wake behaviour as it passes through a fixed downstream plane.

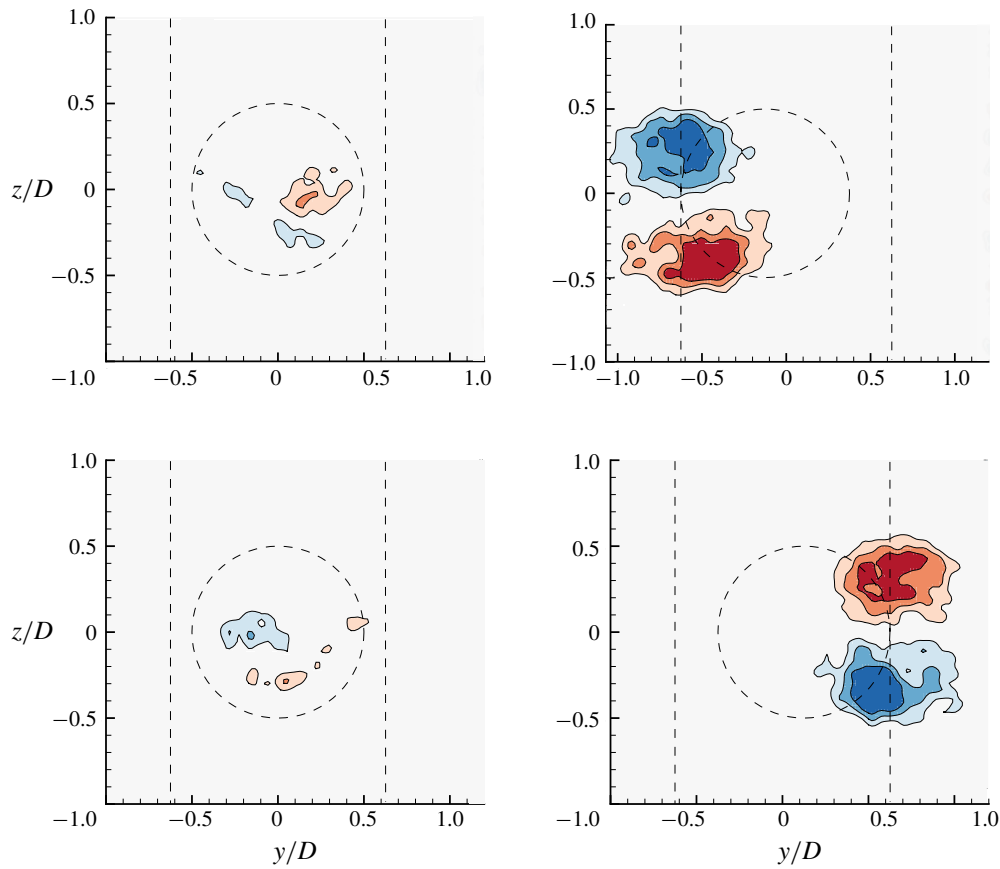
730 *A. Sareen, J. Zhao, J. Sheridan, K. Hourigan and M. C. Thompson*


FIGURE 23. (Colour online) Streamwise vorticity plots showing the dominant counter-rotating vortex pair in mode I ( $U^* = 6$ ) for  $f_R = 1.1$  during the lock-on phenomenon. Refer to figure 21 for further details.

On the other hand, the streamwise vorticity plot for  $f_R = 1$ , as shown in figure 25, is similar to that for a sphere without any imposed rotation; there is seen to be a similar timing of vortex (loop) shedding. Again, this is consistent with the data reported in figure 4. One can conclude here that there is a change in the timing of vortex formation as the vortex shedding locks to  $f_R$  with no appreciable change in the vortex structures. The streamwise vorticity field consists of a counter-rotating vortex pair which flips sign as the sphere traverses from one side to the other, as for the wake of a sphere with no imposed rotation. Another interesting case to examine is that of higher frequency ratios ( $f_R > 2$ ), where the vibrations lock in to  $f_{nw}$  again and the amplitude response recovers. Figure 26 shows streamwise vorticity plots for  $f_R = 3$  for the same parameters discussed earlier for other cases. The timing of vortex formation is similar to that for the non-rotating case. However, there is an evident reduction in the streamwise vorticity in this case. As also shown in figure 4, the vibration amplitude and the total transverse force coefficient are smaller than for the non-rotating case. Therefore, it can be concluded here that although the vibration frequency reverts to locking in to  $f_{nw}$  instead of  $f_r$  in this case, a reduction in the vibration amplitude could still be observed due to the reduction in the streamwise

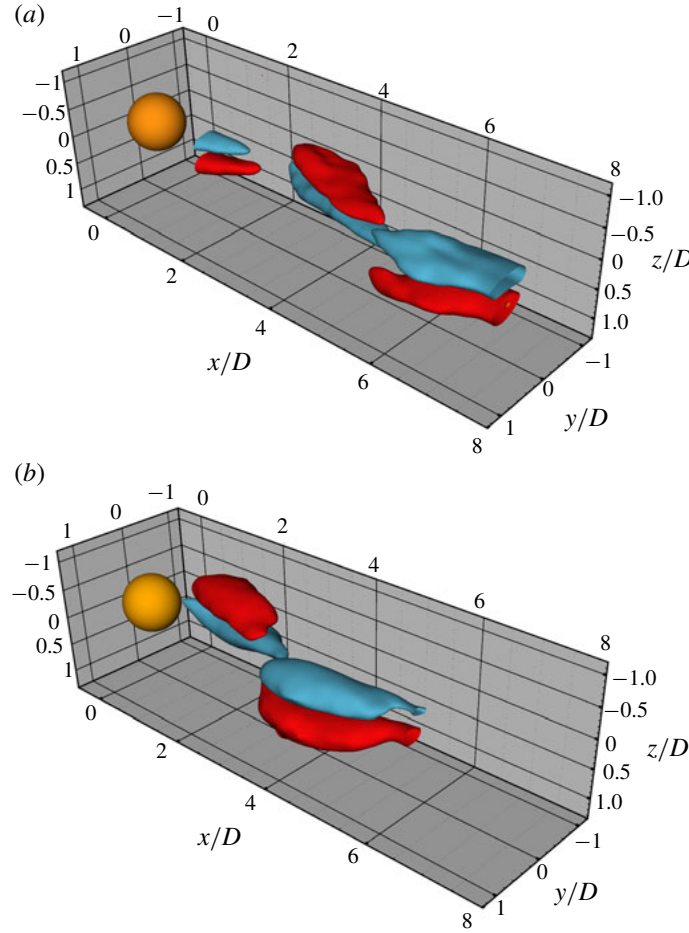


FIGURE 24. (Colour online) Three-dimensional spatio-temporal reconstruction of the sphere wake based on phase-averaged streamwise vorticity (crossing the transverse plane at a distance  $1.5D$  from the sphere rear surface) for (a)  $f_R = 0$  and (b)  $f_R = 1.1$  and  $\alpha_R = 1$  in the lock-in regime. The wake is shown for mode I ( $U^* = 6$ ), corresponding to a Reynolds number of  $\sim 8000$ . Blue indicates anti-clockwise vorticity, and red clockwise vorticity (both in the  $x-y$  plane). The figure clearly shows that the dominant wake structures remain the same for both the cases; however, there is a clear change in the timing of vortex shedding for  $f_R = 1.1$  compared to  $f_R = 0$ .

vorticity, in turn leading to a lower total transverse force acting on the sphere. The effect of high  $f_R$  is more pronounced in mode II and mode III, where the vibrations were highly suppressed, as shown in figures 9 and 10.

## 6. Conclusions

A comprehensive series of experiments and wake measurements were performed to examine the effect of imposed rotary oscillation on the FIV of a sphere that is elastically mounted in the cross-flow direction. The response was investigated for a wide range of forcing parameters, non-dimensional forcing frequency,  $f_R$ , in the range  $0 \leq f_R \leq 5$ , forcing amplitude,  $\alpha_R$ , in the range  $0 \leq \alpha_R \leq 2$ , and reduced velocity

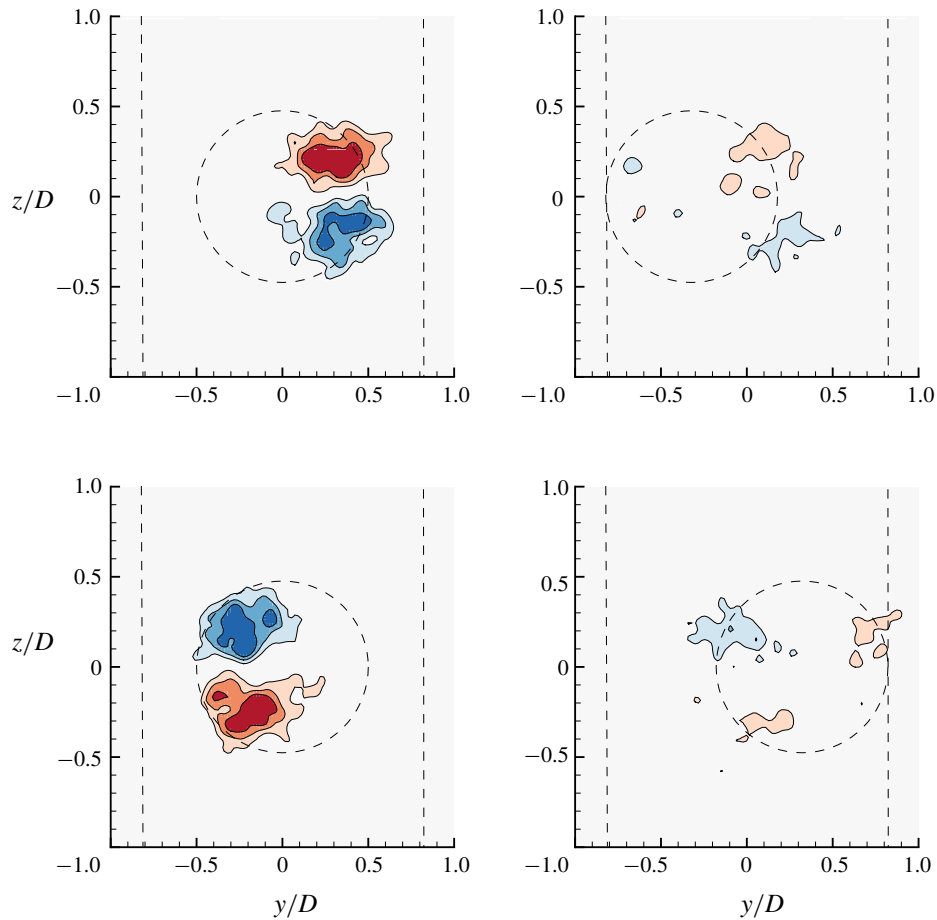
732 *A. Sareen, J. Zhao, J. Sheridan, K. Hourigan and M. C. Thompson*


FIGURE 25. (Colour online) Streamwise vorticity plots showing the dominant counter-rotating vortex pair in mode I ( $U^* = 6$ ) for a frequency ratio of  $f_R = 1.0$  under resonance. Refer to figure 21 for further details.

$U^*$  between  $0 \leq U^* \leq 20$ . It was found that when the forcing frequency  $f_r$  was in close proximity to the natural frequency  $f_{nw}$ , the vibrations locked on to  $f_r$  instead of  $f_{nw,l}$  inhibiting the resonance response. The vibrations were greatly suppressed in the lock-on region, except for the case when  $f_R = f_{nw}$ , where an ‘enhanced resonance’ response was observed leading to very large amplitudes, even greater than those observed for the non-rotating sphere in some cases. In the lock-on region, a sudden jump in the total phase was observed from  $0^\circ$  to  $180^\circ$ . The displacement signal was highly modulated in the non-lock-on regions. Near the lock-on boundaries, a wide spectrum of frequencies was observed. Interestingly, suppression was also observed in the non-lock-on regions for very high  $f_R$  and  $\alpha_R$  values. Mode I was found to be quite resistant to control, requiring very high velocity ratios for the suppression of vibrations. On the other hand, control (suppression) was most effective for mode III. Overall, relatively high velocity ratios (quantified in this paper) were required to suppress the vibrations. The width of the RLO region increased with an increase in  $\alpha_R$  for all three modes. When the reduced velocity was increased progressively, several types of responses with different characteristic behaviours were observed.



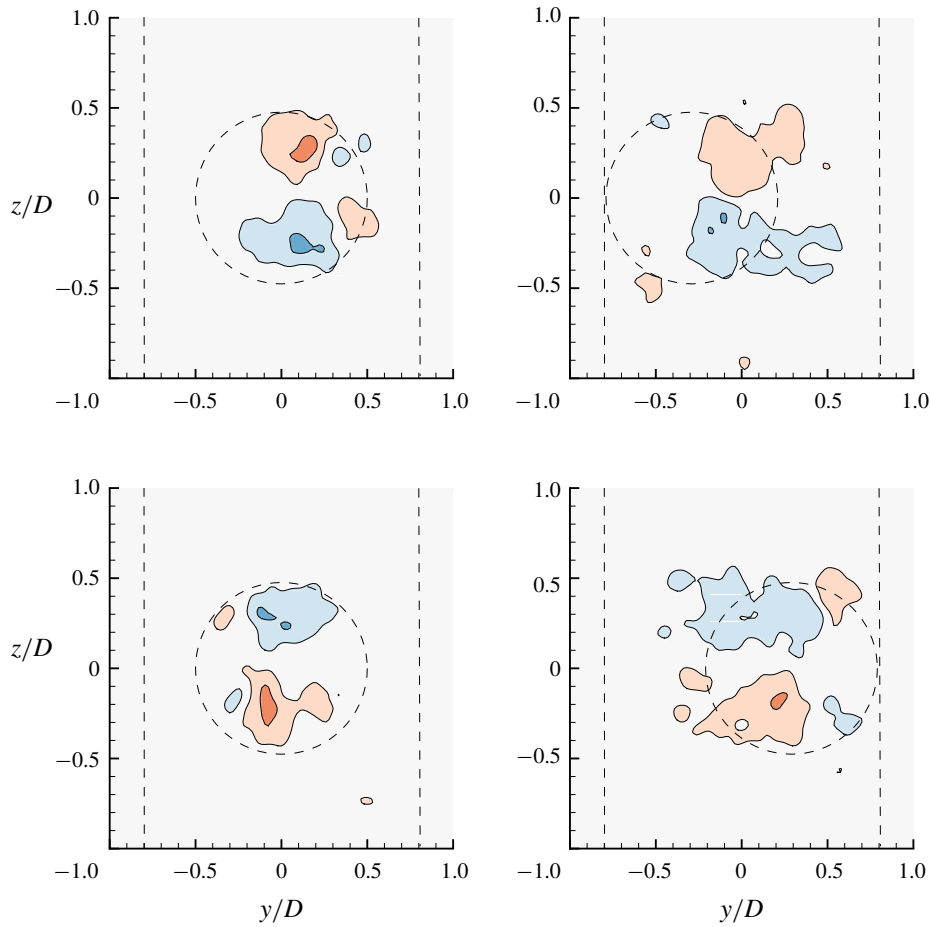


FIGURE 26. (Colour online) Streamwise vorticity plots showing the dominant counter-rotating vortex pair in mode I ( $U^* = 6$ ) for  $f_R = 3$ . Refer to figure 21 for further details.

For some cases, the vibration amplitudes increased monotonically with an increase in  $U^*$ . Such vibrations have been termed ‘rotary-induced vibrations’. The phase difference between the rotary oscillations and the sphere displacement  $\phi_{rot}$  was found to be crucial in determining the response. Monotonically decreasing  $\phi_{rot}$  values were always associated with the monotonically increasing responses. Wake measurements performed in the cross-plane revealed structures similar to those for an oscillating sphere without imposed rotation; however, there was a change in the timing of vortex formation. For a high frequency ratio of  $f_R = 3$ , there was a clear reduction in the streamwise vorticity consistent with a reduced amplitude response.

### Acknowledgements

A.S. acknowledges the support of a Monash Graduate Scholarship (MGS) and Monash International Postgraduate Research Scholarship (MIPRS). The research was supported by Australian Research Council Discovery Project grants DP150102879 and DP170100275. She also acknowledges the Postgraduate Publication Award (PPA). The current manuscript was revised and submitted during the award period. J.Z. also acknowledges post-doctoral salary support through the latter grants.



734 A. Sareen, J. Zhao, J. Sheridan, K. Hourigan and M. C. Thompson

## REFERENCES

- ASSI, G. R. S., BEARMAN, P. W. & MENEGHINI, J. R. 2010 On the wake-induced vibration of tandem circular cylinders: the vortex interaction excitation mechanism. *J. Fluid Mech.* **661**, 365–401.
- BAEK, S. J. & SUNG, H. J. 2000 Quasi-periodicity in the wake of a rotationally oscillating cylinder. *J. Fluid Mech.* **408**, 275–300.
- BEARMAN, P. W. 1984 Vortex shedding from oscillating bluff bodies. *Annu. Rev. Fluid Mech.* **16** (1), 195–222.
- BEHARA, S., BORAZJANI, I. & SOTIROPOULOS, F. 2011 Vortex-induced vibrations of an elastically mounted sphere with three degrees of freedom at  $Re = 300$ : hysteresis and vortex shedding modes. *J. Fluid Mech.* **686**, 426–450.
- BEHARA, S. & SOTIROPOULOS, F. 2016 Vortex-induced vibrations of an elastically mounted sphere: the effects of Reynolds number and reduced velocity. *J. Fluids Struct.* **66**, 54–68.
- BLEVINS, R. D. 1990 *Flow-Induced Vibration*, 2nd edn. Krieger Publishing Company.
- BOKAIAN, A. & GEOOLA, F. 1984 Wake-induced galloping of two interfering circular cylinders. *J. Fluid Mech.* **146**, 383–415.
- BRIKA, D. & LANEVILLE, A. 1999 The flow interaction between a stationary cylinder and a downstream flexible cylinder. *J. Fluids Struct.* **13** (5), 579–606.
- CHENG, M., CHEW, Y. T. & LUO, S. C. 2001 Numerical investigation of a rotationally oscillating cylinder in mean flow. *J. Fluids Struct.* **15** (7), 981–1007.
- CHOI, H., JEON, W. & KIM, J. 2008 Control of flow over a bluff body. *Annu. Rev. Fluid Mech.* **40**, 113–139.
- CHOI, S., CHOI, H. & KANG, S. 2002 Characteristics of flow over a rotationally oscillating cylinder at low Reynolds number. *Phys. Fluids* **14** (8), 2767–2777.
- CHOU, M. H. 1997 Synchronization of vortex shedding from a cylinder under rotary oscillation. *Comput. Fluids* **26** (8), 755–774.
- DONG, S., TRIANTAFYLLOU, G. S. & KARNIADAKIS, G. E. 2008 Elimination of vortex streets in bluff-body flows. *Phys. Rev. Lett.* **100** (20), 204501.
- DU, L. & SUN, X. 2015 Suppression of vortex-induced vibration using the rotary oscillation of a cylinder. *Phys. Fluids* **27** (2), 023603.
- FOURAS, A., LO JACONO, D. & HOURIGAN, K. 2008 Target-free stereo PIV: a novel technique with inherent error estimation and improved accuracy. *Exp. Fluids* **44** (2), 317–329.
- GOVARDHAN, R. & WILLIAMSON, C. H. K. 1997 Vortex-induced motions of a tethered sphere. *J. Wind Engng Ind. Aerodyn.* **69**, 375–385.
- GOVARDHAN, R. N. & WILLIAMSON, C. H. K. 2005 Vortex-induced vibrations of a sphere. *J. Fluid Mech.* **531**, 11–47.
- VAN HOUT, R., KRAKOVICH, A. & GOTTLIEB, O. 2010 Time resolved measurements of vortex-induced vibrations of a tethered sphere in uniform flow. *Phys. Fluids* **22** (8), 087101.
- JAUVTIS, N., GOVARDHAN, R. & WILLIAMSON, C. H. K. 2001 Multiple modes of vortex-induced vibration of a sphere. *J. Fluids Struct.* **15** (3–4), 555–563.
- KRAKOVICH, A., ESHBAL, L. & VAN HOUT, R. 2013 Vortex dynamics and associated fluid forcing in the near wake of a light and heavy tethered sphere in uniform flow. *Exp. Fluids* **54** (11), 1615.
- KUMAR, S., LOPEZ, C., PROBST, O., FRANCISCO, G., ASKARI, D. & YANG, Y. 2013 Flow past a rotationally oscillating cylinder. *J. Fluid Mech.* **735**, 307–346.
- LEE, H., HOURIGAN, K. & THOMPSON, M. C. 2013 Vortex-induced vibration of a neutrally buoyant tethered sphere. *J. Fluid Mech.* **719**, 97–128.
- LEE, S. & LEE, J. 2006 Flow structure of wake behind a rotationally oscillating circular cylinder. *J. Fluids Struct.* **22** (8), 1097–1112.
- LU, X. Y. & SATO, J. 1996 A numerical study of flow past a rotationally oscillating circular cylinder. *J. Fluids Struct.* **10** (8), 829–849.
- MAHFOUZ, F. M. & BADR, H. M. 2000 Flow structure in the wake of a rotationally oscillating cylinder. *Trans. ASME J. Fluids Engng* **122** (2), 290–301.

*The effect of imposed rotary oscillation on the FIV of a sphere* 735

- MITTAL, S. 2001 Control of flow past bluff bodies using rotating control cylinders. *J. Fluids Struct.* **15** (2), 291–326.
- NAUDASCHER, E. & ROCKWELL, D. 2012 *Flow-Induced Vibrations: An Engineering Guide*. Courier Corporation.
- PAÏDOUSSIS, M. P., PRICE, S. & DE LANGRE, E. 2010 *Fluid-Structure Interactions: Cross-Flow-Induced Instabilities*. Cambridge University Press.
- PREGNATALO, C. J. 2003 Flow-induced vibrations of a tethered sphere. PhD thesis, Monash University.
- SAKAMOTO, H. & HANIU, H. 1990 A study on vortex shedding from spheres in a uniform flow. *Trans. ASME J. Fluids Engng* **112**, 386–392.
- SAREEN, A., ZHAO, J., LO JACONO, D., SHERIDAN, J., HOURIGAN, K. & THOMPSON, M. C. 2018a Vortex-induced vibration of a rotating sphere. *J. Fluid Mech.* **837**, 258–292.
- SAREEN, A., ZHAO, J., SHERIDAN, J., HOURIGAN, K. & THOMPSON, M. C. 2018b Vortex-induced vibrations of a sphere close to a free surface. *J. Fluid Mech.* **846**, 1023–1058.
- SARPKAYA, T. 2004 A critical review of the intrinsic nature of vortex-induced vibrations. *J. Fluids Struct.* **19** (4), 389–447.
- SHIELDS, D. & LEONARD, A. 2001 Investigation of a drag reduction on a circular cylinder in rotary oscillation. *J. Fluid Mech.* **431**, 297–322.
- TANEDA, S. 1978 Visual observations of the flow past a circular cylinder performing a rotatory oscillation. *J. Phys. Soc. Japan* **45** (3), 1038–1043.
- THIRIA, B., GOUJON-DURAND, S. & WESFREID, J. E. 2006 The wake of a cylinder performing rotary oscillations. *J. Fluid Mech.* **560**, 123–147.
- TOKUMARU, P. T. & DIMOTAKIS, P. E. 1991 Rotary oscillation control of a cylinder wake. *J. Fluid Mech.* **224**, 77–90.
- VENNING, J. A. 2016 Vortex structures in the wakes of two- and three-dimensional bodies. PhD thesis, Monash University.
- WILLIAMSON, C. H. K. & GOVARDHAN, R. 1997 Dynamics and forcing of a tethered sphere in a fluid flow. *J. Fluids Struct.* **11** (3), 293–305.
- WILLIAMSON, C. H. K. & GOVARDHAN, R. 2004 Vortex-induced vibrations. *Annu. Rev. Fluid Mech.* **36** (1), 413–455.
- WONG, K. W. L., ZHAO, J., LO JACONO, D., THOMPSON, M. & SHERIDAN, J. 2018 Experimental investigation of flow-induced vibrations of a sinusoidally rotating circular cylinder. *J. Fluid Mech.* **848**, 430–466.
- ZHAO, J., LEONTINI, J. S., LO JACONO, D. & SHERIDAN, J. 2014a Chaotic vortex induced vibrations. *Phys. Fluids* **26** (12), 121702.
- ZHAO, J., LEONTINI, J. S., LO JACONO, D. & SHERIDAN, J. 2014b Fluid–structure interaction of a square cylinder at different angles of attack. *J. Fluid Mech.* **747**, 688–721.
- ZHAO, J., LO JACONO, D., SHERIDAN, J., HOURIGAN, K. & THOMPSON, M. C. 2018 Experimental investigation of in-line flow-induced vibration of a rotating circular cylinder. *J. Fluid Mech.* **847**, 664–699.



## Chapter 8

# Conclusions and Recommendations for Future Work

*The important thing is to never stop questioning*

---

Albert Einstein

This thesis endeavours to understand the effect of transverse rotation and rotary oscillation on the flow-induced vibration of a sphere and opens up the possibilities of utilising such methods as effective control mechanisms of regulating flow-induced vibration of a 3D bluff body. It also attempts to broaden the current understanding of the dynamic response of an elastically mounted sphere in close proximity to a free surface. However, inevitably, a number of new fundamental questions have also emerged from the current thesis. In this final chapter, the important conclusions are drawn in § 8.1, followed by § 8.2, where some of the newly emerged questions from this thesis are discussed along with some recommendations for future work to follow.

### 8.1 Conclusions

#### 8.1.1 VIV of a transversely rotating sphere

A comprehensive series of experiments and flow visualisations were performed to study the effect of transverse rotation on the VIV response of a sphere. The vibration response was studied for a wide parameter space of  $0 \leq \alpha \leq 7.5$  and  $3 \leq U^* \leq 18$ . Interestingly, unlike its two dimensional counterpart, the cylinder, the VIV response of the sphere reduced gradually and steadily with increasing rotation ratio, leading to an almost complete suppression for  $\alpha \geq 6.0$ . It was also found that the synchronisation regime became narrower with increasing  $\alpha$ , and the peak amplitude response gradually decreased almost linearly for  $\alpha \lesssim 1$ . The oscillation frequency remained close to the natural frequency of the system for all cases indicating that the vibrations remain locked-in for a transversely rotating sphere at least in the parameter space tested in the current study.

Furthermore, it was found that the oscillation amplitudes not only decreased but also the oscillations became less periodic with increasing rotation. Recurrence analysis of the structural vibration response demonstrated a transition from a periodic state to a

chaotic state in a modified recurrence map complementing the appearance of broadband spectra at the onset of bifurcation. The time-averaged displacement increased towards the retreating side of the sphere with increasing  $\alpha$ , due to an increase in the mean Magnus force. However, the peak fluctuating transverse force coefficient,  $C'_{y_{rms}}$ , was found to decrease consistently with the rotation rate, following a trend similar to that of the vibration amplitude.

Hydrogen-bubble visualisations and PIV measurements revealed that the sphere wake deflected progressively towards the advancing side as the rotation ratio was increased. Also, the flow was continuously drawn from the retreating side to the advancing side of the sphere with increasing rotation ratio, which led to fluid entrainment at the advancing side. This entrainment gave rise to a large-scale one-sided vortex shedding. For the rotation ratios where the VIV was found to be completely suppressed, the wake was found to be always deflected towards the advancing side with large-scale flow structures for all shedding cycles. The wake deflection towards the advancing side led to an increased Magnus force and mean sphere displacement towards the retreating side. A lack of an oscillating force acting on the sphere led to near suppression of the VIV.

### 8.1.2 Effect of free surface on the VIV response of a sphere

To study the effect of free surface, the sphere response was studied over a wide range of reduced velocities,  $3 \leq U^* \leq 20$ , and immersion ratios of  $-1 < h^* \leq 1$ . For a fully submerged sphere, the vibration amplitude decreased and the synchronisation region narrowed gradually with the decrease in the immersion ratio. Mode II occurred for progressively lower  $U^*$  values with decreasing  $h^*$ . In contrast, a different dynamics was observed for the semi-submerged sphere. Two regimes were identified showing different characteristic responses. In regime I ( $-0.5 < h^* < 0$ ), the synchronisation region widened and the vibration amplitude increased with decreasing  $h^*$ . However, in regime II ( $-0.5 \leq h^* < -1$ ), the vibration amplitude decreased with a decrease in  $h^*$ . The amplitude response in regime II was characterised by two distinct peaks corresponding to mode I and mode II of the vibration response unlike regime I, where the response gradually progressed from mode I to mode II similar to that of a fully submerged sphere.

The response was found to be relatively insensitive to the Froude number in the range tested ( $0.05 \leq Fr \leq 0.45$ ). The response curve shape was independent of  $Fr$  and the peak vibration amplitude only slightly reduced with increasing the Froude number. PIV wake measurements revealed reduction in vorticity of the upper vortex (closer to a free surface) of the longitudinal vortex pair due to vorticity diffusion into the free surface. For the piercing sphere case, only the lower vortex of the pair was visible at  $1.5D$  downstream; it appears that the upper vortex was effectively lost through diffusion into the free surface.

### 8.1.3 Effect of rotary oscillation on the VIV response of a sphere

To study the effect of rotary oscillation, the sphere response was investigated for a wide range of frequency ratios,  $0 \leq f_R \leq 5$ , forcing amplitude ratios,  $0 \leq \alpha_R \leq 2$ , and reduced velocities of  $0 \leq U^* \leq 20$ . It was found that when the forcing frequency ratio was close to 1, i.e., when the forcing frequency  $f_r$  was in close proximity to the natural frequency  $f_{nw}$ , the vibrations locked-on to  $f_r$  instead of  $f_{nw}$  inhibiting the resonance response. The vibrations were greatly suppressed in the lock-on region, except for the case when  $f_R = 1$ , where an ‘enhanced resonance’ response was observed leading to

very large amplitudes, even greater than those observed for the non-rotating sphere in some cases. In the lock-on region, a sudden jump in the total phase difference,  $\phi_{total}$ , was observed from  $0^\circ$  to  $180^\circ$ . The displacement signal was highly modulated in the non lock-on regions. Near the lock-on boundaries, a wide spectrum of frequencies was observed. Interestingly, suppression was also observed in the non lock-on regions for very high  $f_R$  and  $\alpha_R$  values. Mode I was found to be quite resistant to control requiring very high velocity ratios for the suppression of vibrations. On the other hand, control (suppression) was most effective for mode III. Overall, relatively high velocity ratios were required to suppress the vibrations. The width of the rotary lock-on region increased with an increase in  $\alpha_R$  for all three modes. When the reduced velocity was increased progressively, several types of responses with different characteristic behaviours were observed. For some cases, the vibration amplitudes increased monotonically with an increase in  $U^*$ . Such vibrations have been termed ‘Rotary induced vibrations’. The phase difference between the rotary oscillations and the sphere displacement  $\phi_{rot}$  was found to be crucial in determining the response. Wake measurements performed in the cross-plane revealed structures similar to those for an oscillating sphere without imposed rotation; however, there was a change in the timing of vortex formation. For high frequency ratios ( $f_R \geq 3$ ), there was a clear reduction in the streamwise vorticity consistent with a reduced amplitude response.

## 8.2 Recommendations for future work

### 8.2.1 Effect of rotary oscillation

- It was found in the current study that for a certain set of forcing parameters, rotary oscillation can instigate ‘Rotary-induced vibrations’ that are intrinsically different to other previously known FIV responses: combining vortex-induced vibrations and galloping. The phase difference between the rotary oscillation and the sphere displacement plays an important role in the dynamics; however, further research is needed to understand completely the dynamics of rotary induced vibration. It might be fairly complicated to understand this mechanism for a 3D wake of a sphere. However, it should be relatively easy to study this for 2D vortex shedding from a cylinder.
- Apart from imposing rotary oscillation onto a bluff body, there might be several other interesting ways of introducing forcing into the wake. Placing another static sphere upstream of an elastically mounted sphere is one possibility, where the interaction of the two wakes will presumably give rise to several types of FIV responses depending on the size and distance between the spheres. This study should be helpful in expanding the knowledge of FIV.

### 8.2.2 Effect of a free surface

- The current thesis investigated the response of a sphere in a close proximity to a free surface for a moderate range of Froude numbers. However, for relatively higher Froude numbers ( $Fr \geq 2$ ), there could be significant surface vorticity generation that can diffuse or convect into the main flow, altering the development of vortex shedding. For a 3D flow past a sphere at high Reynolds numbers, it could be complicated to capture the time-varying surface deformations and their effect on the 3D structures. Nevertheless, this remains open for future studies.

- It was found in the current study that the FIV response of a semi-submerged sphere is fairly sensitive to the change in the mass-damping compared to a fully-submerged sphere. However, due to limitations of the experimental set-up, it was not possible to quantify the effect of mass ratio at higher mass-damping ratios. It is recommended to investigate this in the future. Presumably, this might be relatively easy to implement in a numerical study.

### 8.2.3 Passive control

- Although passive control methods are extensively studied for a circular cylinder, such methods remain unexplored for a sphere. Depending on the practical situation, sometimes passive control is the most feasible and easy to implement control method. It is expected that simple geometric modifications like a trip wire or dimples on the sphere surface will not only reduce drag but also be able to limit vibrations. It is recommended that such VIV control methods for a sphere should be explored in the future.
- An MIT team (Terwagne *et al.* 2014) developed spherical balls with ‘*smart morphable surfaces*’ that can change their surface texture from smooth to dimpled and vice versa depending on the flow conditions. Made of soft polymer with a hollow centre and a thin coating of a stiffer polymer, the sphere becomes dimpled when the air is pumped out of the hollow centre, causing it to shrink. Increasing pressure returns the surface to a smooth state. Using this, they were able to control the drag of a sphere by up to a factor of two, over a range of flow conditions. It is expected that such approaches may provide real-time control of VIV for a wide range of Reynolds numbers. It is recommended that such innovative methods should be explored in the future as a means to control flow-induced vibration.

# References

- ADRIAN, R. J. 1991 Particle-imaging techniques for experimental fluid mechanics. *Annual Review of Fluid Mechanics* **23** (1), 261–304.
- ARISTOFF, J. M. & BUSH, J. W. M. 2009 Water entry of small hydrophobic spheres. *Journal of Fluid Mechanics* **619**, 45–78.
- ARISTOFF, J. M., TRUSCOTT, T. T., TECHET, A. H. & BUSH, J. W. M. 2010 The water entry of decelerating spheres. *Physics of Fluids* **22** (3), 032102.
- ASSI, G. R. S., BEARMAN, P. W. & MENEGHINI, J. R. 2010 On the wake-induced vibration of tandem circular cylinders: the vortex interaction excitation mechanism. *Journal of Fluid Mechanics* **661**, 365–401.
- BAEK, S. J. & SUNG, H. J. 2000 Quasi-periodicity in the wake of a rotationally oscillating cylinder. *Journal of Fluid Mechanics* **408**, 275–300.
- BARLOW, J. B. & DOMANSKI, M. J. 2008 Lift on stationary and rotating spheres under varying flow and surface conditions. *AIAA Journal* **46** (8), 1932–1936.
- BEARMAN, P. W. 1984 Vortex shedding from oscillating bluff bodies. *Annual Review of Fluid Mechanics* **16** (1), 195–222.
- BEHARA, S., BORAZJANI, I. & SOTIROPOULOS, F. 2011 Vortex-induced vibrations of an elastically mounted sphere with three degrees of freedom at  $Re = 300$ : hysteresis and vortex shedding modes. *Journal of Fluid Mechanics* **686**, 426–450.
- BEHARA, S. & SOTIROPOULOS, F. 2016 Vortex-induced vibrations of an elastically mounted sphere: The effects of Reynolds number and reduced velocity. *Journal of Fluids and Structures* **66**, 54–68.
- BLEVINS, R. D. 1990 *Flow-Induced Vibration*, 2nd edn. Malabar: Krieger Publishing Company.
- BOKAIAN, A. & GEOOLA, F. 1984 Wake-induced galloping of two interfering circular cylinders. *Journal of Fluid Mechanics* **146**, 383–415.
- BOURGUET, R. & LO JACONO, D. 2014 Flow-induced vibrations of a rotating cylinder. *Journal of Fluid Mechanics* **740**, 342–380.
- BRIKA, D. & LANEVILLE, A. 1999 The flow interaction between a stationary cylinder and a downstream flexible cylinder. *Journal of Fluids and Structures* **13** (5), 579–606.
- CHENG, M., CHEW, Y. T. & LUO, S. C. 2001 Numerical investigation of a rotationally oscillating cylinder in mean flow. *Journal of Fluids and Structures* **15** (7), 981–1007.



## References

---

- CHOI, H., JEON, W. & KIM, J. 2008 Control of flow over a bluff body. *Annual Review of Fluid Mechanics* **40**, 113–139.
- CHOI, S., CHOI, H. & KANG, S. 2002 Characteristics of flow over a rotationally oscillating cylinder at low Reynolds number. *Physics of Fluids* **14** (8), 2767–2777.
- CHOU, M. H. 1997 Synchronization of vortex shedding from a cylinder under rotary oscillation. *Computers and Fluids* **26** (8), 755–774.
- DE OLIVEIRA BARBOSA, J. M., QU, Y., METRIKINE, A. V. & LOURENS, E. 2017 Vortex-induced vibrations of a freely vibrating cylinder near a plane boundary: Experimental investigation and theoretical modelling. *Journal of Fluids and Structures* **69**, 382–401.
- DONG, S., TRIANTAFYLLOU, G. S. & KARNIADAKIS, G. E. 2008 Elimination of vortex streets in bluff-body flows. *Physical Review Letters* **100** (20), 204501.
- DU, L. & SUN, X. 2015 Suppression of vortex-induced vibration using the rotary oscillation of a cylinder. *Physics of Fluids* **27** (2), 023603.
- FENG, C. C. 1968 The measurement of vortex induced effects in flow past stationary and oscillating circular and D-section cylinders. PhD thesis, University of British Columbia.
- FOURAS, A., LO JACONO, D. & HOURIGAN, K. 2008 Target-free stereo PIV: a novel technique with inherent error estimation and improved accuracy. *Experiments in Fluids* **44** (2), 317–329.
- FOURAS, A. & SORIA, J. 1998 Accuracy of out-of-plane vorticity measurements derived from in-plane velocity field data. *Experiments in Fluids* **25** (5-6), 409–430.
- GHARIB, M. R., LEONARD, A., GHARIB, M. & ROSHKO, A. 1998 The absence of lock-in and the role of mass ratio. In *Proceedings of the 1998 Conference on Bluff-Body Wakes and Vortex-Induced Vibration*. Cornell University Ithaca.
- GHIDERSA, B. & DUŠEK, J. 2000 Breaking of axisymmetry and onset of unsteadiness in the wake of a sphere. *Journal of Fluid Mechanics* **423**, 33–69.
- GOVARDHAN, R. N. & WILLIAMSON, C. H. K. 1997 Vortex-induced motions of a tethered sphere. *Journal of Wind Engineering and Industrial Aerodynamics* **69**, 375–385.
- GOVARDHAN, R. N. & WILLIAMSON, C. H. K. 2000 Modes of vortex formation and frequency response of a freely vibrating cylinder. *Journal of Fluid Mechanics* **420**, 85–130.
- GOVARDHAN, R. N. & WILLIAMSON, C. H. K. 2005 Vortex-induced vibrations of a sphere. *Journal of Fluid Mechanics* **531**, 11–47.
- GUMOWSKI, K., MIEDZIK, J., GOUJON-DURAND, S., JENFFER, P. & WESFREID, J. E. 2008 Transition to a time-dependent state of fluid flow in the wake of a sphere. *Physical Review E* **77** (5), 055308.
- VAN HOUT, R., KATZ, A. & GREENBLATT, D. 2013 Time-resolved particle image velocimetry measurements of vortex and shear layer dynamics in the near wake of a tethered sphere. *Physics of Fluids* **25** (7), 077102.

- HOVER, F. S., DAVIS, J. T. & TRIANTAFYLLOU, M. S. 2004 Three-dimensionality of mode transition in vortex-induced vibrations of a circular cylinder. *European Journal of Mechanics-B/Fluids* **23** (1), 29–40.
- HOVER, F. S., MILLER, S. N. & TRIANTAFYLLOU, M. S. 1997 Vortex-induced vibration of marine cables: experiments using force feedback. *Journal of Fluids and Structures* **11** (3), 307–326.
- HOVER, F. S., TECHET, A. H. & TRIANTAFYLLOU, M. S. 1998 Forces on oscillating uniform and tapered cylinders in cross flow. *Journal of Fluid Mechanics* **363**, 97–114.
- INOUE, M., BABA, N. & HIMENO, Y. 1993 Experimental and numerical study of viscous flow field around an advancing vertical circular cylinder piercing a free-surface. *Journal of the Kansai Society of Naval Architects of Japan* **220**, 57–64.
- JAUVTIS, N., GOVARDHAN, R. N. & WILLIAMSON, C. H. K. 2001 Multiple modes of vortex-induced vibration of a sphere. *Journal of Fluids and Structures* **15** (3-4), 555–563.
- JOHNSON, T. A. & PATEL, V. C. 1999 Flow past a sphere up to a Reynolds number of 300. *Journal of Fluid Mechanics* **378**, 19–70.
- KAWAMURA, T., MAYER, S., GARAPON, A. & SORENSEN, L. 2002 Large eddy simulation of a flow past a free surface piercing circular cylinder. *Journal of Fluids Engineering* **124** (1), 91–101.
- KHALAK, A. & WILLIAMSON, C. 1997 Fluid forces and dynamics of a hydroelastic structure with very low mass and damping. *Journal of Fluids and Structures* **11** (8), 973–982.
- KHALAK, A. & WILLIAMSON, C. H. K. 1996 Dynamics of a hydroelastic cylinder with very low mass and damping. *Journal of Fluids and Structures* **10** (5), 455–472.
- KHALAK, A. & WILLIAMSON, C. H. K. 1999 Motions, forces and mode transitions in vortex-induced vibrations at low mass-damping. *Journal of Fluids and Structures* **13** (7-8), 813–851.
- KIM, D. 2009 Laminar flow past a sphere rotating in the transverse direction. *Journal of Mechanical Science and Technology* **23** (2), 578–589.
- KIM, J., CHOI, H., PARK, H. & YOO, J. Y. 2014 Inverse Magnus effect on a rotating sphere: when and why. *Journal of Fluid Mechanics* **754**, R2.
- KRAKOVICH, A., ESHBAL, L. & VAN HOUT, R. 2013 Vortex dynamics and associated fluid forcing in the near wake of a light and heavy tethered sphere in uniform flow. *Experiments in Fluids* **54** (11), 1615.
- KRAY, T., FRANKE, J. & FRANK, W. 2012 Magnus effect on a rotating sphere at high Reynolds numbers. *Journal of Wind Engineering and Industrial Aerodynamics* **110**, 1–9.
- KUMAR, S., LOPEZ, C., PROBST, O., FRANCISCO, G., ASKARI, D. & YANG, Y. 2013 Flow past a rotationally oscillating cylinder. *Journal of Fluid Mechanics* **735**, 307–346.

## References

---

- LEE, H., HOURIGAN, K. & THOMPSON, M. C. 2013 Vortex-induced vibration of a neutrally buoyant tethered sphere. *Journal of Fluid Mechanics* **719**, 97–128.
- LEE, S. & LEE, J. 2006 Flow structure of wake behind a rotationally oscillating circular cylinder. *Journal of Fluids and Structures* **22** (8), 1097–1112.
- LEWEKE, T., PROVANSAL, M., ORMIERES, D. & LEBESCOND, R. 1999 Vortex dynamics in the wake of a sphere. *Physics of Fluids* **11** (9), S12–S12.
- LIGHTHILL, J. 1986 Fundamentals concerning wave loading on offshore structures. *Journal of Fluid Mechanics* **173**, 667–681.
- LOTH, E. 2008 Lift of a spherical particle subject to vorticity and/or spin. *AIAA Journal* **46** (4), 801–809.
- LU, X. Y. & SATO, J. 1996 A numerical study of flow past a rotationally oscillating circular cylinder. *Journal of Fluids and Structures* **10** (8), 829–849.
- MACOLL, J. W. 1928 Aerodynamics of a spinning sphere. *Journal of the Royal Aeronautical Society* **28**, 777–798.
- MAGARVEY, R. H. & BISHOP, R. L. 1961 Transition ranges for three-dimensional wakes. *Canadian Journal of Physics* **39** (10), 1418–1422.
- MAHFOUZ, F. M. & BADR, H. M. 2000 Flow structure in the wake of a rotationally oscillating cylinder. *Transactions-American Society of Mechanical Engineers Journal of Fluids Engineering* **122** (2), 290–301.
- MIRAUDA, D., PLANTAMURA, A. V. & MALAVASI, S. 2014 Dynamic response of a sphere immersed in a shallow water flow. *Journal of Offshore Mechanics and Arctic Engineering* **136** (2), 021101.
- MITTAL, S. 2001 Control of flow past bluff bodies using rotating control cylinders. *Journal of Fluids and Structures* **15** (2), 291–326.
- MOE, G. & WU, Z. 1990 The lift force on a cylinder vibrating in a current. *Journal of Offshore Mechanics and Arctic Engineering* **112** (4), 297–303.
- NAKAMURA, I. 1976 Steady wake behind a sphere. *Physics of Fluids* **19** (1), 5–8.
- NAUDASCHER, E. & ROCKWELL, D. 2012 *Flow-Induced Vibrations: An Engineering Guide*. Courier Corporation.
- PAÏDOUSSIS, M. P., PRICE, S. & DE LANGRE, E. 2010 *Fluid-Structure Interactions: Cross-Flow-Induced Instabilities*. Cambridge University Press.
- POON, E. K. W., OOI, A. S., GIACOBELLO, M., IACCARINO, G. & CHUNG, D. 2014 Flow past a transversely rotating sphere at Reynolds numbers above the laminar regime. *Journal of Fluid Mechanics* **759**, 751–781.
- POON, E. K. W., OOI, A. S. H., GIACOBELLO, M. & COHEN, R. C. Z. 2010 Laminar flow structures from a rotating sphere: effect of rotating axis angle. *Int. J. Heat Fluid Flow* **31** (5), 961–972.
- PREGNATALO, C. J. 2003 Flow-induced vibrations of a tethered sphere. PhD thesis, Monash University.

- RAFFEL, M., WILLERT, C. E., KOMPENHANS, J. *et al.* 2007 *Particle image velocimetry: a practical guide*. Springer Science & Business Media.
- REICHL, P., HOURIGAN, K. & THOMPSON, M. C. 2005 Flow past a cylinder close to a free surface. *Journal of Fluid Mechanics* **533**, 269–296.
- SAKAMOTO, H. & HANIU, H. 1990 A study on vortex shedding from spheres in a uniform flow. *ASME, Transactions, Journal of Fluids Engineering* **112**, 386–392.
- SAREEN, A., ZHAO, J., LO JACONO, D., SHERIDAN, J. & THOMPSON, M. C. 2018a Vortex-induced vibration of a rotating sphere. *Journal of Fluid Mechanics* **837**, 258–292.
- SAREEN, A., ZHAO, J., SHERIDAN, J., HOURIGAN, K. & THOMPSON, M. C. 2018b Vortex-induced vibrations of a sphere close to a free surface. *Journal of Fluid Mechanics* **846**, 1023–1058.
- SARPKAYA, T. 2004 A critical review of the intrinsic nature of vortex-induced vibrations. *Journal of Fluids and Structures* **19** (4), 389–447.
- SEYED-AGHAZADEH, B. & MODARRES-SADEGHI, Y. 2015 An experimental investigation of vortex-induced vibration of a rotating circular cylinder in the crossflow direction. *Physics of Fluids* **27** (6), 067101.
- SHERIDAN, J., LIN, J. C. & ROCKWELL, D. 1995 Metastable states of a cylinder wake adjacent to a free surface. *Physics of Fluids* **7** (9), 2099–2101.
- SHERIDAN, J., LIN, J. C. & ROCKWELL, D. 1997 Flow past a cylinder close to a free surface. *Journal of Fluid Mechanics* **330**, 1–30.
- SHIELS, D. & LEONARD, A. 2001 Investigation of a drag reduction on a circular cylinder in rotary oscillation. *Journal of Fluid Mechanics* **431**, 297–322.
- SUMER, B. MUTLU, F. J. 2006 *Advanced Series on Ocean Engineering, Volume 26: Hydrodynamics around Cylindrical Structures (Revised Edition)*. World Scientific.
- TANAKA, T., YAMAGATA, K. & TSUJI, Y. 1990 Experiment of fluid forces on a rotating sphere and spheroid. *Proc. 2nd KSME-JSME Fluids Engineering Conference* **1**, 366.
- TANEDA, S. 1956 Experimental investigation of the wake behind a sphere at low Reynolds numbers. *Journal of the Physical Society of Japan* **11** (10), 1104–1105.
- TANEDA, S. 1978 Visual observations of the flow past a circular cylinder performing a rotatory oscillation. *Journal of the Physical Society of Japan* **45** (3), 1038–1043.
- TECHET, A. H., HOVER, F. S. & TRIANTAFYLLOU, M. S. 1998 Vortical patterns behind a tapered cylinder oscillating transversely to a uniform flow. *Journal of Fluid Mechanics* **363**, 79–96.
- TERWAGNE, D., BROJAN, M. & REIS, P. M. 2014 Smart morphable surfaces for aerodynamic drag control. *Advanced materials* **26** (38), 6608–6611.
- THIRIA, B., GOUJON-DURAND, S. & WESFREID, J. E. 2006 The wake of a cylinder performing rotary oscillations. *Journal of Fluid Mechanics* **560**, 123–147.

## References

---

- THOMPSON, M. C., LEWEKE, T. & PROVANSAL, M. 2001 Kinematics and dynamics of sphere wake transition. *Journal of Fluids and Structures* **15** (3), 575–585.
- TOKUMARU, P. T. & DIMOTAKIS, P. E. 1991 Rotary oscillation control of a cylinder wake. *Journal of Fluid Mechanics* **224**, 77–90.
- TOMBOULIDES, A. G. & ORSZAG, S. 2000 Numerical investigation of transitional and weak turbulent flow past a sphere. *Journal of Fluid Mechanics* **416**, 45–73.
- TRUSCOTT, T. T. & TECHET, A. H. 2009a A spin on cavity formation during water entry of hydrophobic and hydrophilic spheres. *Physics of Fluids* **21** (12), 121703.
- TRUSCOTT, T. T. & TECHET, A. H. 2009b Water entry of spinning spheres. *Journal of Fluid Mechanics* **625**, 135–165.
- TSUJI, Y., MORIKAWA, Y. & MIZUNO, O. 1985 Experimental measurement of the Magnus force on a rotating sphere at low Reynolds numbers. *Journal of Fluids Engineering* **107** (4), 484–488.
- VAN HOUT, R., KRAKOVICH, A. & GOTTLIEB, O. 2010 Time resolved measurements of vortex-induced vibrations of a tethered sphere in uniform flow. *Physics of Fluids* **22** (8), 087101.
- WILLIAMSON, C. H. K. & GOVARDHAN, R. N. 1997 Dynamics and forcing of a tethered sphere in a fluid flow. *Journal of Fluids and Structures* **11** (3), 293–305.
- WILLIAMSON, C. H. K. & GOVARDHAN, R. N. 2004 Vortex-Induced Vibrations. *Annual Review of Fluid Mechanics* **36** (1), 413–455.
- WONG, K. W. L., ZHAO, J., LO JACONO, D., THOMPSON, M. & SHERIDAN, J. 2018 Experimental investigation of flow-induced vibrations of a sinusoidally rotating circular cylinder. *Journal of Fluid Mechanics* (accepted on 30 April 2018) .
- WONG, K. W. L., ZHAO, J., LO JACONO, D., THOMPSON, M. C. & SHERIDAN, J. 2017 Experimental investigation of flow-induced vibration of a rotating circular cylinder. *Journal of Fluid Mechanics* **829**, 486–511.
- YU, G., AVITAL, E. J. & WILLIAMS, J. J. 2008 Large eddy simulation of flow past free surface piercing circular cylinders. *Journal of Fluids Engineering* **130** (10), 101304.
- ZHAO, J. 2012 Flow-induced vibration of circular and square cylinders with low mass and damping. PhD thesis, Monash University.
- ZHAO, J., LEONTINI, J. S., LO JACONO, D. & SHERIDAN, J. 2014a Fluid–structure interaction of a square cylinder at different angles of attack. *Journal of Fluid Mechanics* **747**, 688–721.
- ZHAO, J., LO JACONO, D., SHERIDAN, J., HOURIGAN, K. & THOMPSON, M. C. 2018 Experimental investigation of in-line flow-induced vibration of a rotating circular cylinder. *Journal of Fluid Mechanics* (accepted on 23 April 2018) .
- ZHAO, M., CHENG, L. & LU, L. 2014b Vortex induced vibrations of a rotating circular cylinder at low Reynolds number. *Physics of Fluids* **26** (7), 073602.